In-Situ Manipulation during Positron Lifetime Spectroscopy in Polymers and Nanoscopic Layers

M.Sc. Ricardo Helm

Vollständiger Abdruck der von dem Institut für Luft- und Raumfahrttechnik der Universität der Bundeswehr München zur Erlangung des akademischen Grades eines

Doktors der Naturwissenschaften (Dr. rer. nat.)

angenommenen Dissertation.

Vorsitzender:	Prof. Dr.-Ing Michael Johlitz
1. Gutachter:	Prof. Dr. rer. nat. Günther Dollinger
2. Gutachter:	Prof. Dr. Roberto S. Brusa

Die Dissertation wurde am 28.11.25 bei der Universität der Bundeswehr München eingereicht und durch die Fakultät für Luft- und Raumfahrttechnik am 19.03.26 angenommen. Die mündliche Prüfung fand am 21.04.26 statt.

Abstract

This dissertation first outlines the relevant physical foundations of positron annihilation spectroscopy (PAS) and subsequently extends the applicability of the method through the development of novel in-situ approaches and technical improvements, enabling investigations under realistic environmental conditions and at buried interfaces.

In the first part, a new instrument – the Temperature–Atmosphere Positron InstRument (TAPIR) – was developed to investigate polymers under controlled gas pressure and variable temperature. Initial measurements on polystyrene in an argon atmosphere showed strong pressure and temperature effects on the free volume, with clearly different behavior observed in the glassy and rubbery states. These results confirm the strong influence of gas infiltration on the free volume of polymers and establish TAPIR as a versatile platform for studying technologically relevant systems such as membrane materials for gas separation, CO_2 capture, and water desalination.

The second part presents recent upgrades to the Pulsed Low Energy Positron System (PLEPS) at FRM-II. These include improved shielding and electrical insulation of the target station, which increased the maximum implantation energy from 18 keV to 21 keV. In addition, the target station was equipped with a broadband plasma-driven light source and three power lines connected to the sample holder, enabling sample illumination, the application of a bias voltage, and the measurement of currents or voltages across the sample.

Together, these developments significantly expand the experimental capabilities of PLEPS, enabling more advanced studies of semiconductor thin-films and electronically active systems, as well as high-Z materials such as tungsten and reactor steels, where bulk defects must be clearly distinguished from surface effects.

The third part introduces drift-assisted positron annihilation lifetime spectroscopy (DA-PALS), which uses externally applied electric fields to steer positrons toward or away from interfaces. Proof-of-concept measurements on $Al/SiO_2/Si$ revealed distinct defect populations and clear asymmetries between the silicon and oxide sides of the interface. These results show that DA-PALS can resolve defect structures in nanoscopic buried layers and interfaces that conventional positron annihilation spectroscopy cannot access, enabling advanced characterization of ultrathin oxides, semiconductor surface regions, and interfaces in modern transistor architectures such as

thin-film transistors, two-dimensional devices, and semiconductor heterostructures.

Overall, this work shows how methodological and instrumental advances in PAS broaden its applicability to both soft matter under realistic environmental conditions and electronic materials at the limits of miniaturization. The results open new experimental pathways for the quantitative investigation of defect structures that are crucial for energy technologies, environmental science, and next-generation semiconductor devices.

Zusammenfassung

Die in dieser Dissertation präsentierten Ergebnisse erweitern den Anwendungsbereich der Positronenannihilationslebensdauerspektroskopie (PALS), indem neue in-situ-Ansätze und technische Verbesserungen entwickelt wurden, die Defektuntersuchungen unter realistischen Umgebungsbedingungen sowie an vergrabenen Grenzflächen ermöglichen.

In dieser Arbeit wurde das Laborinstrument TAPIR (Temperature–Atmosphere Positron Instrument) entwickelt, das PALS-Messungen an Polymeren unter kontrolliertem Gasdruck und variabler Temperatur erlaubt. Erste Experimente an Polystyrol unter Argonatmosphäre belegten deutliche Druck- und Temperatureinflüsse auf das freie Volumen, wobei sich charakteristische Unterschiede zwischen Glas- und gummielastischer Phase zeigten. Diese Ergebnisse verdeutlichen den Einfluss der Gasinfiltration auf die Nanostruktur polymerer Materialien und etablieren TAPIR als vielseitige Plattform für die Untersuchung technologisch relevanter Systeme wie Membranen zur Gasseparation, CO_2-Abscheidung und Meerwasserentsalzung.

Am Pulsed Low Energy Positron System (PLEPS) des FRM-II wurden darüber hinaus technische Erweiterungen implementiert, darunter eine verbesserte Abschirmung und Isolierung der Hochspannungseinheit für einen Betrieb bis 21 kV sowie die Einführung einer Probenvorspannung für PALS-Messungen unter elektrischer Belastung. Die erhöhte Beschleunigungsspannung vergrößert die zugängliche Eindringtiefe und ermöglicht zuverlässigere Analysen von Materialien mit hoher Ordnungszahl wie Wolfram oder Reaktorstählen, bei denen eine eindeutige Trennung von Bulk- und Oberflächeneffekten erforderlich ist.

Mit der Entwicklung der driftunterstützten Positronenlebensdauerspektroskopie (DA-PALS) wurde zudem ein neues Verfahren etabliert, das externe elektrische Felder einsetzt, um das Implantationsprofil der Positronen gezielt zu beeinflussen. Machbarkeitsstudien am Schichtsystem $Al/SiO_2/Si$-Kondensatoren zeigten unterschiedliche Defektpopulationen und asymmetrische Eigenschaften zwischen Silizium- und Oxidseite der Grenzfläche. Damit demonstriert DA-PALS das Potenzial, Defektstrukturen in nanoskopischen Schichten und Grenzschichten aufzulösen, die mit konventionellen PALS-Methoden nur eingeschränkt zugänglich sind und eröffnet neue Perspektiven für die Charakterisierung ultradünner Oxid- und Grenzschichten in modernen Transistorarchitekturen wie Dünnschichttransistoren, zweidimensionalen Bauelementen und Gate-all-around-FETs.

Die im Rahmen dieser Arbeit entwickelten methodischen und instrumentellen Innovationen erweitern die Anwendungsmöglichkeiten von PALS sowohl auf Polymere unter realitätsnahen Bedingungen als auch auf neuartige elektronische Materialien im Nanometermaßstab. Damit werden neue experimentelle Zugänge zur quantitativen Untersuchung von Defektstrukturen geschaffen, die für Energietechnologien, Polymerforschung und zukünftige Halbleiterbauelemente von zentraler Bedeutung sind.

Declaration of Prior Publication

Some of the material presented in this dissertation has previously been published in peer-reviewed journals. These sections have been adapted for inclusion in the present work. The publications are open-access, and reprinting is carried out with the permission of the corresponding publishers and/or in accordance with the journal copyright policies.
The relevant publications are:

> **R. Helm**, J. Lehtonen, M. Mayerhofer, J. Mitteneder, W. Egger, R. Verbeke, P. Sperr, G. Dollinger and M. Dickmann, *Positron-annihilation lifetime spectroscopy with in-situ control of temperature, pressure and atmosphere to determine the free-volume of soft materials*, Nuclear Instruments and Methods in Physics Research Section B: Beam Interactions with Materials and Atoms **549**, 165263 (2024), 10.1016/j.nimb.2024.165263
>
> **R. Helm**, W. Egger, C. Corbel, P. Sperr, M. Butterling, A. Wagner, M. O. Liedke, J. Mitteneder, M. Mayerhofer, K. Lee, G. S. Duesberg, G. Dollinger and M. Dickmann, *Defect studies in thin-film SiO2 of a Metal-Oxide-Silicon Capacitor using Drift-Assisted Positron Annihilation Lifetime Spectroscopy*, Nanomaterials **15**, 1142 (2025), 10.3390/nano15151142
>
> **R. Helm**, W. Egger, C. Corbel, P. Sperr, M. Butterling, A. Wagner, M. O. Liedke, E. Hirschmann, J. Mitteneder, M. Mayerhofer, K. Lee, G. S. Duesberg, G. Dollinger and M. Dickmann, *Defect Characterization of the SiO2/Si Interface investigated by Drift-Assisted Positron Annihilation Lifetime Spectroscopy*, Nanomaterials 16, 156 (2026), 10.3390/nano16030156

The text, figures, and results reprinted or adapted from these works are clearly indicated in the respective chapters. The candidate is the primary author of these publications and has obtained approval to include the material in this dissertation.

Contents

Abstract i

Zusammenfassung iii

Decleration of Prior Publication v

Contents ix

List of Figures xi

List of Tables xv

Abbrevations xvii

1. Introduction 1

2. Positrons for Materials Science 5
2.1. Positron Annihilation Techniques 5
2.1.1. Positron Annihilation Lifetime Spectroscopy (PALS) 5
2.1.2. Doppler Broadening Spectroscopy (DBS) 8
2.2. Positron Generation 10
2.3. Positrons Matter Interaction 12
2.3.1. Implantation and Thermalization 12
2.3.2. Diffusion and Drift 16
2.3.3. Positron Trapping and Annihilation 18
2.3.4. Positronium Formation and Annihilation 25

3. Metal-Oxide-Silicon System 29
3.1. Gate (Al) and Substrate (Si) 29
3.2. Gate Oxide (amorphous SiO_2) 31
3.3. SiO_2/Si Interface 32
3.4. Band Structure and Operation Modes 34
3.5. Capacitance-Voltage Profiling 40

4. Subnanometer Porosimetry in Extreme Ambient Conditions 45
4.1. The Temperature - Atmosphere Positron InstRument (TAPIR) 45
4.1.1. General Instrument Design 46

4.1.2. Sample Holder Design . . . 50
4.1.3. Data Acquisition Unit . . . 52
4.2. Operating Characteristics of TAPIR . . . 55
4.2.1. Sample Heating . . . 55
4.2.2. Atmosphere Stability . . . 57
4.2.3. Detection System Characteristics . . . 58
4.3. Semi-crystalline Polystyrene in Ar Atmosphere . . . 61
4.3.1. Material Properties . . . 61
4.3.2. Experiment . . . 61
4.3.3. Results . . . 62
4.3.4. Discussion . . . 68
4.4. Conclusion . . . 71

5. The Pulsed Low Energy Positron System (PLEPS) 73
5.1. Current Status of PLEPS . . . 73
5.2. PLEPS Target Station . . . 77
5.2.1. Modification to the Target Station . . . 77
5.2.2. System Improvements . . . 79

6. Positron Drift for Interface Defect Characterization 83
6.1. Drift-Assisted Positron Annihilation Spectroscopy . . . 83
6.2. Experimental Methods . . . 87
6.3. $Al/SiO_2/Si$ Capacitor Characteristics . . . 88
6.3.1. Sample Preparation . . . 88
6.3.2. Electronic Characterization . . . 89
6.3.3. Electric Field Simulation . . . 91
6.4. Positron Annihilation in the Al-Gate . . . 93
6.5. Positron Annihilation in the Si-Substrate . . . 94
6.5.1. Bulk annihilation properties . . . 96
6.5.2. Surface annihilation and Diffusion . . . 97
6.6. Positron Quantum States in the Oxide/Si Stack . . . 100
6.6.1. Oxide Annihilation Characteristics . . . 100
6.6.2. Depth-dependent Annihilation Characteristics . . . 102
6.6.3. Positron Diffusion in the Oxide . . . 104
6.7. Positron Quantum States in the MOS Capacitor . . . 107
6.7.1. Electric-Field Influence on Positron Annihilation . . . 109
6.7.2. Depth-dependent Annihilation Characteristics . . . 111
6.7.3. Bias-dependent Annihilation in the Oxide . . . 116
6.7.4. Bias-dependent Annihilation in the Substrate . . . 121
6.7.5. Positron Drift–Derived Microstructure . . . 125
6.8. Conclusion . . . 128

7. Summary and Outlook 131

Bibliography **135**

A. Appendix: Supplementary Data **149**

List of Publications **155**

Danksagung **159**

List of Figures

2.1. Calculated positron lifetime spectrum 7
2.2. Experimental Doppler broadening spectrum measured at the VEP . . 8
2.3. Schematic of a positron beam interacting with a solid. 13
2.4. Calculated depth profile of a slow monoenergetic positron beam and high-energy positrons emitted by a ^{22}Na source 14
2.5. Illustration of the kinetic processes of a thermalized positron in the host lattice. 16
2.6. Probability density of electrons and a positron in a SiC lattice for defect-free bulk and a silicon vacancy 19
2.7. Feynman diagrams of the electron–positron annihilation process. . . . 21
2.8. Schematic of the two-state trapping model. 22

3.1. Schematic representation of the principal composition of the metal-oxide-semiconductor system. 30
3.2. Illustration of two bonded SiO_4 tetrahedra. 31
3.3. Schematic of the band diagram of the MOS capacitor for the different operation modes. 37
3.4. Schematic illustration of the capacitance–voltage (C–V) method for a p-doped metal–oxide–semiconductor (MOS) capacitor 41

4.1. Detailed schematic of the TAPIR instrument. 46
4.2. Operating parameter limits of TAPIR 48
4.3. Explosion drawing of the sample holder. 50
4.4. Electric wiring of the sample holder from the pressure vessel to the exterior. 52
4.5. Principal overview of the data acquisition circuit. 53
4.6. Sample core temperature versus the surface temperature for the single heater and dual heater simulation. 56
4.7. Long-term pressure stability of the pressure vessel. 58
4.8. Positron annihilation lifetime spectrum of p-doped silicon measured with the TAPIR instrument. 59
4.9. Experimental lifetime spectrum and results of the applied fit model for PS in vacuum condition at 21 °C. 63
4.10. τ_3 and I_3 as a function of temperature at 0.1 MPa of Argon pressure. 64
4.11. The intensities of the three decay components as a function of temperature for vacuum condition and 4 MPa argon pressure. 65

4.12. Long lifetime component (τ_3, I_3) as a function of argon gas pressure for two different temperatures. 66
4.13. Long component (τ_3, I_3) as a function of temperature for vacuum and three different Argon gas pressures. 67

5.1. Schematic of the Pulsed Low Energy Positron System (PLEPS). . . . 75
5.2. Schematic cross-sectional view of the upgraded PLEPS target station with sample holder, connector housing, and receiver. 78
5.3. Technical implementation of the new design at the PLEPS target station. 80
5.4. Positron lifetime spectra of the p-i-n diode recorded at 4 keV under different gate voltages. 81

6.1. Schematic of the MOS system showing the implantation profile and the effect of an electric field on the positron spatial distribution prior to annihilation. 85
6.2. Results of the CV measurements of the MOS capacitor. 90
6.3. Comparison of the positron implantation profile to the absolute electric field distribution in the MOS capacitor. 92
6.4. Positron annihilation in the Al-gate. 93
6.5. Positron Annihilation in the silicon substrate. 95
6.6. Positron decay spectrum of p-type Silicon at 8 keV measured with the MePS instrument. 96
6.7. Two-component decomposition of the bare silicon sample as a function of positron implantation energy. 98
6.8. Extraction of the positron diffusion constant D_+ and the surface transition rate ν from the energy-dependent lifetime results. 99
6.9. Positron annihilation in the oxide. 101
6.10. Example lifetime spectrum with a three-component decomposition for the bare oxide on silicon at 2 keV. 102
6.11. Results of the three-component analysis of the bare oxide on silicon as a function of the implantation energy. 103
6.12. S and W parameter analysis of the Doppler Broadening measurements of the bare oxide on silicon sample. 106
6.13. Schematic explanation of the drift-assisted positron annihilation spectroscopy experiment on the MOS capacitor. 108
6.14. Positron annihilation lifetime spectra of the bare oxide at 2 keV and the buried oxide at 4 keV are shown for three bias voltage conditions. 110
6.15. Results of the three-component analysis of the buried oxide lifetime spectra as a function of implantation energy for three different applied gate voltages. 111
6.16. S-W plot of the MOS capacitor under three applied gate voltages. . . 115
6.17. Results of the three-component analysis of the lifetime spectra as a function of the applied gate bias at 4 keV. 117

6.18. τ_{p} (blue, p-Ps), τ_2 (green) and intensities I_{p}, I_2 as a function of the gate voltage U_{g} at an implantation energy of 4 keV. 120
6.19. Three-component decomposition of the lifetime spectra at an implantation energy of 11 keV as a function of the gate voltage U_{g}. 122
6.20. Comparison of lifetime components as a function of the applied gate voltage for oxide-side and silicon-side drift toward the interface. . . . 127

List of Tables

4.1. Summary of the used detector properties. 60

5.1. PLEPS instrument characteristics as of February 2020. 74

6.1. Relevant physical properties of the materials of each layer comprising the Al/SiO_2/Si capacitor at 300 K. 88
6.2. Results of the lifetime analysis of the PVD aluminum gate. 94
6.3. Summary of the key transport parameters derived from the positron annihilation measurements for SiO_2, silicon in accumulation, and silicon in inversion. 109
6.4. Summary of selected applied gate voltage steps and their corresponding electric field over the 180(10) nm oxide layer. 116

A.1. Analysis results of the o-Ps component (τ_3, I_3) as a function of temperature and pressure. 151
A.2. Results of the three-component analysis of the lifetime spectrum of buried SiO_2 at 4 keV implantation energy. 152
A.3. Results of the three- and four-component analysis of the lifetime spectrum of bare SiO_2 at 2 keV implantation energy. 153
A.4. Results of the three-component analysis of the 11 keV measurements as a function of the applied gate voltage. 154

Abbrevations

PAS	Positron Annihilation Spectroscopy
PALS	Positron Annihilation Lifetime Spectroscopy
DA-PALS	Drift-Assisted Positron Annihilation Lifetime Spectroscopy
DBS	Doppler Broadening Spectroscopy
AMOC	Age-Momentum Correlation
ACAR	Angular Correlation of Annihilation Radiation
TAPIR	Temperature Atmosphere Positron InstRument
MOS	Metal-Oxide-Semiconductor
FET	Field-Effect Transistor
TFT	Thin-Film Transistor
IRF	Instrument Resolution Function
NEPOMUC	NEutron-induced POsitron source MuniCh
FRM-II	Forschnugs Reaktor München II
ELBE	Electron Linac for beams with high Brilliance and low Emittance Helmholtz-Center Dresden-Rossendorf
LINAC	LInear ACcelerator
STM	Standard Trapping Model
DTM	Diffusion Trapping Model
sc	single-crystal
NBO	Non-Bridging Oxygen
NBOHC	Non-Bridging Oxygen Hole Center
XPS	X-ray Photpelectron Spectroscopy

AES	Auger Electron Spectroscopy
ESR	Electron Spin Resonance
RT	Room Temperature
PMT	Photo Multiplier Tube
FPGA	Field-Programmable Gate Array
FWHM	Full Width Half Maximum
PBR	Peak-to-Background Ratio
CFD	Constant Fraction Discriminator
FVE	Free-Volume Element
PLEPS	Pulsed Low Energy System
PEEK	Poly Ether Ether Keton
MePS	Mono-energetic Positron Source
VEP	Variable Energy Positron
HPGe	High-Purity Germanium
PVD	Physical Vapor Deposition
DLTS	Deep Level Transient Spectroscopy

1. Introduction

Since Dirac's prediction of the positron in 1928 [1] and Anderson's experimental discovery in 1932 [2], the positron has been firmly established as the antiparticle of the electron, sharing the same rest mass but carrying opposite charge. In the decades since, theoretical models and experimental procedures have advanced considerably, establishing positrons as powerful atomic probes for studying defects in a wide range of materials. Analytical techniques exploiting positron–electron interactions have evolved steadily, from early theoretical [3] and experimental [4] works, through conventional laboratory-based setups [5], to advanced beam-based methods at large-scale user facilities [6–10]. These developments have made positron annihilation spectroscopy (PAS) particularly valuable for the study of metals, semiconductors, and polymers [11–13].

Among the various PAS methods developed to probe different aspects of the annihilation process, positron annihilation lifetime spectroscopy (PALS) has become the most widely applied and informative technique. PALS provides quantitative information on the size, type, and concentration of defects by measuring the time between positron implantation and annihilation. Other established approaches include Doppler broadening of annihilation radiation (DBS) and angular correlation of electron–positron annihilation radiation (ACAR), which probe momentum distributions rather than lifetimes. More advanced methods, such as age–momentum correlation (AMOC) spectroscopy, combine lifetime and momentum information, offering highly detailed insights into defect structures [14]. However, due to their long measurement times and complex data analysis, AMOC methods are generally limited to processes that evolve slowly and are not suitable for in situ studies requiring fast acquisition times.

PALS has thus emerged as the workhorse technique for defect studies across materials science. First applied to vacancies in metals [15], it remains an important non-destructive method capable of probing atomistic defects. In this method, a positron is implanted into a solid and rapidly thermalizes before diffusing randomly through the lattice, where it eventually annihilates with an electron. The annihilation can occur in the in interstitial regions of the defect-free lattice, or at atomic-scale defects. Since the positron lifetime is directly related to the local electron density – equivalently, the overlap between positron and electron wavefunctions – the measured lifetime provides characteristic fingerprints of the electronic environment at the annihilation site. This capability makes PALS uniquely suited for quantitative

defect characterization.

The power of PALS increases further when combined with in-situ variation of the thermodynamic state of the material under investigation. A common approach is to measure the positron lifetime as a function of temperature, which can change defect type (e.g. via annealing) or alter positron trapping probability, thereby yielding insights into defect nature, kinetics, and binding energies [16, 17]. Other external stimuli have also been demonstrated: for example, illuminating the sample can switch the charge state of defects, enhancing or suppressing positron trapping at specific sites [18]. This approach enabled the first experimental verification of positively charged NV centers in diamond [12], a result not accessible with conventional semiconductor analysis techniques.

One objective of this work is to substantially extend the applicability of positron annihilation lifetime spectroscopy (PALS) beyond existing approaches by introducing two innovative in-situ techniques. Chapters 2 and 3 establish the theoretical framework for the subsequent experimental investigations.

The first part of the results (Chapter 4) examines the influence of ambient gas pressure on the free volume in polymers – an approach previously identified as highly promising [19, 20]. Open-volume defects and their selective molecular transport properties in polymeric materials are central to applications such as gas separation [21], carbon capture [22], and water desalination [23], where performance critically depends on the free-volume structure and its response to external conditions. However, conventional PALS experiments are typically carried out in air and at room temperature or under vacuum conditions that do not accurately reflect real-world operating environments. However, in realistic conditions, the gas composition, pressure, and temperature strongly influence gas diffusion and free-volume behavior [19, 20, 24, 25]. To address this limitation, a dedicated positron annihilation instrument, the Temperture Atmosphere Positron InstRument (TAPIR) was developed and was tested for the first time on semi-crystalline polystyrene.

The second part of the results (Chapters 5 and 6) focuses on defect identification at buried interfaces, which cannot be directly resolved using conventional beam-based positron lifetime techniques due to the broad implantation profile of mono-energetic slow positrons [26]. To overcome this limitation, externally applied electric fields are employed to shift the effective implantation profile toward or away from interfaces, thereby enabling selective probing. This approach is particularly relevant for the characterization of modern electronic devices.

The rapid advancement of artificial intelligence, quantum computing, and high-performance data processing has intensified the demand for energy-efficient transistors with enhanced scalability. Continued device miniaturization, a key driver of performance improvements, has prompted a transition from conventional silicon MOSFETs to advanced architectures such as thin-film transistors (TFTs) [27], two-

dimensional integrated devices [28], and three-dimensional gate-all-around FETs (GAAFETs) [29, 30]. These devices increasingly rely on complex material systems, including transition metal dichalcogenides deposited on high-k dielectrics such as HfO_2 [31] and Gd_2O_5 [32].

As device dimensions continue to shrink and material systems become more diverse, defects at dielectric–semiconductor interfaces emerge as a critical performance bottleneck. Such defects introduce interface states that trap charge carriers and degrade carrier mobility [27, 33], ultimately limiting device efficiency and reliability. Each material system exhibits its own intrinsic defect landscape and distinct interface-related defect configurations. To sustain device scaling and ensure long-term stability, precise identification and characterization of these defects are indispensable – particularly in ultrathin oxide layers and their interfaces. The development of advanced experimental techniques, such as drift-assisted positron annihilation lifetime spectroscopy (PALS), represents a significant step toward this goal by enabling direct, interface-sensitive defect characterization.

2. Positrons for Materials Science

This chapter provides a concise introduction to the physics of positron–matter interactions, serving as the foundation for the experiments and results presented in the Chapters 4 and 6. It is not intended as a comprehensive textbook on positron physics; thus, certain theoretical aspects will only be outlined briefly. Readers seeking a more in-depth treatment are referred to the many excellent textbooks and reviews available on positron physics and its applications in materials science, such as [14, 25, 26, 34–38].

2.1. Positron Annihilation Techniques

In general, positron annihilation spectroscopy (PAS) is a non-destructive technique for defect characterization that is widely used across materials science. It is well suited for investigating atomistic and structural open volume defects in a broad range of materials, provided the defect concentration exceeds approximately 100 ppb ($\approx 1 \times 10^{16}\,\mathrm{cm}^{-3}$) [14].

In this work, two positron annihilation spectroscopy (PAS) techniques are employed: positron annihilation lifetime spectroscopy (PALS) and Doppler broadening spectroscopy (DBS). The primary emphasis is placed on PALS, which provides detailed insights into the defect landscape – including defect type, distribution, and concentration – and enables quantitative analysis of positron bound states such as positronium. DBS serves as a complementary technique, primarily used to confirm features of the annihilation process that cannot be fully resolved by lifetime measurements alone.

2.1.1. Positron Annihilation Lifetime Spectroscopy (PALS)

Positron Annihilation Lifetime Spectroscopy (PALS) measures the statistical distribution of positron "ages" by detecting millions of annihilation events. The start of each positron age measurement is defined either by the prompt radiation emitted from a radioactive source or, in the case of a pulsed positron beam, by the beam's timing structure. The annihilation event is recorded through the detection of high-energy photons (annihilation radiation) using a setup of scintillator crystals coupled to fast photomultiplier tubes. The scintillator converts the high-energy γ quanta

into UV–visible light via Compton scattering and the photoelectric effect, which is subsequently detected by the photomultiplier [39]. The time interval between positron implantation and annihilation with an electron defines the positron's age.

Collecting several million annihilation events yields an experimental lifetime spectrum that may contain one or more exponential decay components, each corresponding to a distinct mean positron age in the material, referred to as positron lifetime. Analyzing these lifetime spectra provides insight into the local electron density, which changes markedly when defects are present in the material system [40].

Figure 2.1 illustrates an artificially generated decay spectrum and the decomposition into its decay components. The horizontal axis represents the positron age within the material, while the vertical axis shows the survival probability $n(t)$ at time t. The decrease of $n(t)$ over time is governed by the annihilation rate of each process [41]. The theoretical decay spectrum, shown in violet, results from the linear combination of the individual annihilation channels, highlighted in blue and orange.

$$-\frac{dn(t)}{dt} = \frac{I_1}{\tau_1} e^{-t/\tau_1} + \frac{I_2}{\tau_2} e^{-t/\tau_2} \tag{2.1}$$

Here, $I_{1,2}$ denotes the relative intensity, and $\tau_{1,2}$ represents the mean positron lifetimes. Due to the finite time resolution of the acquisition electronics and detectors, the decay spectrum is convoluted with the instrument response (shown in red), which in this case is approximated by a single Gaussian function with $\sigma = 76\,\mathrm{ps}$, corresponding to a FWHM of 180 ps. In practice, the measured spectrum is further affected by constant background counts originating from unrelated radiation events, which are mistakenly registered as lifetime events by the acquisition system. When all contributions are combined, the resulting spectrum corresponds to the simulated spectrum shown in Figure 2.1.

The lifetime measurement represents a classical *inverse problem*: the observed lifetime spectrum is known, but the underlying factors that produce it – namely the instrument resolution function (IRF), the background (B), and the annihilation components – must be inferred. This is achieved by fitting a suitable model function to the experimental spectrum, thereby estimating its constituent components. The model, which is a solution of the standard trapping model (Section 2.3.3) takes the form:

$$D_{\mathrm{exp}}(t) = \left(IRF * \sum_{\mathrm{i}=1}^{\mathrm{n}} \frac{I_{\mathrm{i}}}{\tau_{\mathrm{i}}} e^{-t/\tau_{\mathrm{i}}} \right) + B \tag{2.2}$$

The instrument resolution function (IRF) is obtained from a reference lifetime spec-

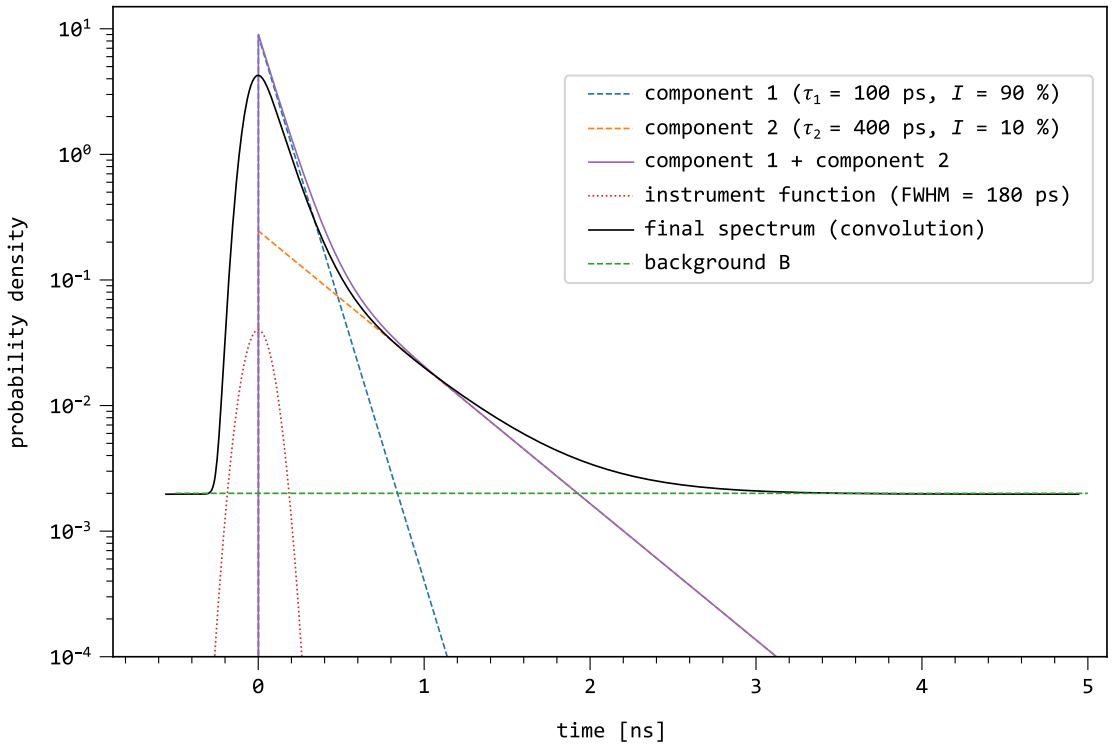

Figure 2.1.: Theoretical positron lifetime spectrum based on Equation (2.2). The individual exponential decay components are shown as orange and blue dashed lines, while their weighted sum is represented by the solid violet line. The simulated measured spectrum – obtained by convolving the decay function with the Gaussian instrument response function (red) and adding a constant background (green) – is shown as a solid black line.

trum with well-known lifetime components, such as silicon, yttria-stabilized zirconia, or silicon carbide. In practice, the IRF is typically represented as a sum of Gaussian functions to capture the non-Gaussian features of the real instrument response. The background (B) is estimated from the mean counts within a predefined channel range at very long times, which, due to the finite time window of the data acquisition unit, can be determined on the left side of the peak. The fitting procedure itself is carried out numerically using the least-squares method [42].

The parameters I_i and τ_i are free fit parameters of the model and correspond to the intensity and lifetime of each component, respectively. Due to information loss introduced by the convolution of the annihilation components with the IRF, the number of resolvable lifetime components is typically limited to $n = 1$–5. However, resolving more than three components requires state-of-the-art beam-based spectrometers with time resolution $\leq 200\,\mathrm{ps}$ and a peak-to-background ratio – defined as the peak counts divided by the mean background counts – of at least $1 \times 10^5 : 1$

[43].

2.1.2. Doppler Broadening Spectroscopy (DBS)

Doppler broadening spectroscopy (DBS) measures the Doppler shift of the annihilation radiation, which arises from momentum conservation during annihilation and the momentum component of the electron–positron pair along the emission direction z of the annihilation γ-rays. With sufficient statistics, this results in an observable energy deviation from 511 keV and thus in a broadening of the annihilation peak [26], quantified by

$$\Delta E = \frac{p_z c}{2}. \tag{2.3}$$

Figure 2.2 illustrates the Doppler broadening effect for a silicon dioxide on silicon sample, measured at the research reactor in Delft [44].

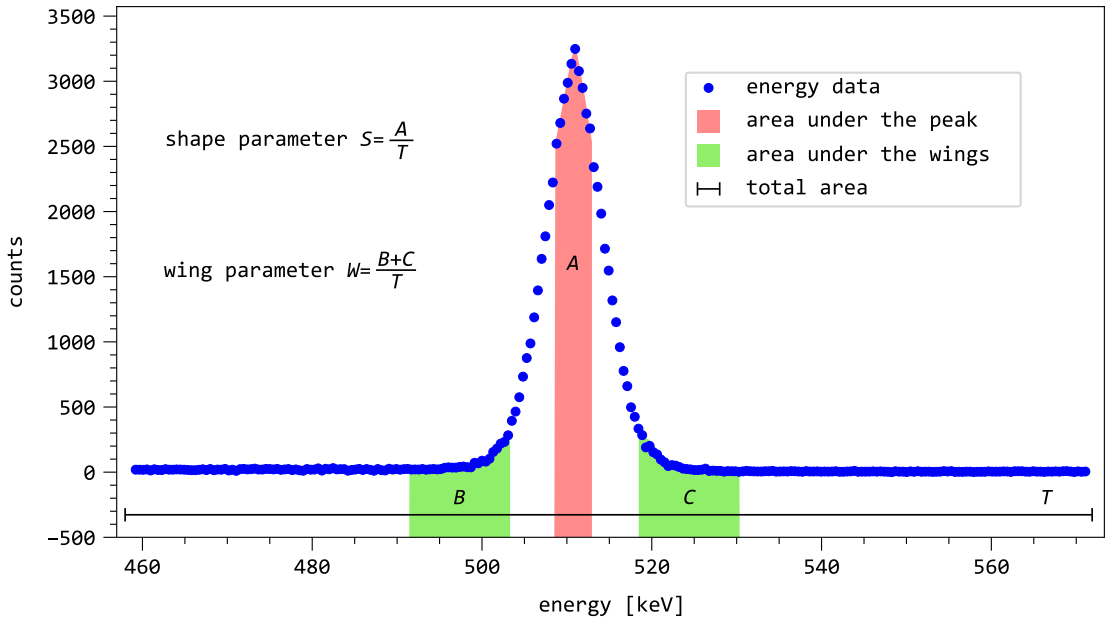

Figure 2.2.: Doppler broadened energy spectrum of silicon dioxide on silicon recorded at the VEP in Delft with channel width $\Delta E = 0.438\,\mathrm{keV/ch}$ and a detector resolution of 1.6 keV. The area for determining the shape parameter S is marked in red (A), which was set to a fraction of $S = 0.5$. The areas for the wing parameter W are marked in green ($B+C$), which is set to a fraction of $W = 0.25$. The total area T is the area under the whole curve.

Because the positron loses most of its energy through thermalization – i.e., reaching

thermal equilibrium with the host lattice – after implantation into the material, its momentum becomes more than an order of magnitude smaller than that of the electrons, and the Doppler shift is therefore dominated by the annihilation electron momentum. [45]. As a result, the technique effectively probes the electron momentum at the annihilation site. According to the Pauli principle, electrons occupy discrete atomic shells with different binding energies. The magnitude of the Doppler shift thus depends on the orbital of the annihilation electron: core electrons, with their high binding energies, cause large Doppler shifts, whereas valence electrons produce only small shifts. If a positron becomes localized in a lattice defect, the local electron density is reduced, making annihilation with valence electrons more likely. This increases the contribution of low-energy Doppler shifts in the energy spectrum [14].

To quantify the Doppler shift and characterize the momentum distribution of the annihilating electrons, so-called line-shape parameters are introduced. The S (shape) parameter represents the fraction of annihilations involving low-momentum electrons, while the W (wing) parameter reflects the contribution from high-momentum electrons. These parameters are defined as ratios of areas — corresponding to the peak or wing regions of the Doppler-broadened spectrum — divided by the total area T under the curve:

$$S = \frac{A}{T} \tag{2.4}$$

$$W = \frac{B + C}{T}. \tag{2.5}$$

Assuming Poisson-distributed counting statistics, the statistical uncertainties of these parameters are given by:

$$\Delta S = \sqrt{\frac{S(1-S)}{T}} \tag{2.6}$$

$$\Delta W = \sqrt{\frac{W(1-W)}{T}}. \tag{2.7}$$

The line-shape parameters are integral quantities without direct physical meaning. For instance, the measured S parameter represents a weighted sum of all partial S parameters arising from different annihilation channels. In a beam-based Doppler experiment, the total S value can therefore be expressed as

$$S_{\text{total}} = f_{\text{s}}(E)S_{\text{s}} + \sum_{l=1}^{m} f_{\text{l}}(E)S_{\text{l}} + \sum_{i=1}^{k} f_i(E)S_i + \sum_{c=1}^{d} f_c(E)S_c. \tag{2.8}$$

Here, $f_{s,i,l,c}(E)$ denotes the energy-dependent fraction of positrons annihilating in the surface (s), layers (m), interfaces (k), or defects (d). In common practice, the S and W parameters are defined as 0.5 and 0.25 for a defect-free reference material, respectively [26]. To facilitate comparison between different measurements, the S and W parameters are normalized to the bulk value of the same material: $S_{\text{n}} = S/S_{\text{bulk}}$ and $W_{\text{n}} = W/W_{\text{bulk}}$ [46]. In this normalized form, variations in defect composition can be identified through changes in the S and W parameters relative to the reference sample.

Doppler spectra are typically recorded using high-purity germanium detectors, whose instrument response function is well approximated by a Gaussian with a FWHM of about 1–2 keV at a gamma energy of 511 keV. This instrumental broadening imposes a fundamental limit on the measurement accuracy. Because of this averaging, single-detector DBS is interpreted only in relative terms. Qualitative insights into the electronic environment are obtained by comparing different samples, treatments, or defect structures, or by varying the positron beam energy to probe different depths.

2.2. Positron Generation

In contrast to electrons, which can be produced by a variety of methods and are abundantly available in the laboratory, positrons are antimatter and a scarce experimental resource that must be laboriously generated and carefully handled. Their production relies on two principal mechanisms: (a) β^+ decay of radioactive isotopes and (b) pair production, where high-energy γ-radiation is converted into electron–positron pairs [14, 26, 39]. In the following, both processes are briefly described, and their respective advantages, disadvantages, and differences are outlined.

Production via radioactive isotopes

The most common method for generating positrons for positron physics is through the radioactive decay of ^{22}Na. This isotope provides a relatively high positron yield and has the practical advantage of a convenient half-life of 2.6 a. The decay reaction can be written as

$$^{22}\text{Na} \longrightarrow {}^{22}\text{Ne}^* + \beta^+ + \nu_e \longrightarrow {}^{22}\text{Ne} + \gamma(1275\,\text{keV}). \tag{2.9}$$

The ^{22}Na isotope decays by emission of a positron with a probability of 90.4 % accom-

panied by an electron neutrino, producing an excited $^{22}Ne^*$ state. The distribution of the emitted positrons has an endpoint energy of 547 keV [47]. The short-lived excited state $^{22}Ne^*$, with a mean lifetime of $\tau = 3.7$ ps, subsequently decays to the ground state by emitting a γ quantum with an energy of $E_\gamma = 1275$ keV. Other competing decay channels, such as electron capture (ϵ) or direct β^+ decay to the ground state, also occur but are not relevant for the production of positrons for Positron Annihilation Spectroscopy (PAS) [14].

For practical use, ^{22}Na is typically processed into a NaCl or $NaCO_3$ solution and deposited onto a µm-thin carrier material (metal foils or Kapton), which is then sealed with another foil of the same material. In Positron Annihilation Lifetime Spectroscopy with a conventional sample-source configuration, the choice of encapsulation material is critical, as a fraction of positrons will always annihilate within the source itself, and the fraction increases with foil thickness. This source contribution manifests as additional positron lifetimes in the spectrum, which are not representative of the investigated material.

High-activity sources for positron beam application in the laboratory can also be realized with positron intensities of $2 \times 10^5\,e^+s^{-1}$ [48]. However, the activity of the source cannot be scaled indefinitely, since the source volume will increase and self-absorption in the source rises.

Production via pair-production

Positrons can also be produced via pair production, in which high-energy γ quanta are converted into electron-positron pairs [49]. The photon must have at least 1.022 MeV of energy – twice the electron rest mass – for pair production to occur. The conversion probability remains low until photon energies reach several MeV, with any excess energy above 1.022 MeV transferred as kinetic energy to the electron and positron [39].

At the NEutron-induced POsitron source MUniCh (NEPOMUC) at FRM-II, γ-rays are generated through the $^{113}Cd(n,\gamma)^{114}Cd$ reaction. The isotope ^{113}Cd is chosen because it efficiently absorbs the entire cold neutron flux that impinges on the cadmium source cap, owing to its large neutron capture cross section of $\sigma = 2 \times 10^{-20}\,cm^{-2}$ for thermal neutrons. ^{114}Cd has a neutron binding energy of about 9 MeV and the excess energy is released via a gamma cascade. On average, 2.3 γ-rays with energies above 1.5 MeV are emitted in the cascade [50]. These photons are subsequently converted into positrons via pair production in a platinum foil located behind the cadmium cap, which also serves as a positron moderator, producing mono-energetic positrons that can be extracted from the surface using electromagnetic optics [51]. A similar approach is employed at the Helmholtz-Zentrum Dresden-Rossendorf, where Bremsstrahlung photons from 40 MeV electrons of the ELBE LINAC interacting with a tungsten converter that serves as the target for pair production [52]. In both

cases, moderators are used to thermalize the positrons, producing monoenergetic beams (several eV) due to the negative work function of the moderator material, with intensities up to $1 \times 10^9\,\mathrm{e^+ s^{-1}}$ at FRM-II [48].

The scale of these experiments necessitates extensive transport infrastructure – such as solenoids, beam optics, remoderators, and heavy shielding – because they are typically located at large research facilities. This makes the method laborious, expensive, and impractical for standard laboratory use.

2.3. Positrons Matter Interaction

This section provides a theoretical overview of positron interactions with the host material into which they are implanted. It begins with the stopping processes during implantation, followed by the behavior of positrons in thermal equilibrium with the host lattice, and continues with their trapping at defects before eventual annihilation with the surrounding electron density. Figure 2.3 gives an overview of the main pathways a slow positron may follow when interacting with a solid surface. For this work, the focus lies on interactions occurring within the solid, i.e., after the positron penetrates the surface, while other processes are included only for context, and some are omitted entirely. The principal loss mechanisms, discussed in Section 2.3.1, are shown at the top of the figure and can be associated with different energy ranges. The diagram also indicates typical time scales for implantation and annihilation, as well as the characteristic depth range. These values should be regarded as approximate, since they strongly depend on material parameters and the incident positron energy.

2.3.1. Implantation and Thermalization

After impinging on the surface of the sample, the positron rapidly loses its initial kinetic energy within a few picoseconds mainly by e^--e^+ scattering. The annihilation cross section at these high energies is much smaller than the e^--e^+ scattering cross section, but a few percent of the annihilation events can already occur during the slowing-down process [53]. The energy loss, dE/dz, is governed by inelastic collisions with electrons and, to a lesser extent, by interactions with nuclei; the latter contribution becomes negligible once the positron energy falls below 500 keV. Core electron excitations may occur in the form of ionization, electron–hole pair generation, or collective plasmon excitation of valence electrons [37, 54]. At lower positron energies, typically below 10 eV down to thermal energies $\frac{3}{2}k_\mathrm{b}T$, phonon interactions dominate the energy-loss process. Upon reaching thermal equilibrium with the medium, the positron interacts with the lattice primarily through phonon emission and absorption, which sustain the equilibrium state [37]. The exact energy thresholds for the individual loss processes depend on the material, since its

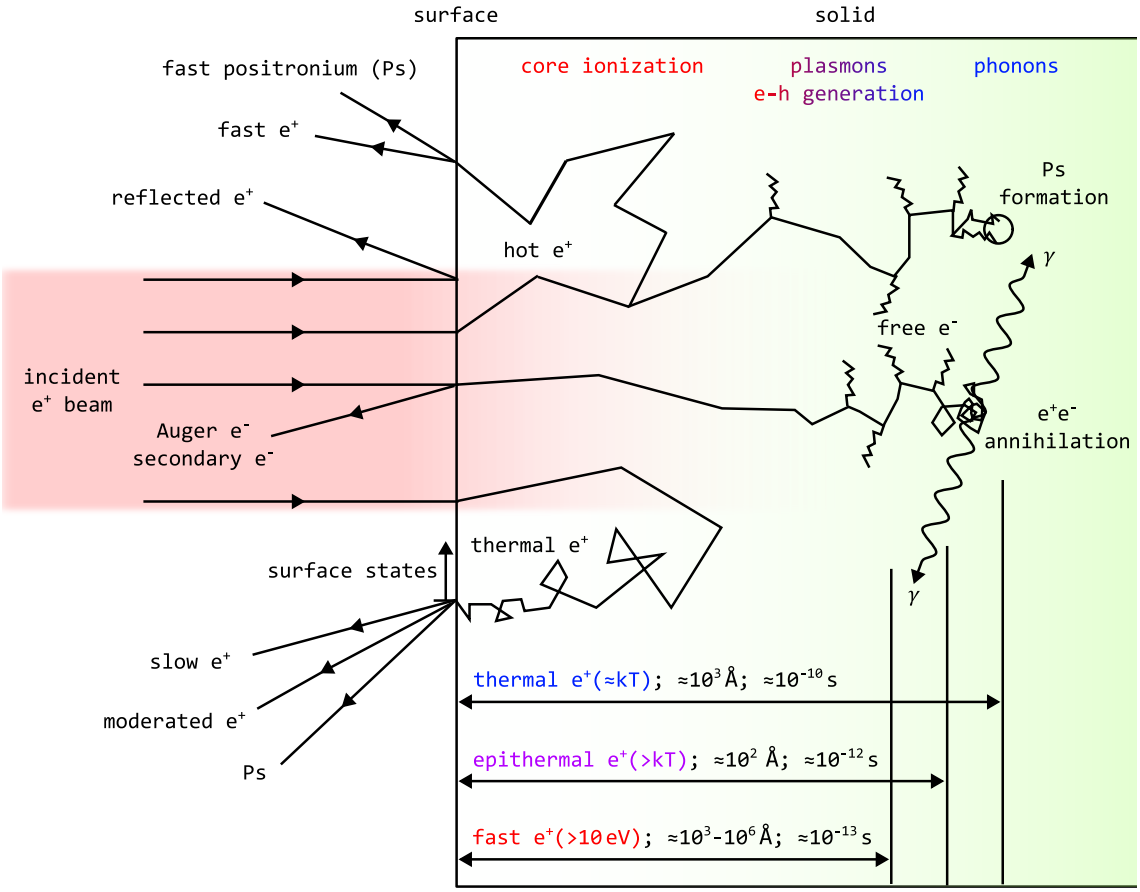

Figure 2.3.: Schematic of a positron beam interacting with a solid. Typical time scales and depth ranges are indicated, along with the primary loss mechanisms corresponding to each energy range

electronic and lattice properties dictate the relative efficiency of competing mechanisms [55]. Regardless of the specific loss process, the total thermalization time remains very short – on the order of 1×10^{-12} s – compared to the average positron lifetime of about 1×10^{-10} s in defect-free bulk materials [56].

Figure 2.4 shows the implantation profiles for (a) low-energy implantation, described by Equation 2.10 for monoenergetic positron beams with implantation energies between 0.1 and 30 keV, and (b) high-energy implantation, described by Equation 2.15, for the radioisotope ^{22}Na, which emits positrons with an energy spectrum extending up to a maximum energy of 540 keV. The penetration depth of high-energy positrons is roughly three orders of magnitude greater than that of low-energy positrons.

The implantation and thermalization of positrons define their penetration depth in a material. This distribution extends from the surface to a maximum depth, which depends mainly on the positron's initial energy and the material density. Two

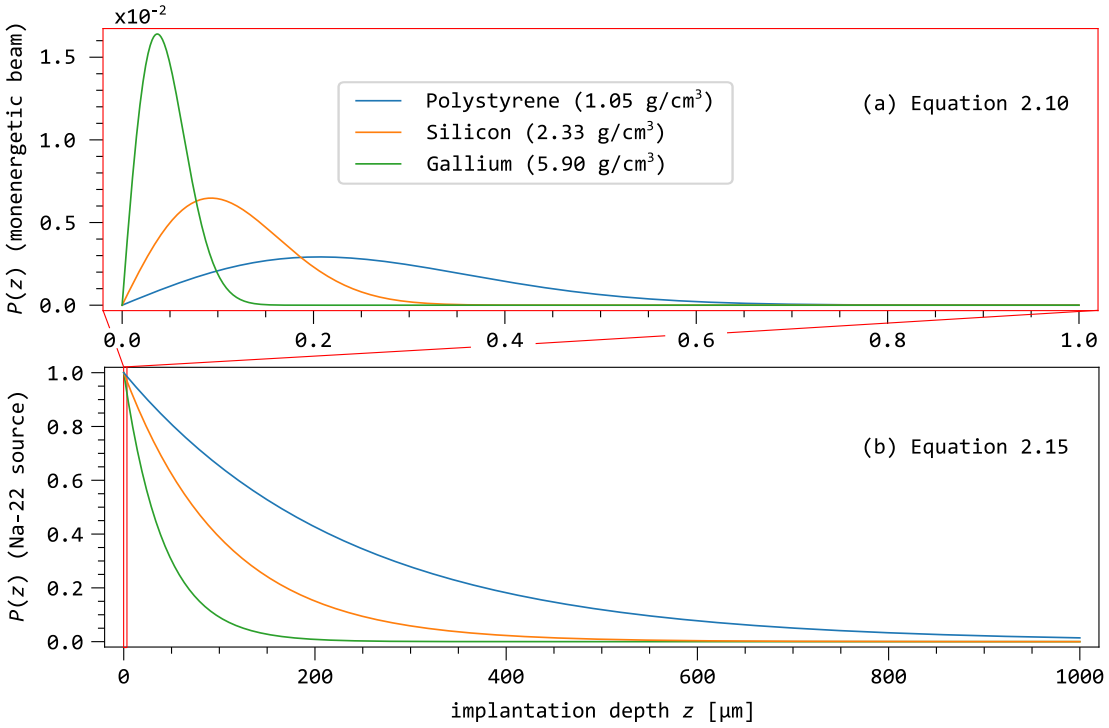

Figure 2.4.: Calculated depth profile of (a) a slow monoenergetic positron beam at 4 keV implantation energy and (b) high-energy positrons, with a energy distribution emitted by a ^{22}Na source ($E_{\max} = 540\,\mathrm{keV}$).

models are commonly used to describe the implantation profile, depending on the positron energy distribution.

For mono-energetic positron beams, with kinetic energies up to several 10 keV, the implantation profile can be described by the Makhovian distribution [57]:

$$dP(z, E, \rho) = \frac{m z^{m-1}}{z_0^m(E, \rho)} \exp\left[-\left(\frac{z}{z_0(E, \rho)}\right)^m\right] dz, \tag{2.10}$$

where z is the depth at which a positron thermalizes, and m is a shape parameter. Monte Carlo simulations indicate that $m \approx 2$ for light elements (e.g., Al, N_2) and decreases with increasing atomic number and implantation energy [58, 59].

The depth parameter $z_0(E, \rho)$ is defined as

$$z_0(E, \rho) = \frac{A}{\rho \Gamma(\frac{1}{m} + 1)} E^n, \tag{2.11}$$

with the mean implantation depth

$$\bar{z} = \Gamma\left(\frac{1}{m}+1\right) z_0 = \frac{A}{\rho} E^n. \tag{2.12}$$

Here, $\Gamma(x)$ denotes the gamma function,

$$\Gamma(x) = \int_0^\infty t^{x-1} e^{-t}, dt, \tag{2.13}$$

which satisfies the recurrence relation. For $m = 2$, this yields

$$\Gamma\left(\frac{1}{2}+1\right) = \frac{1}{2}\Gamma\left(\frac{1}{2}\right) = \frac{\sqrt{\pi}}{2}. \tag{2.14}$$

Here, E is the implantation energy and ρ the material density. The material-dependent parameters A and n can be obtained either from simulations or experiments. Extensive tabulations of A, n, and m for various materials are available in the literature [37, 59, 60].

Although high-energy positrons lose energy rapidly, most of their implantation path is traversed while their energy remains above 10 eV (see also Figure 2.3). Consequently, for high-energy positrons such as those emitted by radioisotopes, the implantation profile becomes significantly broader and due to the broad energy distribution, it can be approximated by an exponential law of the form

$$dP(z, \alpha) = \alpha \exp\left(-\alpha z\right) dz, \tag{2.15}$$

with the mass absorption coefficient $\alpha(E, \rho)$ defined as

$$\alpha(E, \rho) = B \frac{\rho\ [\mathrm{gcm}^{-3}]}{E[\mathrm{MeV}]^n},$$

where E is the maximum positron energy of the distribution. The mean implantation depth is defined as $\bar{z} = 1/\alpha$. The empirical parameters n and B were introduced by Brandt et al. [61], who reported $n = 1.43$ and $B = 17\,\mathrm{MeV}^n\mathrm{cm}^2\mathrm{g}^{-1}$. Alternative parameter values and refinements have also been proposed in the literature [62, 63]. The information depth $\hat{z}$ is defined as the depth at which the integrated depth profile up to $\hat{z}$ corresponds to a cumulative probability of $P(\hat{z}) = 0.999$. This also represents the minimum sample thickness that still allows measurements to be performed while ensuring that only a negligible fraction of positrons escape from the material [14].

As shown in Figure 2.4, these models are particularly useful for experimental plan-

ning – for example, to estimate the minimum sample thickness required for conventional PALS using a ^{22}Na source, or to determine suitable energy steps for investigating thin multilayer systems with slow-positron beams.

2.3.2. Diffusion and Drift

Diffusion mechanism

After reaching thermal equilibrium with the host material, the positron diffuses through the lattice while continuously exchanging energy with phonons via excitation and absorption processes. During this diffusion, the positron propagates with its average of the squared thermal velocity:

$$\langle v_{\mathrm{th}}^2 \rangle = \frac{3k_{\mathrm{b}}T}{m^*} \tag{2.16}$$

where k_{b} is the Boltzmann constant, T is the temperature of the host lattice, and m^* is the positron effective mass. The latter accounts for the interaction between the positron and the lattice and is typically larger than the free positron mass [36]. The thermal motion of positrons can be described as a random walk with no net positron current, as illustrated schematically in Figure 2.5 (a). During this motion, the positron effectively samples atomic sites within a volume of about 100 nm^3 [56].

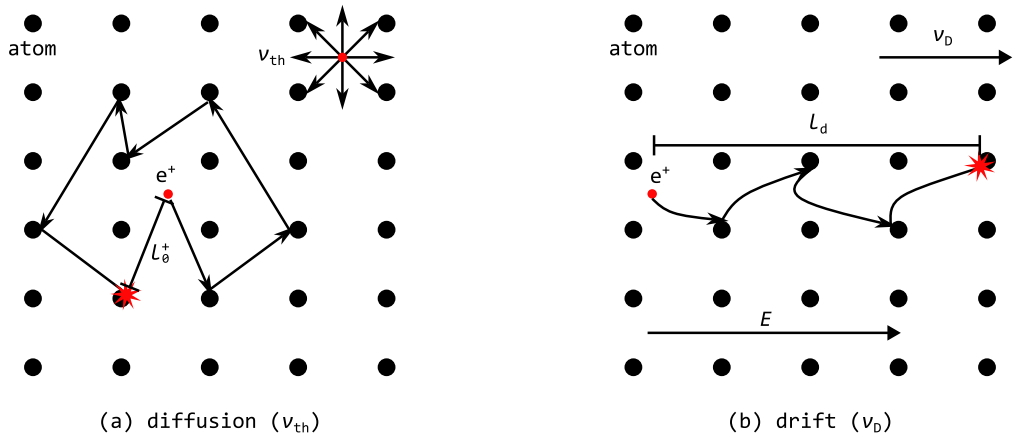

Figure 2.5.: Illustration of the kinetic processes of a thermalized positron in the host lattice. (a) Thermal motion governed by Maxwell-Boltzmann statistics, where the net current is zero and the average displacement between start and end points defines the diffusion length l^+. (b) Motion in the presence of an electric field, where a directional drift is superimposed on the diffusion, resulting in a net current along the field and a characteristic drift length l_{d}.

In good approximation, positron diffusion can be described by the classical collision model (Drude model), where the propagation through the lattice depends on the mean free path λ_+ and the collision rate ν_+ [56]. These microscopic quantities define the macroscopic parameter of practical importance, the diffusion constant [64]:

$$D_+ = \frac{1}{3}\lambda_+^2 \nu_+ = \frac{1}{3}\langle v_{\mathrm{th}}^2 \rangle \tau_+ \tag{2.17}$$

where $\langle v_{\mathrm{th}}^2 \rangle$ is the mean squared thermal velocity from Equation (2.16), ν_+ the collision frequency, and $\tau_+ = 1/\nu_+$ the relaxation time between collisions.

With the knowledge of the diffusion constant, the diffusion length of the positron in a defect-free lattice can be calculated:

$$l_0^+ = \sqrt{\frac{D_+}{\lambda_{\mathrm{b}}}} \tag{2.18}$$

with $\lambda_{\mathrm{b}} = 1/\tau_{\mathrm{b}}$ being the bulk trapping rate. This is the distance a positron covers from its point of thermalization to the point of annihilation and is usually in the order of 100 nm in metals and 10 nm for insulators. In case a defect is present, the diffusion length needs to be corrected for the trapping in defects, which reduce the effective diffusion length by the trapping rate κ [65]:

$$l^+ = \sqrt{\frac{D_+}{\lambda_{\mathrm{b}} + \kappa}} \tag{2.19}$$

Another important parameter is the positron mobility, which can be derived from the diffusion constant by the Einstein relation:

$$\mu_+ = \frac{eD_+}{k_{\mathrm{b}}T} \tag{2.20}$$

with e being the elementary charge, $k_{\mathrm{b}}T$ the thermal energy and D_+ the diffusion constant from Equation (2.17).

Drift-diffusion transport

In case an electric field, internal or external, is present, it can exert a force on the positron. The thermal motion $\langle v_{\mathrm{th}}^2 \rangle$ (Eq. (2.16)) gets superimposed by the drift motion in the electric field as depicted in Figure 2.5 (b). The resulting drift velocity is further:

$$v_\mathrm{d} = \mu_+ E \tag{2.21}$$

The additional electric field superimposes a preferred direction on the otherwise random motion of the positron, leading to an average drift velocity v_d. This process is similar to the drift–diffusion model widely applied in semiconductor physics to describe the transport of free charge carriers [66]. Within this classical framework, if a positron drifts with velocity v_d during its lifetime τ_b in a defect-free crystal, the characteristic drift length can be expressed as

$$l_d = v_d \tau_b \tag{2.22}$$

This provides a useful estimate for the distance traveled by a positron with a drift velocity v_d in its lifetime τ_b. Furthermore, when a positron is subjected to an electric drift field with an exponential spatial distribution, as typically found near the surface region of a semiconductor, it is useful to define a maximum distance $l_\mathrm{d,max}$ from the interface within which a positron can still reach the interface during its lifetime, as determined by the corresponding drift velocity:

$$\frac{dz}{dt} = -\mu_+ E(z); \quad E(z) = E_0 e^{-z/L} \tag{2.23}$$

$$\int_{\mathrm{l_{d,max}}}^{0} \frac{1}{e^{-z/L}} dz = -\mu_+ E_0 \int_0^{\tau_\mathrm{b}} dt \tag{2.24}$$

$$l_\mathrm{d,max} = L \ln\left(1 + \mu_+ E_0 \frac{\tau_\mathrm{b}}{L}\right) \tag{2.25}$$

Here, L is the characteristic length at which E_0 decreased to the value $1/e$.

The sum of the maximum drift distance $l_\mathrm{d,max}$ and the effective diffusion length l_+ (see Equation (2.19)) provides an estimate of the maximum distance from the interface from which positrons can still reach it.

2.3.3. Positron Trapping and Annihilation

In the periodic potential of a crystal lattice, a free positron can be described as a plane matter wave with a de Broglie wavelength

$$\lambda_+ = \frac{h}{m^* v_\mathrm{th}}, \tag{2.26}$$

where h is Planck's constant, m^* is the effective mass of the positron, and v_{th} is its root-mean-squared thermal velocity $\sqrt{\langle v_{\mathrm{th}}^2 \rangle}$[37].

At 300 K, this wavelength is about 50 Å, which corresponds to roughly 50 interatomic spacings. In positron annihilation spectroscopy, it is assumed that only one positron is present in the crystal at any given time. Therefore, the Pauli exclusion principle for positron quantum states is fulfilled for all low-energy positron states [36, 37].

Figure 2.6 shows a silicon carbide (4H-SiC) crystal in the [001] plane together with the calculated probability density $\sum_{i=1}^{n} |\psi|^2$ for n electrons (top) and $|\psi|^2$ for one positron (bottom). The yellow and red surfaces represent iso-surfaces of the electron and positron densities, respectively. Each iso-surface corresponds to a cutoff value of $|\psi|^2$, defined as an arbitrary fraction of its maximum value. The wavefunctions were calculated by M. Dickmann using the Density Functional Theory code ABINIT [67].

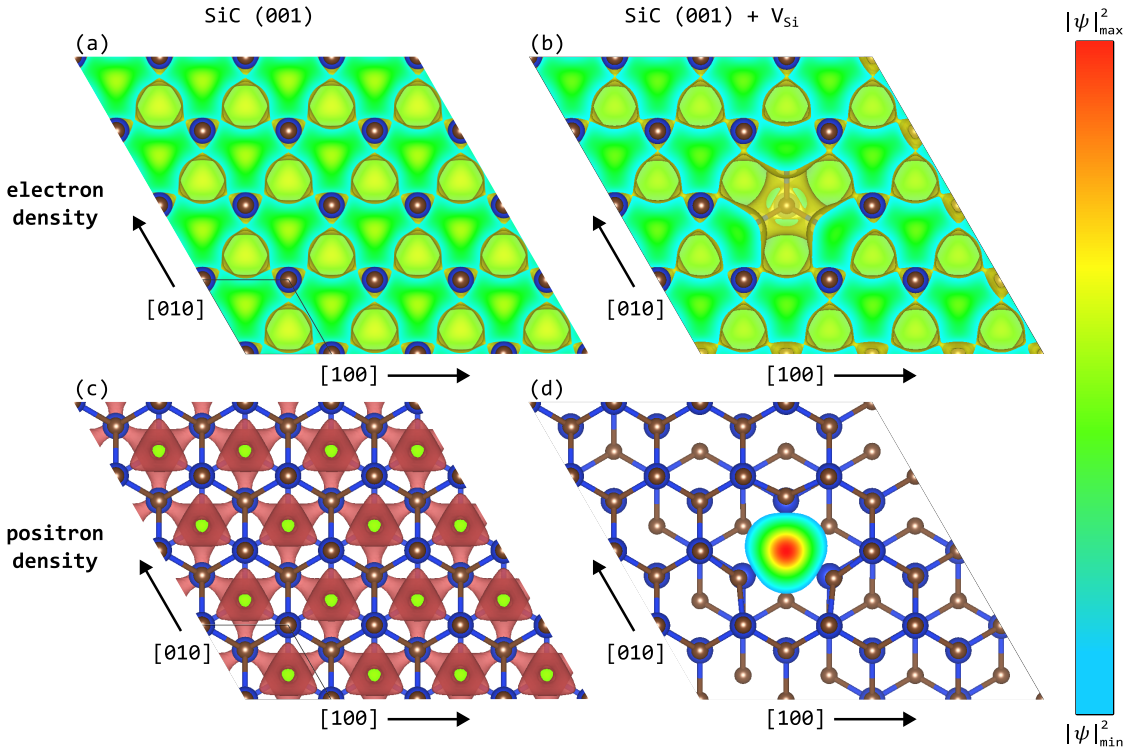

Figure 2.6.: Density Functional Theory calculations of a 4H-SiC crystal. Panels (a) and (b) show the electron probability density for a perfect lattice and for a silicon vacancy, respectively. Panels (c) and (d) show the corresponding positron probability density. The localization of the positron becomes apparent when a silicon atom is removed from the periodic lattice.

Figure 2.6 (a) shows that the electron probability density is strongly localized around

the atoms and along the covalent Si–C bonds. In contrast, due to Coulomb repulsion from the positively charged nuclei, the positron wavefunction remains delocalized in the regions between atoms and spreads throughout the lattice, as shown in Figure 2.6 (c). If the periodic structure is disturbed, for example by an atomic vacancy like in Figure 2.6 (b), the absence of the atom creates an attractive potential well for the positron because of the missing positive nuclear charge. This is illustrated in Figure 2.6 (d), where the positron experiences a binding energy of the order of 1 eV, which is much higher than typical thermal energies in the order of 1/40 eV for 300 K.

When a thermalized positron approaches within about one de Broglie wavelength of such a defect, it may be trapped at the site [68]. The trapping process requires that the positron dissipates its binding energy, released upon falling into the potential well of a defect, through loss channels such as phonon excitation or electron–hole pair generation [35, 37]. After this dissipation, the positron wavefunction collapses, and the positron becomes localized at the defect site. The number of scattering events required depends on the dominant phonon type, typically a single event for optical phonons, but several for acoustic phonons.

Once trapped, the positron may eventually annihilate with an electron from the surrounding electron density, satisfying all conservation laws – namely, conservation of charge, linear momentum, angular momentum, and total net matter. This process is illustrated by the Feynman diagrams in Figure 2.7.

The selection rule for the annihilation of an electron-positron pair is determined by conservation of orbital angular momentum and charge parity [69, 70]:

$$(-1)^{l+s} = (-1)^n \tag{2.27}$$

It follows, that an anti-parallel spin configuration (singlet state) with orbital angular momentum $l = 0$ and total spin $s = 0$, annihilate into an even number of n photons as shown in Figure 2.7 for two vertices. The parallel spin configuration (triplet state) with $l = 0$ and $s = 1$ annihilates into odd numbers of photons as shown for three vertices in Figure 2.7 [69, 70].

In the case of annihilation of an electron–positron pair, the two-gamma annihilation process is the dominant channel, as described by

$$e^- + e^+ \rightarrow \gamma + \gamma \tag{2.28}$$

In this process, two gamma photons are emitted, each with an energy of 511 keV, corresponding to the total rest mass energy $2m_e c^2$ of the electron–positron pair. In the center-of-mass frame, the photons are emitted in opposite directions (180° apart), each carrying exactly 511 keV. However, in the laboratory frame, both the

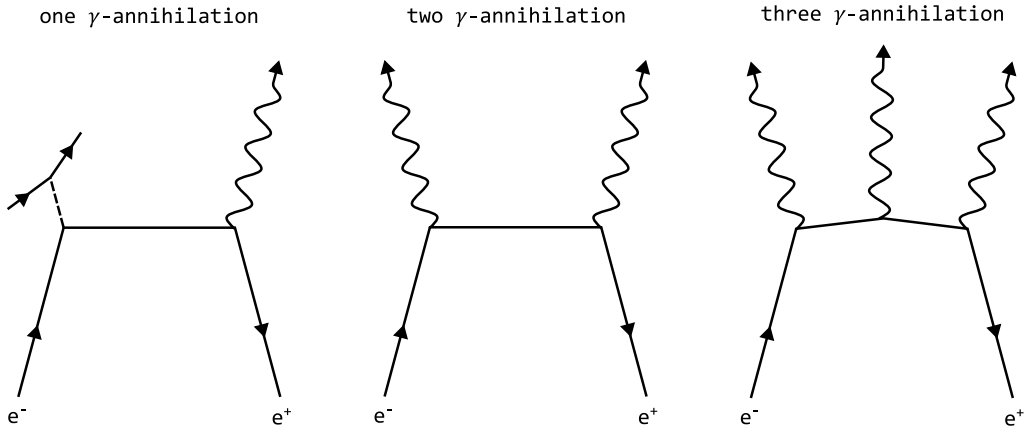

Figure 2.7.: Feynman diagrams of the electron–positron annihilation process. Left: single-photon emission, possible only if a third body absorbs the residual momentum. Middle: two-photon emission, which is the dominant annihilation channel in matter. Right: three-photon emission, suppressed by the fine-structure constant α, but the most probable channel for annihilation of the triplet state of positronium in vacuum (see Section 2.3.4).

photon energies and their emission angles deviate slightly from these values due to the non-zero momentum of the annihilating electron in its atomic orbital.

For non-relativistic positrons, the two-γ annihilation depends on the scattering cross-section of electron and positron:

$$\sigma_{2\gamma} = \frac{\pi r_0^2 c}{v} \tag{2.29}$$

with r_0 being the classical electron radius, v is the positron velocity and c the velocity of light [71].

Momentum conservation strictly forbids the single-photon branch unless a third body absorbs the excess momentum. The emission of three or more γ quanta is possible but strongly suppressed, with the scattering cross section decreasing proportionally to the fine-structure constant:

$$\alpha = e^2/(4\pi\epsilon_0\hbar c) \approx 1/137. \tag{2.30}$$

Thus, the cross-section of the three-γ branch $\sigma_{3\gamma} \approx \alpha\sigma_{2\gamma}$, whereas for the five-$\gamma$ process is $\sigma_{5\gamma} \approx \alpha^3\sigma_{2\gamma}$ [71]. However, if we consider the phase space factor of the three-γ annihilation and the spin statistics of the singlet and triplet states of 1:3, the three-γ process is $\approx \frac{1}{370}$ less likely to occur for the annihilation of an electron-

positron pair [72].

Standard trapping model

The trapping and annihilation processes can be described by the Standard Trapping Model (STM) [35, 73, 74], which, in its basic form, assumes that diffusion, drift, and detrapping are negligible [68]. In the simplest scenario, the two-state STM, a positron may either annihilate in the bulk or become trapped at a single type of defect, as illustrated in Figure 2.8. Here, n_b denotes the time-dependent population of positrons in the bulk, while n_d represents the population of positrons trapped at defects. The annihilation rate in the bulk is λ_b, the trapping rate is κ_d, and the annihilation rate at defects is λ_d.

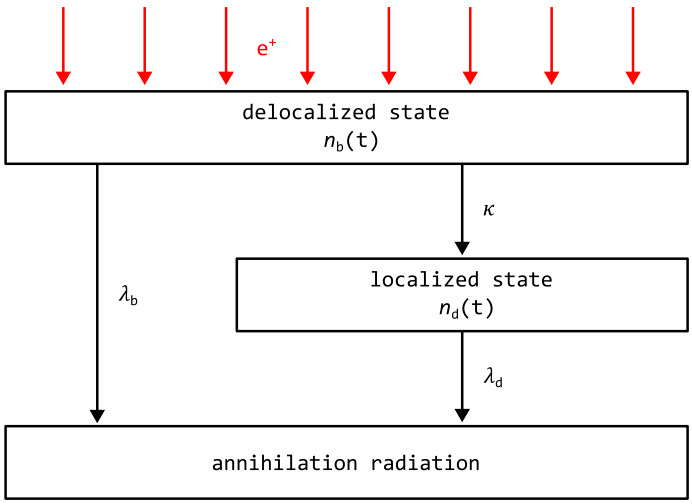

Figure 2.8.: Schematic of the two-state trapping model. Positrons in the bulk can either annihilate with rate λ_b or become trapped at defects with rate κ, where they subsequently annihilate with rate λ_d.

This leads to the following set of differential rate equations for the two-state trapping model [35, 73, 74]:

$$\frac{dn_\mathrm{b}(t)}{dt} = -\lambda_\mathrm{b} n_\mathrm{b}(t) - \kappa n_\mathrm{b}(t) = -(\lambda_\mathrm{b} + \kappa) n_\mathrm{b}(t) \tag{2.31}$$

$$\frac{dn_\mathrm{d}(t)}{dt} = -\lambda_\mathrm{d} n_\mathrm{d}(t) + \kappa n_\mathrm{b}(t) \tag{2.32}$$

Solving for the total time-dependent positron population in the lattice at time t, given by $n(t) = n_\mathrm{b} + n_\mathrm{d}$, with the initial conditions $n_\mathrm{b}(0) = 1$ and $n_\mathrm{d}(0) = 0$, yields

$$n(t) = \left(1 - \frac{\kappa}{\lambda_\mathrm{b} + \kappa - \lambda_\mathrm{d}}\right) e^{-(\lambda_b + \kappa)t} + \frac{\kappa}{\lambda_\mathrm{b} + \kappa - \lambda_\mathrm{d}} e^{-\lambda_d t}. \tag{2.33}$$

By using the following parameters, the solution of the two-state trapping model yields the theoretical decay spectrum in Section 2.1.1 Equation (2.1):

$$\tau_1 = \frac{1}{\lambda_\mathrm{b} + \kappa} \tag{2.34}$$

$$\tau_2 = \frac{1}{\lambda_d} \tag{2.35}$$

$$I_2 = \frac{\kappa}{\lambda_\mathrm{b} + \kappa - \lambda_\mathrm{d}} \tag{2.36}$$

$$I_1 = 1 - I_2. \tag{2.37}$$

Equation (2.34) shows that when positrons are trapped in a defect ($\kappa \neq 0$), the effective rate is enhanced by adding κ to the annihilation rate λ_b [35]. Thus, an reduced bulk lifetime τ_1 is obtained.

The bulk lifetime can be derived from the measured quantities to verify whether the annihilation process follows the two-state standard trapping model (STM) [41]:

$$\frac{1}{\tau_\mathrm{b}} = \frac{I_1}{\tau_1} + \frac{I_2}{\tau_2} \tag{2.38}$$

In general, the simple trapping model (STM) can be extended to include additional defect types. In such cases, the corresponding set of differential rate equations must be expanded by adding terms for each additional defect type [14]. For a three-state trapping model, the rate equations take the following form:

$$\frac{dn_\mathrm{b}(t)}{dt} = -(\lambda_\mathrm{b} + \kappa_\mathrm{d1} + \kappa_\mathrm{d2}) n_\mathrm{b}(t) \tag{2.39}$$

$$\frac{dn_\mathrm{d1}(t)}{dt} = -\lambda_\mathrm{d1} n_\mathrm{d1}(t) + \kappa_\mathrm{d1} n_\mathrm{b}(t) \tag{2.40}$$

$$\frac{dn_\mathrm{d2}(t)}{dt} = -\lambda_\mathrm{d2} n_\mathrm{d2}(t) + \kappa_\mathrm{d2} n_\mathrm{b}(t) \tag{2.41}$$

Here, $n_{\mathrm{b}}(t)$ denotes the time-dependent positron population in the bulk, while $n_{\mathrm{d1}}(t)$ and $n_{\mathrm{d2}}(t)$ represent the populations in the first and second defect types, respectively. The parameters κ_{d1} and κ_{d2} are the corresponding trapping rates for the two defect types.

Diffusion Trapping model

In the case that diffusion and drift have an influence on the annihilation behaviour of positrons, the interaction of free positrons with the host material must be described by the Diffusion Trapping Model (DTM), which modifies Equation (2.39) [37, 75]:

$$\frac{\partial n_{\mathrm{b}}(z,t)}{\partial t} = D_+ \nabla^2 n_{\mathrm{b}}(z,t) - \nabla \mu_+ E n_{\mathrm{b}}(z,t) - \left(\lambda_{\mathrm{b}} + \kappa_{\mathrm{d1}} + \kappa_{\mathrm{d2}}\right) n_{\mathrm{b}}(z,t) + P(z,0) \tag{2.42}$$

with D_+ being the diffusion constant, μ_+ the positron mobility, E an electric field, λ_{b} the annihilation rate in the defect-free lattice, κ the trapping rate in a defect and $P(z)$ the implantation distribution. Here, the time derivative of the positron population $n(r,t)$ initially determined by the implantation profile $P(z)$ is influenced by these processes: Diffusion, drift, trapping, and annihilation. The rate equations describing trapping and annihilation from defect states remain unchanged and are given by Equations (2.40) and (2.41). An analytic treatment of this Fokker-Planck type Equation (2.42) was given by Kögel et al. [76], which directly derives the dependence of experimental observables with the DTM. The Kögel models were first experimentally tested on different silicon samples [77]. By applying the back-diffusion method [26, 65], it is possible to fit these models to the experimental data and further extract important kinetic properties of the positron, such as the diffusion constant D_+ and the surface capture rate ν. The latter can be interpreted as the effective velocity at which positrons escape from the bulk into surface states. Building on the theoretical framework established in [76], Werner Egger developed a numerical method for determining diffusion parameters from experimental observables.

For the surface intensity I_2, one obtains

$$I_2 = \frac{\nu\left(1 - p\sqrt{\frac{\pi}{2}}\exp\left(\frac{p^2}{4}\right)\operatorname{erfc}\left(\frac{p}{2}\right)\right)}{\left(1 + \sqrt{D_+\left(\lambda_b - \lambda_s\right)}\right)} \tag{2.43}$$

and for the average positron lifetime:

$$\tau_{\mathrm{av}} = \frac{\tau_{\mathrm{b}} + (\tau_{\mathrm{s}} - \tau_{\mathrm{b}}) \left(1 - p\sqrt{\frac{\pi}{2}} \exp\left(\frac{p^2}{4}\right) \operatorname{erfc}\left(\frac{p}{2}\right)\right)}{\left(1 + \frac{D_+}{\nu^2 \tau_{\mathrm{b}}}\right)}. \tag{2.44}$$

with an approximated implantation parameter of the form:

$$p = 14\sqrt{\frac{\lambda_b - \lambda_{surf}}{D_+}} \left(\frac{E_{imp}}{\mathrm{keV}}\right)^{1.7}$$

D_+ and ν denote the diffusion constant and the surface transition rate, respectively. The annihilation rates in the bulk and at the surface are given by $\lambda_b = 1/\tau_{\mathrm{b}}$ and $\lambda_s = 1/\tau_s$. The erfc is the complementary error function. A Python script implementing Equations (2.43) and (2.44) for use with experimental observables $\bar{\tau}$ and I_2 was developed in this work and is provided in Appendix A.

2.3.4. Positronium Formation and Annihilation

Besides free positron annihilation, a positron can also bind with an electron to form the positronium atom. This bound state is similar to the hydrogen atom, with a binding energy of $-6.8\,\mathrm{eV}$ in vacuum. In vacuum, the center-of-mass radius is twice the Bohr radius, $2a_0 = 1.058 \times 10^{-10}\,\mathrm{m}$. However, since $a_0 \propto \epsilon$, the radius depends on the material's relative permittivity and can become significantly larger, leading to a correspondingly lower binding energy [70].

Positronium typically forms during the thermalization process, when positrons ionize atoms or create electron-hole pairs, thereby generating free electrons along their stopping path. Several formation mechanisms are reported in the literature [25]: the Ore model [38], the spur model [78], and the blob model [79]. The formation of positronium is suppressed in metals due to the high density of conduction electrons and the strong Debye screening of the positron [80]. As the electron density decreases, screening effects weaken, electron–positron correlations become more important, and the probability of positronium formation increases [80]. Once the positron has lost sufficient energy, it can bind to a free electron produced in the spur, resulting in positronium formation.

Positronium can exist in two spin states: the singlet state, ${}^1S_0$ ($S = 0, m_{\mathrm{s}} = 0$), known as para-positronium (p-Ps), and the triplet state, ${}^3S_1$ ($S = 1, m_{\mathrm{s}} = -1, 0, 1$), known as ortho-positronium (o-Ps). According to their spin statistics, the formation ratio of p-Ps to o-Ps is $1:3$.

Due to the same spin statistics and cross section as the unbound electron-positron pair in vacuum, the same annihilation kinetics apply to the positronium. Thus, the

vacuum lifetime of the singlet spin configurations is:

$$\tau_{\text{para}} = 1/\lambda_{\text{para}} = 125\,\text{ps} \tag{2.45}$$

and the triplet spin configuration:

$$\tau_{\text{ortho}} = 1/\lambda_{\text{ortho}} = 142\,\text{ns} \tag{2.46}$$

The spin-averaged annihilation rate of positronium is [71, 80]

$$\lambda_{\text{av}} = \frac{1}{4}\lambda_{\text{para}} + \frac{3}{4}\lambda_{\text{ortho}} \approx 2.003\,\text{ns}^{-1} \tag{2.47}$$

With $\lambda = 1/\tau$, this yields the low-density limit of positron lifetimes and implies that positron lifetimes cannot exceed 500 ps, because at low electron densities, a positron with its screening electrons, which can have parallel or opposite spin, is similar to positronium. If a measured lifetime exceeds this limit, it can be attributed to the formation of o-Ps.

Several mechanisms can influence the formation or annihilation of positronium, such as quenching [38, 81] and inhibition by electron scavenging [82]. In the context of this work, the relevant effect is inhibition by an electric field. This field effect arises from the charge separation of electron and positron before the bound state can form [38, 83].

The most important mechanism, however, is the reduction of the o-Ps vacuum lifetime in matter through pick-off annihilation, where the positron annihilates with an electron from the surroundings with opposite spin [84]. This process results in two-γ annihilation. Experimentally, pick-off annihilation is highly significant because it produces an observable lifetime in matter that directly reflects the characteristic dimensions of defects in the material.

The correlation between the o-Ps lifetime and the size of defects arises from the formation of positronium in subnanoscopic and nanoscopic pores or free-volume elements with diameters ranging from a few ångströms to several nanometers. Once formed, the o-Ps lifetime is primarily determined by the overlap between the positronium wave function and the electron wave function of the surrounding pore walls.

In the approximation proposed by Tao [85], the Ps wave function is localized inside a square potential well representing the pore, while the electron wave function of the surrounding atoms extends into the well. This creates a border region where the Ps and wall electron wave functions overlap, enabling pick-off annihilation. The width of this overlap region depends on the overall pore size. Consequently, larger pores reduce the overlap, resulting in longer o-Ps lifetimes.

A quantitative way to relate measured o-Ps lifetimes to defect dimensions was introduced by Tao [85] and later refined by Eldrup et al. [86]. This approach is now commonly referred to as the Tao–Eldrup model:

$$\lambda_{\mathrm{ortho}}(R) = \lambda_{\mathrm{av}} \left[1 - \frac{R}{R + \Delta R} + \frac{1}{2\pi} \sin \frac{2\pi R}{R + \Delta R} \right] \tag{2.48}$$

Here, λ_{ortho} denotes the annihilation rate of o-Ps due to pick-off annihilation, $\lambda_{\mathrm{av}} = 2.003\,\mathrm{ns}^{-1}$ is the spin-averaged annihilation rate from Equation (2.47), R is the radius of the free-volume element, another word for pore, for which the equation is solved, and $\Delta R = 0.165\,\mathrm{nm}$ is an empirical size parameter. The model is valid for spherical pore geometries and o-Ps lifetimes up to approximately 20 ns.

In real materials, pores are often non-spherical, and the spherical approximation may no longer be valid. Therefore, the Tao–Eldrup model has been extended to describe different pore shapes and larger pore dimensions [87, 88].

3. Metal-Oxide-Silicon System

In this chapter, the metal–oxide–semiconductor (MOS) system, which forms the foundation of the drift experiment presented in Chapter 6, is introduced. The microstructure and defects of the key constituent materials are briefly described, with emphasis on the most relevant defect types. Since the focus of this work lies on the oxide–semiconductor interface, particular attention is directed toward the oxide layer and its technologically important interface with the substrate.

In addition, the fundamental physical principles of the MOS device are outlined, with special emphasis on the mechanisms that establish an electric field across its different regions. To avoid ambiguity with energy, the electric field is denoted by the symbol $\mathscr{E}$ throughout this chapter.

Collectively, these concepts provide the theoretical framework required to understand the positron drift experiment and to interpret the results presented in Chapter 6.

3.1. Gate (Al) and Substrate (Si)

The principal metal-oxide-semiconductor (MOS) system is comprised out of three different materials, that is, a conductive gate material, an insulator material, and a semiconducting material. This ultimately forms the MOS capacitor as represented schematically in Figure 3.1.

The gate primarily serves as a means to apply a voltage to the MOS system, thereby controlling interface inversion and the concentration of charge carriers in the channel. Possible gate materials include highly doped poly-silicon, metals (e.g., Al) [89], or 2D materials (e.g., graphene) [90]. The material requirements include strong adhesion to the oxide, thermal and chemical stability, and low resistivity. The most critical electronic property, however, is the work function Φ_m, which ultimately defines the electronic characteristics of the MOS capacitor. For an n-type semiconductor, a low Φ_m – smaller than the intrinsic Fermi level of the semiconductor – is preferred, whereas for a p-type semiconductor, a high Φ_m – larger than the intrinsic Fermi level – is desired [91].

The substrate constitutes the single-crystal (sc) semiconductor component of the

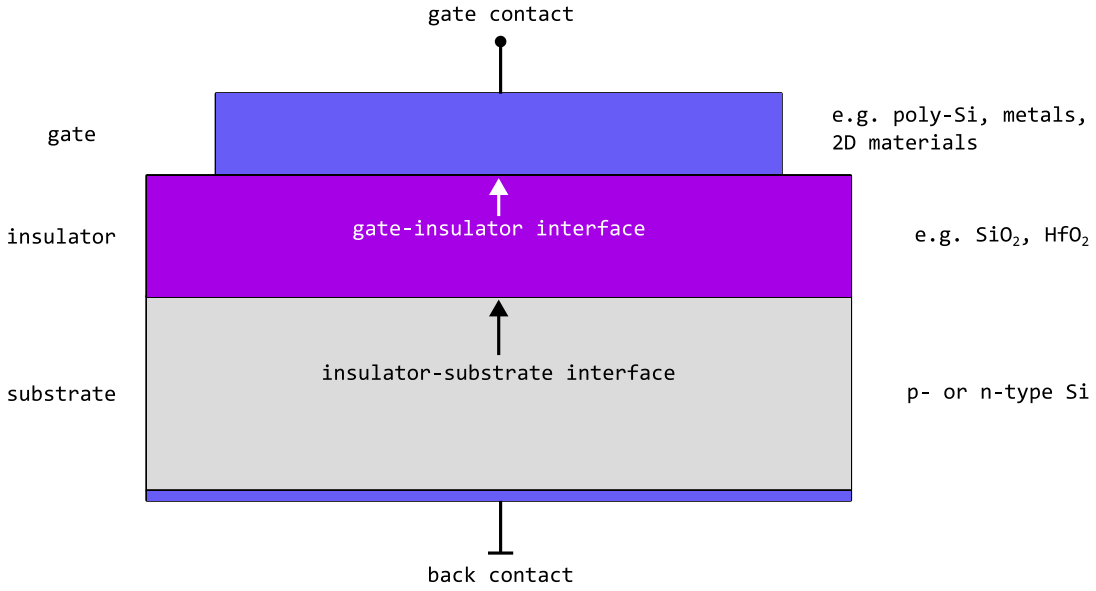

Figure 3.1.: Schematic representation of the principal composition of the metal-oxide-semiconductor system. On the left side of the layered system, the role of the layer is labeled with typical materials on the right side.

MOS system. High purity and a low concentration of impurities are essential, as impurities act as recombination centers. In silicon technologies, the substrate further serves as the basis for the straightforward fabrication of high-quality silicon dioxide via thermal oxidation. The backside of the semiconductor is equipped with an ohmic contact that serves as the ground of the MOS device.

The doping concentration of the semiconductor substrate determines the maximum charge carrier concentration achievable in the interface channel through the mass-action law [92], which, for a p-doped substrate, is expressed as

$$p_{\mathrm{o}} n_{\mathrm{o}} = n_{\mathrm{i}}^2 \tag{3.1}$$

where n_{i} is the intrinsic charge carrier concentration, and p_{o} and n_{o} are the equilibrium densities of holes and electrons, respectively. For p-doped silicon with $p_{\mathrm{po}} \approx N_{\mathrm{A}} = 1 \times 10^{15}\,\mathrm{cm}^{-3}$ and an intrinsic carrier concentration of $n_{\mathrm{i}} = 1 \times 10^{10}\,\mathrm{cm}^{-3}$, the equilibrium electron concentration is $n_{\mathrm{o}} = 1 \times 10^{5}\,\mathrm{cm}^{-3}$.

Although the defect concentration is very low in sc-Si – lower than the resolution limit of most analysis methods – defects do exist. The main defect types are point defects, such as vacancies and larger clusters of vacancies, which typically play a minor role in technologic-grade silicon compared to the impurities introduced during doping [91].

3.2. Gate Oxide (amorphous SiO_2)

The most common and technologically relevant oxide used in the metal–oxide–silicon (MOS) system is thermally grown silicon dioxide. Its main advantages lie in the straightforward fabrication process, the high level of control over growth conditions, and the relatively sharp, low-defect interface with crystalline silicon [93].

As illustrated in Figure 3.2, silicon dioxide can be described as a continuous network of SiO_4 tetrahedra (chemical formula SiO_2).

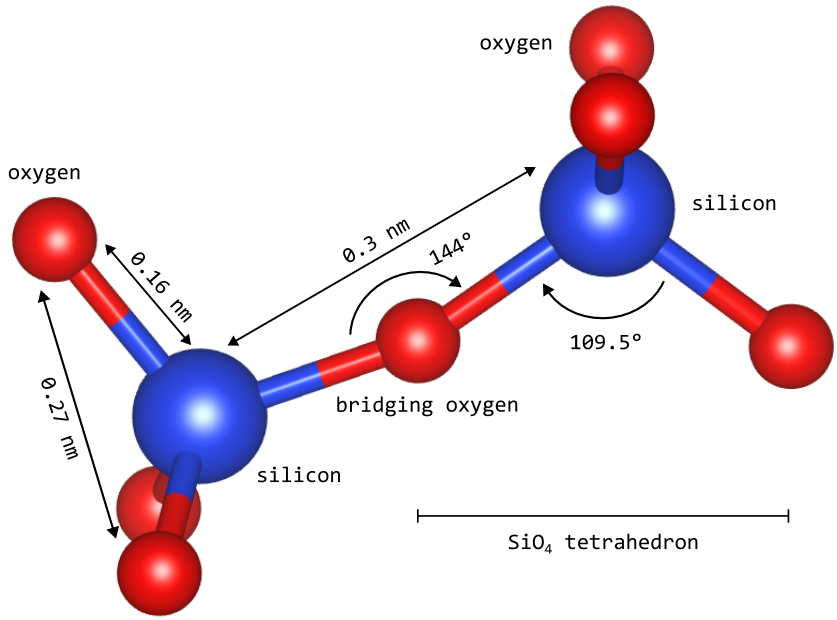

Figure 3.2.: Illustration of two bonded SiO_4 tetrahedra. For the crystalline polymorph α-quartz, typical bond lengths and a Si–O–Si bond angle of 144° are shown. In the amorphous state, the Si–O–Si bond angle can vary between $120 - 180°$, and the dihedral angle is random, resulting in significant variations of the intermolecular geometry [94].

Each tetrahedron consists of a central silicon atom bonded to four oxygen atoms at the corners, with a fixed O–Si–O bond angle of 109.5°, characteristic of tetrahedral coordination. The tetrahedra are connected via bridging oxygen atoms. In the crystalline polymorph α-quartz, the Si–O–Si bond angle is fixed at about 144°. In contrast, in amorphous SiO_2 the Si–O–Si bond angle varies within the range of $120 - 180°$ [95]. Furthermore, the dihedral angle, i.e., the relative rotational orientation of adjacent tetrahedra, is random in the amorphous state, introducing significant structural disorder [94].

From this point onward, thermally grown amorphous SiO_2 will be referred to simply

as thermally grown SiO_2, or, for brevity, as SiO_2.

Defects in SiO_2 mainly arise from process conditions, and the inherent structural disorder, i.e., variations in bond angles, bond lengths, and dihedral orientations [91]. Given the wide variety of possible defects, such as abnormal Si-O bonds, non-bridging oxygen, interstitial atoms (e.g. Si, O, Na^+, OH^-) and vacancies (Si, O) [91].

Oxygen-related defects are much more versatile and include the following representative examples:

- Non-bridging oxygen (NBO): An oxygen atom bonded to only one silicon atom, leaving a dangling bond toward an adjacent SiO_4 tetrahedron. This defect is amphoteric, existing in positive, neutral, or negative charge states. Energetically, the NBO is located close to the valence band of SiO_2 and can trap holes, forming the so-called non-bridging oxygen hole center (NBOHC) [91].
- Oxygen vacancy: The absence of an oxygen atom results in two configuration because the missing oxygen can either be bridging or non-bridging. The bridging oxygen results in neighboring Si dangling bonds that weakly bond with each other. This is a neutral oxygen vacancy.
- E'-center: The neutral oxygen vacancy is the precursor to the E'-center, one of the most prominent and technologically relevant defects in SiO_2, especially in thin SiO_2 layers, since these defects are located close to the interface and can trap electrons from the silicon side of the interface via tunneling [96]. The E'-center is amphoteric but predominantly exists as in its positive state, typically formed when one silicon dangling bond captures a hole and relaxes into a planar trigonal configuration [91], while the other silicon atom remains in a tetrahedral coordination with an unpaired electron. This way, the oxygen vacancy will change its charge state from neutral to positive. The unpaired spin makes the defect paramagnetic and detectable via electron spin resonance (ESR). E'-centers are frequently encountered in thermally grown SiO_2 [97].

The silicon vacancy is the most important defect related to silicon, but it is less likely to form in SiO_2 than in crystalline silicon due to the higher binding energy of the Si–O bond [91].

3.3. SiO_2/Si Interface

The interface between the oxide and the semiconductor is the most critical region of the MOS system, as defects located at or near the interface directly affect carrier transport in the inversion channel. For thermally grown oxides, the SiO_2/Si interface is known to be very sharp, though not perfectly abrupt. Early X-ray Photoelectron

Spectroscopy (XPS) [98] and Auger Electron Spectroscopy (AES) [95] studies showed that the interface region extends over approximately 3–5 nm.

The interface region can be divided into two distinct transition layers. First, a structural transition layer arises from the relaxation and adaptation of stoichiometric SiO_2 to the underlying silicon lattice. This layer has been shown to exhibit a denser SiO_2 structure, resembling crystalline SiO_2 polymorphs, as a result of strain during oxidation [96]. Its thickness is typically $1-2\,\mathrm{nm}$ [99, 100]. Beyond this, a chemical transition layer is formed, characterized by the presence of silicon in intermediate oxidation states (Si^{+1}, Si^{+3}). This leads to non-stoichiometric SiO_x, where $2 > x > 0$ [99]. Depth profiling with XPS has shown that this chemical transition layer extends about 1 nm into the oxide and a few monolayers into the silicon [101]. It should be emphasized that the thickness of the interface region strongly depends on the oxidation conditions, including pre-treatment, oxidation temperature, ambient atmosphere, and post-oxidation annealing [102].

The most prominent structural defect associated with the Si/SiO_2 interface is the P_b center ($\cdot Si \equiv Si^3$), consisting of a silicon atom bonded to three other Si atoms, leaving one unsaturated orbital ($\cdot$). In its simplest form on the (111) crystal face, this dangling bond orbital is oriented perpendicular to the interface. For the technologically important (100) orientation, two distinct types of defects exist: P_{b0}, similar to P_b on (111), and P_{b1} [96, 103]. Their dangling bonds are tilted relative to the surface normal and are oriented according to the silicon lattice symmetry [95].

Because the dangling orbital contains an unpaired spin, the P_b center acts as an amphoteric trap with multiple charge states: neutral (P_b^0), negative (P_b^-), or positive (P_b^+). Under operating conditions, the application of a gate bias can switch the charge state of the defect. The existence of P_b centers has been unambiguously demonstrated using electron spin resonance (ESR) spectroscopy [104].

The P_b center is an inherent structural defect resulting from the lattice mismatch between crystalline silicon and amorphous SiO_2. It forms during the thermal oxidation process and is generally the dominant contributor to the interface trap density D_{it} [95]. Since it is localized on the silicon side of the interface, its volume density can be approximated as

$$N_{P_b} = \frac{N_{it}}{E_g t_{eff}} \approx \frac{1\times10^{11}\,\mathrm{eV^{-1}cm^{-2}}}{1.12\,\mathrm{eV}\;3\times10^{-8}\,\mathrm{cm}} \approx 3\times10^{18}\,\mathrm{cm^{-3}}. \tag{3.2}$$

Here, N_{it} represents the typical magnitude of the interface trap area density for a wet-oxidized SiO_2 layer on Si without annealing [105], $E_g = 1.12\,\mathrm{eV}$ is the band gap of silicon at room temperature, and t_{eff} denotes the thickness of the structurally distorted silicon transition layer, which is approximately two monolayers thick.

3.4. Band Structure and Operation Modes

The metal–oxide–semiconductor (MOS) junction is a key structure with wide-ranging applications in electronic and information technologies. Its layered composition enables the formation of an ultra-thin conductive channel – only a few nanometers thick – at the oxide/semiconductor interface. The density of charge carriers in this channel can be precisely controlled by the voltage applied to the metal gate across the oxide. This principle forms the foundation of the metal–oxide–semiconductor field-effect transistor (MOSFET), the fundamental building block of modern semiconductor technology.

When the working principle of a MOS capacitor is discussed, it is necessary to define basic rules under which the following model is valid: (1) the oxide is a perfect insulator with zero current flowing in static conditions; (2) charges only exist in the gate and semiconductor; (3) the semiconductor is uniformly doped; (4) the MOS properties only change in one direction depth z [92].

When the three layers are separated, each layer is in its own thermal equilibrium condition, which means that the Fermi levels are constant and at a material characteristic distance (work function) from their respective vacuum levels. As soon as they are in contact, the entire MOS structure forms a single system that seeks a new equilibrium condition. This requires that the Fermi levels must align, which is a defining characteristic of thermal equilibrium. In the usual case that the work function of the metal and the semiconductor are different, this alignment results in a built-in potential difference across the structure.

$$\Phi_{\mathrm{ms}} = \Phi_{\mathrm{m}} - \Phi_{\mathrm{s}} = \Phi_{\mathrm{m}} - \left(q\chi_{\mathrm{s}} + (E_{\mathrm{C}} - E_{\mathrm{F}})\right)_{\mathrm{bulk}} . \tag{3.3}$$

With Φ_{m} being the work function of the metal gate. $q\chi_{\mathrm{s}}$ is the electron affinity of the semiconductor, E_{C} and E_{F} are the conduction band minimum and Fermi level of the semiconductor, respectively, with respect to the bulk, since far away from the interface, charge neutrality still holds, and no band bending exists.

Since no current can flow across the insulating oxide, the Fermi level remains constant throughout the structure ($dE_{\mathrm{F}}/dz = 0$). The system establishes a new equilibrium through bending of the valence and conduction bands near the interface and a redistribution of charge [106].

Under flat-band conditions, the ideal case is $\Phi_{\mathrm{m}} = \Phi_{\mathrm{s}}$, where the MOS device is electrically neutral, exhibiting neither band bending nor a built-in voltage across the oxide and semiconductor. In the non-ideal case, where $\Phi_{\mathrm{m}} \neq \Phi_{\mathrm{s}}$, flat-band conditions can still be established by applying a gate voltage that compensates the built-in voltage, such that

$$U_{\mathrm{bi}} = \frac{\Phi_{\mathrm{m}} - \Phi_{\mathrm{s}}}{q} = -U_{\mathrm{g}} = -U_{\mathrm{fb}} \tag{3.4}$$

To compensate for this built-in voltage, an opposite gate voltage must be applied. This gate voltage is defined as the flat-band voltage, U_{fb} [107]. For a combination of aluminum, SiO_2 and p-type (100) silicon the ideal work function difference is $\phi_{\mathrm{ms}} = -0.8\,\mathrm{eV}$.

As shown in Figure 3.3, when an external gate voltage is applied, the MOS system is driven out of thermal equilibrium. Depending on the polarity of the voltage, the Fermi level of the gate is shifted upward or downward. To maintain Fermi-level continuity, the energy bands bend toward the metal's Fermi level, and the opposite charge must be accumulated at the oxide-semiconductor interface to maintain a balance of charge. The direction and magnitude of this band bending depend directly on the sign and strength of the applied gate voltage, and charge neutrality demands that the charge area density of the metal interface Q_{m} is opposite to the semiconductor interface Q_{s}

$$Q_{\mathrm{m}} = -(Q_{\mathrm{p}} + Q_{\mathrm{n}} + qN_{\mathrm{A}}w) = -Q_{\mathrm{s}} \tag{3.5}$$

with Q_p and Q_n are the charge area densities of holes and electrons, respectively. N_{A} is the doping concentration of the semiconductor and w is the width of the depletion region [92].

The charge redistribution results in an electric field $\mathscr{E}$ across the oxide and extends into the near-surface region of the semiconductor. The electric field can be derived by using Poisson's equation:

$$\frac{d\mathscr{E}(x)}{dx} = -\frac{\rho}{\epsilon_{\mathrm{r}}\epsilon_0} \tag{3.6}$$

In the semiconductor, the electric field $\mathscr{E}$ depends on the charge density and its dependence on the distance z to the interface. The band bending can be characterized by the difference of the intrinsic Fermi level $E_{\mathrm{i}}(z)$ at the interface to the bulk level $E_{\mathrm{i}}(\infty)$. The intrinsic Fermi level is the Fermi level of the undoped semiconductor, and lies approximately in the middle of the band gap at large distances from the interface $z \to \infty$. Close to the interface, due to the band bending, this energy becomes a function of z, and the energy difference $\Delta E_{\mathrm{i}} = E_{\mathrm{i}}(z) - E_{\mathrm{i}}(\infty)$ results in a nonlinear function of the electric field.

The charge density of a p-type semiconductor can be distinguished using the boundary condition at large distances from the interface of $E_{\mathrm{i}}(z) - E_{\mathrm{i}}(\infty) = 0$ and $\rho(z) = 0$ by

$$\rho(z) = -\frac{q}{\epsilon_{\mathrm{si}}\epsilon_0}(p_{\mathrm{p}}(z) - p_{\mathrm{po}} - (n_{\mathrm{p}}(z) - n_{\mathrm{po}})) \tag{3.7}$$

with $\epsilon_{\mathrm{si}} = 11.9$ being the relative permittivity of silicon. p_{po} and n_{po} are the equilibrium densities [92].

The total hole and electron densities at position z is

$$p_{\mathrm{p}}(z) = p_{\mathrm{po}} e^{-\frac{\Delta E_{\mathrm{i}}(z)}{kT}} \tag{3.8}$$

$$n_{\mathrm{p}}(z) = n_{\mathrm{po}} e^{\frac{\Delta E_{\mathrm{i}}(z)}{kT}} \tag{3.9}$$

With Equation (3.6), this yields the expression for the electric field in the band banding region of the semiconductor:

$$\mathscr{E}(x) = \pm\frac{\sqrt{2}kT}{qL_{\mathrm{D}}}\sqrt{\left(e^{-\frac{\Delta E_{\mathrm{i}}(x)}{kT}} + \frac{\Delta E_{\mathrm{i}}(x)}{kT} - 1\right) + \frac{n_{\mathrm{po}}}{p_{\mathrm{po}}}\left(e^{\frac{\Delta E_{\mathrm{i}}(x)}{kT}} - \frac{\Delta E_{\mathrm{i}}(x)}{kT} - 1\right)} \tag{3.10}$$

with L_{D} being the Debye length for holes

$$L_{\mathrm{D}} = \sqrt{\frac{kT\epsilon_{\mathrm{si}}\epsilon_0}{p_{\mathrm{po}}q^2}} \tag{3.11}$$

An extensive derivation of the electric field formula can be found in [106].

The electric field at the interface of the semiconductor ($z = 0$) is equal to the electric field across the oxide, which is

$$\mathscr{E}_{\mathrm{ox}} = \frac{\Delta\phi_{\mathrm{ox}}}{d_{\mathrm{ox}}} = \frac{U_{\mathrm{g}} - U_{\mathrm{bi}}}{d_{\mathrm{ox}}} \tag{3.12}$$

this directly follows from rules (1) and (2) and means that $\rho = 0$ in the oxide.

Further, the electric field in the semiconductor at the oxide-substrate interface is given by

$$\mathscr{E}_S = \frac{\epsilon_{\mathrm{ox}}}{\epsilon_{\mathrm{si}}}\mathscr{E}_{\mathrm{ox}} \tag{3.13}$$

Figure 3.3 illustrates the gate voltage relation of a p-type MOS capacitor. The top panel depicts the characteristic band bending in each mode, the middle shows the corresponding electric field distribution, and the bottom indicates the charge density in a block diagram. The MOS capacitor can be biased to three distinct states:

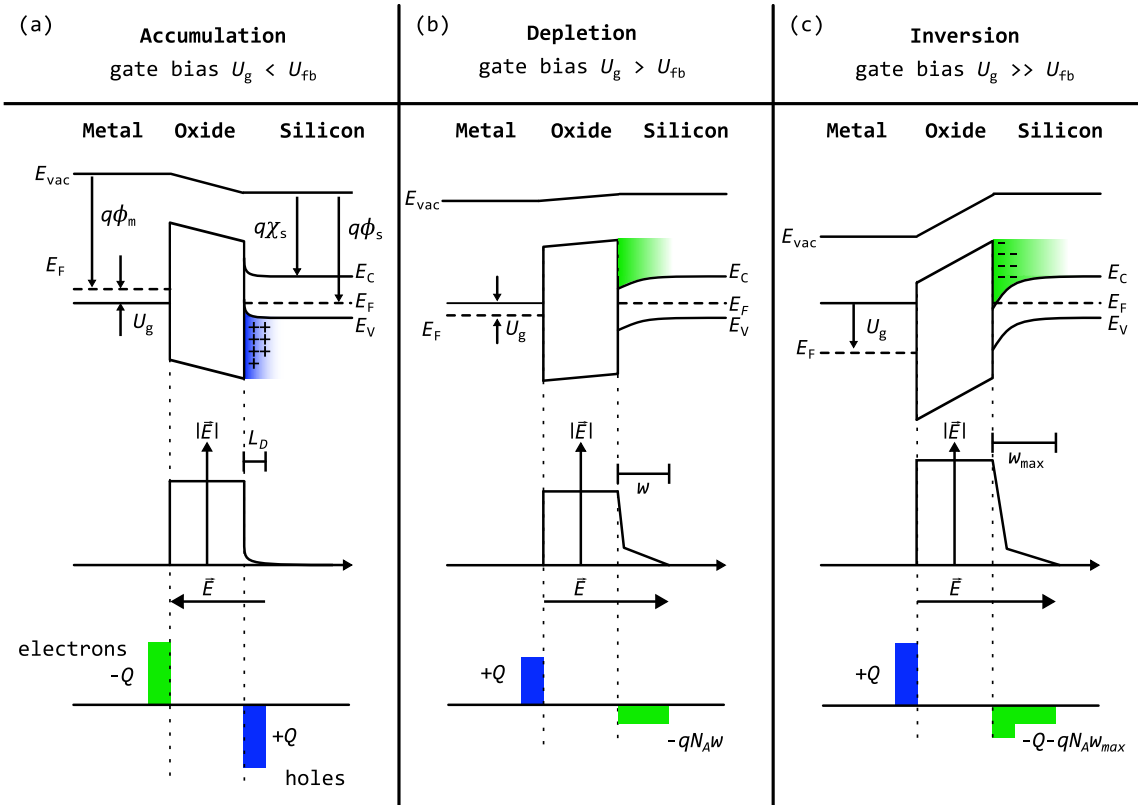

Figure 3.3.: Schematic representation of the band diagram, the electric field distribution and direction in z, and the charge density of a MOS capacitor operating in (a) accumulation, (b) depletion, and (c) inversion. Different operation modes result in different field distributions in the silicon substrate. U_g is the applied gate voltage, $U_{\mathrm{fb}} = 0\,\mathrm{V}$ the flat-band voltage, E_{F} the Fermi energy, E_{C} the conduction band minimum, E_{V} the valence band maximum, $q\chi_{\mathrm{s}}$ the electron affinity of the semiconductor, Φ_m and $q\Phi_s$ the work functions of the metal and semiconductor, respectively.

Accumulation mode ($U_{\mathrm{g}} < U_{\mathrm{fb}}$)

In accumulation (Figure 3.3), holes are accumulated at the interface. The bands bend upward, and the area charge density of the metal gate must be equal to the semiconductor $Q_{\mathrm{m}} = -Q_{\mathrm{p}}$. This means the valence band moves closer to the Fermi level. The electric field from Equation (3.10) is dominated by the first term and is

directed from the semiconductor to the metal gate. The extent of the accumulation layer can be approximated by the Debye length, $\pi L_{\mathrm{D}}/\sqrt{2}$, for gate voltages close to the flat-band condition. However, under strong accumulation ($U_{\mathrm{g}} \ll U_{\mathrm{fb}}$), the accumulation layer becomes confined to only a few nanometers near the interface. For silicon at $T = 300\,\mathrm{K}$ with a doping concentration of $1 \times 10^{15}\,\mathrm{cm}^{-3}$, the thickness of the accumulation layer is approximately 250 nm.

To estimate the drift velocities of charged particles in the interface region of a semiconductor, it is useful to consider the mean electric field in this region. The electric field decreases exponentially with distance from the surface, and the mean field can be approximated by the field value at the point where it has decayed to $1/e$ of its surface value, which gives a mean electric field of

$$\langle \mathscr{E}_{si} \rangle = \frac{\mathscr{E}_{\mathrm{S}}}{e} \tag{3.14}$$

with e being the Euler number. For strong accumulation, the expression for the Debye length, Equation (3.11), no longer holds, and L_D reduces to a few nanometers because of the high density of charge carriers accumulated at the semiconductor interface [92].

Depletion mode ($U_{\mathrm{g}} > U_{\mathrm{fb}}$)

As soon as the gate voltages exceed the flat-band condition, the band will bend in the other direction, and the conduction band edge moves closer to the Fermi level. The hole carriers are pushed out of the interface region into the semiconductor bulk. The ionized dopant atoms are left in this region, which balances out the charge at the metal interface

$$Q_{\mathrm{m}} = -Q_{\mathrm{s}} = qN_{\mathrm{A}}w \tag{3.15}$$

The electric field is therefore dominated by the second term in Equation 3.10 and can also be written as

$$\mathscr{E}(z) = \int_x^w \frac{qN_{\mathrm{A}}}{\epsilon_{\mathrm{r}}\epsilon_0} dz = \frac{qN_{\mathrm{A}}}{\epsilon_{\mathrm{r}}\epsilon_0}(w - z) \quad (0 \leq z \leq w) \tag{3.16}$$

with N_{A} being the concentration of dopants and w being the width of the depletion region. The depletion region width w can be derived from capacitance measurements and increases with increasing gate voltage up to a maximum width, where the interface gets electronically inverted.

The electric field in the depletion region decreases linearly from the interface and

the mean electric field is given by

$$\langle \mathscr{E}_{si} \rangle = \frac{1}{2} \mathscr{E}_{\mathrm{S}} \tag{3.17}$$

Inversion mode ($U_{\mathrm{g}} \gg U_{\mathrm{fb}}$)

When the conduction band edge is bends below the Fermi level, the interface becomes inverted. In this condition, minority carriers — electrons in the p-type semiconductor — accumulate at the interface. Inversion begins once the electron concentration at the interface equals the equilibrium hole concentration in the bulk, i.e.,

$$n_{\mathrm{p}}(z = 0) = p_{\mathrm{bulk}} = N_{\mathrm{A}}. \tag{3.18}$$

The corresponding charge balance can be written as

$$Q_{\mathrm{m}} = -Q_{\mathrm{n}} + qN_{\mathrm{A}} w_{\mathrm{max}}. \tag{3.19}$$

Unlike the pn-junction, the MOS system exhibits a maximum depletion width w_{max}, which is reached under strong inversion. Beyond this point, further increases in gate voltage no longer widen the depletion region; instead, they primarily generate additional minority carriers that shield the semiconductor bulk from the electric field. The spatial extent of the inversion layer is therefore governed by the Debye screening length, analogous to the accumulation regime.

The entire region over which the electric field penetrates into the semiconductor has a width of

$$w_{\mathrm{max}} = \sqrt{\frac{4\epsilon_{\mathrm{si}} k_{\mathrm{b}} T \ln\left(N_{\mathrm{A}}/n_{\mathrm{i}}\right)}{q^2 N_{\mathrm{A}}}} \tag{3.20}$$

The electric field described by Equation (3.10) is dominated by the second and fourth terms, with the second term alternatively expressed as Equation (3.16) for $z \leq w_{\mathrm{max}}$.

Similar to the case of depletion, the electric field in this operation mode decreases linearly from the interface and the mean electric field is thus given by

$$\langle \mathscr{E}_{si} \rangle = \frac{1}{2} \mathscr{E}_{\mathrm{S}} \tag{3.21}$$

3.5. Capacitance-Voltage Profiling

The standard method for electronic characterization of MOS devices is capacitance-voltage (C–V) profiling, often complemented by conductance and current measurements. This technique provides key information on depletion layer width, doping concentration, interface trap density, and the flat-band voltage. The principle is based on measuring the capacitance and conductance of the layer system as a function of gate voltage.

Depletion width $w_{\max}$

The MOS capacitor can be modeled as a series connection of capacitors with area A, with the applied gate voltage determining how the total capacitance is distributed among them. Figure 3.4 shows a schematic high-frequency C–V curve for a p-doped silicon substrate, along with equivalent circuit diagrams for accumulation, depletion, and inversion.

In accumulation, the capacitance is governed solely by the oxide,

$$C_{\mathrm{ox}} = \frac{\epsilon_{\mathrm{ox}}\epsilon_0 A}{d_{\mathrm{ox}}} = C_{\max} \tag{3.22}$$

which is constant with respect to voltage variation and represents the maximum capacitance of the system.

In the depletion regime, ionized dopant atoms contribute to an additional capacitance of the depletion region with width w

$$C_{\mathrm{dep}} = \frac{\epsilon_{\mathrm{s}}\epsilon_0 A}{w} \tag{3.23}$$

in series with C_{ox}, reducing the total capacitance to

$$\frac{1}{C_{\mathrm{total}}} = \frac{1}{C_{\mathrm{ox}}} + \frac{1}{C_{\mathrm{dep}}} \tag{3.24}$$

Once inversion sets in, the maximum depletion width is reached, and the total capacity reaches a minimum. The minimum capacitance $C_{\min}$ thus reflects the maximum extent of the depletion region. In this case, $C_{\mathrm{total}} = C_{\min}$ and with $C_{\mathrm{dep}} = \frac{\epsilon_{\mathrm{s}}\epsilon_0}{w_{\max}}$. By using Equation (3.24) the maximum depletion width $w_{\max}$ can be determined:

$$w_{\max} = \epsilon_{\mathrm{s}}\epsilon_0 A \left(\frac{1}{C_{\min}} - \frac{1}{C_{\max}} \right). \tag{3.25}$$

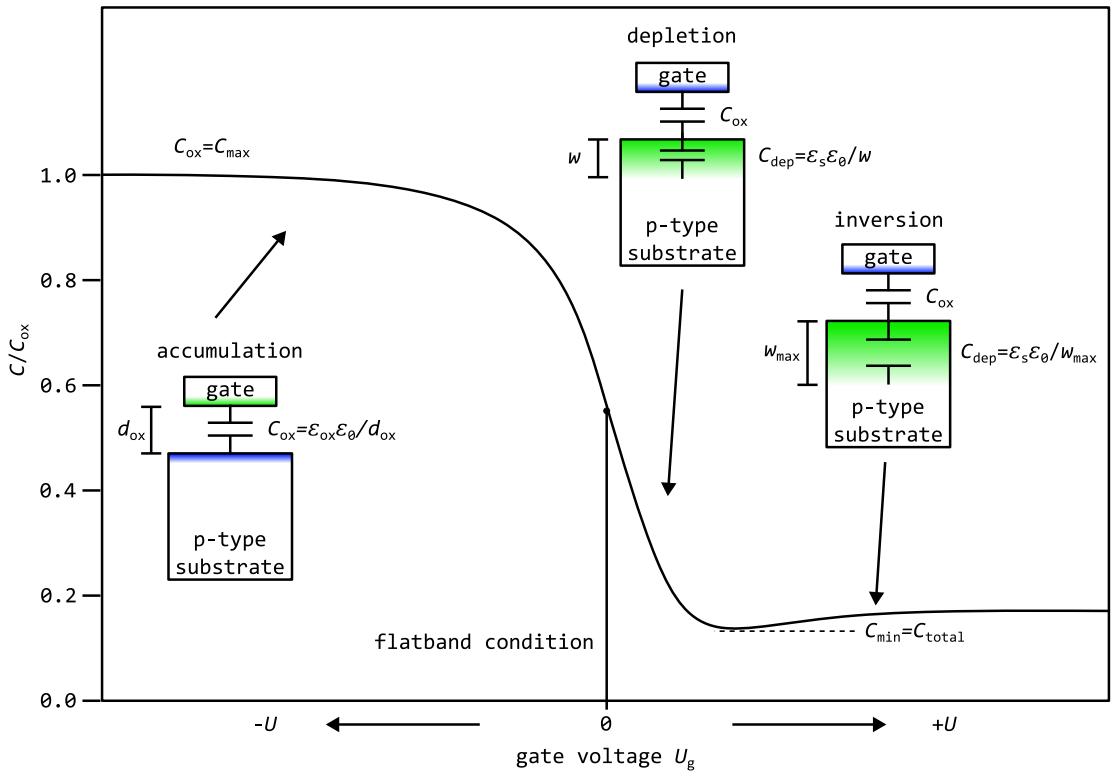

Figure 3.4.: Schematic illustration of the capacitance–voltage (C–V) method for a p-doped metal–oxide–semiconductor (MOS) capacitor. The curve depicts the normalized capacitance as a function of gate voltage, indicating the characteristic trend across the operation regimes. Equivalent circuit diagrams for each regime are shown, together with key parameters such as the maximum and minimum capacitance and the flat-band condition.

Flat-band voltage U_{fb}

The flat-band voltage can also be extracted from the C–V curve by calculating its second derivative. The zero-crossing of this derivative marks the transition from accumulation to depletion and thus defines the flat-band condition [108]. In the ideal case, where $\Phi_{\mathrm{m}} = \Phi_{\mathrm{s}}$, this point occurs at 0 V as illustrated in Figure 3.4. In real MOS systems, however, deviations arise from the finite work function difference as well as from oxide charges and interface traps. These effects shift the flat-band voltage, which appears as a displacement of the C–V curve along the voltage axis.

Doping concentration N_{A}

Further, the doping concentration can be determined from the capacitance measurements by using the Mott-Schottky analysis [109]. The capacitance of the system varies with the thickness of the dielectric layer. Since the depletion region is charac-

terized by charge compensation and its width depends on the dopant concentration, the doping level can be determined from the change in capacitance during the formation of the depletion layer, as this change is governed solely by the dopant ions within the depletion region The methods uses the inverse of the squared capacitance $1/C^2$ as a function of the gate voltage V to approximate the doping concentration from the total charge of the semiconductor depletion region of width w:

$$C(z) = -\frac{dQ_{\mathrm{t}}(z)}{dV} = qA\frac{d}{dV}\int_0^w N_{\mathrm{A}}(z)dz = qAN_{\mathrm{A}}\frac{dw}{dV} \tag{3.26}$$

where A is the area of the gate and N_A is the doping concentration of the semiconductor. This is only valid if the doping is uniform and N_{A} is linearly dependent on z. Solving Equation (3.23) for dw/dV, substituting into Equation (3.26), and using

$$\frac{1}{2}\frac{d}{dV}\left(\frac{1}{C^2}\right) = -\frac{1}{C^3}\frac{dC}{dV}, \tag{3.27}$$

yields the following expression for the doping concentration:

$$N_{\mathrm{A}} = \frac{2}{qA^2\epsilon_{\mathrm{s}}\epsilon_0\, d(1/C^2)/dV} \tag{3.28}$$

The term $d(1/C^2)/dV$ corresponds to the slope of the linear region of the $1/C^2$ versus V curve, i.e., while the MOS capacitor is in depletion.

Interface trap density D_{it}

The interface trap density D_{it} quantifies the charged defects located at the oxide–semiconductor interface, which interact with the semiconductor's charge carriers. By capturing carriers, these defects reduce the free carrier concentration at the surface and thus hinder efficient carrier transport. They introduce additional energy levels within the semiconductor band gap, i.e., between the conduction and valence bands. The trap density is defined as the trapped surface charge Q_{it} per unit energy interval [92]:

$$D_{\mathrm{it}} = \frac{1}{q}\frac{dQ_{\mathrm{it}}}{dE} \tag{3.29}$$

When a gate voltage is applied, the semiconductor bands bend to balance the potential drop between the metal and the semiconductor. As a result, the semiconductor Fermi level sweeps across the interface energy levels within the band gap. Occupation of the traps follows Fermi–Dirac statistics: In accumulation, where the Fermi

level lies near the valence band edge, the traps are essentially empty, while in inversion, with the Fermi level close to the conduction band edge, the traps are filled. In both regimes, no significant time-dependent exchange of carriers occurs, so little information about D_{it} can be extracted.

In contrast, during depletion, an applied AC signal superimposed on the DC gate bias causes the Fermi level to traverse the interface traps. Carriers are then captured and emitted with a finite time delay, which adds a loss component to the device. This additional loss manifests as an effective parallel conductance G_{p}, represented in the equivalent circuit by a conductance branch parallel to the depletion capacitance C_{dep} [110].

By measuring G_{p} as a function of gate voltage at constant frequency, the interface trap density can be profiled across the band gap. The conductance exhibits a peak in the depletion regime, where the characteristic trap time constant matches the angular measurement frequency ω. A practical expression for extracting D_{it} from the peak conductance was given in [111]:

$$D_{\mathrm{it}} = \frac{G_{\mathrm{p}}}{\omega} \frac{1}{qAf_{\mathrm{D}}} \tag{3.30}$$

Here, G_{p}/ω is the peak conductance in depletion normalized to the measurement frequency, A is the gate area, and f_{D} is a correction factor accounting for the non-uniform distribution of interface trap energy levels and their capture/emission time constants across the band gap. For Si/SiO_2, values of $f_{\mathrm{D}} \approx 0.4$–$0.5$ are typically used [112].

4. Subnanometer Porosimetry in Extreme Ambient Conditions

The measurements, results, figures, discussion, and conclusions presented in this chapter are, in part, reprinted from a publication derived from the experiments described herein.

> **R. Helm**, J. Lehtonen, M. Mayerhofer, J. Mitteneder, W. Egger, R. Verbeke, P. Sperr, G. Dollinger and M. Dickmann, *Positron-annihilation lifetime spectroscopy with in-situ control of temperature, pressure and atmosphere to determine the free-volume of soft materials*, Nuclear Instruments and Methods in Physics Research Section B: Beam Interactions with Materials and Atoms **549**, 165263 (2024), 10.1016/j.nimb.2024.165263

This approach has been adopted because the original publications provide the most rigorous and coherent presentation of the data and its interpretation.

4.1. The Temperature - Atmosphere Positron InstRument (TAPIR)

The Temperature-Atmosphere Positron InstRument (TAPIR) was specifically developed to enable in-situ PALS experiments on soft matter materials under controlled gas atmospheres and vacuum conditions, while also allowing simultaneous temperature variation. This setup facilitates the investigation of free-volume behavior, including the size and distribution of free-volume elements, as a function of gas species, pressure, and temperature. For polymers with a glass transition temperature above room temperature, this apparatus also enables the study of phase transitions under gaseous loads, offering deeper insights into material behavior under application-relevant conditions.

4.1.1. General Instrument Design

Design considerations and limitations

The TAPIR system was developed to facilitate a broad variable parameter space, including adjustable temperature, pressure, and atmospheric conditions, for positron annihilation experiments on soft matter materials. The design of the vacuum section necessitated a minimum of four ports: one for the turbo pump and pre-vacuum pump, one for the transfer rod feedthrough, one for the pressure gauge, and one for the connection to the pressure vessel (see Figure 4.1).

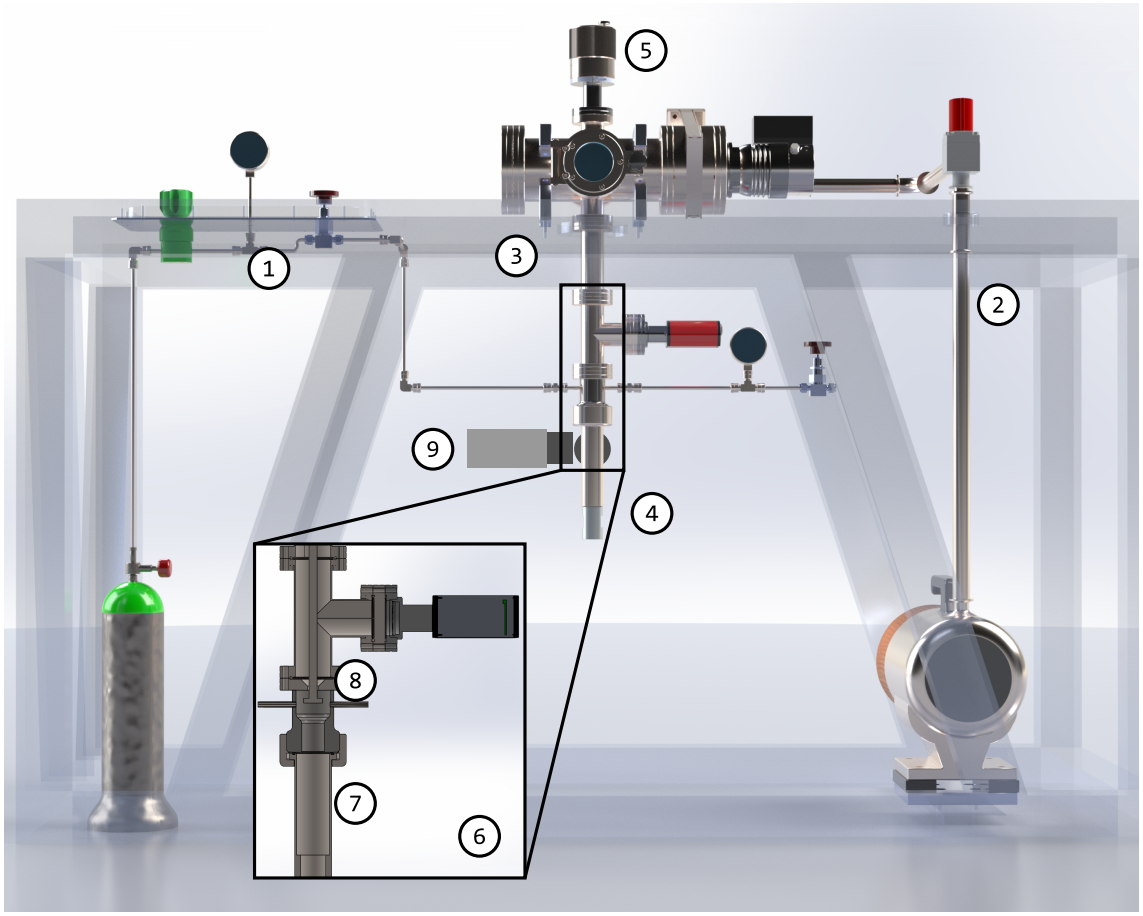

Figure 4.1.: Detailed schematic of the TAPIR instrument: ① gas circuit, ② vacuum circuit, ③ vacuum section, ④ pressure section, ⑤ transfer rod, ⑥ vacuum-pressure transition, ⑦ pressure vessel, ⑧ pressure seal and ⑨ photomultiplier detectors in 90° arragement.

The pressure section (Figure 4.1 ④) presented additional design constraints, as it must ensure both pressure and vacuum tightness while allowing accurate measurement of annihilation radiation. Materials with high atomic numbers (e.g., steel or lead) increase the scattering of annihilation radiation away from the detectors (Fig-

ure 4.1 ⑨). Since the pressure vessel walls are made from stainless steel, this may lead to an increase in measurement time and potentially influence the time resolution of the lifetime spectra. The pressure vessel wall should be as thin as possible to mitigate these effects. Furthermore, the vessel's diameter should be minimized to maximize the solid angle coverage of the detectors.

For the temperature range of the heater, a range from room temperature (RT) to 200 °C was deemed sufficient, as many polymers exhibit a glass transition temperature T_g within this range (RT $< T_g <$ 200 °C) [113]. This temperature range is also technically straightforward to implement using standard off-the-shelf components. Although, some polymer materials exhibit their glass transition below room temperature the sample cooling was not implemented in this iteration of the system. Static thermo-mechanical calculations performed by J. Lehtonen [114] indicated that the steel pressure vessel wall must have a minimum thickness of 2 mm at room temperature to ensure structural integrity. As most polymer and membrane applications operate below 20 MPa, this value serves as a practical upper limit for measurements under extreme conditions.

Based on calculations and simulations, the feasible combinations of pressure and temperature during operation can be estimated. The resulting two-dimensional parameter space is shown in Figure 4.2. Temperature–pressure combinations in the red zone are considered unsafe, while those in the green and yellow zones are regarded as permissible, although the yellow region has not yet been experimentally validated.

The pressure vessel can be evacuated down to 1×10^{-6} mbar to degass the sample under vacuum and elevated temperatures before introducing the desired atmosphere, effectively removing residual gases or solvents. The atmosphere inside the pressure vessel can be any available gas or gas mixture, such as N_2, Ar, CO_2, or CH_4. However, He gas should be used with caution, since its volatility and ability to penetrate the photomultiplier (PMT) can damage the detectors.

Vacuum section and pressure section

The instrument can be divided into two main regions for different pressures. The purpose of the vacuum reservoir is facilitating and maintaining a vacuum pressure below at least 1×10^{-3} mbar. A scroll pump (Edwards nXDS10i) is used for the pre-vacuum (1×10^{-2} mbar) and a turbo-pump (Edwards EXT70H) for the high-vacuum. In front of the turbo-pump all flanges are CF40-type, and behind the turbo-pump KF25-type flanges are used. The turbo pump can be separated from the main chamber with a (Highvac 11120-0404), and only the scroll pump can be used by using a vacuum bypass. The vacuum is measured by a combination of DPG202 and an HPT200 vacuum cathode.

On the top port of the vacuum chamber, a transfer rod is installed with a length of

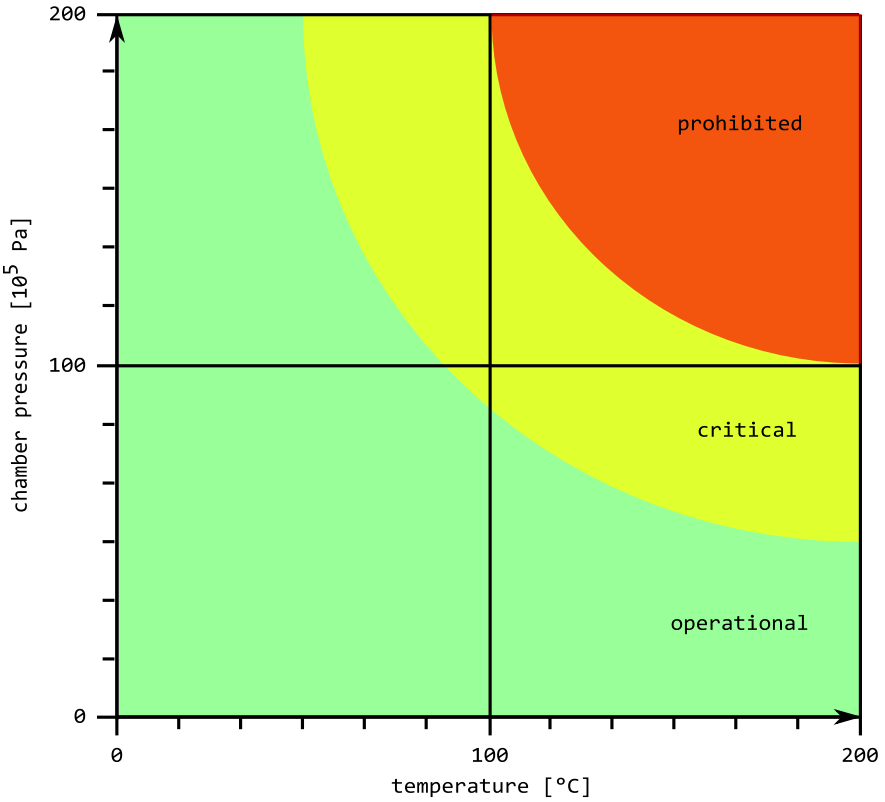

Figure 4.2.: Based on static thermo-mechanical simulations, the usable temperature–pressure range of the pressure vessel was estimated. The green region marks parameter combinations that can be used without concern, the yellow region indicates conditions that require caution, and the red region denotes operating points that are not permitted.

500 mm and a travel of 30 mm (see Figure 4.1 ⑤). At the lower end of the transfer rod the pressure seal is mounted (see Figure 4.1 ⑧). The pressure seal separates the vacuum reservoir from the high-pressure reservoir. When closed, during high-pressure operation, the pressure seal maintains the vacuum tightness of the vacuum reservoir, since commercially available vacuum components can only withstand a differential pressure of about 2 bar. The transition tube connects the vacuum reservoir to the pressure section. It has a CF40 flange on one side and a thread for the pressure vessel on the other side. A steel plate is welded into the transition tube, between flange and thread, with a 10 mm hole, which is needed to separate the vacuum reservoir and pressure section with the pressure seal. The pressure seal consists of a steel plug with a diameter of 20 mm and a Viton® ring gasket with a diameter of 15 mm. The size of the pressure seal is slightly larger than the hole in the steel plate of the transition tube, against which the pressure seal presses when closed. On application of a gas pressure the pressure seal is pressed against the steel

plate, consequently self-sealing the pressure section.

The main element of the pressure section is the pressure vessel, which is a steel tube with an inner diameter of 28 mm, a wall thickness of 2 mm, and a length of 200 mm. Towards the pressure seal, the tube ends in a sealing plate with a groove for a 25 mm Viton® ring gasket. The pressure vessel is screwed onto the thread of the transition tube using a 35 mm union nut. When tightened, the Viton® gasket seals the pressure vessel (see Figure 4.1 ⑧).

At the opposite site, the pressure vessel terminates in a feedthrough. The feedthrough is pressure and vacuum tight and establishes electrical transmission to the heating foils and heater (see Chapter 4.1.2). The feedthrough consists of a screw-on steel frame with an epoxy core, which holds the power lines in place. The epoxy casting is widened from 10 mm to 18 mm radius in the steel frame to make it stiffer and prevent the epoxy body from being pushed out during high-pressure operation. An 8-pin connector socket is attached to the top of the feedthrough frame. A detailed circuit diagram is shown in Figure 4.4.

Gas circuit

The gas circuit, which can be seen in Figure 4.1 ①, is used to establish the desired gaseous atmosphere with a defined pressure inside the pressure vessel, where the sample-source sandwich will be placed during operation. For now, this system is designed for measurements with standard gases, e.g. N_2, Ar, CO_2, or CH_4. The gas circuit consists of an inlet and an outlet with one-directional gas flow through the pressure vessel. The gas inlet and outlet, consisting of 6 mm Swagelok® pressure tubing welded to both sides of the pressure vessel. The gas pressure is regulated by a gas reducer directly attached to the bottle. An inlet valve, which is located between the reducer and the pressure vessel inlet part of the circuit (see Figure 4.1). At the inlet valve an analogue manometer with a pressure range from $0 - 30$ MPa is installed. This acts as a coarse pressure monitor and can be use for measurements where $\Delta p = \pm 0.1$ MPa is acceptable. For a more precise adjustment of the pressure ($\Delta p = \pm 0.001$ MPa), a digital manometer LEO5 from KELLER Druckmesstechnik AG, with a range from $0.01 - 30$ MPa, is installed near the pressure vessel [115]. The drain valves to release the gas from the pressure vessel is located in the inlet part of the circuit, for fast release, and a second reducer, which is located at the end of the outlet. With the drain-reducer, the gas can be released more carefully and controlled, with a much smaller drain rate. Under high-pressure operation ($p > 1$ MPa), the slow depressurization can be advantageous for the durability of the radioactive source and the overall radiation safety.

4.1.2. Sample Holder Design

The sample holder depicted in Figure 4.3 was designed by J. Lehtonen as part of his Master thesis [114].

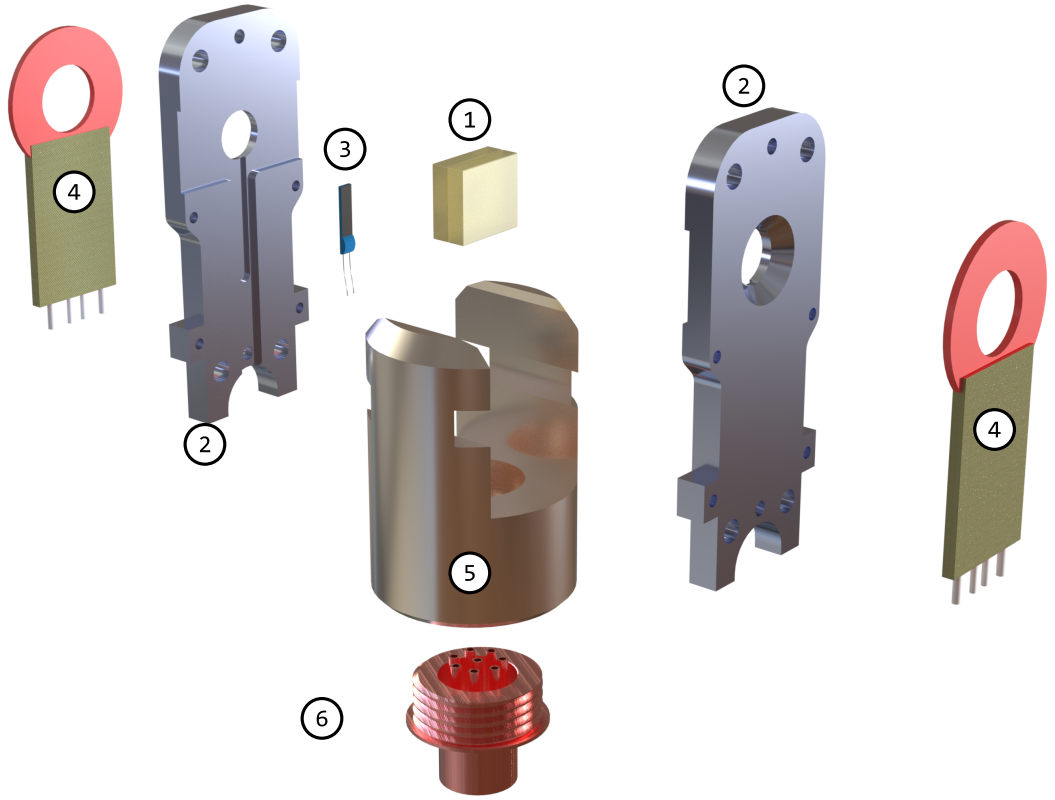

Figure 4.3.: Explosion drawing of the sample holder: ① source-sample sandwich, ② jaws, ③ Pt-100, ④ heater foils, ⑤ jaw mount with guiding rail and ⑥ male electric connector.

Sample clamping and positioning

An exploded view of the sample holder is shown in Figure 4.3. It consists of two jaws ② with attached heater foils ④. The jaws have conic-shaped center bores ($\approx 5\,\mathrm{mm}$) to minimize scattering of the annihilation gammas. The two jaws are mounted into the rail of the jaw mount ⑤ and fastened by four screws. The jaw mount is attached to an integral male 8-pin connector ⑥ that connects the sample holder to the pressure feedthrough and positions the sample holder at the right height. The source-sample sandwich ① will be placed between the two jaws. For this purpose, there is a rectangular cavity with the dimensions $12 \times 20\,\mathrm{mm}^2$ cut into the jaws. The size of the recess and the center bore result in upper and lower limits

for the permissible sample sizes. With the four screws, the jaws can be tightened together, holding the source-sample sandwich in place. When the sample holder is inserted into the connector of the feedthrough, the position of the sample is 20 mm from the upper end of the pressure tube. This allows precise positioning of the detectors, which is necessary to achieve the maximum possible count rate.

Heater and temperature sensors

For temperature control above RT, silicon rubber heater foils from Freek GmbH ④ are mounted on the outer surface of both jaws. These heaters are circular, with a diameter of 20 mm and a central recess of 12 mm that aligns with the jaws' center bore. Each heater operates with a maximum power of 2.5 W at a maximum voltage of 5 V and is rated for operational temperatures up to 200 °C.

Temperature monitoring is achieved using a thin-film Pt-100 ③, measuring 2.1 mm in width and 10 mm in length, mounted on a ceramic support from Heraeus Sensor Technology GmbH. The sensor covers a temperature range from −70 °C to 500 °C and exhibits a thermal resistance of $0.3\,\mathrm{Km^{-1}W^{-1}}$ at 0 °C (self-heating). To ensure accurate temperature measurement of the sample rather than the aluminum jaws, another Pt-100 is embedded in a 2.2 mm wide channel within one jaw, extending into the sample cavity and making direct contact with the back of the sample.

Pressure feedthrough and electrical wiring

Figure 4.4 illustrates the electrical wiring between the external and the insight of the pressure vessel. For high-pressure or vacuum operations, ensuring a robust and reliable connection between the heating foils ⑤ and Pt-100 sensor ③ within the pressure tube and the power supply ⑧ and PID controller ⑨ located externally is essential. A custom-designed feedthrough was developed to meet this requirement, offering vacuum-tight integrity and capable of withstanding pressures up to 200 bar. The feedthrough comprises an aluminum hollow body featuring an inner stepped profile, where eight power lines are embedded in epoxy resin. The epoxy resin fills the internal cavity of the bushing, providing structural stability. The stepped profile enhances compressive strength, enabling the assembly to endure peak pressures of 200 bar. The Pt-100 ④ is placed between the back of one of the samples and the jaw and is thermally insulated towards the jaws. The power line colors match those of the installed cables, streamlining the reconnection process after sample exchanges. Furthermore, the sample holder and pressure feedthrough were designed with provisions for the future integration of additional lines, ensuring adaptability for evolving experimental requirements.

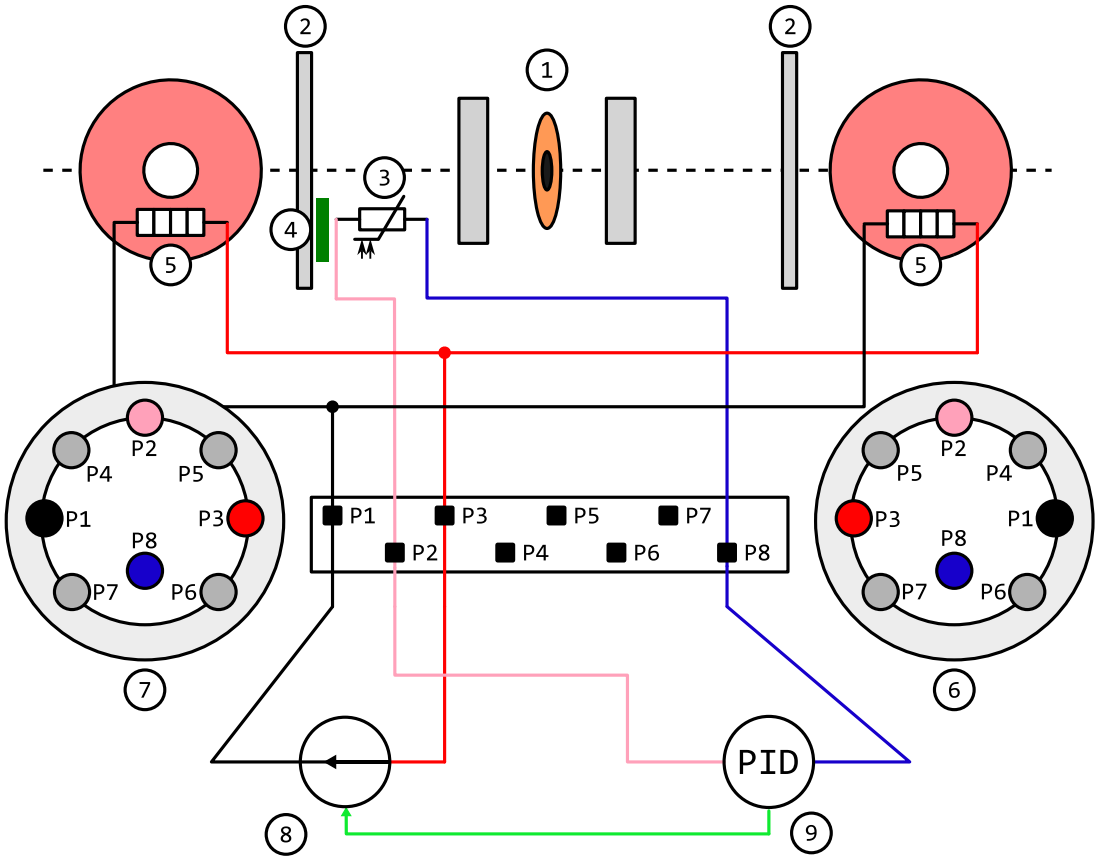

Figure 4.4.: Electric wiring of the sample holder from the pressure vessel to the exterior: ① source-sample sandwich, ② jaws, ③ Pt-100, ④ thermal insulation (green), ⑤ heater foils, ⑥ male connector (sample holder), ⑦ female connector (feedthrough), ⑧ power supply and ⑨ PID temperature controller. The colors correspond to the colors of the wires used outside of the pressure vessel.

4.1.3. Data Acquisition Unit

This section discusses the process from the measurement of gamma radiation to a material-related quantity, namely the positron lifetime in a material. The focus of this section is on the explanation of the detectors used and the signal processing, which ultimately have a major influence on the quality of the recorded lifetime spectra. The data acquisition circuit is shown in Figure 4.5.

Detector system and data processing

To evaluate the positron lifetime within a material, as described in Section 2.1.1, it is necessary to measure the temporal interval between distinct gamma events

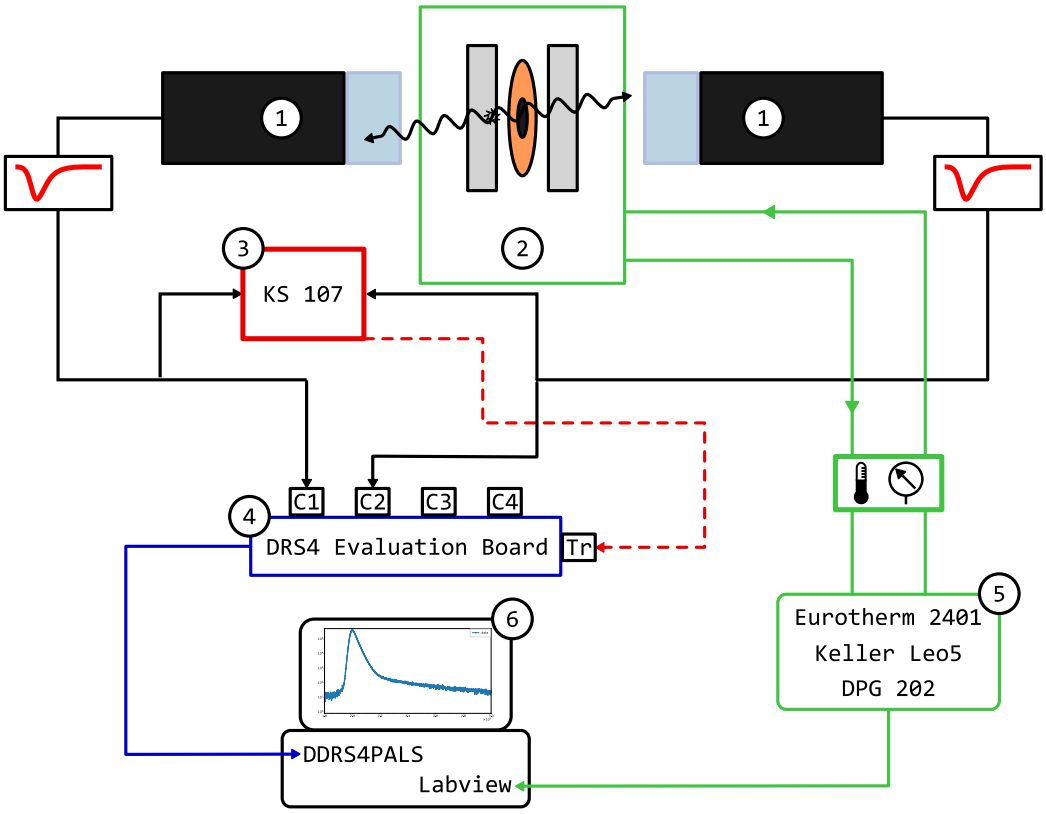

Figure 4.5.: Principal overview of the data acquisition circuit: ① detectors, ② source-sample sandwich, ③ Coincidence Module KS 107 for external trigger generation, ④ DRS4 Evaluation Board, ⑤ temperature and pressure control and ⑥ Master PC.

originating from ^{22}Na decay and electron-positron annihilation, respectively. Given that positron lifetimes in matter typically fall within the ps-ns range, the timing performance of the detection system becomes a critical factor. Unlike the high-purity germanium detector, which is widely employed for gamma-ray detection, this method necessitates a significantly faster detection system, such as the photomultiplier tube (PMT), prioritizing time resolution over energy resolution. To utilize PMTs for gamma detection, it is essential to convert high-energy gamma rays into visible-wavelength photons, a process achieved via a scintillator crystal. In our research group, BaF_2 scintillators are commonly employed due to their exceptionally fast decay time of $\sim 0.6\,\text{ns}$ (fast component) [39], rendering them among the fastest available scintillator materials.

Only two alternative scintillator materials are viable for positron lifetime experiments. Plastic scintillators, comparable to BaF_2 in timing properties, exhibit a fast decay time of $\sim 0.7\,\text{ns}$ (BC422Q) [39] and deliver a light yield approximately seven

times greater, at ~ 10 photons/keV. However, their low atomic number results in reduced detection efficiency [39]. Cerium Bromide, while offering the highest detection efficiency among these scintillator materials, is characterized by a significantly longer decay time of ~ 17 ns [116], which likely compromises the timing resolution. The selection of the scintillation crystal should ultimately be based on various criteria, including timing resolution, energy resolution, count rate, and the long-term stability of the detector.

When employing BaF_2, the scintillator crystal must be manually coupled to the photocathode using a high-viscosity silicone oil, such as Rhodosil 10000, to ensure effective optical contact. A significant drawback of this approach lies in the gradual degradation of the optical coupling between the scintillator and the photocathode over time. This degradation ultimately results in the deterioration of the time resolution and adversely impacts the overall quality of the data. The process occurs progressively and may remain undetected initially.

To eliminate this issue, SCIONIX offers a low-maintenance, pre-built detector system. Their detector systems are equipped with a PMT, scintillator, a permanent optical interface, electronics and a μ-metal shielding. For the TAPIR, two of the SCIONIX detector systems are in use with a Hamamatsu R13089-10 PMT and a $CeBr_3$ scintillator with a diameter of 51 mm and a thickness of 25 mm. The R13089-10 has two output terminals for the dynode signal and the anode signal and an HV terminal for a supply voltage up to -1500 V. A Keithley Model 248 High Voltage Supply is used with an HV splitter cable to supply both PMT with the same source, which negates a possible relative drift of the detectors. The anode signal of each detector is connected to one of four available input channels of a switched capacitor array for digitization of the detector pulses [117]. Further, in case the amplitude of the detector signals is above the maximum input amplitude of the DRS4 board of 500 mV, additional attenuators have to be used, to avoid hardware side trimming of the energy spectrum. The DRS4 evaluation board proved to be suitable for PALS [118, 119]. In contrast to the conventional analog setups, no separate timing and energy circuits are needed since the DRS4 board extracts all relevant information from the anode signal. All former analog filters for timing (Constant Fraction) and energy (Single Channel Analyzer) are now implemented into the FPGA logic and after digitization, several additional filters can be applied to further enhance the spectrum quality. Sophisticated, well-maintained, and open-source software can be obtained from Danny Petschke's GitHub project DDRS4PALS [120, 121], which is also in use at the TAPIR.

Ambient parameter monitoring

The variable ambient parameter must be controlled as precisely as possible during in-situ experiments. Therefore, a Eurotherm 2401 PID controller controls the temperature, and the pressure must be regulated manually, either by opening the

pressure seal to evacuate or by setting a gas pressure with the pressure valve connected to the gas container. The Eurotherm 2401, the DPG202, and the LEO5 are read out by a LabVIEW monitoring program. The temperature and pressure as a function of time can be manually stored in a parameter log file for later examination.

4.2. Operating Characteristics of TAPIR

This chapter summarises the performance of the sample heating, atmosphere control, and detection system. This is essential information for setting up the instrument correctly and producing reliable and reproducible positron lifetime data with TAPIR. For this purpose, some benchmark measurements, i.e. temperature calibration, atmosphere-time stability, and instrument resolution of the detectors are presented.

4.2.1. Sample Heating

As shown in Figure 4.3 the temperature sensor is placed at the outer surface of the sample, thermally insulated towards the aluminum jaw (see Figure 4.3 ④). Due to the construction of the sample holder, the middle of the sample-source sandwich is the point of lowest temperature. For practical reasons, it is not feasible to constantly measure the core temperature of the sample-source sandwich. It is therefore necessary to ascertain the relationship between surface temperature and core temperature of the sample, which diverges due to heat losses. To investigate the temperature gradient between the surface and the core of the sample, two temperature detectors were placed at the surface and the middle of the source-sandwich detector, as depicted in inlet a) of Figure 4.6. The sample holder was equipped with a single heating foil in this early experiment, carried out by J. Lehtonen [114].

In Figure 4.6 inlet (a), the surface sensor position is marked in red and the core sensor position is marked in green. Two sheets of Polychlorotrifluoroethylene (PCTFE) with a total thickness of 4 mm were used with a recess at 2 mm for the core sensor. The temperature was measured with the sample holder mounted in the closed pressure vessel filled with air at 0.1 MPa and with the core sensor as the input parameter for the PID controller. Since most polymers have a similar thermal conductivity (0.1 - 0.5 W/mK), the thermal behavior of the PCTFE should be comparable to other polymer materials [113]. A more detailed experiment description can be found in [114].

Additionally, a stationary heat transfer simulation was performed using Comsol Multiphysics. The simplified sample holder geometry is depicted in the inlet (b) of Figure 4.6. With a constant temperature at the heating element, the heat loss

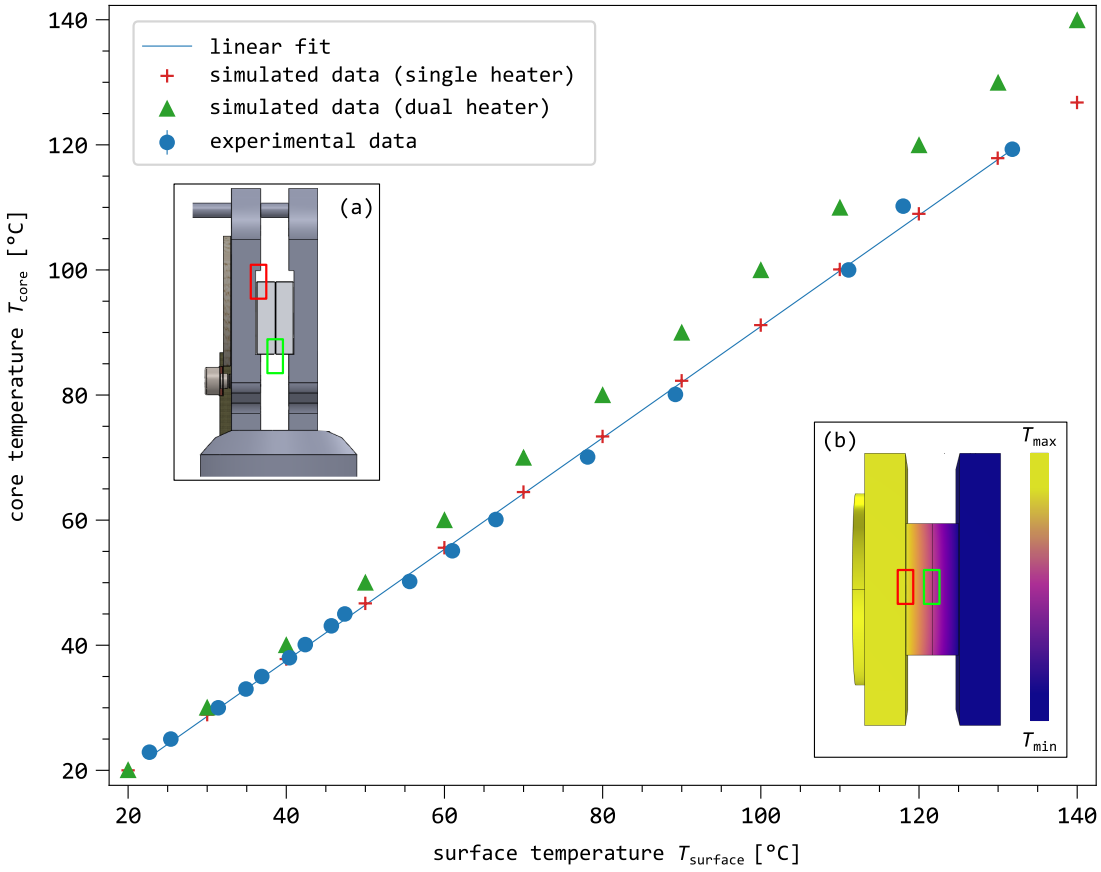

Figure 4.6.: Sample core temperature versus the surface temperature for the single heater experiment (inlet (a)), the single heater (inlet (b)), and the dual heater simulation. The linear fit of the experimental data yields the linear equation $T_{\text{core}} = 0.89 * T_{\text{surface}} + 1.91$. The Comsol Multiphysics simulation shows that the dual heater setup is necessary to counteract the heat losses and establish a well-defined core temperature within $\pm 2\,\text{K}$ of the surface temperature.

over the sample holder as a function of heater temperature was calculated using convection as the main loss factor. Radiation losses were neglected due to the low-temperature range. Based on the experimental setup, free convection of gas at rest can be assumed, which is why a convective heat transfer coefficient of $h = 1$ - $10\,\text{W/m}^2\text{K}$ was used in the simulation [122]. The heat transfer coefficient was varied until the single heater calculation matched the experimental data. The heat transfer coefficient was determined to be $h = 1.5\,\text{W/m}^2\text{K}$. With the resulting simulation settings, a second simulation was carried out with two heater foils, which resembles the actual heater configuration of the sample holder introduced in Figure 4.4).

Figure 4.6 shows the measured and simulated temperature difference between the

surface and the center of the samples. As in inlet (a), the colored rectangles in inlets (b) show the position of the surface (red) and the core (green) sensor for the simulation. The simulation evaluated a temperature line profile along a center axis. The experimental data of the single heater setup shows a maximum temperature difference between the surface and the sample core of $\Delta T = 10\,\mathrm{K}$ at a temperature $T = 130\,^{\circ}\mathrm{C}$. A linear model was applied to the experimental data, resulting in the linear equation:

$$T_{\mathrm{core}} = 0.89 * T_{\mathrm{surface}} + 1.91\,^{\circ}\mathrm{C} \tag{4.1}$$

After calibrating the simulation parameter of the single heater simulation the trend is comparable to the trend of the experimental data. For the dual heater simulation, the difference between surface and core temperature is in the order of 1 K. Even for higher heat transfer coefficients, up to $10\,\mathrm{W/m^2K}$, ΔT stays below 1 K.

For a single-heater configuration, the results indicate that precise calibration of the center temperature of the sample-source sandwich to the measured surface temperature is essential. Additionally, the simulations suggest that employing a dual heater setup compensates for heat loss, enabling the maintenance of a significantly more stable core temperature close to the surface temperature. It is critical to emphasize that the simulation parameters should be reassessed and adjusted if the thermodynamic properties of the sample material differ substantially from the assumptions made in this study.

4.2.2. Atmosphere Stability

For pressure-dependent measurements, it is critical to ensure a consistent gas pressure within the pressure vessel throughout the measurement period. Specifically, the pressure must remain stable over the entire range, from vacuum to 20 MPa, for a sufficient duration to accumulate a positron lifetime spectrum. This duration is adequate for acquiring 2×10^6 counts in the positron lifetime spectrum, as detailed in [123]. Two primary approaches can be utilized to maintain pressure stability within the vessel: (1) setting the desired gas atmosphere and pressure, followed by isolating the vessel from the supply, or (2) keeping the gas cylinder valve open to compensate for minor pressure fluctuations.

The temporal pressure stability for two different gas species is depicted in Figure 4.7. Stability tests were conducted using CO_2 at low pressures ($0.01 - 0.2\,\mathrm{MPa}$) and Argon at high pressures ($0.2 - 14\,\mathrm{MPa}$). In both pressure ranges, measurements were recorded over a 21-hour period, as shown in the lower panel of the figure. Additionally, a long-term stability test was conducted at 13.7 MPa over a duration of 216 h. The results demonstrated excellent pressure stability across all measurements, with only minor variations in the range of 10 to 50 kPa, which were attributed to

ambient temperature changes.

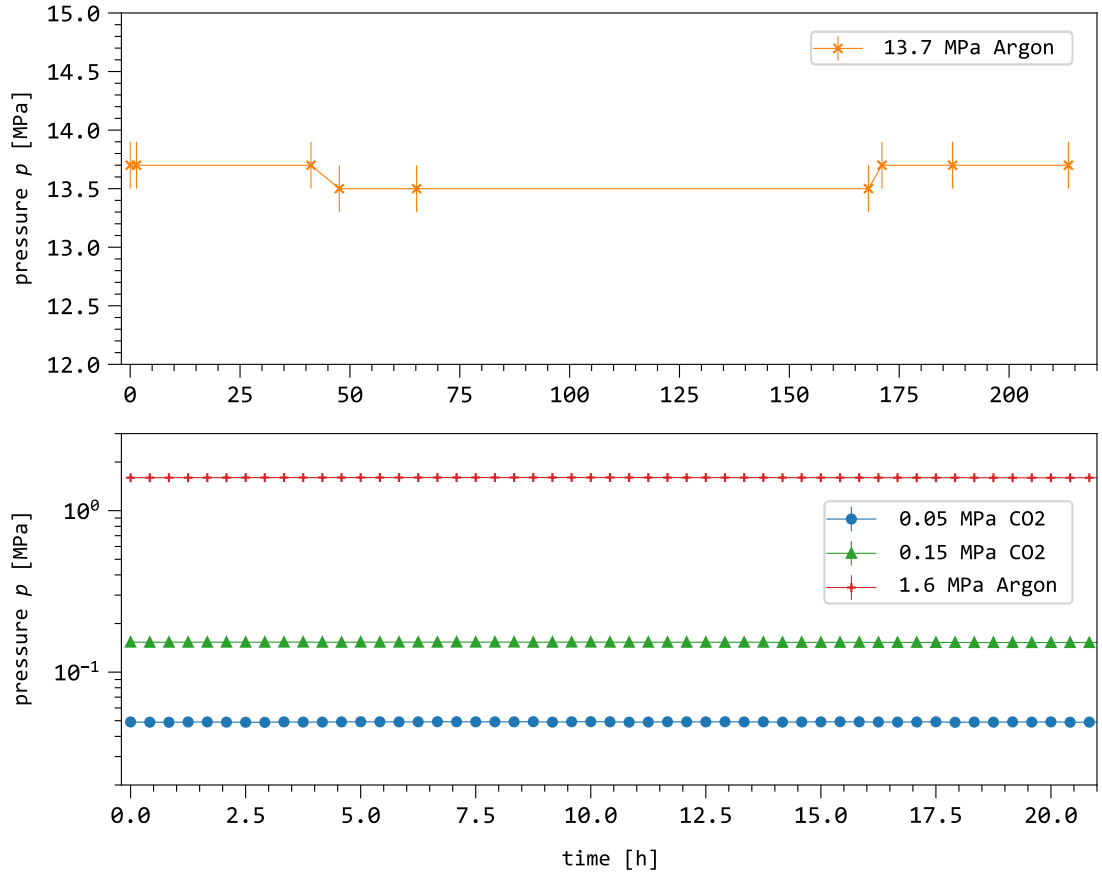

Figure 4.7.: Pressure stability of the pressure vessel for different atmospheres and pressures. The period of 21 h, in comparison, the time needed to accumulate 4×10^6 counts in the lifetime spectrum is ~ 15 h.

Figure 4.7 presents the time stability of pressure measurements for two distinct gas species. Stability assessments were performed using CO_2 in a low-pressure range ($0.01 - 0.2$ MPa) and Argon in a high-pressure range ($0.2 - 14$ MPa). In each pressure range, two measurements were recorded over 21 hours, as illustrated in the lower panel of the graph. Additionally, a long-term stability test was conducted at 13.7 MPa over 216 h. The results consistently indicated excellent pressure stability, with minor fluctuations between 10 and 50 kPa, attributable to ambient temperature variations.

4.2.3. Detection System Characteristics

As outlined in Section 2.1.1, the positron annihilation lifetime spectrum is characterized by a sum of exponential decay functions, each of which encodes information

about positron annihilation processes. This sum is convoluted with the instrument resolution function and overlaid by a constant background signal. Consequently, precise quantification and control of the instrument resolution and the peak-to-background ratio are of critical importance.

The instrument's time resolution is influenced by the timing uncertainties of the photomultiplier tube, the scintillation crystal, and the DRS4 evaluation board. Among these, the DRS4 board's contribution is relatively minor, ranging from 20 to 30 ps. Due to its negligible magnitude, this component is often disregarded in practical analyses. The overall instrument time resolution can be expediently estimated by fitting the leading edge of the decay spectrum, as shown in Figure 4.8 for a p-doped silicon sample.

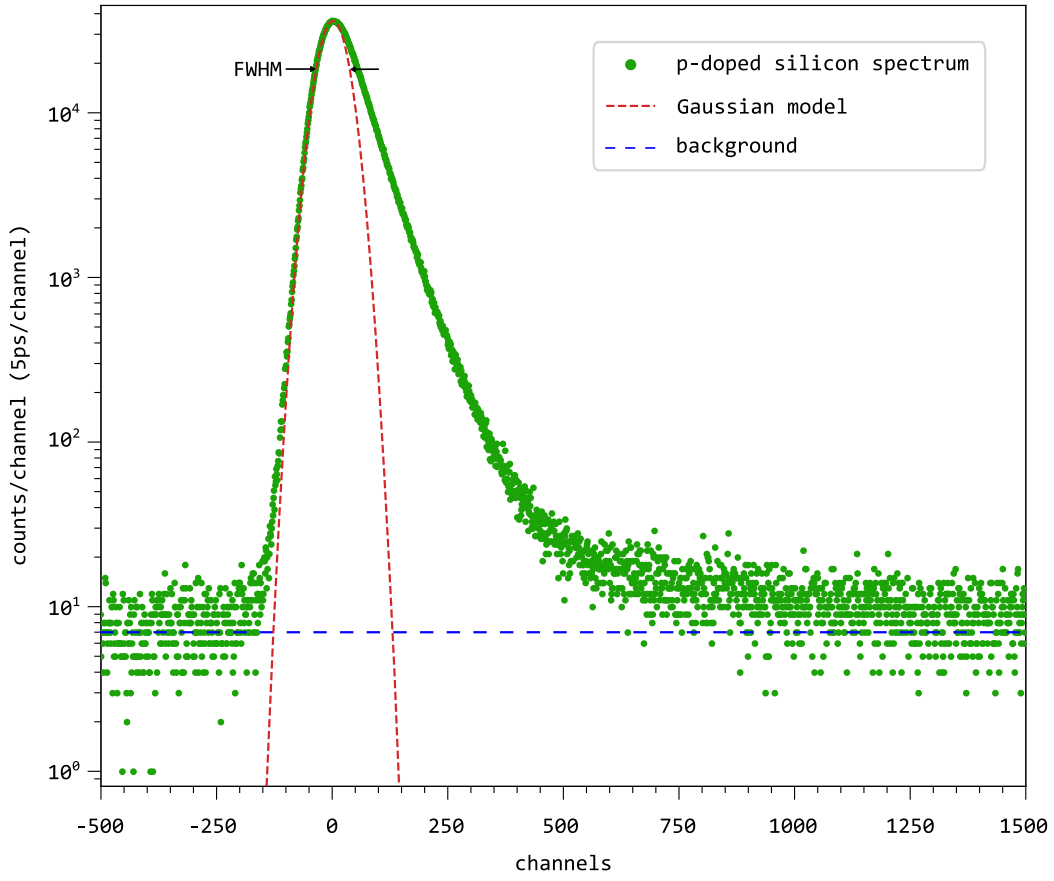

Figure 4.8.: Positron annihilation lifetime spectrum of p-doped silicon measured with the TAPIR instrument to estimate the setup's time resolution. The dashed red line shows the Gaussian model that was fitted to the left side of the lifetime spectrum.

Using a Gaussian approximation for the resolution function, the total time resolution of the detector setup (full width at half maximum, FWHM) is 75 channels,

corresponding to 376(1) ps with a channel width of 5 ps. For systems with identical detector components, such as equivalent photomultiplier and scintillator properties, the time resolution of a single detector can also be estimated. Table 4.1 summarizes the detector properties and the corresponding instrument resolution values.

Scintillator	U_{op}	I_{op}	U_{a}	IR (FWHM)
$CeBr_3$	$-1299(2)$ V	0.30(1) mA	-1 V	266(1) ps

Table 4.1.: Summary of the used detector properties. U_{op} is the detector operation voltage, I_{op} the operation current and U_{a} a typical amplitude of the anode signal. The instrument resolution (IR) is the setup's single-detector time resolution.

False coincidence events also have a detrimental influence on the quality of the recorded decay spectra. They mainly originate from Compton-scattered photons into the allowed energy windows and are responsible for the constant background. The most common way to quantify the background is using the peak-to-background ratio (PBR), which is the quotient of the peak counts to the background counts. In the current configuration, the PBR is in the order of $1 : 5 \times 10^3$.

Another critical aspect of data acquisition is the efficiency in detecting coincident lifetime events, which are the counts contributing effectively to a lifetime spectrum. The count rate, expressed in counts per second (cps), can be enhanced by reducing the dead time of the DRS4 board. This is achieved by triggering the detector pulse processing using an external trigger. An additional coincidence circuit facilitates the generation of this external trigger. Specifically, the anode signals from both detectors are split using a 50 Ω signal splitter. One branch of the split signal is directed to the input channel of the DRS4 board, while the other branch is processed by a constant fraction discriminator (CFD) connected to the input of the coincidence module K 701. If both CFD signals occur within a predefined time window (approximately μs), the K 701 module generates a gate signal, which serves as the external trigger for the DRS4 board. By adjusting the lower threshold of the CFD, the Compton background can be significantly suppressed, resulting in fewer events being registered by the digitizer and thereby reducing the dead time. Consequently, the count rate was improved from approximately 24 cps [123] to around 80 cps, without compromising the instrument's resolution.

4.3. Semi-crystalline Polystyrene in Ar Atmosphere

In this chapter, two test measurements are presented to illustrate potential application fields of the TAPIR instrument. These measurements address not only pressure- and temperature-dependent treatments, but also demonstrate in-situ experimental capabilities. Using the Polystyrene (PS) system, we investigate the influence of a high-pressure argon atmosphere (up to 4 MPa) on the free volume of the polymer as a function of temperature.

The first high-pressure experiments with in-situ heating were carried out on the thermoplastic PS. As polystyrene is a well-studied polymer system [124, 125], it serves as a suitable reference material for validating the performance of the newly developed instrument.

4.3.1. Material Properties

The semi-crystalline PS samples were purchased from Sigma-Aldrich as a $30 \times 30\,\mathrm{mm}^2$ sheet with a thickness of $d = 2\,\mathrm{mm}$. The polymer has a density of $\rho = 1.05\,\mathrm{g/cm}^3$. The typical glass transition of Polystyrene is between $90 - 100\,^\circ\mathrm{C}$, which is suitable to utilize the temperature range of the TAPIR. The gas transport characteristics of polystyrene are known for some common gases like CO_2, N_2, and Ar. Argon has a kinetic diameter of $d_{\mathrm{Ar}} = 172\,\mathrm{pm}$ [126]. Its solubility in the polymer is $S = 0.38\,\mathrm{cm}^3_{\mathrm{STP}}\mathrm{cm}^{-3}_{\mathrm{pol}}$, which represents the amount of gas at standard temperature and pressure per unit volume of polymer [127]. The diffusion coefficient of argon in the polymer is $D_{\mathrm{Ar}} = 7.5 \times 10^{-8}\,\mathrm{cm}^2\mathrm{s}^{-1}$ [128]. Unfortunately, no information about the molecular weight is available for the polystyrene samples. Despite the limited solubility of argon in polystyrene compared to the other gases [128], a plasticization or hydrostatic compression of the polymer at sufficiently high pressures ($\leq 10\,\mathrm{MPa}$) can be expected. The Argon gas was purchased by Linde with a purity of 99.99 %.

4.3.2. Experiment

A thickness of 2 mm is sufficient to ensure the implantation of all positrons into the sample materials, as demonstrated by the exponential implantation profile detailed in Section 2.3.1 (Figure 2.4). Given that the performance of the TAPIR system was initially validated using argon gas, argon was chosen for the first series of measurements due to its ease of acquisition and handling, as well as the absence of additional safety requirements. For the experiment, two samples with dimensions $10 \times 10\,\mathrm{mm}^2$ were cut from a polystyrene sheet to assemble the source-sample sandwich. The Na-22 source employed had an approximate activity of 370 kBq.

In this study, three constant argon pressure conditions were established within the pressure vessel. For each isobaric state of the polymer, the temperature was incre-

mentally increased from room temperature to 150 °C in steps of 25 °C. This allowed for the observation of the impact of gas pressure on the free volume in two distinct polymer phases, namely the glassy and rubbery states [129].

The argon pressure measurements were performed as follows: the samples were first degassed at a pressure of approximately 1×10^{-2} mbar and a temperature of 30 °C. After applying the pressurized argon atmosphere, the characteristic loading time of a PS sample with thickness d and argon diffusion constant D_{Ar} can be estimated from Fick's second law as

$$(d)^2/8D_{\mathrm{Ar}} \approx 18\,\mathrm{h}. \tag{4.2}$$

This timescale corresponds to the period required for the polymer matrix to reach equilibrium with the surrounding atmosphere. Because all sample surfaces were exposed uniformly to the gas phase, the effective diffusion length was reduced to $d/2$.

Subsequently, positron annihilation lifetime spectra were recorded at each temperature step. To ensure sufficient statistical significance, at least 2×10^6 counts were collected for each spectrum. It is important to note that a portion of the spectra was obtained using an analog fast-slow setup that preceded the implementation of the DRS4 board. The channel width of these "analog" spectra is 12.6 ps/channel.

4.3.3. Results

The positron lifetime spectra are analyzed using the model described in Section 2.1.1. A three-lifetime component model provided the best fit for the spectra. An example analysis of the positron lifetime spectrum for polystyrene under vacuum at 21 °C is shown in Figure 4.9. The blue dots represent the decay spectrum data points, while the green dots highlight the data points used in the fit model to determine the decay components. The decay components produced by the fit model are illustrated as dotted, colored lines. In Figure 4.9, the residuals from the fit model are displayed beneath the spectrum, providing an initial assessment of the suitability of the chosen fit parameters and the instrument resolution function. The constant background is shown as a red dotted line and was calculated from the background counts at the far left side of the spectrum peak, where the influence of the instrument resolution function is negligible.

The short component (τ_1, I_1, blue dotted line) exhibited a slight variation of $\sim$ 10 ps in lifetime across all analyzed spectra. Therefore, it was fixed at the para-positronium vacuum lifetime of $\tau_1 = 125$ ps for all evaluations. However, these minor variations did not significantly affect the other decay components. In the example shown in Figure 4.9, fixing τ_1 at 125 ps resulted in an intensity of $I_1 = 14\,\%$. The

middle component (τ_2, I_2, orange dotted line) was determined to have a lifetime of $\tau_2 = 388(2)$ ps with an intensity of $I_2 = 45\,\%$. The long component (τ_3, I_3, green dotted line) was fitted to a lifetime of $\tau_3 = 1998(5)$ ps and an intensity of $I_3 = 38\,\%$. The uncertainties in the intensities were omitted, as they were less than $1\,\%$.

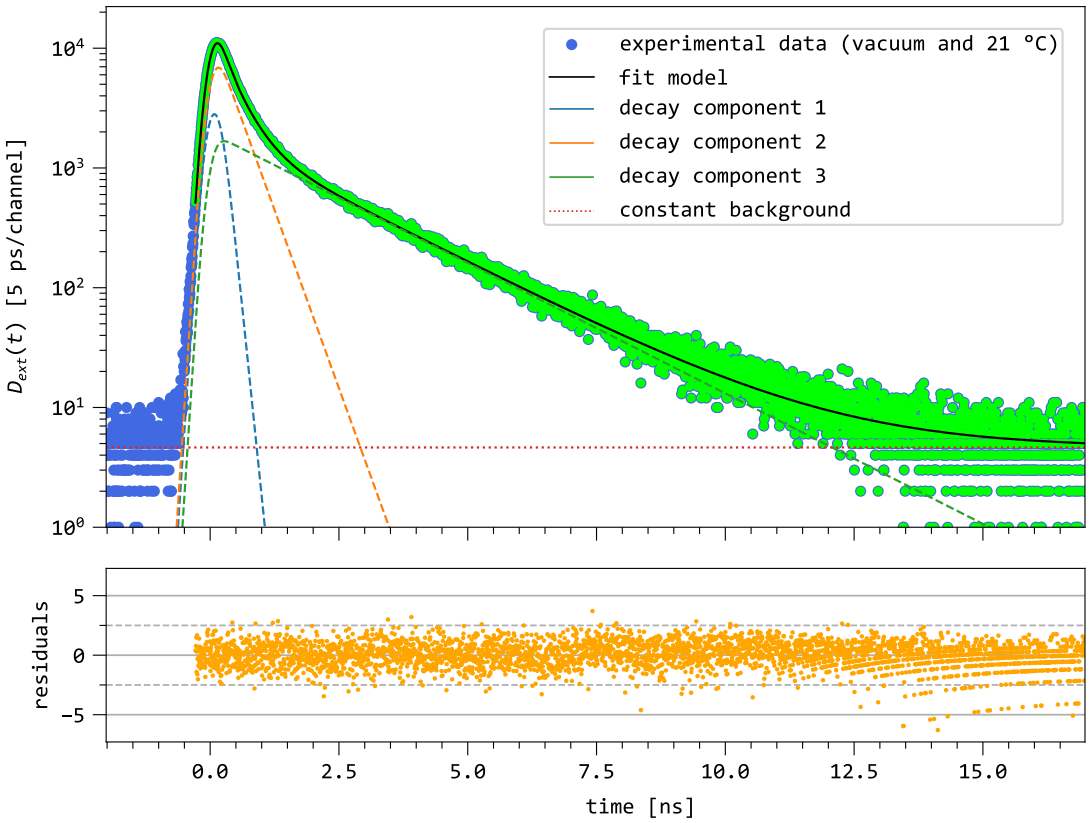

Figure 4.9.: Experimental lifetime spectrum and results of the applied fit model for PS in vacuum condition at 21 °C [123]. The blue dots are the experimental data points. The green dots show the fit range used by the fitting model. The bottom graph shows the residuals of the fit model. Reprinted from [123].

Temperature dependency of the long component τ_3 and I_3

Figure 4.10 presents the long component (τ_3 and I_3) as a function of temperature up to $T \leq 150\,°C$. The corresponding radius related to the long lifetime is indicated on the right-hand axis. The radius was calculated using the Tao-Eldrup Model (Section 2.3.4). The lifetime (τ_3) increases progressively with increasing temperature, from 2.056(3) ns to 2.724(6) ns. For temperatures below a transition temperature T_g, the increase in τ_3 is slower compared to the more rapid increase observed for temperatures above the transition temperature T_g. By assuming linear behavior of

the lifetime increase in these two temperature regions, the intersection of each linear model yields a transition temperature of $T_g = 91(5)\,°C$. In contrast to the positron lifetime, the intensity (I_3) does not display a transition temperature. Instead, the intensity increases linearly with temperature, from 40.9 % to 42.8 %. This is an increase of $\sim 4\,\%$.

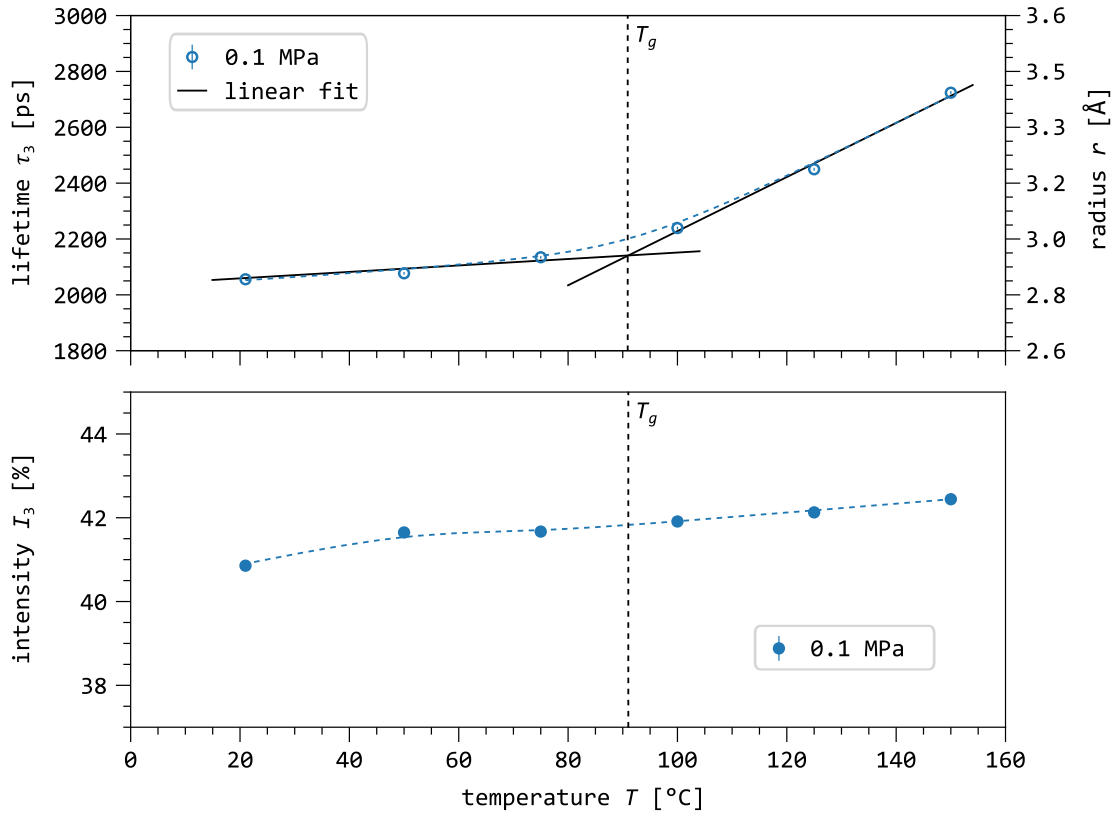

Figure 4.10.: τ_3 and I_3 as a function of temperature at 0.1 MPa of Argon pressure [123]. The long pick-off lifetime as well as the related intensity exhibit an increase with increasing temperature. The Tao-Eldrup radius of the free volume elements is given as a size reference on the right-hand axis. By applying a linear fit model to both linear regions, the glass transition temperature can be approximated to 91(5) °C.

In Figure 4.11 the intensities of the three decay components depending on increasing temperature are shown. The intensity of the short component (I_1) stays quasi-constant over the whole temperature range. The middle component (I_2) decreases with increasing temperature from 43.0 % at room temperature to 40 % at 150(3) °C. The long component (I_3) shows an increase with increasing temperature as described above. Interestingly, the long and the middle components show opposite behavior with regard to the temperature increase. The crossing point of the two intensities happens before the transition temperature of $T_g = 91(5)\,°C$ is reached.

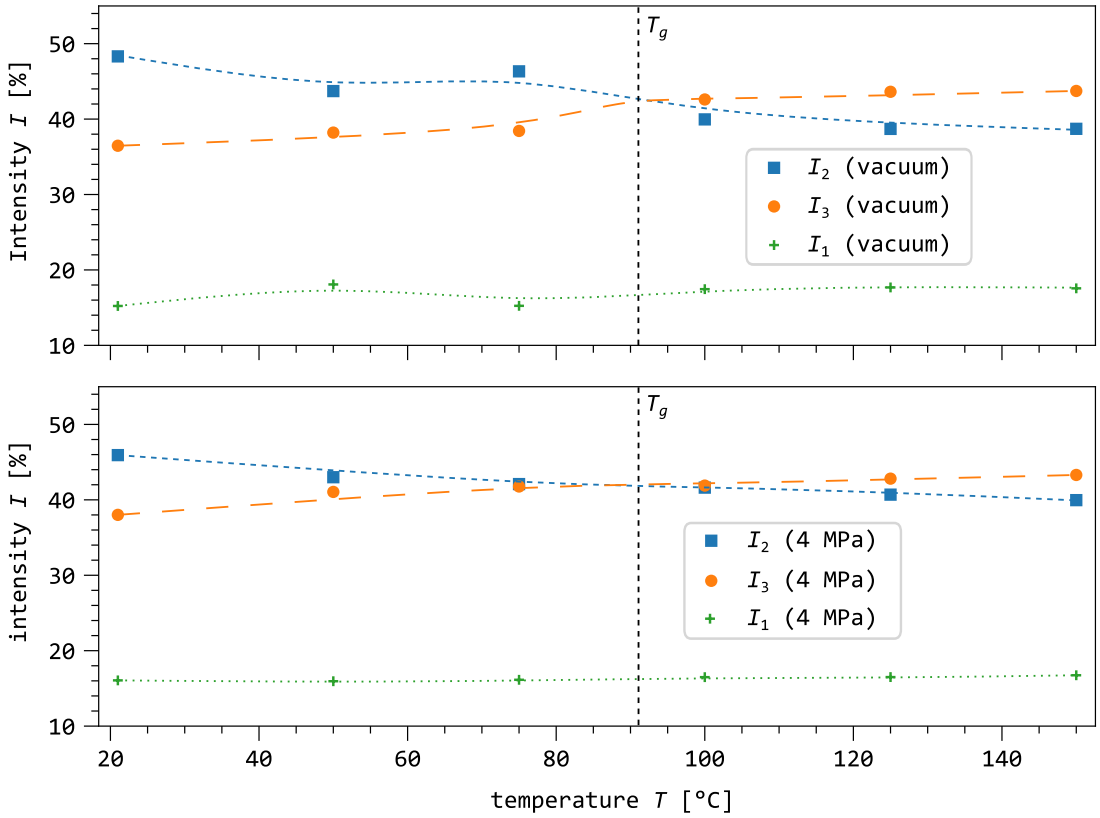

Figure 4.11.: The intensities of the three decay components as a function of temperature for vacuum condition (top) and 4 MPa (bottom) argon pressure. The black dashed line marks the transition temperature $T_g = 91(5)$ °C. The colored dotted lines are eye guides to the data.

Pressure dependency of the long component τ_3 and I_3

Figure 4.12 illustrates the behavior of the longest component, specifically the lifetime (τ_3) and intensity (I_3), as a function of argon gas pressure at two different temperatures. At room temperature ($T < T_g$), the long lifetime (τ_3) reaches its minimum value of 2021(5) ps under vacuum conditions (1×10^{-9} MPa). As the pressure increases to 0.1 MPa, the lifetime rises to 2056(5) ps, and it continues to increase, reaching 2183(6) ps at 4 MPa. In contrast, at 125(2) °C ($T > T_g$), higher lifetime values are observed, as noted in the previous section. Starting from a vacuum, the lifetime slightly decreases from 2475(5) ps to a minimum of 2448(5) ps at 2 MPa, followed by an increase to a maximum of 2606(6) ps at 4 MPa. The intensity of the long component (I_3) at 21(2) °C increases from 36.3 % under vacuum conditions to 40.9 % at 0.1 MPa. Beyond this point, the intensity decreases, reaching 38.5 % at 4 MPa. For a temperature of 125 °C, the intensity reaches its maximum value of 43.6 % under vacuum conditions and decreases to 42.3 % at 0.1 MPa.

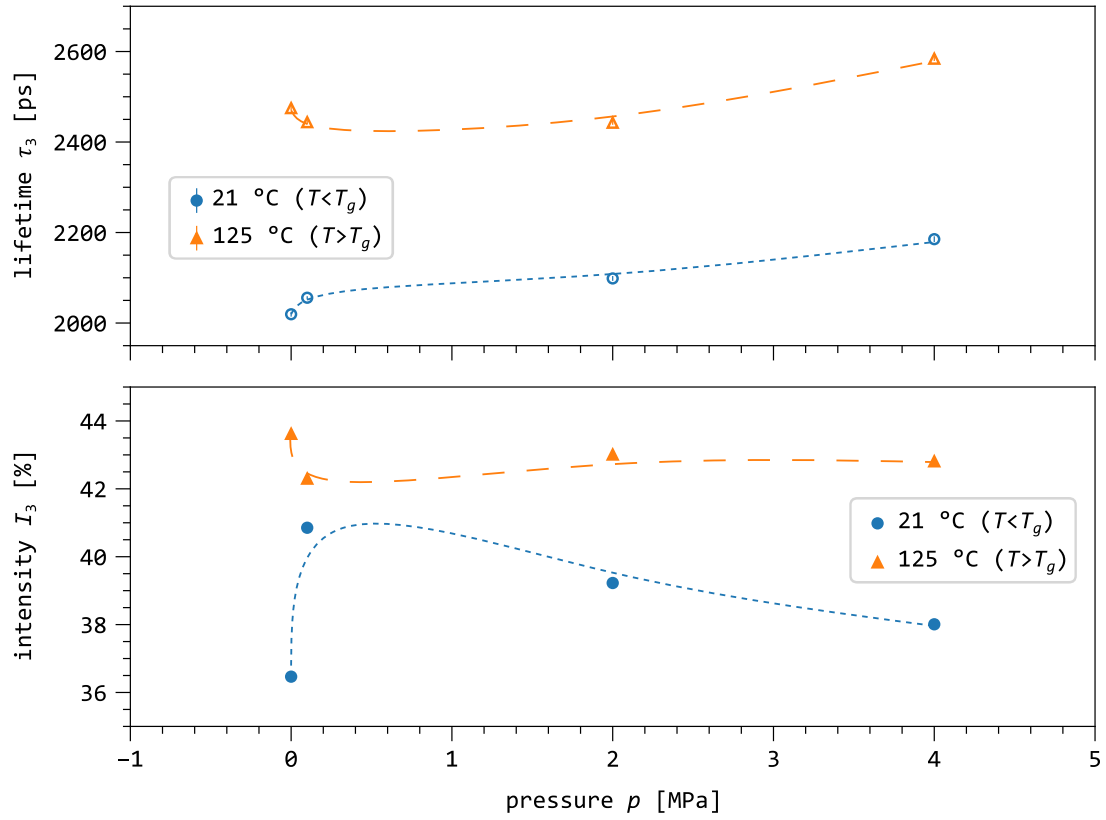

Figure 4.12.: Long lifetime component (τ_3, I_3) as a function of argon gas pressure for two different temperatures below and above the transition temperature of 91(5) °C, i.e. 21 °C (blue) and 125 °C (orange). The dashed lines are eye-guides.

With further pressure increases, the intensity rises slightly and stabilizes at approximately 43.0 %. It is noteworthy that for pressures $p \leq 0.1$ MPa, the relationship of the lifetime and intensity to pressure is reversed when transitioning from low temperatures ($T < T_g$) to high temperatures ($T > T_g$).

Pressure-temperature dependency of the long component τ_3 and I_3

Figure 4.13 shows the long component (τ_3, I_3) as a function of temperature up to 150 °C for vacuum conditions and three different Argon pressures (0.1, 2.0, 4.0 MPa). The transition temperature is marked as a dotted vertical line, and the corresponding free volume radius is depicted on the right-hand axis. The increase in the long lifetime (τ_3) below the transition temperature (T_g) exhibits a similarly gradual slope for all pressure conditions. Only the initial lifetime value varies for the different pressure states, with higher gas pressure corresponding to a higher initial lifetime. Once the temperature exceeds the transition temperature, the lifetime increases more

sharply, as already shown in Figure 4.10. A notable aspect of the measurement is the behavior of the vacuum condition curve, which surpasses the 0.1 MPa measurement near the transition temperature and exceeds the 2 MPa measurement at temperatures above 100 °C.

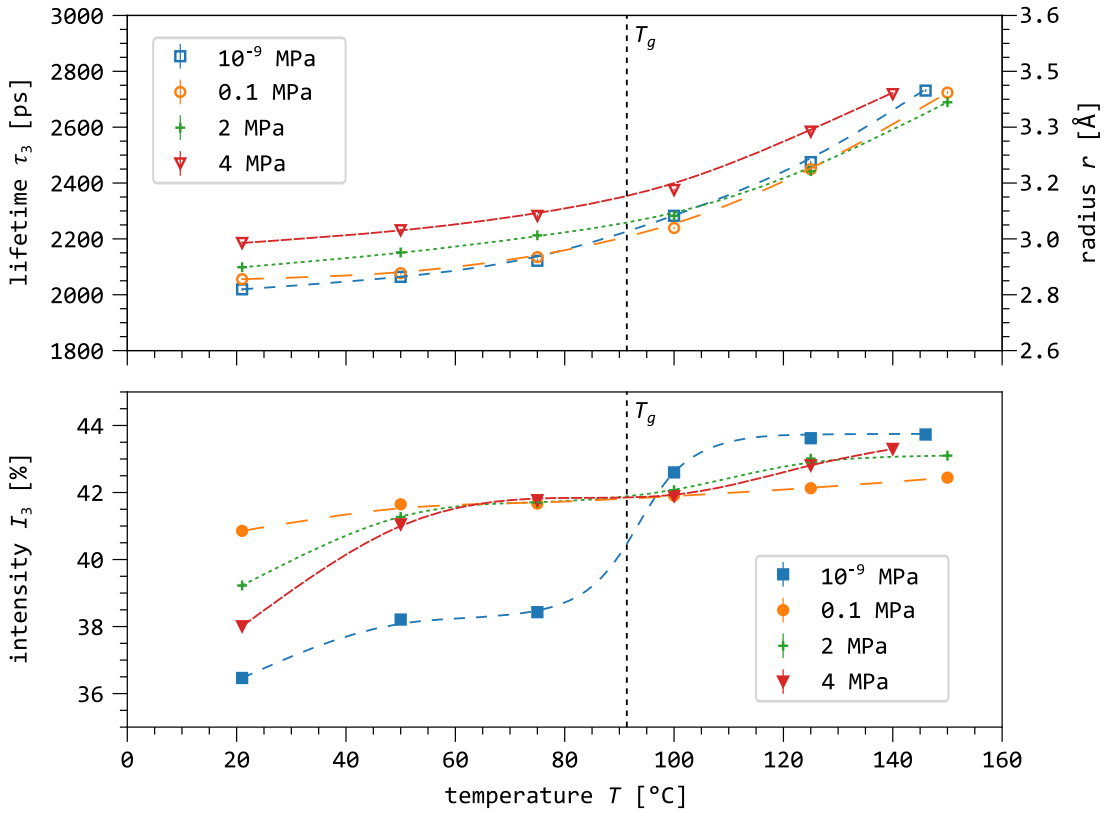

Figure 4.13.: Long component (τ_3, I_3) as a function of temperature for vacuum and three different Argon gas pressures. The corresponding radius calculated with the Tao-Eldrup Model is on the right-hand axis of the lifetime axis. The dashed lines are eye guides.

The intensity of the long component, I_3, for the various pressure conditions presented in Figure 4.13, exhibits a significantly more complex temperature dependence. At 21 °C, the intensities vary considerably across different pressure states (see Figure 4.13). The lowest intensity is observed under vacuum conditions, with $I_3 = 36.3\,\%$, while the highest value, 40.9 %, is recorded at 0.1 MPa. As the temperature increases toward the transition temperature T_g, the intensity curves for the three Argon pressure conditions rise and converge around 42.0 %. As shown in Figure 4.13, the intensities continue to increase with higher temperatures, although no distinct transition effect is observed. In contrast, the intensity behavior under vacuum conditions follows a different trend. It initially increases from 36.3 % at room temperature to 38.2 %, remaining nearly constant up to the transition temperature.

In the transition region ($T \sim T_g$), a sharp rise occurs, and the intensity stabilizes at 43.6 %, surpassing all other measured intensities.

4.3.4. Discussion

The short component in Figure 4.9, characterized by a lifetime of $\tau_1 = 125\,\text{ps}$ and an intensity of $I_1 = 14\,\%$ can be attributed to the annihilation of para-positronium. The middle component, with $\tau_2 = 388(2)\,\text{ps}$ and $I_2 = 45\,\%$, represents a combination of the mean lifetime corresponding to free positrons annihilating within the polymer matrix and positrons annihilating in the source material, such as ^{22}Na salt or the Kapton encapsulation. The long component, with $\tau_3 = 1998(5)\,\text{ps}$ and $I_3 = 38\,\%$, originates from ortho-positronium (o-Ps) pick-off annihilation within the free-volume elements of the polymer. This component is the primary indicator of annihilation related to the free volume element size. Therefore, the long component will be referred to as the o-Ps component. In the following, the evolution of the o-Ps component as a function of temperature and gas pressure will be used to make assumptions about the effect of temperature and gas pressure on the size and kinetics of the free-volume elements.

Temperature influence on the free-volume

As described in Chapter 4.3.3, the o-Ps component is strongly influenced by temperature. In Figure 4.10, two distinct regions with different growth rates can be identified, represented by the two linear fits. The transition between the low-growth and high-growth regimes of the o-Ps component occurs at $T_g = 91(5)\,^\circ\text{C}$, corresponding to the glass transition temperature of the polymer. The glass transition marks the temperature range over which the polymer undergoes a phase transition from the glassy to the rubbery state [129]. Below T_g, a modest increase of approximately 4 % in o-Ps lifetime is observed. This behavior reflects the restricted segmental chain mobility and the inability of rigid chains to rearrange. Above T_g, a steeper increase of about 18 % in o-Ps lifetime is observed, which can be attributed to the enhanced mobility of polymer chains and their ability to relax into more stable conformations.

Below T_g, the polymer exists in a glassy, non-equilibrium state, where the chains are rigid and segmental mobility is highly restricted [113]. Above T_g, in the rubbery state, segmental mobility increases, allowing chains to rearrange toward equilibrium [113]. This transition is directly connected to the packing density and, consequently, the relative free volume of the polymer [130, 131]. As the polymer cools, the loss of thermal energy causes molecules to pack more closely, reducing the available free volume. At T_g, the restricted mobility effectively freezes the chains in a non-equilibrium state, preventing structural relaxation toward thermodynamic equilibrium [132]. Below this temperature, the limited chain mobility results in only a slight reduction in free volume with decreasing temperature [132].

The relation between the middle and o-Ps components as a function of temperature, shown in Figure 4.11, further supports these conclusions. The p-Ps component remains nearly constant with temperature, exhibiting no clear dependence. By contrast, the middle component (τ_2, I_2) shows its highest intensity at low temperatures and decreases gradually as the temperature increases. The o-Ps component (τ_3, I_3) exhibits the opposite behavior. Interestingly, the intersection of the middle and o-Ps components for both pressure states occurs close to T_g. This observation is consistent with a reduction of free volume during the transition from the rubbery to the glassy state. In the glassy phase, the limited segmental mobility and reduced free volume suppress o-Ps formation, favoring annihilation in smaller voids and thus enhancing the middle component. As the temperature approaches and exceeds T_g, the increasing free volume facilitates o-Ps formation, leading to a corresponding rise in the o-Ps component.

Pressure influence on the free-volume

Before discussing the influence of gas pressure on the ortho-positronium (o-Ps) component, several theoretical concepts previously outlined in [123] are revisited. The analysis is based on the dual-mode sorption model [133–138], which describes the transport of penetrant species within polymer matrices. In the glassy state, two processes coexist: dissolution of gas atoms and hole-filling [133, 135]. The contribution of hole-filling decreases during the transition to the rubbery state, where dissolution becomes the dominant mechanism [134, 137].

Since the present measurements probe the average size and abundance of free-volume elements (FVEs), the dual-mode sorption model is adapted to a free-volume description consistent with the observed o-Ps annihilation parameters. In the glassy phase, FVEs can be distinguished as dynamic (Henry species) and static (Langmuir species). The static FVEs reflect the non-equilibrium structure of the glassy state, where limited segmental mobility prevents structural relaxation. In the rubbery phase, increased mobility eliminates static FVEs, leaving only dynamic ones.

Figure 4.12 demonstrates that gas pressure affects the o-Ps component differently depending on the polymer phase.

At 125 °C (rubbery state), τ_3 decreases from vacuum up to 2 MPa and increases again at higher pressures. This trend indicates the interplay of hydrostatic compression and plasticization. At low pressures ($p \leq 2$ MPa), hydrostatic compression dominates, compacting the matrix and reducing FVE size. At higher pressures, plasticization becomes more significant, enhancing segmental mobility and increasing τ_3. At pressures beyond those investigated, hydrostatic compression is expected to dominate again, leading to a renewed reduction of free volume [19].

At 21 °C (glassy state), τ_3 increases with pressure, which is attributed to plasticization of the rigid polymer matrix by argon atoms. Plasticization increases chain

mobility and free volume [136, 139, 140], consistent with earlier studies in other polymers such as polycarbonate under N_2 and CO_2 atmospheres [19]. The o-Ps intensity is lowest in vacuum, rises sharply at 0.1 MPa, and then decreases gradually with further pressure increase. The initial rise is consistent with plasticization, whereas the subsequent decline suggests either dissolution of argon into static FVEs or their occupation via sorption, both of which reduce o-Ps formation.

The observed behavior raises questions regarding the nature of static FVEs. Three interpretations are possible: they are intrinsically immobile, their apparent immobility results from the limited solubility of argon, or they are mobile but not detectable within the positronium annihilation timescale.

While plasticization is often associated with a reduction of the glass transition temperature T_g under elevated pressure [19, 138, 140], the data in Figures 4.12 and 4.13 do not indicate such an effect. Alternative explanations include polymer swelling or competing mechanisms of swelling and plasticization. Due to the limited literature on the interaction of polystyrene with argon, it remains difficult to determine which effect predominates.

Pressure-temperature influence on the free-volume

In the final step, the temperature-dependent behavior of the polymer under varying argon gas pressures should be analyzed. This discussion integrates arguments previously presented, particularly those related to the T_g and the dual-mode sorption model. Figure 4.13 depicts the o-Ps lifetime component as a function of temperature for four different pressures. In the glassy state, the o-Ps lifetime exhibits a direct proportionality to pressure, increasing with both ambient parameters: pressure and temperature. This suggests that the rising concentration of argon atoms in the polymer matrix induces a plasticizing effect on the polymer.

As the temperature approaches the glass transition, the vacuum o-Ps lifetime surpasses that of the 0.1 MPa condition at approximately 70 °C. Beyond the glass-to-rubber transition, the vacuum o-Ps lifetime further exceeds the lifetime observed at 2 MPa. This observation challenges the initial explanation of plasticization, indicating that multiple mechanisms govern the evolution of free volume. Specifically, the increasing free volume at higher temperatures and lower pressures suggests that while gas penetrants facilitate plasticization, they also inhibit the temperature-driven expansion of free volume in the rubbery phase. The fact that the vacuum o-Ps lifetime remains below the 4 MPa o-Ps lifetime implies that, at higher pressures, the plasticization effect outweighs the suppression of polymer chain reorganization by argon atoms.

In the glassy state, the o-Ps intensities shown in Figure 4.13 are strongly influenced by both pressure and temperature. At room temperature, the o-Ps intensity decreases with increasing argon pressure, an effect attributed to gas molecules' oc-

cupation of static FVE. As temperatures rise, these intensities converge and nearly overlap around $\sim 60\,^{\circ}\mathrm{C}$. Above the T_g, the diverging intensity curves and their direct proportionality to temperature indicate a greater abundance of free volume. This behavior suggests a swelling effect in the polymer matrix and highlights the differences in pressure states. It is also important to consider that dynamic free-volume elements can be occupied by gas atoms.

Interestingly, the vacuum condition appears to be governed by a different mechanism, as the absence of significant gas penetration minimizes plasticization compared to the 0.1 MPa state. In the glassy phase under vacuum, the free-volume elements collapse, reducing the availability of FVEs. This collapse results from the inability of the polymer matrix to accommodate external stresses, leading to a lower o-Ps intensity as observed in the vacuum condition [123]. During the glass-to-rubber transition, the intensity under vacuum conditions jumps to the highest value among all measured pressure states. This is likely due to the relaxation of the polymer matrix, which adapts to external stresses. Unlike the argon pressure conditions, where gas atoms occupy dynamic FVEs, the absence of gas under vacuum allows o-Ps to probe the highest abundance of free-volume elements [123].

The analysis results for the o-Ps components (τ_3 and I_3) for all pressure and temperature conditions are listed in Table A.1 in the Appendix (from [123]).

4.4. Conclusion

The newly developed TAPIR instrument was presented, with its overall design and individual components defined and characterized. Its operational characteristics were benchmarked against design values, and optimal conditions for investigating free-volume defects in polymers were established.

As a first application, the interaction of polystyrene with argon gas was studied under pressures ranging from 1×10^{-9} MPa to 4 MPa, focusing on the effect of gas pressure on the polymer's free volume using positron annihilation lifetime spectroscopy (PALS). In addition, in-situ heating from room temperature up to $150\,^{\circ}\mathrm{C}$ was employed to drive the polymer across the glass-to-rubber transition.

The results demonstrate that argon pressure has a significant influence on both the size and abundance of free-volume elements (FVEs) in the glassy and rubbery phases. In the glassy state, the increasing concentration of dissolved argon reveals two distinct FVE subtypes – static and dynamic – that can be interpreted within the framework of the dual-mode sorption model. In the rubbery state, the matrix becomes more flexible, and free volume is dominated by dynamic FVEs, reflected by a pronounced increase in the o-Ps lifetime, indicating an enlargement of FVE size.

At elevated temperatures, the polymer exhibits a pressure-dependent swelling effect,

as inferred from deviations in the o-Ps intensity at higher pressures. A reference measurement on polystyrene under vacuum confirms that, while FVE size (o-Ps lifetime) generally increases with gas pressure, the abundance of FVEs (o-Ps intensity) shows a distinct temperature dependence, particularly near the glass transition. This contrast highlights that the underlying mechanisms differ in the absence of penetrant gas. Overall, the observed pressure-dependent effects can be attributed to the interaction of argon atoms with the polymer matrix.

5. The Pulsed Low Energy Positron System (PLEPS)

In this chapter, the current status of the Pulsed Low Energy Positron System (PLEPS) at the NEutron induced POsitron Source MUniCh (NEPOMUC) of the Forschungs Reaktor München II (FRM-II) research reactor is presented. Planned upgrades, initiated in 2019, were postponed following the reactor shutdown in 2020, which was officially confirmed in 2022. The chapter focuses on the completed upgrade of the target station, enabling the application of a sample bias during measurements.

5.1. Current Status of PLEPS

The PLEPS is one of only two pulsed positron beams worldwide capable of depth-resolved positron lifetime measurements in the implantation energy range of 0.5 keV to 20.0 keV. It provides both sufficient time resolution better than 250 ps and a high peak-to-background ratio better than $1 \times 10^5 : 1$, which are essential threshold values for reliable data analysis. These performance criteria are generally required for defect studies across a wide range of material systems, including metals, semiconductors, and polymers.

The PLEPS system was originally developed in the late 1980s by Peter Sperr and colleagues at the University of the Bundeswehr Munich, designed for laboratory use with a ^{22}Na source in combination with a tungsten moderator. Since then, numerous advancements by various researchers have evolved PLEPS into one of the most reliable and versatile positron beam instruments worldwide [141–143].

In the early 2000s, PLEPS was relocated to the NEPOMUC at FRM-II in Garching. The motivation was to drastically reduce acquisition times by increasing the available positron intensity from the laboratory-based source ($1 \times 10^5\,e^+s^{-1}$) to the remoderated NEPOMUC positron beam ($1 \times 10^7\,e^+s^{-1}$) [48]. The transfer was completed in 2007, with the first test measurements reported in the same year [7]. Table 5.1 summarizes the instrument characteristics as determined during the last beam time at the FRM-II in February 2020.

Figure 5.1 shows the current state of PLEPS. The schematic outlines the instru-

Implantation energy range	$0.5 - 21.0\,\mathrm{keV}$
Beam spot diameter	$\leq 1\,\mathrm{mm}$ (FWHM)
Time resolution (pulsing)	$\approx 100\,\mathrm{ps}$ (FWHM)
Time resolution (pulsing + detector)	$\leq 200\,\mathrm{ps}$ (FWHM)
Peak-to-background counts	$1 \times 10^5 : 1$
System setup time	$24 - 48\,\mathrm{h}$
Maximum sample dimension	$10 \times 10\,\mathrm{mm}^2$
Sample temperature	$80 - 600\,\mathrm{K}$
Sample bias ($\Delta U = 12.5\,\mathrm{mV}$)	$\pm 400\,\mathrm{V}$
Light source	$190 - 2200\,\mathrm{nm}$
Light source bandwidth	$1 - 20\,\mathrm{nm}$ (FWHM)
Measurement time (single spectrum)	$5 - 10\,\mathrm{min}$
Depth profile (15 implantation energies)	$2 - 3\,\mathrm{h}$

Table 5.1.: PLEPS instrument characteristics as of February 2020.

ment's functionality and highlights the main beamline components. In the following, a brief overview of the most important elements, their roles, and the latest updates to the instrument is provided.

The most recent major hardware upgrades were carried out by Luca Ravelli [43]. He extended the pulsing section by adding a pre-chopper plate to the chopper, one of the most critical components, thereby enlarging the time window from 20 ns to 40 ns, improving the capability of measuring samples which exhibit very long lifetimes. In addition, he redesigned the PLEPS main buncher to optimize the temporal width of the positron pulses, significantly enhancing the system's time resolution. He further studied the backscattering behavior of positrons from the sample surfaces, which can re-enter the beam path and cause spectral artifacts, particularly in high-Z materials such as tungsten [43].

Subsequently, Tönjes Koschine developed new LabVIEW-based control software, integrating electronics and data acquisition into a unified system [144]. Over time, the

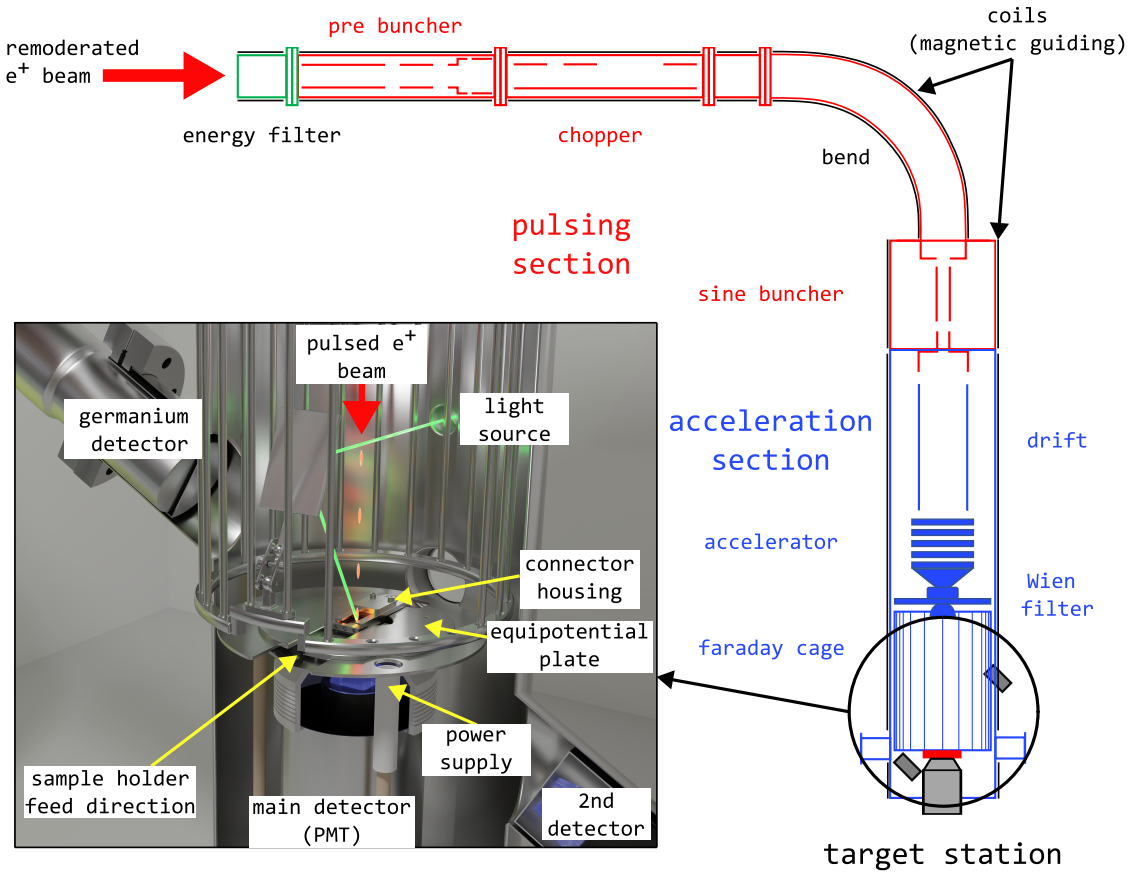

Figure 5.1.: Schematic of the Pulsed Low Energy Positron System (PLEPS) installed at the FRM-II research reactor, originally developed by P. Sperr [7]. The diagram depicts the key components required to generate a pulsed positron beam, while the enlarged section highlights the PLEPS target chamber (image courtesy of M. Dickmann).

original custom-built pulsing electronics were replaced by modern industry-standard components, further improving stability and long-term reliability.

Beam transport and guiding

The positron beam is magnetically guided from the primary moderator in NEPOMUC through its remoderator to the PLEPS entrance by a beam-parallel solenoidal field. The entire beamline is maintained under high vacuum, with pressures below 1×10^{-7} mbar, corresponding to a mean free pathof the positrons of approximately 500 m. In continuous-wave (cw) operation, the beam arrives at the PLEPS entrance with a mean kinetic energy of about 20 eV. An energy filter allows the determination of the beam's kinetic energy spread by acting as an electrode with a retarding

electrostatic field that can be controlled by the operator. The guiding magnetic flux density – parallel to the optical axis – is designed to be $B = 70\,\mathrm{G}$ $(7 \times 10^{-3}\,\mathrm{T})$ [7]. To counteract disturbances near electrical feedthroughs or flanges, additional windings are integrated into the solenoid to locally boost the magnetic flux density and ensure field continuity.

Pulsing section

The pulsing section of PLEPS comprises four main components: the pre-buncher (sawtooth buncher), the pre-chopper (time-window extension), the main chopper, and the main buncher (sine buncher). These stages compress the continuous-wave (cw) positron beam into pulses with a pulse width of about 100 ps. In combination with the detector system, this yields an overall time resolution of better than 200 ps. The original design operated at 50 MHz, corresponding to a 20 ns time window in the lifetime spectrum.

The pre-buncher operates at 50 MHz with a sawtooth signal and provides the first stage of pulse compression, producing positron bunches with pulse widths of a few nanoseconds. The width can be adjusted by changing the sawtooth amplitude. After this stage, the positrons are accelerated to 200 eV before entering the chopper. To extend the available measurement time window, a pre-chopper operating at 25 MHz was later added. The main chopper creates a transmission window by applying a sine signal that compensates the DC offset, producing zero electric field at the chopper plate in the center of the window [43]. The width of this transmission window, typically around 2 ns, is controlled by the sine amplitude. The prebunched positron pulse passes through the chopper plate within the transmission window, while positrons arriving outside the window are deflected by the $E \times B$ drift resulting from the electric field at the chopper plate and the magnetic guiding field. These deflected positrons are removed from the beam via an aperture, reducing inter-pulse intensity. A second chopper plate (corrector) compensates for distortions introduced by the main chopper.

After the chopper, the positron bunch is accelerated to 800 eV before entering the bend section, which also serves as an energy filter to remove positrons with incorrect kinetic energy. Final pulse compression is achieved using a sine buncher, reworked by Luca Ravelli [43]. A sine voltage is applied to the central electrode so that the positron pulse passes through the linear region of the sine wave. The reference particle crosses the gap when the sine signal is zero, while earlier-arriving particles are decelerated and later-arriving ones are accelerated. This reduces the pulse width to approximately 100 ps before the acceleration section, thereby defining the instrument's time resolution.

Optical column

After passing through the main buncher, the positron pulses enter the optical column, which consists of the drift tube, accelerator, Wien filter, and Faraday cage. The drift tube, whose potential can be adjusted, regulates the drift time between the buncher exit and the sample, thereby maintaining stable bunching conditions when the implantation energy – defined by the accelerator – is varied. The linear accelerator allows tuning of the implantation energy over a wide range, from 0.5 keV to 21.0 keV.

Further downstream, the Wien filter fulfills several functions. Its primary role is to suppress secondary maxima in the spectra by filtering out re-emitted positrons in the eV range. Additionally, it acts as a differential pumping stage between the pulsing section and the target chamber of the beamline. A tungsten cup is positioned at the filter exit to shield the annihilation radiation generated in this region from the reflected or remitted positrons. The filter also establishes an optimized particle-optical configuration for coupling the beam into the Faraday cage.

The accelerated positrons then enter the target chamber – shown in the enlargement in Figure 5.1 – which consists of the Faraday cage and the target station. The Faraday cage provides a nearly field-free environment and suppresses external electric-field disturbances. The target chamber is also equipped with several ports that allow for auxiliary detectors, diagnostic tools (e.g., camera), or sample manipulation devices (e.g., light sources) to be integrated as needed.

5.2. PLEPS Target Station

After passing through the Faraday cage, the positrons strike the sample mounted on the sample holder, which is positioned within the receiver of the target station. The target station – located beneath the Faraday cage in Figure 5.1 – comprises the equipotential plate, held at the maximum acceleration potential, and the receiver, into which the sample holder can be inserted from outside the station. The receiver supports multiple modes of sample manipulation and is mounted on a sapphire crystal that provides thermal coupling to both the cryostat and the heater. In addition, three electrical feedthroughs allow the application of a bias voltage to the sample (see Figure 5.1). The main detector, a photomultiplier tube (PMT) coupled to a BaF_2 scintillator, is positioned approximately 9 mm below the sample.

5.2.1. Modification to the Target Station

The application of a sample bias has been possible since the last major PLEPS upgrade [143], but contacting the sample holder remained cumbersome and unreliable. To address this issue, a new concept for sample contacting using the three available

external power lines was developed, which led to a reconfiguration of the PLEPS target station.

Design considerations

The requirements for the new contacting system were defined as follows: it had to be fully compatible with existing components, non-invasive, and free of electric field distortions at the target position. Furthermore, it needed to remain thermally stable up to 600 K, use vacuum-compatible and strictly non-magnetic materials, and avoid sparking through the omission of sharp conductive edges.

These constraints significantly limited the design freedom for the target station upgrade. The resulting design, which meets the requirements, is shown schematically in cross-section in Figure 5.2. The sample holder was modified to accommodate up to three beryllium copper contact strips, each electrically insulated from the rest of the holder. A connector housing was added to the receiver to interface with the external power lines, functioning analogously to a USB connector: when the sample holder is inserted into the receiver, its contact strips slide into the housing and establish electrical contact with the connector springs, which are connected to the external power lines. The complex geometry of the sample holder insulators required fabrication via rapid prototyping, which at that time was only available in polyurethane. Consequently, these parts are unsuitable for experiments above 450 K.

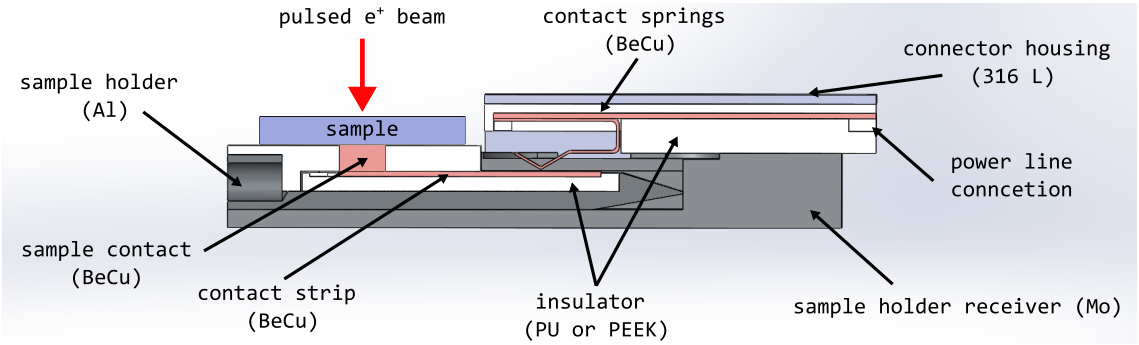

Figure 5.2.: Schematic cross-sectional view of the upgraded PLEPS target station with sample holder, connector housing, and receiver for PALS measurements, including an additional sample bias option. The sample holder is designed to accommodate up to three electrically isolated contacts, which are connected to external power lines via a connector housing mounted on the receiver. The materials used are given in parentheses.

Unlike the sample holder, the connector housing cannot be removed prior to high-temperature experiments. Therefore, it must be constructed from temperature-resistant materials. To meet this requirement, the connector housing insulators

were manufactured from individual polyether ether ketone (PEEK) components, which can withstand short-term exposure to temperatures up to 600 K and ensure safe operation without requiring disassembly of the setup.

Technical implementation

Figure 5.3 provides a realistic illustration of the upgraded target station. Panel (a) shows the complete target station with its upgrades. ① marks the equipotential plate, which defines the system ground and is typically set to the target energy of the positrons ($E_{\mathrm{imp}} = eU$). ② indicates the connection of the external power lines to the connector housing shown in panel ⓓ. ③ highlights the sapphire interface that links the receiver to the cryostat. The green arrow shows the manual transfer direction of the sample holder into the receiver, onto which the connector housing is mounted. Finally, ④ denotes the feedthrough for the external power lines.

The initial configuration, shown in Figure 5.3 (a), violated several requirements and limited the maximum feasible acceleration voltage due to enhanced sparking caused by sharp edges on the connector housing and unshielded connector springs facing the Faraday cage. In the subsequent upgrade iteration, shown in panel (b), these issues were addressed by shielding the contacts, smoothing the connector housing edges, replacing simple silver wires with high-performance PEEK-insulated wires, and adding additional insulation. A color-coding scheme was also introduced to simplify identification and routing of the individual power lines.

Panel (c) shows the most recent sample holder, consisting of a 3D-printed corpus with a polyurethane insulator that secures the beryllium-chopper contact strips in place. Panel (d) presents a bottom view of the connector housing, where the beryllium-chopper contact springs are held in position by PEEK insulators. Both the springs and the external power lines are spot-welded to the contact strips, ensuring stable and reliable electrical connections.

5.2.2. System Improvements

By implementing the modifications to the target station, the application of an external sample bias was successfully realized. The functionality of each power line and the integrity of the electrical contacts were first verified using a dedicated test sample holder. In this setup, each contact strip was connected to a differently colored diode, all referenced to the system ground (equipotential plate). Applying a voltage to one of the contact lines caused the corresponding diode to illuminate, which could be monitored via the sample camera. This procedure confirmed the proper operation of each line under standard PLEPS operating conditions.

The sample biasing capability was subsequently tested at PLEPS on a p-i-n diode, used for high-energy ion detection in the Elastic Recoil Detection instrument of A.

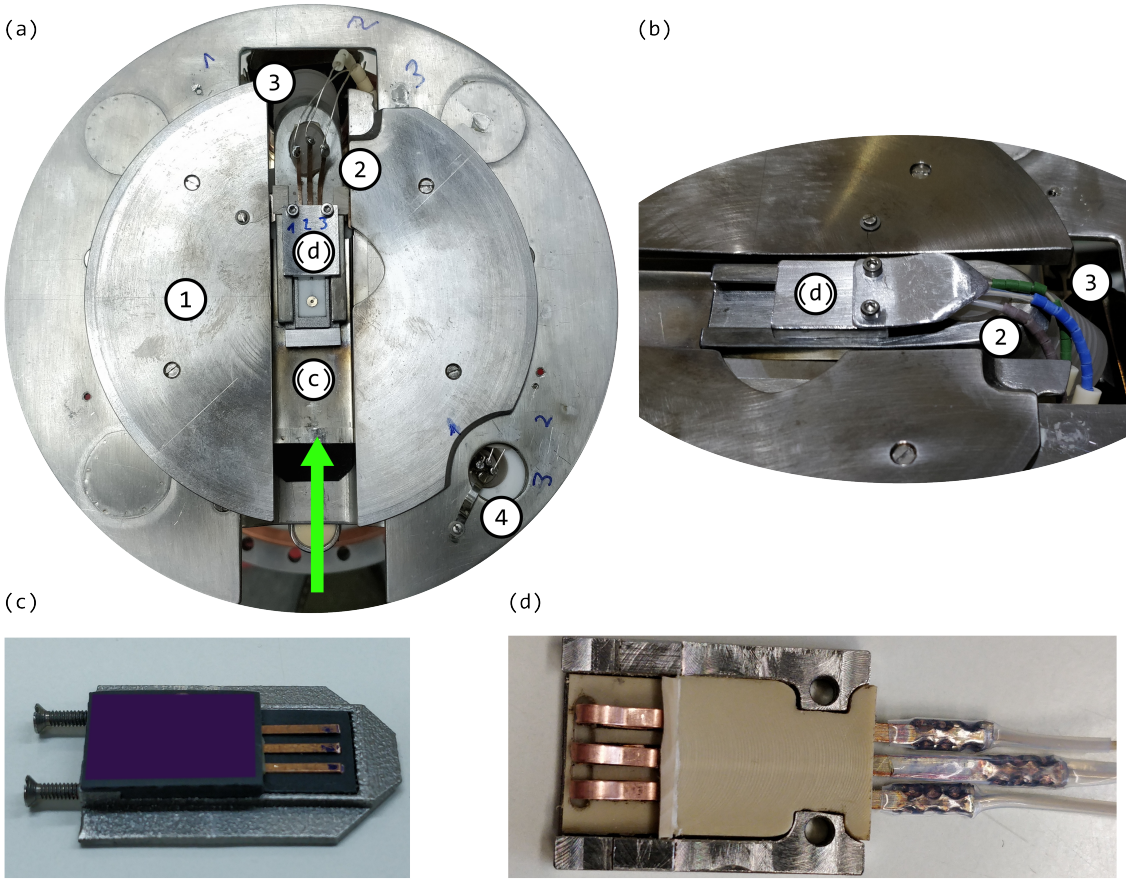

Figure 5.3.: Technical implementation of the new design at the PLEPS target station. (a) Top view of the target station at an early, now obsolete design stage. The green arrow indicates the direction of sample holder insertion into the target station. (b) Final design with improved shielding and insulation of critical components. (c) Sample holder with a dummy sample mounted on the bottom contact. (d) Bottom view of the connector housing, showing the contact springs and their connections to the external power lines.

Bergmaier [145]. A p-i-n diode is a specialized p-n junction comprising a highly doped p-region, a highly doped n-region, and a thick intrinsic layer sandwiched in between. The intrinsic layer thickness is typically several orders of magnitude larger than that of the edge regions. Due to the high doping concentrations of the p- and n-regions, the depletion region under reverse bias extends predominantly into the intrinsic layer [92].

Figure 5.4 shows the lifetime spectra of the p-i-n diode at 4 keV for three different gate voltage configurations. The zero-voltage spectrum serves as a reference corresponding to thermal equilibrium, where only the built-in potential remains,

establishing an internal electric field. At negative 1200 V, the p–i–n diode operates under reverse bias, which is the standard mode for ion or photon detection. At a positive 1200 V the diode is driven into forward bias, thereby reducing the depletion width within the intrinsic layer. In all configurations, an electric field persists across the intrinsic silicon layer, with its orientation and magnitude determined by the applied gate bias.

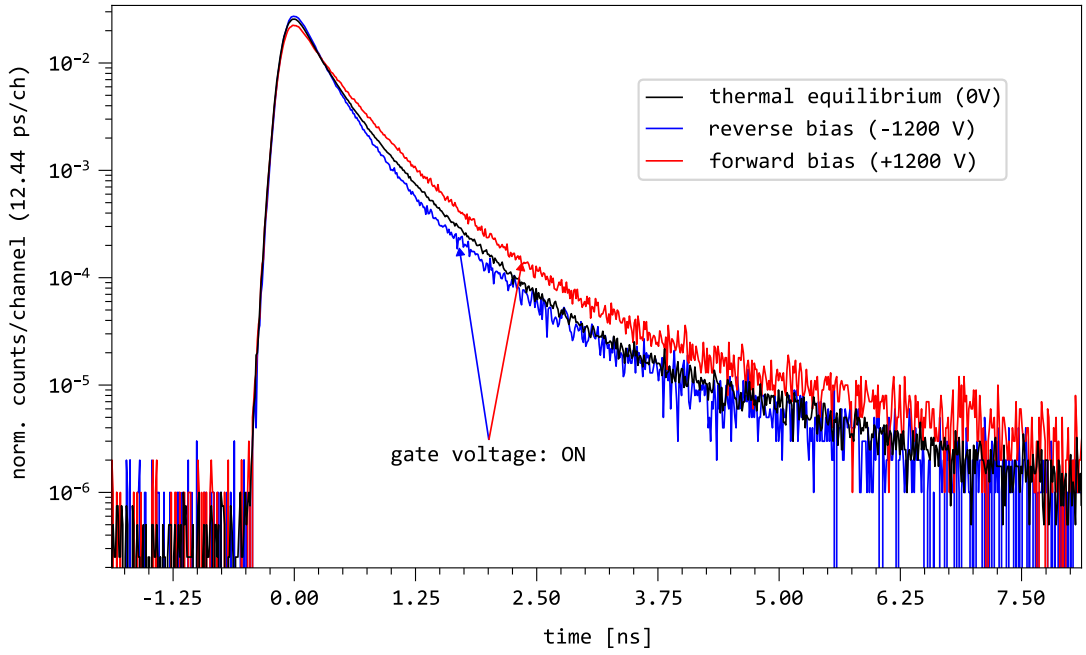

Figure 5.4.: Positron lifetime spectra of the p-i-n diode recorded at 4 keV under different gate voltages, showing polarity-dependent variations in the long-lifetime components due to positron drift.

The distinct changes in the annihilation characteristics under different gate conditions demonstrate the dependence of the annihilation characteristics on the polarity of the applied field. This behavior indicates that the applied electric field steers positrons into slightly different regions of the material, leading to measurable, drift-dependent variations in their annihilation behavior. A more detailed discussion of positron drift and its implications for annihilation processes is presented in the following chapter on metal–oxide–silicon (MOS) capacitors.

During the conversion of the target station, all wiring and conductive components on or near the station were re-examined. The resulting improvements, including enhanced cable insulation and the removal of sharp edges and points on conductive surfaces, allowed the maximum acceleration voltage for positron implantation to increase from 18 keV in 2019 to 21 keV. This increase is particularly important for future studies on high-Z materials, such as tungsten or reactor steels, which require higher implantation energies to achieve sufficient penetration depths and reduce

surface contributions in the spectra. The acceleration voltage of 21 keV was dry-tested for 12 min, exceeding the typical acquisition time of a single lifetime spectrum (see Table 5.1).

6. Positron Drift for Interface Defect Characterization

The measurements, results, figures, discussion, and conclusions presented in this chapter are, in part, reprinted from two publications derived from the experiments described herein.

> **R. Helm**, W. Egger, C. Corbel, P. Sperr, M. Butterling, A. Wagner, M. O. Liedke, J. Mitteneder, M. Mayerhofer, K. Lee, G. S. Duesberg, G. Dollinger and M. Dickmann, *Defect studies in thin-film SiO2 of a Metal-Oxide-Silicon Capacitor using Drift-Assisted Positron Annihilation Lifetime Spectroscopy*, Nanomaterials **15**, 1142 (2025), 10.3390/nano15151142
>
> **R. Helm**, W. Egger, C. Corbel, P. Sperr, M. Butterling, A. Wagner, M. O. Liedke, E. Hirschmann, J. Mitteneder, M. Mayerhofer, K. Lee, G. S. Duesberg, G. Dollinger and M. Dickmann, *Defect Characterization of the SiO2/Si Interface investigated by Drift-Assisted Positron Annihilation Lifetime Spectroscopy*, Nanomaterials 16, 156 (2026), 10.3390/nano16030156

This approach has been adopted because the original publications provide the most rigorous and coherent presentation of the data and its interpretation.

6.1. Drift-Assisted Positron Annihilation Spectroscopy

The work presented in this chapter was originally intended to test and validate the upgraded PLEPS target station, described in Chapter 5, in order to enable the defect characterization required to address the scientific questions outlined above. However, following the shutdown of the FRM-II research reactor in Garching in early 2020, the planned measurements could not be carried out at PLEPS. Instead, the experiments were performed at the MePS instrument at the Helmholtz-Zentrum Dresden-Rossendorf.

Low-energy positron beam techniques have been a key tool in materials science for decades, enabling detailed investigation of atomistic defects. Many research groups have developed or continue to develop slow-positron beam systems for various an-

nihilation methods [7, 8, 44, 146, 147]. Since almost all defect-related problems benefit from positron annihilation spectroscopy (PAS), it is widely applied in materials science and solid-state physics.

In semiconductor technology, ongoing miniaturization – driven by the pursuit of Moore's law – has reduced device features to the subnanometer scale, pushing the limits of positron annihilation spectroscopy (PAS). The implantation depth profile of slow positrons is as broad as several hundreds of nanometers and depends on material density and beam energy. As a result, buried layers and interfaces in the nanometer range remain difficult to probe directly.

Another challenge is positron diffusion. Positrons implanted near a surface or interface can migrate into adjacent layers, altering the annihilation signal. This is particularly significant in materials with long positron diffusion lengths ($\approx 100\,\mathrm{nm}$), such as crystalline semiconductors and metals. As device layers approach these lengths, it becomes increasingly difficult to unambiguously assign defect signals to a specific layer.

Overcoming these limitations requires more than improvements to the beam system alone; sample manipulation techniques can significantly enhance the sensitivity of positron annihilation spectroscopy (PAS) to thin layers and interfaces. Several studies have shown that applying an electric field to the material can drive thermalized positrons toward interfaces or thin layers, thereby increasing the relative contribution of their annihilation channel compared to other annihilation processes [148–152]. These studies – conducted using Doppler Broadening Spectroscopy (DBS, Section 2.3) – highlight the potential of field-assisted techniques. While DBS provides chemical information and qualitative insight into lattice defects, it lacks the ability to determine specific defect parameters such as type, size, and concentration.

Drift-Assisted Positron Annihilation Lifetime Spectroscopy (DA-PALS) extends conventional lifetime spectroscopy (see Section 2.1.1) by incorporating an externally applied electric field to manipulate positron motion after implantation. The principle is exemplified in this work using a metal–oxide–semiconductor (MOS) capacitor consisting of Al, SiO_2, and Si layers.

As a schematic example of the drift process a mono-energetic slow positrons beam is considered whose depth profile $P(z)$ peaks within the SiO_2 layer (Figure 6.1 (a), black dashed line). Under zero-field conditions, the annihilation distribution $A(z)$ (red line) is similar to $P(z)$, only broadened by positron diffusion. Interfaces are theoretically ideal positron sinks, preventing migration across layers. In practice, the broad implantation profile leads to annihilation events in both adjacent layers and the narrow interface regions. This makes it difficult to attribute defect signals unambiguously to a specific layer – particularly in thin layers and interfaces. Figure 6.1 (b) and (c) illustrate how an electric field affects the distribution of implanted and thermalized positrons.

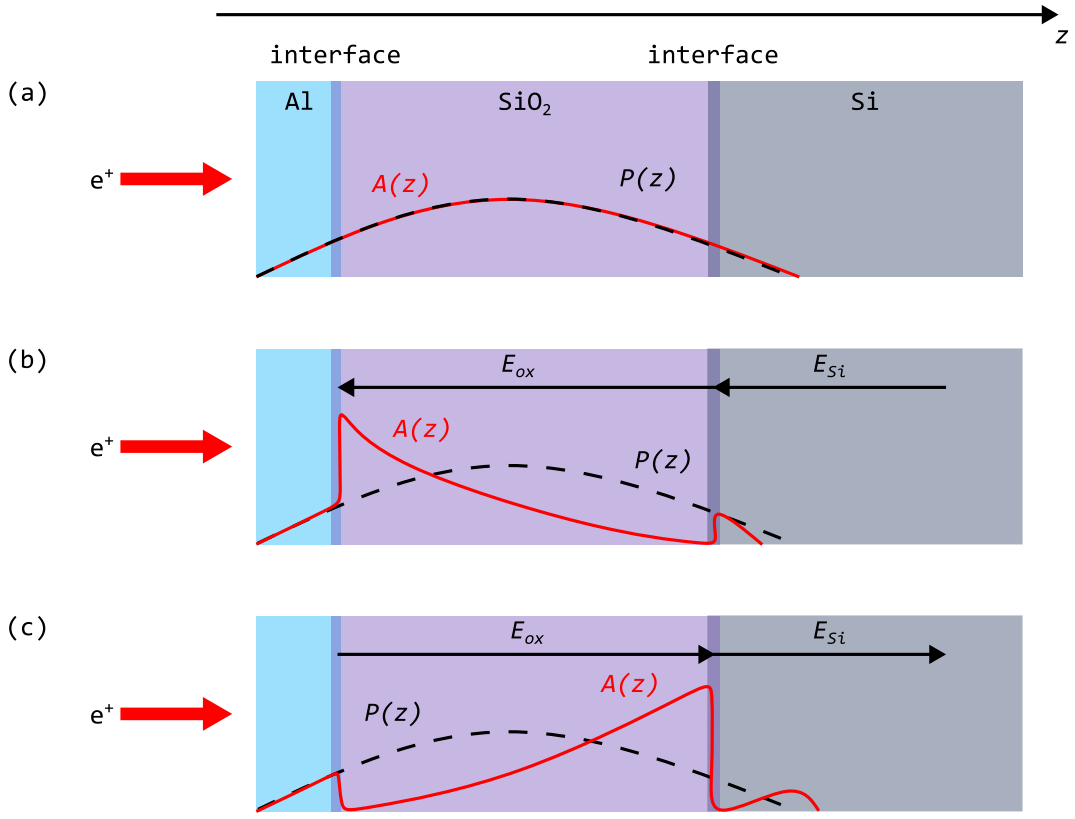

Figure 6.1.: Schematic of the three-layer MOS capacitor and its interfaces. The mono-energetic positrons enter the stack through the aluminum gate, thermalize, and result in the implantation distribution $P(z)$, which is dependent on the positron implantation energy and the density of the material (see Section 2.3.1). Different electric field configurations lead to a drastically altered spatial distribution $A(z)$ before annihilation, but after diffusion and drift have occurred.

In practice, positron transport under an internal electric field is more complex, as it is strongly influenced by the material's electronic properties and the specifics of positron–matter interactions. These dependencies must be taken into account when interpreting the kinetics and transport behavior in field-assisted measurements. The key considerations are outlined below to provide context before discussing the details of the drift experiment in the metal–oxide–semiconductor capacitor.

Drift and diffusion

As described in Section 2.3.2, positron diffusion is a thermally activated random walk driven by scattering with phonons. In the presence of an electric field, positrons are

accelerated between scattering events, and the resulting transport becomes a superposition of drift and diffusion, producing a net drift current in the direction of the field vector, similar to the drift–diffusion model for semiconductors [92]. Diffusion and drift are characterized by the positron diffusion constant D_+ and the mobility μ_+. Both parameters are macroscopically describing the scattering processes between positrons and lattice atoms, and must be either known or experimentally determined.

Electric field distribution

In insulating materials, the electric field can be approximated as constant across the entire layer, so it is primarily necessary to ensure that the field strength is sufficiently high to drift the positrons. In semiconductors, however, the internal electric field varies with depth from the surface due to charge neutrality in the bulk. Therefore, it is important to carefully consider the overlap between the positron implantation profile and the electric field distribution in accumulation, depletion, and inversion regimes to maximize the fraction of positrons influenced by the drift. See Chapter 3 for a detailed discussion.

Doping concentration

For semiconductors, the doping concentration plays a crucial role in determining both the extent and direction of the internal electric field. Careful consideration of doping is essential to engineer an electric field distribution that aligns with the objectives of the positron drift experiment. With increasing doping concentration the Debye length as well as the extent of the depletion zone into the near-surface region of the silicon substrate decreases. By consulting Equation (3.20), a doping concentration of $1 \times 10^{15}\,\mathrm{cm}^{-3}$ yields a maximum depletion width of approximately 900 nm, whereas a concentration of $1 \times 10^{19}\,\mathrm{cm}^{-3}$ results in a substantially smaller width of about 10 nm.

Positron affinity

The positron affinity A_+ is an important parameter when investigating positron drift toward buried interfaces. During PAS measurements, only a single positron is, on average, present in the lattice. After thermalization, it remains near the bottom of its energy band and behaves as a delocalized Bloch wave. The affinity represents the potential energy of the ground state relative to the vacuum level [153]. At the interface between two materials, differences in positron affinities create a potential step, which can either confine positrons or facilitate positron injection into a material, depending on the magnitude of the potential step and the direction of the drift.

6.2. Experimental Methods

Drift-Assisted Positron-Annihilation Lifetime Spectroscopy (DA-PALS)

Positron annihilation lifetime spectra (PALS) were collected over an implantation energy range from 1 to 11 keV at the Mono-energetic Positron Source (MePS) facility at the Helmholtz Center Dresden-Rossendorf [8]. Each spectrum included at least 1×10^7 counts, and the peak-to-background ratio exceeded 1×10^6:1. The overall time resolution of the MePS system, combining pulsing and detection, was measured to be 230 ps (FWHM) during the experiments and remained consistent across all implantation energies.

Lifetime spectra were analyzed using a three-component fitting model, yielding well-resolved lifetime components with fit quality indicated by $\chi^2 \leq 1.20$ for unconstrained fits. This approach provided the best statistical representation compared to alternative fitting methods, which either failed to converge or produced poorer fits. Reported uncertainties for lifetimes and intensities reflect statistical errors from the fitting procedure. Consistent initial parameters and channel ranges were maintained for all spectra.

For drift-assisted PALS measurements, spectra were recorded while varying the implantation energy and applying voltages between -30 V to 30 V. This voltage range was stable without causing breakdown and generated internal electric fields exceeding $1 \times 10^6\,\mathrm{MVcm^{-1}}$ within the oxide layer, sufficient to induce strong positron drift effects previously observed in Doppler broadening studies [151, 152]. The gate bias was supplied using an iseg DPS High Precision high-voltage module with a voltage accuracy of ± 0.5 V.

Electric field-Assisted Doppler Broadening Spectroscopy (EA-DBS)

The Doppler Broadening Spectroscopy measurements were conducted at the Variable Energy Positron (VEP) beam facility of the Reactor Institute of TU Delft [44]. For detecting the Doppler broadened energy of the 511 keV annihilation photons, a Canberra high-purity germanium detector (HPGe) equipped with a "Big MAC" cryostat was used. The HPGe detector was energy-calibrated using the reactor background and calibration sources (^{241}Am, ^{22}Na, ^{137}Cs, and ^{60}Co), allowing determination of the detector resolution at 511 keV. The measured resolution was 1.65 keV. The positron beam diameter (FWHM) was measured across various beam energies and ranged between 2.5 and 3.8 mm, with an average size of approximately 3.1 mm.

Doppler broadening spectra were recorded for implantation energies from 0.25 keV to 25 keV, accumulating at least 1.8×10^5 counts per energy step. The S- and W-parameters were extracted after each implantation energy measurement. For the variation of the gate voltage, an Ortec Model 556 power supply was employed, and

measurements were taken at five voltage levels: −30 V, −19 V, 0 V, +17 V, and +30 V.

6.3. Al/SiO_2/Si Capacitor Characteristics

This section describes the metal-oxide-semiconductor (MOS) system used in the drift experiments. While Chapter 3 provided a general overview of the physical properties of such systems, here we focus on the fabrication process and the specific characteristics of the aluminum–silicon dioxide–silicon structure studied. This system was selected because it is well characterized using established semiconductor analysis techniques such as Electron Spin Resonance (ESR) [154] and Deep Level Transient Spectroscopy (DLTS) [155]. Furthermore, various positron research groups have previously examined this system using both beam-based and source-based positron annihilation methods [156–158], facilitating direct comparison with existing literature. Table 6.1 lists the material properties relevant to positron–matter interactions that were not measured in this work but adopted from established literature values.

layer	d [nm]	process	ρ [g/cm$_3$]	ϵ_r	Φ [eV]
Al	40(5)	PVD	2.69 [159]	∞	−4.26 [160]
SiO_2	180(10)	oxidation	2.20 [161]	3.8 [161]	—
p-Si(100)	5×10^5	sc	2.34 [161]	11.7 [161]	−5.05 [162]

Table 6.1.: Relevant physical properties of the materials of each layer comprising the Al/SiO_2/Si capacitor at 300 K.

6.3.1. Sample Preparation

The starting material was a commercial 5″ p-type silicon wafer oriented in the (100) direction. The wafer thickness was 500 µm, with a resistivity of 10–20 Ωcm, corresponding to a doping concentration of approximately 1×10^{15}–5×10^{15} cm^{-3}. Thermal oxidation was performed in an H_2O atmosphere for 75 min at 950 °C, producing an inward-grown SiO_2 layer with a thickness of 180(10) nm.

For the aluminum gate fabrication, the wafer was coated with a photoresist using a custom-made mask from Toppan Photomask Germany GmbH. Aluminum was then vapor-deposited onto the wafer using a physical vapor deposition (PVD) evaporation system, followed by photoresist removal. The resulting gate electrodes had a thickness of 40(10) nm, an edge length of 10 mm, and were separated by gaps of approximately 4 mm. The wafer backside was coated with aluminum to form an

ohmic contact. Finally, the wafer was cut between the gate electrodes to obtain MOS samples with an edge length of 14 mm. A general visualization of the layered system is shown in Figure 3.1.

The sample was prepared by S. Boche from the Institute of Physics at the University of the Bundeswehr Munich. The MOS capacitor consists of an aluminum gate, a silicon dioxide dielectric layer, and a p-doped silicon substrate.

6.3.2. Electronic Characterization

The electronic properties of the MOS capacitor were characterized by Capacitance –Voltage (C–V) profiling using an IV–CV needle prober (see Section 3.5). This measurement provided key electronic parameters prior to the electric field-assisted positron annihilation experiments. The C–V measurements were conducted at the Institute of Physics, University of the Bundeswehr Munich, by Dr. K. Lee.

Figure 6.2 shows the electronic characterization for a gate voltage sweep from $-8\,\mathrm{V}$ to $+7\,\mathrm{V}$ at an AC frequency of $f = 20 \times 10^3\,\mathrm{Hz}$. Three distinct regions can be identified in the curve, corresponding to the operating modes of the device according to Section 3.5:

1. A high-capacitance region (C_{max}) at large negative gate voltages, which reflects the oxide capacitance. This corresponds to hole accumulation.

2. A decreasing-capacitance region, corresponding to the formation of the depletion layer in the semiconductor. This corresponds to hole depletion.

3. A low-capacitance region (C_{min}), reached when the depletion width is at its maximum. This corresponds to carrier inversion.

A slight recovery of capacitance above $+2\,\mathrm{V}$ is attributed to the low measurement frequency, which allows minority carriers to respond and reach the interface.

Following [108], the fla-tband voltage U_{fb} can be obtained from the inflection point of the second derivative of C. This yields $U_{\mathrm{fb}} = -0.9\,\mathrm{V}$. The minimum capacitance near $+2\,\mathrm{V}$ marks the depletion-to-inversion transition. Using the measured values C_{min} in Equation (3.25), the maximum depletion width is calculated as $w_{\mathrm{max}} = 618(62)\,\mathrm{nm}$.

From the linear region of the $1/C^2$ versus U_{g} curve in Figure 6.2 b), the doping concentration of the silicon substrate can be estimated. In principle, a linear fit in this region reflects carrier depletion in the semiconductor and is valid for any semiconductor junction. For MOS structures, factors such as interface traps and minority carrier generation can affect the slope and thus the extracted doping concentration. Neglecting these effects and fitting data points near the flat-band voltage gives an acceptor concentration $N_{\mathrm{A}} = 1.2(9) \times 10^{15}\,\mathrm{cm}^{-3}$ [109], which is consistent with the

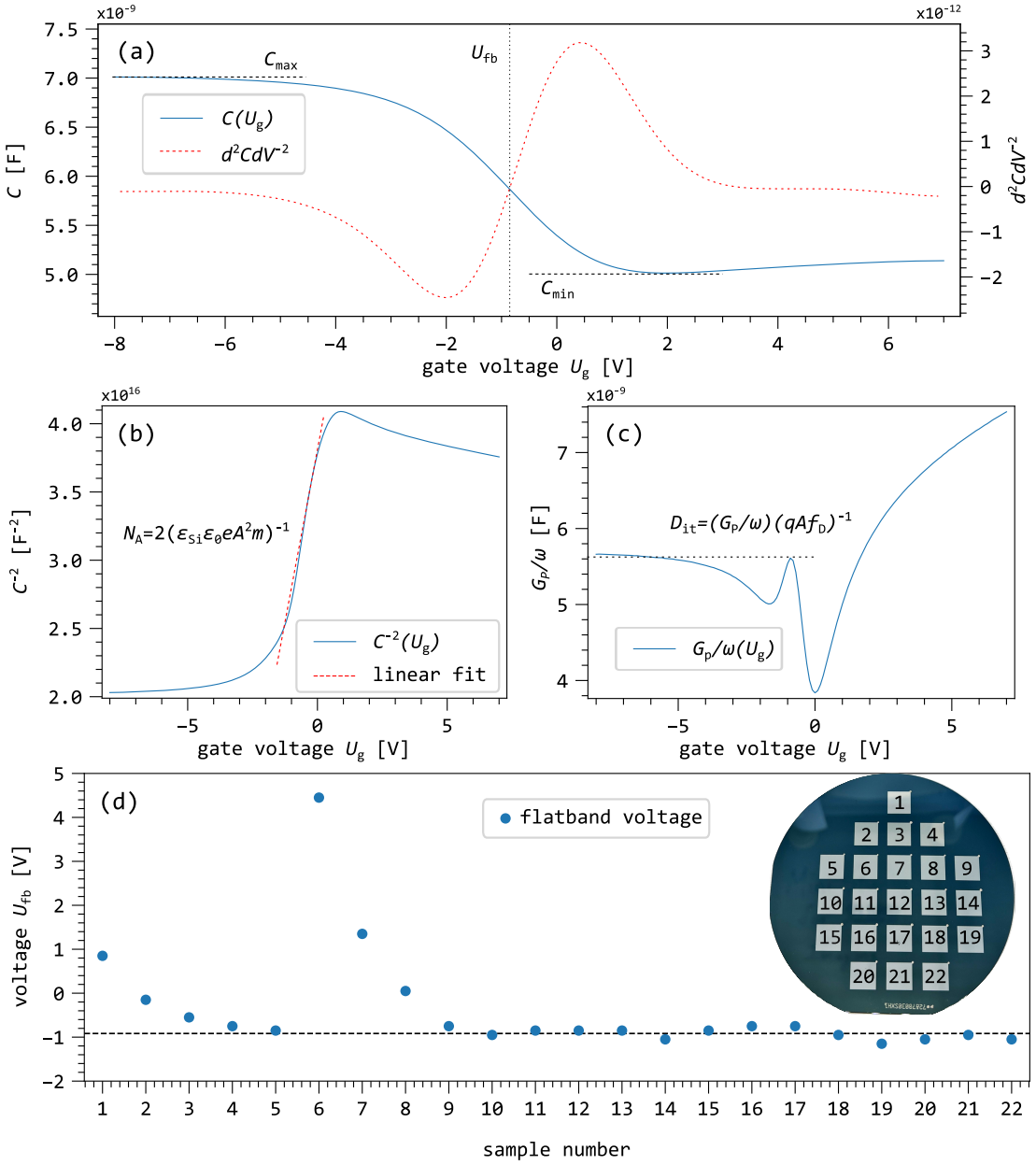

Figure 6.2.: (a) Capacitance C, (b) inverse squared capacitance C^{-2}, and (c) normalized parallel conductance G_p/ω as a function of gate voltage for sample 11. Panel (d) shows the extracted flat-band voltages U_{fb} for all samples on the wafer.

manufacturer's specifications.

From the conductance data, normalized to the measurement frequency ω, in Figure 6.2 c), the interface trap density D_{it} can be determined by using Equation (3.30) [110, 111]. The observed peak originates from carrier capture and emission by in-

terface states. Using the Equation (3.30), the interface trap density is estimated to be $D_{\mathrm{it}} = 10^{10} - 10^{11}\,\mathrm{eV}^{-1}\mathrm{cm}^{-2}$. Such values of D_{it} are typical for technical grade thermally grown oxides and indicate a high-quality oxide-semiconductor interface [163, 164].

Figure 6.2 d) presents the flat-band voltage results for each MOS sample across the wafer. Samples numbered 9 to 22 show an average flat-band voltage of approximately $-0.9\,\mathrm{V}$, which closely matches the theoretical work function difference introduced in Equation (3.3) to be $\Delta\phi = -0.7$ to $-0.9\,\mathrm{V}$. This suggests that the oxide growth process did not introduce significant additional oxide charges or interface traps. These samples were selected for the drift experiments.

In contrast, samples 1 to 8 display a substantial deviation of up to $5\,\mathrm{V}$ from the expected theoretical value. This deviation likely arises from additional oxide and SiO_2/Si interface charges, introduced during the oxide growth. As a result, these samples were not included in the current drift experiments; however, it may be valuable to investigate them in the future for comparison purposes.

6.3.3. Electric Field Simulation

In monoenergetic slow-positron beam experiments, the implantation energy determines the probing depth. The resulting stopping profile, often modeled by a Makhovian distribution, extends from the surface into the material to a depth governed mainly by beam energy and material density. An example for 11 keV positrons is shown in the upper panel of Figure 6.3. This distribution represents the location of thermalized positrons before drift and diffusion occur. Given the low probability ($\leq 1\,\%$) of positron thermalization in the aluminum gate at this energy, its thickness is neglected in the simulation. In this case, the overall fraction of positrons implanted into the oxide is $\approx 8\,\%$ and in the silicon substrate $\approx 92\,\%$. All one-dimensional implantation profiles presented in this chapter are obtained using a custom Python script that solves Equation (2.10) as a function of depth z.

To aid interpretation of the drift experiments, near-surface electric fields in the MOS structure were simulated using MOScap [166], based on the PADRE device code [167]. The model consists of an idealized infinitely thin aluminum gate, a 180 nm SiO_2 dielectric, and a 5 µm p-type silicon substrate with a doping concentration of $1.20 \times 10^{15}\,\mathrm{cm}^{-3}$, matching experimental values. The work function difference between gate and substrate was set to $\Delta\Phi = -0.7\,\mathrm{eV}$, giving $U_{\mathrm{fb}} = \Delta\Phi/q$ in the absence of fixed oxide charges or interface traps. Simulations were performed for $U_{\mathrm{g}} = -20\,\mathrm{V}$ (**accumulation**), $0\,\mathrm{V}$ (**depletion**), and $+20\,\mathrm{V}$ (**inversion**), all distinct from the flat-band condition to ensure fully developed space-charge regions and field distributions.

For small gate voltages on the order of the flat-band voltage, the Debye length L_{D}

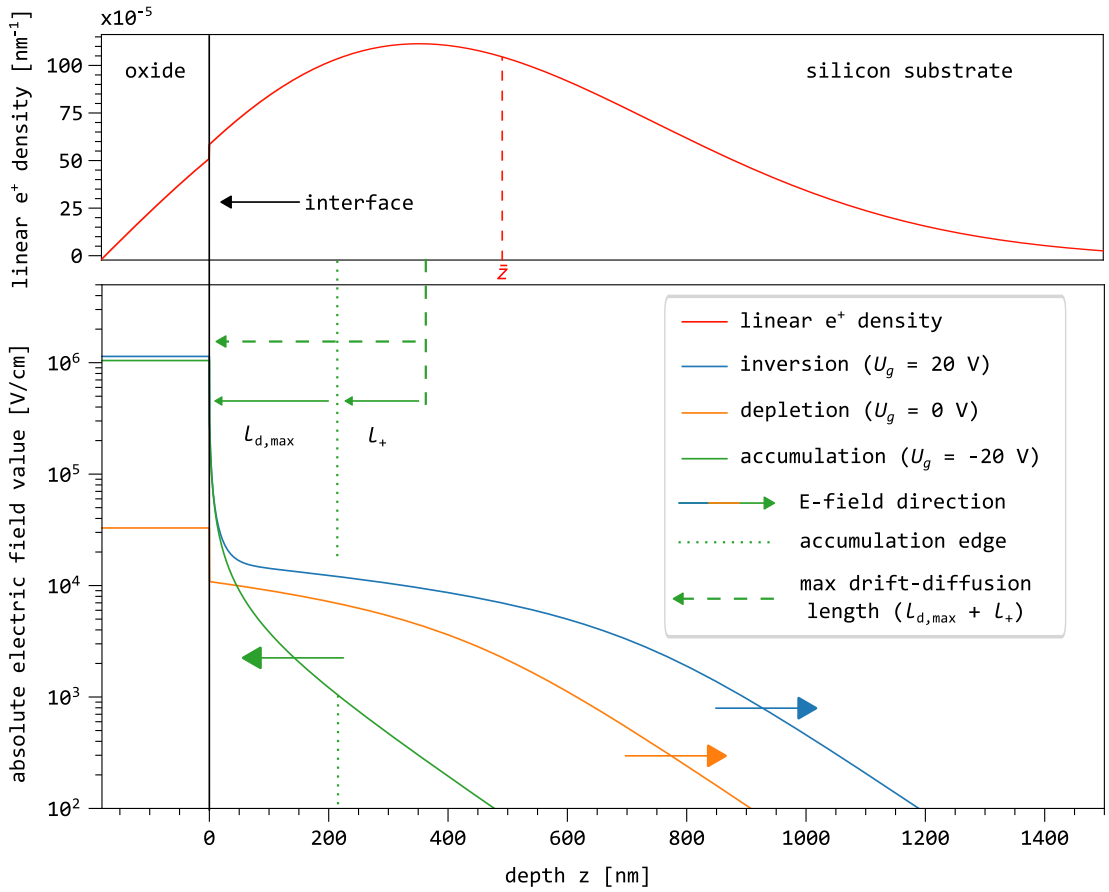

Figure 6.3.: The top graph shows the positron implantation profile as a function of depth for 11 keV, with $\bar{z}$ representing the mean implantation depth. The bottom graph displays the simulated electric field distribution in the oxide and silicon substrate as a function of depth for the different operating modes of the MOS capacitor. The dashed green line denotes the maximum distance from which a positron can still reach the interface under combined drift–diffusion transport, obtained from the superposition of Equations (2.19) and (2.25), and by using a $\mu_+ = 35\,\mathrm{cm^2V^{-1}s^{-1}}$. Figure reprinted from [165].

in silicon is approximately 120 nm at 300 K and a doping concentration of $1.2 \times 10^{15}\,\mathrm{cm^{-3}}$. At high gate voltages, the Debye length becomes significantly shorter than 120 nm; an approximate value for the characteristic length can be inferred from the transition of the two different exponential components in the accumulation curve (green curve in Figure 6.3), which occurs at around 40 nm.

Using Equation (2.25) with the positron mobility of $\mu_+ = 35\,\mathrm{cm^2V^{-1}s^{-1}}$ (this value will be derived in Section 6.5), a mean electric field $\langle E \rangle \approx 1 \times 10^5\,\mathrm{Vcm^{-1}}$ and the silicon bulk lifetime $\tau_\mathrm{b} = 221$ ps, the maximum drift distance of $l_\mathrm{d,max} \approx 220$ nm can be

estimated. This threshold is referred to as the accumulation edge in Figure 6.3. The accumulation edge, therefore, marks the maximum distance from which positrons can be drift-transported to the interface. The dashed green arrow in Figure 6.3 indicates the drift–diffusion length, which represents a more realistic upper limit that accounts for both drift and diffusion processes, as discussed in Section 2.3.3. Comparing these characteristic distances with the implantation profile illustrates the degree of overlap between the positron density and the electric field for each operating mode.

6.4. Positron Annihilation in the Al-Gate

This section describes the annihilation characteristics of positrons implanted into the aluminum gate (PVD-Al). Since implantation occurs from the gate side, the 40(5) nm thick aluminum layer mainly contributes to the annihilation signal at 1 keV implantation energy. The implantation profile is plotted in Figure 6.4 together with the schematic of the MOS capacitor.

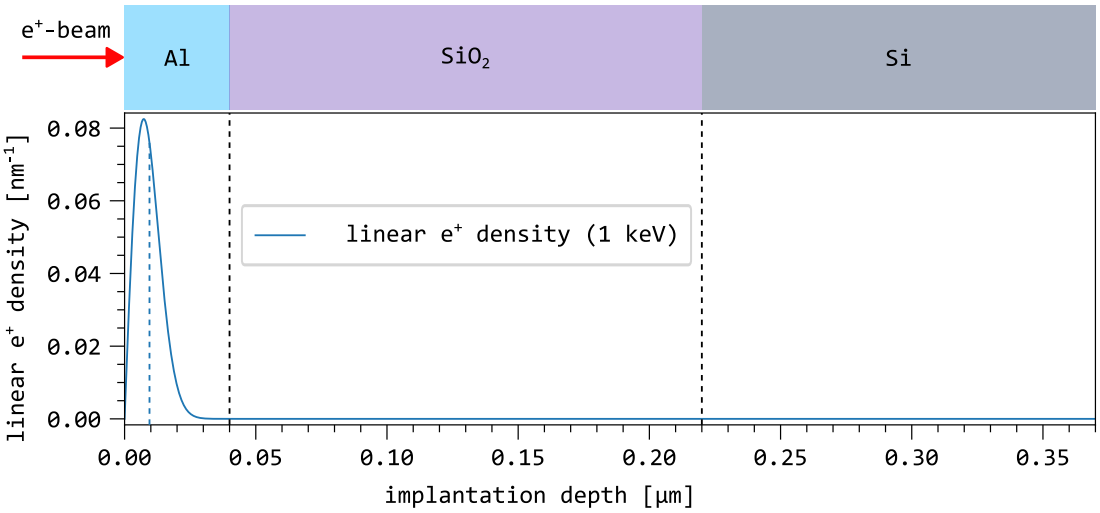

Figure 6.4.: Schematic depiction of the measured layered system for the determination of the gate positron lifetime properties. For a spatial reference, the calculated implantation distribution of 1 keV positrons is shown below. The one-dimensional mean implantation depth $\bar{z}$ is shown as a dashed vertical line. At a positron energy of 1 keV, all positrons are implanted into the vapor-deposited aluminum gate.

It demonstrates that the positrons with an implantation energy of 1 keV are fully stopped within the 40(5) nm aluminum layer. Consequently, the observed lifetime components at this energy are expected to originate from the aluminum layer and its interfaces.

To characterize the lifetime parameters of the physical vapor deposited (PVD) aluminum electrode, measurements were performed at 1 keV at the MePS facility. A three-component fit provided the best match to the measured decay spectrum and are listed in Table 6.2.

lifetime component	lifetime τ [ps]	Intensity I [%]
component 1	266(2)	64(1)
component 2	454(3)	35(2)
component 3	2700(40)	0.6(2)

Table 6.2.: Results of the lifetime analysis of the PVD aluminum gate measured with an 1 keV pulsed positron beam at MePS.

Egger et al. [168] performed positron lifetime measurements on fatigued Al-6013 alloys. At an implantation energy of 1 keV, a three-component analysis yielded a short lifetime of $\tau_1 = 257(1)$ ps with an intensity of $I_1 = 75\,\%$, a medium lifetime of $\tau_2 = 452(1)$ ps with $I_2 = 23\,\%$, and a long lifetime of $\tau_3 = 1984(72)$ ps with $I_3 = 2\,\%$. The short component was attributed to complete defect-saturation trapping of positrons at mono-vacancies, the medium component to annihilation in surface states (typically 360 ps - 500 ps [36, 65, 76, 77]), and the long component to ortho-positronium (o-Ps) annihilation at the surface.

The lifetimes obtained for the PVD-Al gate are comparable to those reported by Egger et al., indicating that in the PVD-Al layer, positrons are predominantly trapped at mono-vacancies, with additional contributions from larger defects [169]. The higher medium-lifetime intensity observed in PVD-Al ($\Delta I_2 = 12\,\%$) is attributed to positron annihilation in void-like defects in addition to surface states.

Overall, these results suggest that the PVD aluminum gate of the MOS capacitor exhibits saturation trapping in vacancies (τ_1, I_1) and voids (τ_2, I_2).

6.5. Positron Annihilation in the Si-Substrate

In this section, the positron annihilation characteristics of the bare silicon substrate are examined. Figure 6.5 shows a schematic of the sample configuration used in the measurements. Below the schematic, the implantation profiles are illustrated for (a) high-energy positrons emitted from a ^{22}Na source, calculated using Equation (2.15) and (b) low-energy positrons from a monoenergetic positron beam, calculated using Equation (2.10). Both implantation profiles are calculated using a Python script that solves each equation as a function of z.

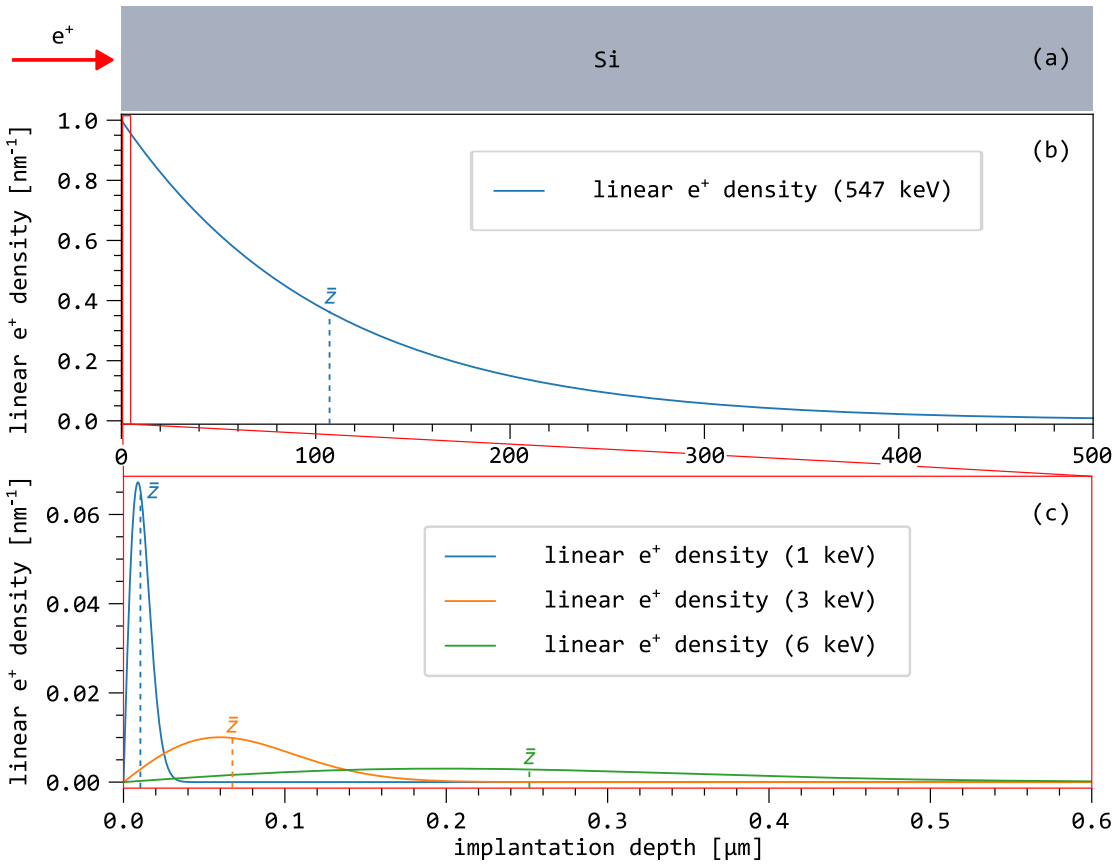

Figure 6.5.: (a) layer configuration used for measuring the annihilation characteristics of the substrate, along with the different implantation schemes for (b) positrons with an endpoint energy of $E_{\max} = 547\,\mathrm{keV}$ from a $^{22}\mathrm{Na}$ source and (c) beam-based low-energy positrons. The vertical dashed lines indicate the one-dimensional mean implantation depth $\bar{z}$ perpendicular to the sample surface.

As shown in Figure 6.5 a), the thermalized positron distribution for high-energy positrons follows an exponential profile (see Figure 2.4), whereas the implantation profile of slow positrons is well described by the Makhov distribution (see Figure 2.4). The mean implantation depth, marked by vertical dashed lines, is roughly 20 times greater for high-energy positrons than for slow positrons. Consequently, high-energy measurements are suitable for probing deeper regions of the material, whereas low-energy positrons are more appropriate for investigating the near-surface region of the silicon substrate. Combining both approaches allows for the characterization of annihilation processes in both the bulk and near-surface regions, as demonstrated in the following.

6.5.1. Bulk annihilation properties

Figure 6.6 shows the positron lifetime decay spectrum of the untreated p-type silicon wafer at an implantation energy of 8 keV. The spectrum shows a typical lifetime measurement collected at the Mono-energetic Positron Source (MePS) as a function of time. The measured data are shown as blue points, while the green points are used to fit the spectrum using the model of Equation (2.2). In the logarithmic representation of the decay spectrum, two distinct exponential contributions are apparent and are separated by the fit model, indicated by dashed lines. The fitted lifetime values, intensity, and their statistical uncertainties are provided in the legend.

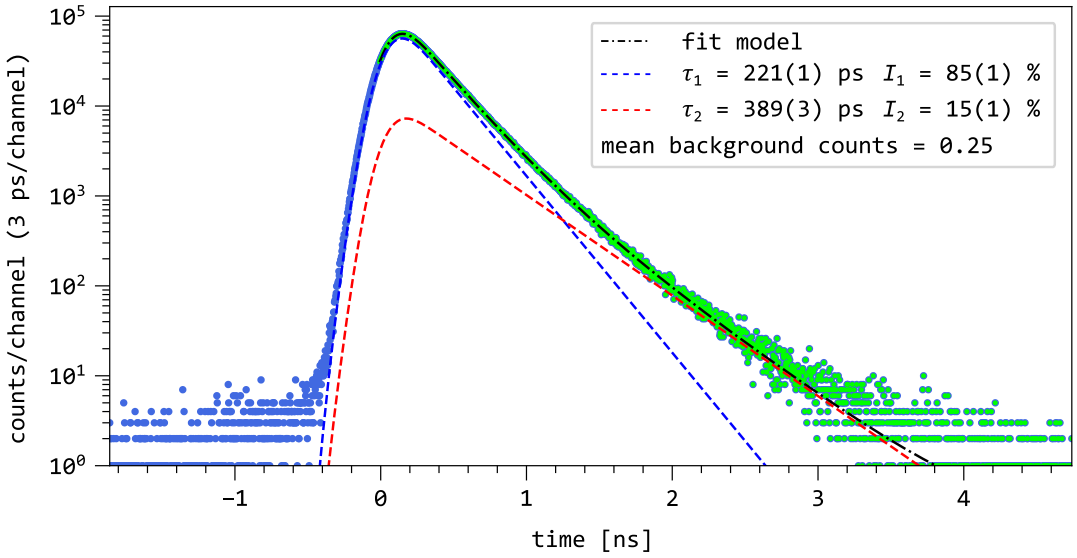

Figure 6.6.: Positron decay spectrum of p-type Silicon at 8 keV measured with the MePS instrument. The blue markers are the measured data points, and the green markers are the data points used for the fit model. The colored dashed line corresponds to the decay components delivered by the model, and the black dash-dotted line corresponds to the fit model. Figure reprinted from [165]

.

The two different lifetime components are: a shorter component of $\tau_1 = 221(1)$ ps with an intensity $I_1 = 85(1)$ % and a longer component of $\tau_2 = 389(3)$ ps with an intensity of 15(1) %. The shortest component, with a lifetime of 221(2) ps, originates from positron annihilation in the defect-free lattice and is identified as the bulk lifetime of the silicon substrate. This value is consistent with the beam measurement and with previous reports on silicon materials [170–172]. The longer component can be attributed to annihilation of positrons at the surface. To confirm the first component's value, a reference measurement was performed using a conventional setup, similar to the setup described in Section 4.1.

The reference spectrum, was evaluated using a three-component fit. The three components consist of a short lifetime component with 221(2) ps and an intensity of 88 %, a medium lifetime component with 398(21) ps and an intensity of about 10.5 %, as well as a longer component with a lifetime between 2895(98) ps and an intensity of 1.5 %. Due to the larger implantation depth of positrons from the ^{22}Na source, the medium and long lifetime components arise not from the surface but from positron annihilation in the ^{22}Na salt and the Kapton cladding. This is commonly referred to as the source contribution (see Section 2.2).

6.5.2. Surface annihilation and Diffusion

In slow-positron beam experiments, surface annihilation superimposes the bulk lifetime information of the bare silicon wafer. This occurs because a significant fraction of positrons remains within their diffusion length from the surface. Consequently, positrons implanted near the surface of defect-free silicon do not annihilate exclusively in the lattice. Instead, part of the positron population diffuses back to the surface, where annihilation occurs in surface states.

Annihilation in surface states

Figure 6.7 presents the two-component decomposition of the bare silicon spectra recorded with the Mono-energetic Positron Source (MePS) as a function of implantation energy. Both lifetime components remain constant in value, but their intensities vary with energy. With increasing implantation energy, the intensity of the first component increases, while that of the second decreases. The first component has a mean lifetime of 222(2) ps and an energy-dependent intensity ranging from 29 % to 98 %. The second component shows a mean lifetime of 385(5) ps, with intensities varying from 68 % to 2 %.

At low implantation energies ($1 - 3\,\mathrm{keV}$), a third, long-lived component appears with a lifetime of $2 - 3\,\mathrm{ns}$ and a low intensity of about 3 %, not shown in the Figure 6.7 and vanishing for energies above 3 keV. The observed decrease in I_2 and I_3 with increasing implantation energy indicates that τ_2 and τ_3 originate from defects close to the surface. The nanosecond component is attributed to o-Ps annihilation near the surface, while the shorter component in the range of $360 - 500\,\mathrm{ps}$ is characteristic of positron annihilation at surfaces [36, 65, 76, 77]. Even at medium implantation energies ($3 - 5\,\mathrm{keV}$), the surface-related component still contributes 50 % to 30 % of the total intensity, showing that positrons can reach and annihilate at the silicon surface even at these depths.

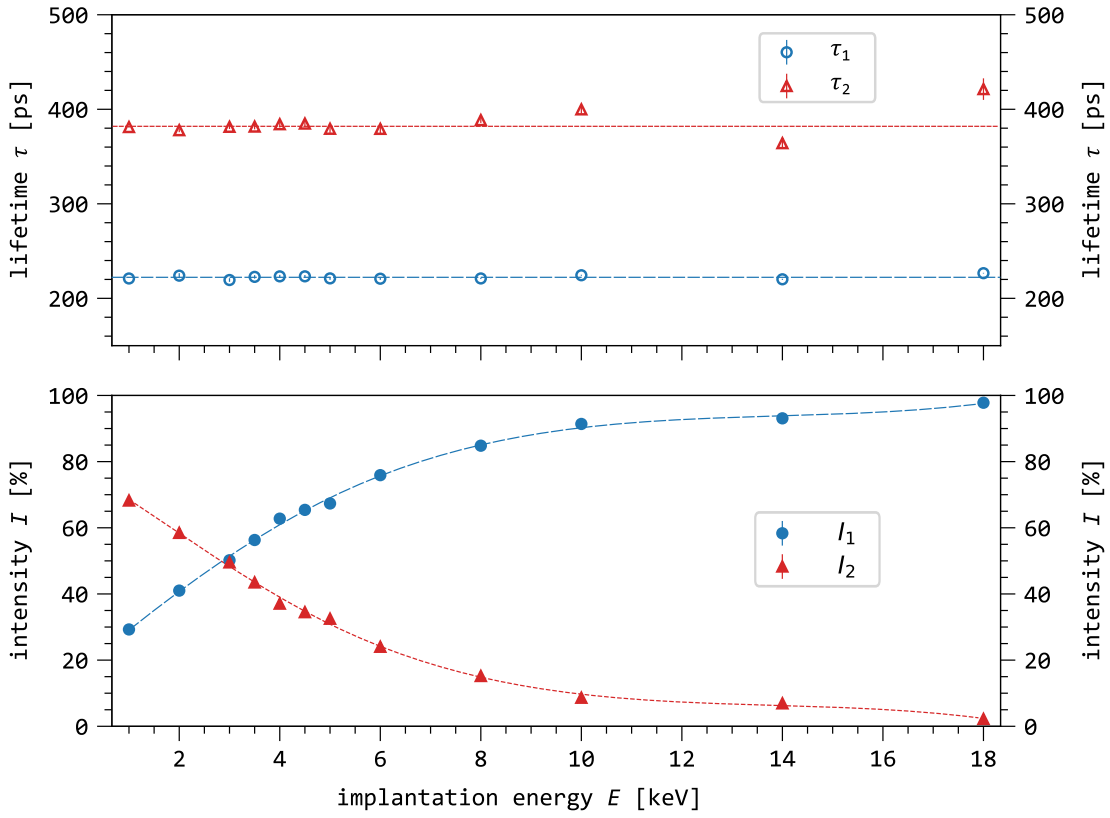

Figure 6.7.: Two-component decomposition of the bare silicon sample measured at the pulsed positron beam facility (MePS) as a function of positron implantation energy. Both lifetime components remain essentially constant over the investigated energy range. However, the intensities of both components show an inverse proportional relationship with increasing implantation energy. This arises from annihilation in surface with lifetimes in the range of 360 − 500 ps [77]. Figure reprinted from [165].

Positron diffusion in silicon

To extract the positron characteristics related to diffusion, drift, and trapping in the surface, the diffusion model introduced in Section 2.3.2 can be used. This model can be applied to various observables obtained from the PALS experiment, such as the intensity of the surface component I_2 or the average positron lifetime τ_{av} as shown in Figure 6.8.

Figure 6.8 presents two key observables from the PALS data: the surface intensity I_2 and the average lifetime τ_{av} of the short and medium lifetime components, each plotted as a function of the positron implantation energy. The dashed black lines correspond to the model fits using Equation (2.43) for the intensity I_2 and Equation

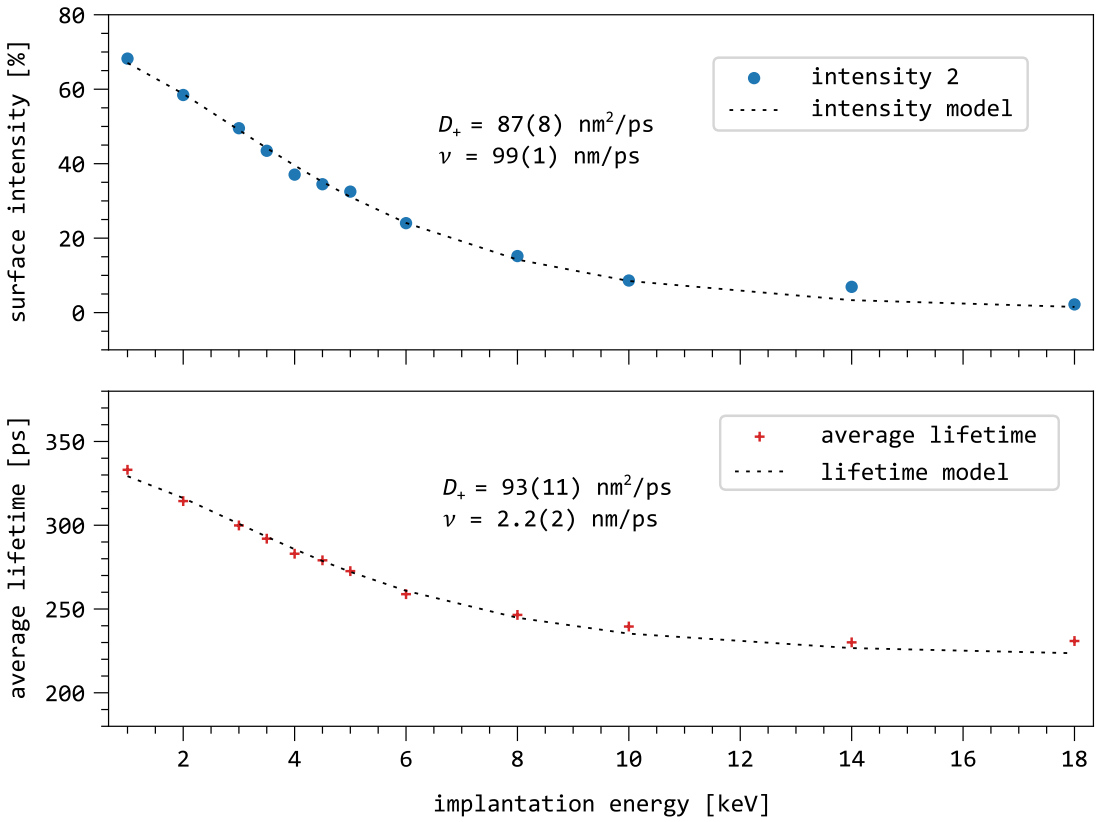

Figure 6.8.: Extraction of the positron diffusion constant D_+ and the surface transition rate ν from the energy-dependent lifetime results. The models are based on Equation (2.43) and Equation (2.44), and rely solely on experimentally observables (I_2 and $\bar{\tau}$) obtained from PALS.

(2.44) for the average lifetime τ_{av}, respectively. The extracted values for the diffusion constant D_+ and the surface transition rate ν are indicated in the respective plots.

The diffusion constants D_+ obtained from both models agree within their uncertainties, yielding an average value of $D_+ = 0.90(14)\,\text{cm}^2\text{s}^{-1}$. From Equation (2.18), the corresponding effective positron diffusion length is $l^+ = 141(22)\,\text{nm}$. This value may not represent the true bulk diffusion length l_0^+, since surface dipoles can induce band bending near the surface and create electric fields that influence positron transport. Nonetheless, both the diffusion constant and diffusion length are consistent with previously reported values for p-type silicon with similar doping levels [77]. Applying the Einstein relation (Equation (2.20)) gives the positron mobility in silicon as $\mu_+ = 35(3)\,\text{cm}^2\text{V}^{-1}\text{s}^{-1}$, which will be relevant when discussing drift in the MOS capacitor substrate.

In contrast, the surface transition rates ν derived from the two models differ significantly. The value obtained from the intensity model is about one order of magnitude

higher than those reported in [77]. This discrepancy is attributed to the presence of a native oxide layer on the silicon surface, as no surface cleaning was performed before the measurements. The surface transition rate ν represents the trapping velocity at the surface and is directly related to the intensity I_2. These results suggest that the surface intensity model is about one order of magnitude more sensitive to the effect of surface trapping and the average lifetime is less sensitive to local inhomogeneities or thin surface layers.

6.6. Positron Quantum States in the Oxide/Si Stack

In this section, the 180 nm SiO_2 layer is characterized by using PALS and DBS on a SiO_2/Si stack, performed without the influence of an external electric field in the oxide or the aluminum gate. The investigated layer structure is shown in Figure 6.9. For the lifetime measurements, the implantation energy was varied between 1 keV and 11 keV. As illustrated at the bottom of Figure 6.9, an implantation energy of 2 keV allows the oxide layer to be probed with minimal contribution from the surface, the interface, or the underlying silicon.

For Doppler broadening spectroscopy, a depth profile was recorded over the energy range from 0.25 keV to 25 keV in steps of 0.25 keV, providing insight into the positron diffusion characteristics of the oxide–silicon stack.

6.6.1. Oxide Annihilation Characteristics

Figure 6.10 shows the lifetime spectrum of the bare oxide layer measured with a pulsed positron beam at an implantation energy of 2 keV. This enables observation of the intrinsic annihilation characteristics of the SiO_2 layer. Similar to Figure 6.6, the blue dots represent the measured decay spectrum and the green dots correspond to the data within the selected time window used for fitting the model function of Equation (2.2).

The three lifetime components, indicated by colored dashed lines in Figure 6.10, consist of two longer lifetimes, $\tau_2 = 595(6)$ ps and $\tau_3 = 1563(3)$ ps, which together contribute approximately 77 % of the total spectrum. The shortest lifetime, $\tau_1 = 137(1)$ ps, accounts for the remaining quarter of the resolved annihilation signal.

Lifetimes above 500 ps are generally attributed to ortho-positronium (o-Ps) annihilation (see Section 2.3.4). We therefore conclude that about 77 % of positrons form o-Ps and subsequently annihilate via pick-off processes. Given the statistical formation ratio of para-positronium (p-Ps) to o-Ps of 1 : 3, the short component can be assigned to p-Ps annihilation, supporting the validity of the expected formation ratio.

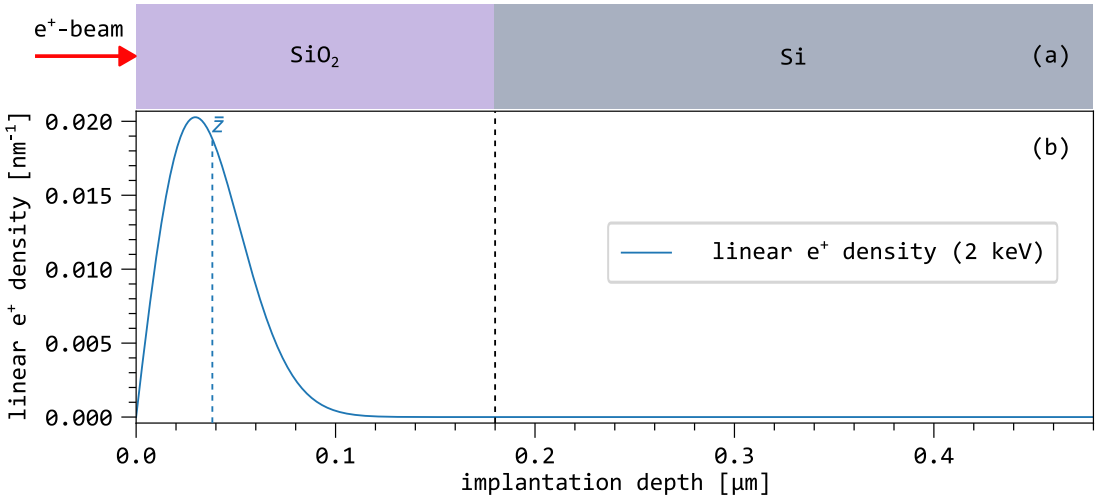

Figure 6.9.: (a) shows a schematic of the layered structure used to determine the positron lifetime characteristics of the oxide layer, along with the depth-dependent S and W parameters obtained from Doppler-broadening measurements. (b) shows the low-energy positron implantation profile beneath the layer stack, with the one-dimensional mean implantation depth indicated by a vertical dashed line. An implantation energy of 2 keV was selected to ensure that the measured lifetime components originate exclusively from the oxide layer.

The longest component ($\tau_3 = 1558(3)$ ps, $I_3 = 52(1)$ %) is a clear fingerprint of o-Ps annihilation in thermally grown SiO_2. Its high intensity reflects substantial positronium formation. The observed lifetime, two orders of magnitude shorter than the o-Ps vacuum lifetime (142 ns), is consistent with pick-off annihilation or quenching processes in the oxide [81]. The intermediate component ($\tau_2 = 585(6)$ ps, $I_2 = 23(1)$ %) likewise corresponds to o-Ps, but confined in smaller subnanometer voids [173]. Applying the Tao–Eldrup model (Equation 2.3.4), the respective void diameters are estimated as 1.5 Å for the medium component and 4.8 Å for the long-lived component.

Comparable results were reported by Suzuki et al. [157] for amorphous SiO_2, where a three-component fit yielded an o-Ps lifetime of ≈ 1.5 ns and the o-Ps formation intensity I_3 is about 15 % higher than in our case. Their data suggested that nearly 90 % of positrons annihilate in Ps states, similar to our findings. They further proposed that Ps annihilation occurs in subnanometer voids where electrons from surrounding oxygen atoms migrate toward the void walls and dominate the annihilation process. The discrepancy in intensities between the two studies may arise from differences in oxidation conditions: while their oxide was 500 nm thick and thermally grown in dry oxygen, no details on the oxidation temperature were provided.

In summary, the data support an interpretation of o-Ps annihilation in two types

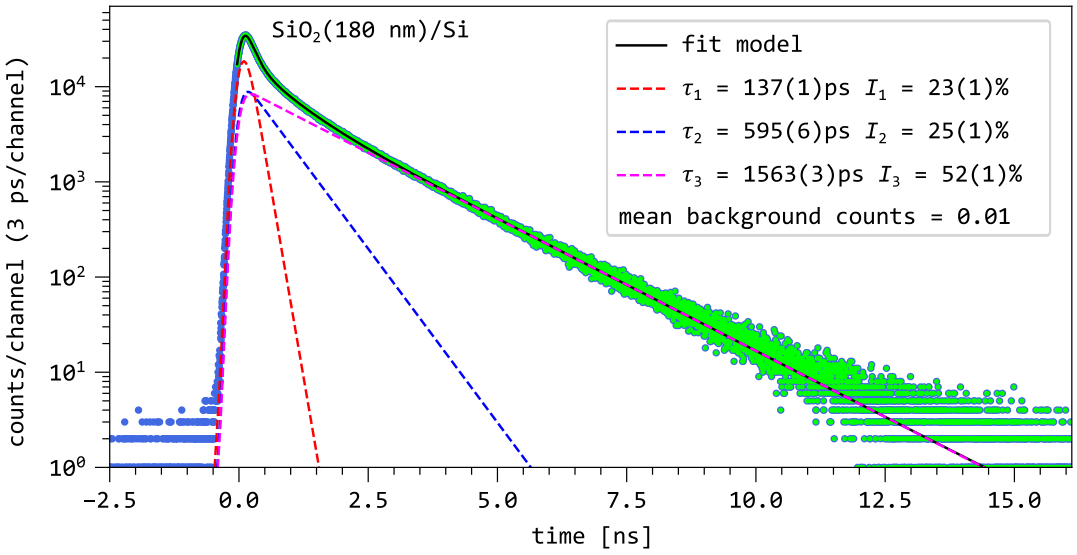

Figure 6.10.: Example lifetime spectrum with a three-component decomposition (see Section 2.1.1) for the bare oxide on silicon at an implantation energy of 2 keV. The blue dots represent the experimental data, the green dots indicate the data range used in the fit model, and the colored dashed lines correspond to the exponential decay components extracted from the fit. Figure reprinted from [174].

of subnanometer voids within the SiO_2 network. This is consistent with the known nanostructural features of thermally grown SiO_2 (see Chapter 3), where a broad bond-angle distribution (120 °C–180 °C) and deviations from stoichiometry promote the formation of both vacancy-like defects and larger subnanometer-scale voids.

6.6.2. Depth-dependent Annihilation Characteristics

Figure 6.11 shows the three-component decomposition of the lifetime spectra as a function of implantation energy. For reference, the energies at which the mean implantation depth lies within the oxide layer are highlighted in purple, and the corresponding oxide-equivalent mean implantation depth $\bar{z}$ is shown on the secondary x-axis.

With increasing implantation energy, the lifetime of the first component (blue) rises from 137 ps to 215 ps, with the most pronounced change occurring between 4 keV and 6 keV. Its intensity also increases steadily, showing the sharpest rise at the transition from the oxide to the underlying semiconductor.

The second component (red) shows an initial lifetime increase between 1 keV and 2 keV, followed by a continuous decrease until the mean penetration depth reaches

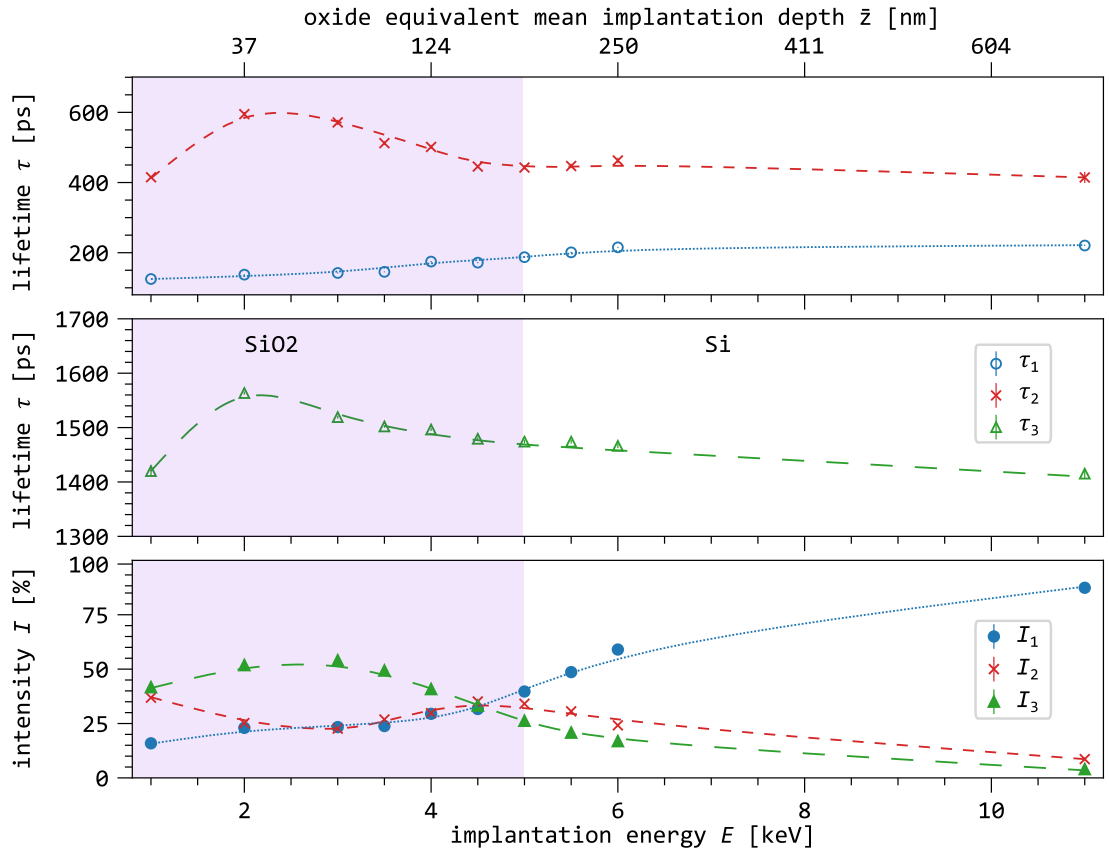

Figure 6.11.: Results of the three-component analysis of the bare oxide as a function of the implantation energy. As a depth reference, the oxide-equivalent mean implantation depth $\bar{z}$ is depicted on the secondary axis. Figure reprinted from [174].

the SiO_2/Si interface. At higher energies, it remains nearly constant. Its intensity displays maxima at 1 keV and 4.5 keV, decreases slightly within the oxide, and then falls continuously outside the oxide.

The third component (green) exhibits a lifetime increase in the same energy range as the second component, followed by a steady decrease at higher energies. Its intensity increases slightly at first and reaches a maximum of $I_3 = 52\,\%$ between 2 keV and 3 keV, before dropping to about 25 % as the oxide–semiconductor interface is approached.

Between 1 keV and 4 keV, most lifetime components are attributed to positronium annihilation. As shown in Section 6.6.1, positronium formation is characteristic of SiO_2 and suppressed in conductive materials such as aluminum and silicon (see Section 2.3.4). Therefore, the observed p-Ps and o-Ps annihilation can be assigned to the SiO_2 layer or the SiO_2/Si interface, consistent with the peak of the longest lifetime components when implantation occurs mainly within the oxide.

This assignment is supported by the parallel behavior of I_1 and I_3 at implantation energies below 3 keV (Figure 6.11) and the ratio $I_3/I_1 \approx 2.5$, close to the expected formation ratio. At higher energies (> 4 keV), as more positrons penetrate into silicon, the o-Ps intensity, I_3, decreases while I_1 rises toward the lifetime expected for defect-free silicon [170, 172], indicating a shift in the origin of the first component from positronium in SiO_2 to annihilation in silicon.

At an implantation energy of 1 keV, surface effects are visible in all three components, with τ_2 exhibiting a typical surface lifetime of about 400 ps [37, 175]. As the energy increases, I_2 initially decreases due to fewer positrons annihilating in surface states. Between 3 keV and 5 keV, I_2 rises while I_3 decreases, reflecting a reduced positron fraction in the oxide and increased annihilation at the SiO_2/Si interface. Above 5 keV, I_2 approaches zero as fewer positrons reach the oxide and near-interface region. The dip in I_2 indicates contributions from void-like defects at the oxide edges and o-Ps annihilation in the oxide bulk. Overall, the trends in I_2 and I_3 suggest that open-volume defects dominate the oxide nanostructure, with smaller defects being more abundant near the interface and surface, while larger defects are more pronounced in the silicon layer. Such defects are not present in the defect-free silicon substrate.

The lifetime value of τ_1 is longer then the vacuum lifetime (125 ps) of p-Ps. This indicates that other annihilation states could contribute to the short lifetime component. They most likely arise from free positron annihilation and give rise to an unknown component τ_1', which cannot be resolved in the lifetime analysis. We use a simple model, which utilizes the positron formation ratio to extract the unknown lifetime τ_1' as follows:

$$\tau_1' = (I_1\tau_1 - I_\mathrm{p}\tau_\mathrm{p})/(I_1 - I_\mathrm{p}) \tag{6.1}$$

This model assumes the para-Ps lifetime equals the vacuum value, $\tau_\mathrm{p} = 125$ ps, with intensity $I_\mathrm{p} = I_3/3$. Using Eq. 6.1, the corresponding lifetime component τ_1' and intensity I_1' are calculated as $\tau_1' = 169.9$ ps and $I_1' = 5.7\,\%$.

Comparable lifetimes and intensities have been reported for crystalline or vitreous SiO_2 [157, 176]. Notably, a lifetime of ≈ 160 ps was observed in crystalline SiO_2, but with a much higher intensity of $\approx 25\,\%$ [176].

6.6.3. Positron Diffusion in the Oxide

Depth-resolved Doppler broadening spectroscopy (DBS) was used to analyze the momentum distribution of the annihilation radiation from the SiO_2/Si stack. Properties of the oxide layer related to positron annihilation were extracted using the VEPFIT method, a numerical approach that fits the depth-dependent evolution of

the S and W parameters to obtain information on positron diffusion and trapping in the material [177]. The diffusion model from Section 6.5 could be applied; however, it requires knowledge of the bulk lifetime, which is difficult to determine in amorphous materials due to saturation trapping in their highly defective lattice.

Figure 6.12 shows the S and W parameters as a function of implantation energy. The solid line represents the VEPFIT model fitted to the experimental data. High S and W values are observed at low implantation energies ($< 5\,\mathrm{keV}$), where positrons are primarily implanted into the oxide and annihilate there. As the implantation energy increases and more positrons reach the substrate, the S increases and W decreases. The oxide-equivalent implantation depth is indicated on the secondary x-axis. Both parameters are normalized to the bulk silicon substrate values at high energies (above $20\,\mathrm{keV}$), where the measured S and W values predominantly originate from annihilation in the substrate.

Both the S and W parameters increase from the lowest energy of $0.25\,\mathrm{keV}$ up to $1\,\mathrm{keV}$, where they form a plateau that persists up to $3\,\mathrm{keV}$. The S parameter then decreases to a minimum at around $4.5\,\mathrm{keV}$, after which it rises again toward the silicon bulk value. The W parameter decreases for energies above $3\,\mathrm{keV}$ and approaches the silicon bulk value as well.

Based on the evolution of the S and W parameters, four distinct regions can be identified:

1. **Surface region** ($0.25-1\,\mathrm{keV}$): At very low positron energies, the annihilation signal is dominated by surface effects. Both S and W parameters increase with increasing implantation energy.

2. **Oxide region** ($1-3\,\mathrm{keV}$): The first local maximum in the S parameter is attributed to the oxide layer, where positronium formation significantly contributes to the annihilation characteristics. In this range, S and W parameters remain nearly constant.

3. **Interface region** ($3-6\,\mathrm{keV}$): The subsequent local minimum corresponds to the SiO_2/Si interface, where positrons preferentially annihilate with electrons at defects before positronium formation can occur [158]. The W parameter decreases without distinct features, while the S parameter exhibits a valley characteristic of the SiO_2/Si interface.

4. **Substrate region** ($6-25\,\mathrm{keV}$): At higher energies, the S parameter gradually increases as positrons penetrate deeper into the substrate, eventually stabilizing once annihilation predominantly occurs in bulk silicon. Both S and W parameters asymptotically approach their bulk values.

The VEPFIT model was applied to the experimental data using three layers: oxide, interface, and substrate. The S and W parameters, together with the diffusion

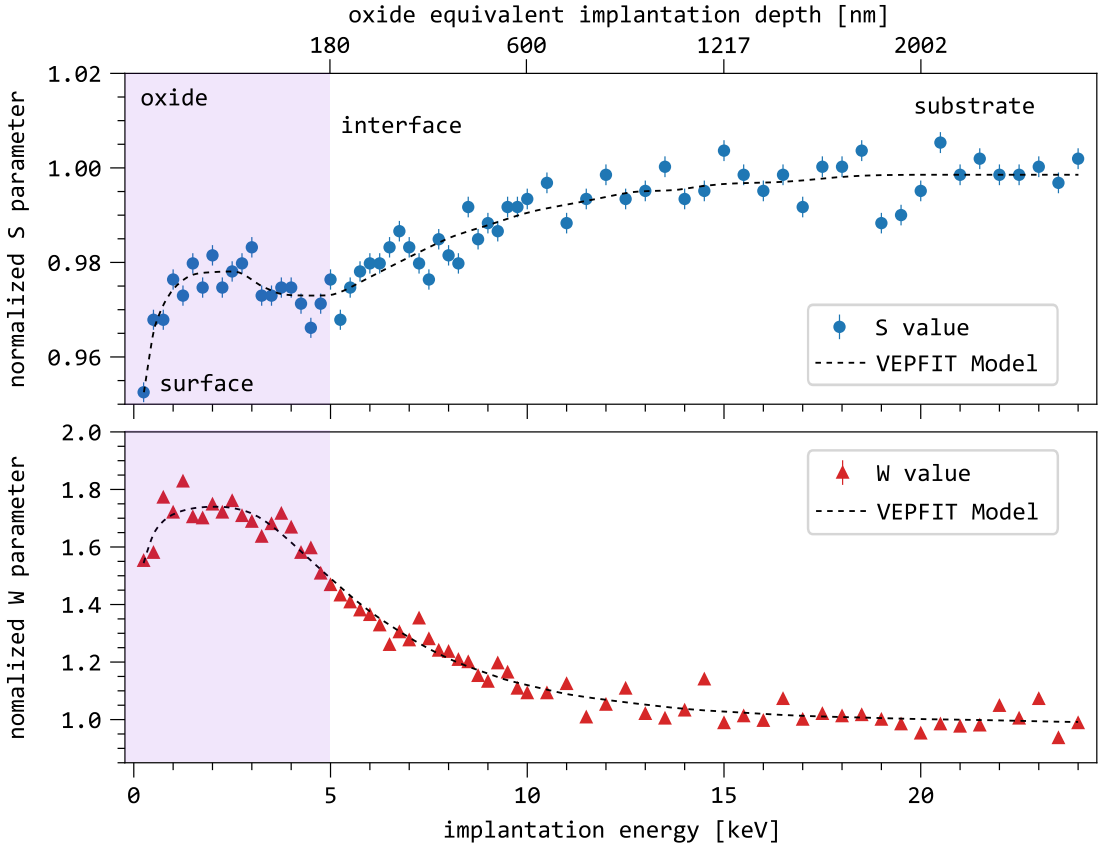

Figure 6.12.: S and W parameter analysis of the Doppler Broadening measurements of the bare oxide on silicon sample. Both parameters were normalized to the substrate bulk value. The VEPFIT model [177] was applied to extract the diffusion length and the effective oxide and interface thicknesses. The S parameter shows a clear valley between the oxide and the substrate, which can be attributed to the different momentum distribution of the defects in the interface sublayer. With increasing implantation energy, the S and W parameters asymptotically approach the silicon bulk values.

lengths and thicknesses of the oxide and interface, were treated as free parameters and determined during the fitting. For the substrate, the diffusion length was fixed to the value obtained in Section 6.5. The analysis yielded an effective positron diffusion length in the oxide of $l^+ = 8(1)\,\mathrm{nm}$ and an effective oxide thickness of $180(25)\,\mathrm{nm}$. The interface thickness was estimated as $d_{\mathrm{int}} = 5(20)\,\mathrm{nm}$. These values should be regarded as order-of-magnitude estimates rather than precise measurements. The diffusion length proved robust against changes in initial conditions, whereas the layer thicknesses were highly sensitive to boundary conditions and starting values.

The short positron diffusion length in the oxide is consistent with expectations for

amorphous SiO_2, where the disordered structure and high defect density strongly limit positron mobility. A similar value of $l^+ = 8(2)\,\mathrm{nm}$ was reported by Petegem et al. for amorphous SiO_2 [178]. The short diffusion length suggests that most positrons annihilate close to their thermalization site, meaning that the measured lifetimes predominantly reflect the oxide itself rather than surface or interface regions. Only a small fraction of positrons thermalizing in the oxide (approximately 5 %) reaches adjacent regions, which is too small to be resolved in the analysis. Overall, the extracted parameters are consistent with literature values in terms of order of magnitude.

The reported positron mobility μ_+ of amorphous SiO_2 spans a wide range from $0.013\,\mathrm{cm^2V^{-1}s^{-1}}$ [179] to $1.20(9)\,\mathrm{cm^2V^{-1}s^{-1}}$ [152]. This large discrepancy strongly influences the interpretation of positron drift in the oxide and has been attributed to differences in fabrication conditions [152]. Although no direct measurement was performed in this study, a rough estimate can be made to guide the analysis of the drift in the MOS capacitor, using Equations (2.18) and (2.20), which yields:

$$\mu_+ = \frac{e l_+^2}{\tau_\mathrm{b} k_\mathrm{B} T} \tag{6.2}$$

The only unknown parameter is the bulk lifetime τ_b. An experimental determination is not feasible, but a reasonable range can be estimated, based on the previous investigation, between 170 ps and 270 ps [180]. Taking the centroid of this interval ($220(50)\,\mathrm{ps}$) yields a mobility of $\mu_+ = 0.12(3)\,\mathrm{cm^2V^{-1}s^{-1}}$.

6.7. Positron Quantum States in the MOS Capacitor

Having examined positron annihilation in the individual layers of a metal–oxide–silicon (MOS) capacitor, the analysis can now be extended to the more complex case of the complete MOS stack, fabricated as explained in Section 6.3.1. Building on the results from the previous sections, drift-assisted positron annihilation spectroscopy (DA-PALS) is applied to the MOS capacitor as a function of implantation energy and gate voltage to investigate positron drift behavior in the oxide and silicon substrate, as well as to analyze defect states at the SiO_2/Si interface.

Figure 6.13 (a) illustrates the structural composition of the MOS capacitor with respect to the incident positron beam. The corresponding linear positron implantation profiles are shown in Figure 6.13 (b) for the two implantation energies used to probe positron drift in the oxide and substrate, respectively.

At an implantation energy of 4 keV, most positrons are implanted into the oxide layer. The mean implantation depth (blue dotted vertical line) lies between the Al/SiO_2 and SiO_2/Si interfaces (black dashed lines). In this configuration, the cu-

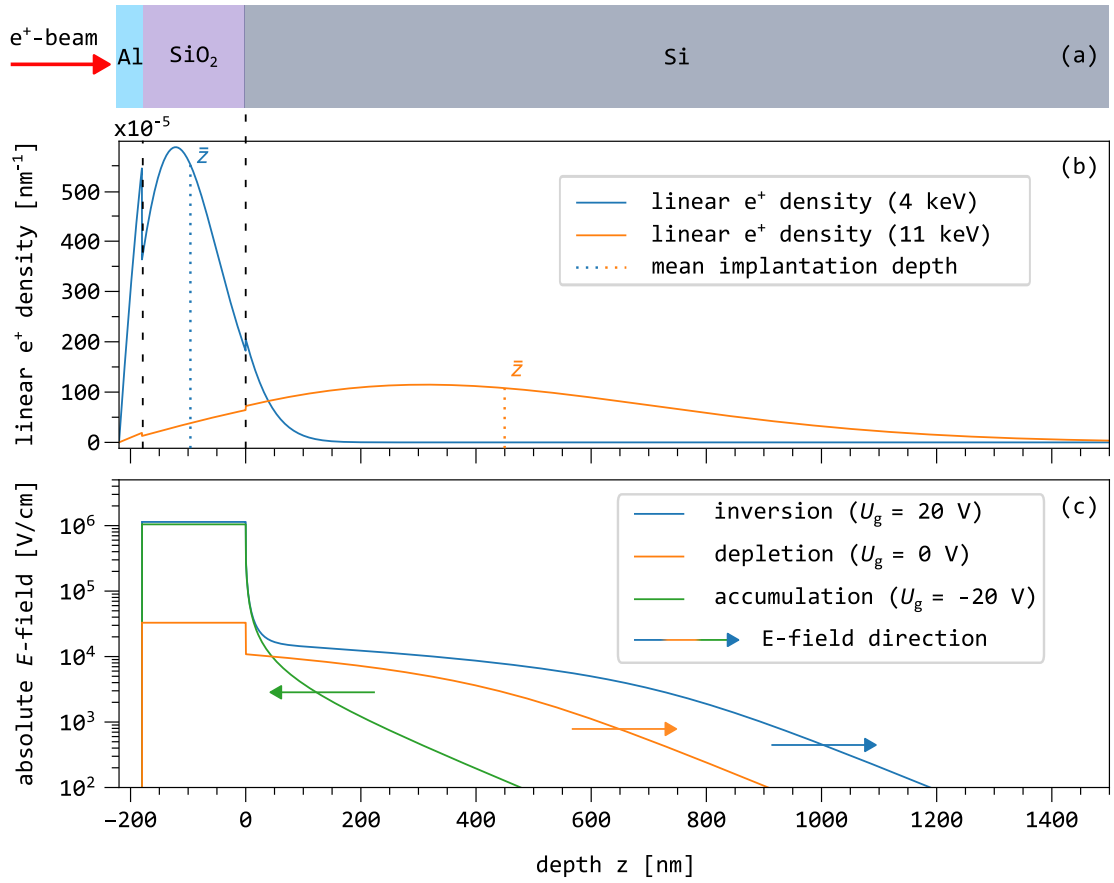

Figure 6.13.: Schematic explanation of the drift-assisted positron annihilation spectroscopy experiment on the MOS capacitor. Top: Structural composition of the MOS capacitor with the incident positron beam. Middle: Positron implantation profiles for the two implantation energies used in the voltage-dependent measurements. Bottom: Simulated electric field distribution in the MOS capacitor with the corresponding field directions.

mulative implantation probability indicates that approximately 80 % of positrons reside within the oxide.

At 11 keV, by contrast, the majority of positrons penetrate beyond the oxide and are implanted into the silicon substrate. The mean implantation depth (orange dotted vertical line) lies well beyond the SiO_2/Si interface, with minimal overlap in the Al and SiO_2 regions. Here, the cumulative implantation probability shows that about 92 % of positrons are implanted in silicon.

In Figure 6.13 (c), the calculated electric field distribution from Section 6.3.3 is shown, illustrating its spatial relationship to the linear positron density. This allows

us to make assumptions about the influence of the electric field on the thermalized positrons and to estimate the field-induced positron drift using transport models similar to charge carriers in semiconductors.

As described in Section 2.3.2, the positron transport is affected by the diffusion, the electric field, the positron mobility, the trapping rate, and the annihilation rate. The some positron transport parameters derived from the previous results are listed in Table 6.3.

Layer	D_+ [cm^2s^{-1}]	l^+ [nm]	μ_+ [$cm^2V^{-1}s^{-1}$]	$\langle E \rangle$ [Vcm^{-1}]	τ_b [ps]
SiO_2	$2.9(3)\times10^{-3}$	8(1)	0.12(3)	1.72×10^6	220(50)
Si (acc)	0.9(1)	141(20)	35(3)	$\approx 2 \times 10^5$	221(2)
Si (inv)	0.9(1)	141(20)	35(3)	$\approx 2.7 \times 10^5$	221(2)

Table 6.3.: Summary of the key transport parameters derived from the positron annihilation measurements for SiO_2, silicon in accumulation, and silicon in inversion. The bulk lifetime of SiO_2 is taken as the centroid of the range between 170 ps and 270 ps of bulk values reported in literature, as discussed in Section 6.6.3. The mean electric field in the near-interface region is estimated based on the maximum theoretical electric field in the oxide at a gate voltage of 30 V.

6.7.1. Electric-Field Influence on Positron Annihilation

Before discussing defects at the oxide-semiconductor interface, the effect of the internal electric field on positron annihilation is addressed. Positron lifetime measurements were performed at two implantation energies (4 keV and 11 keV) and analyzed as a function of the applied gate voltage. At a specific implantation energy, positrons reach the same mean depth on average, providing consistent starting conditions for their interaction with the electric field. This ensures that any changes in the lifetime signal can be directly attributed to the applied gate voltage.

Figure 6.14 shows the first evidence of an electric field effect on the positron lifetime by comparing the normalized positron lifetime spectra of the bare oxide at 2 keV with those of the MOS structure at 4 keV under three bias conditions: open circuit (0 V), −30 V, and 30 V.

The distinct bias conditions provide clear evidence of the electric field's effect on the annihilation characteristics of the oxide. Comparing the decay spectra at $U_g = 0\,V$

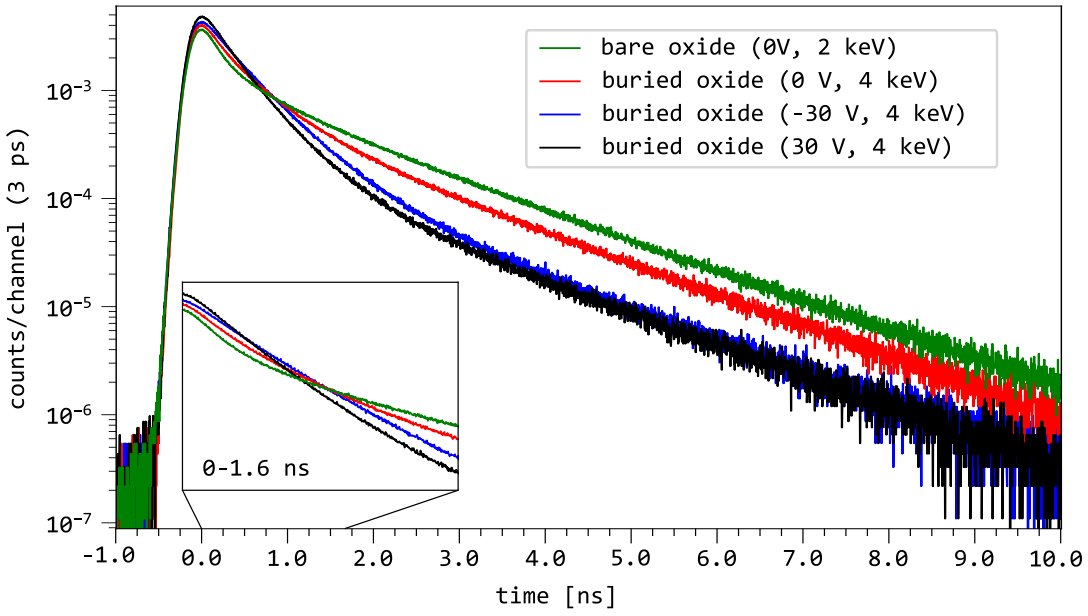

Figure 6.14.: Positron annihilation lifetime spectra of the bare oxide at 2 keV and the buried oxide at 4 keV are shown for three bias voltage conditions, $U_g = -30$, 0, and 30 V, over the time range from -1 ns to 10 ns. The spectra are enlarged for short decay times ($0 - 1.6$ ns) for clarity. All spectra were recorded with the same statistics of 1×10^7 counts per spectrum and are normalized to their area. Figure reprinted from [174].

for the bare oxide on silicon at 2 keV (green curve) and the buried oxide at 4 keV (red curve) indicates that the decay in the $5 - 10$ ns time range is influenced by the deposition of the aluminum gate on the buried oxide. Specifically, the presence of the Al gate reduces the intensity of the longest-lived component, while the decay slope – and thus the positron lifetime in the SiO_2 layer – remains largely unaffected.

By comparing the red, blue, and black curves, it is apparent that the intensity of the longest-lived component in the $5 - 10$ ns range decreases with increasing magnitude of U_g, from 0 to 30 V, independent of polarity. For clarity, only the two highest gate voltages and two representative spectra are shown, but the observed trend holds across the entire range of gate voltages. Notably, the decay slope remains nearly constant regardless of the magnitude or polarity of U_g. In the $0 - 1.6$ ns range, the MOS capacitor curves exhibit a different trend depending on U_g, as shown in the inset of Figure 6.14. This behavior indicates that, at short decay times, the gate voltage influences positron annihilation in a magnitude- and polarity-dependent manner, suggesting the presence of distinct annihilation states near the Al/SiO_2 and SiO_2/Si interfaces due to drifting positrons in the SiO_2.

6.7.2. Depth-dependent Annihilation Characteristics

Positron Lifetime versus Implantation Energy

Figure 6.15 shows how the lifetime components evolve in the different layers of the MOS capacitor as a function of the implantation energy for three different gate voltages: 0 V and the two extreme cases of 30 V and −30 V. As a depth reference, the oxide-equivalent mean implantation depth $\bar{z}$ is shown on the upper axis, and the different MOS layers are highlighted using colors (blue for aluminum and purple for the oxide). In this graph, the different colors of the data points correspond to the different gate voltage configurations. The lines connecting the data points are intended to guide the eyes.

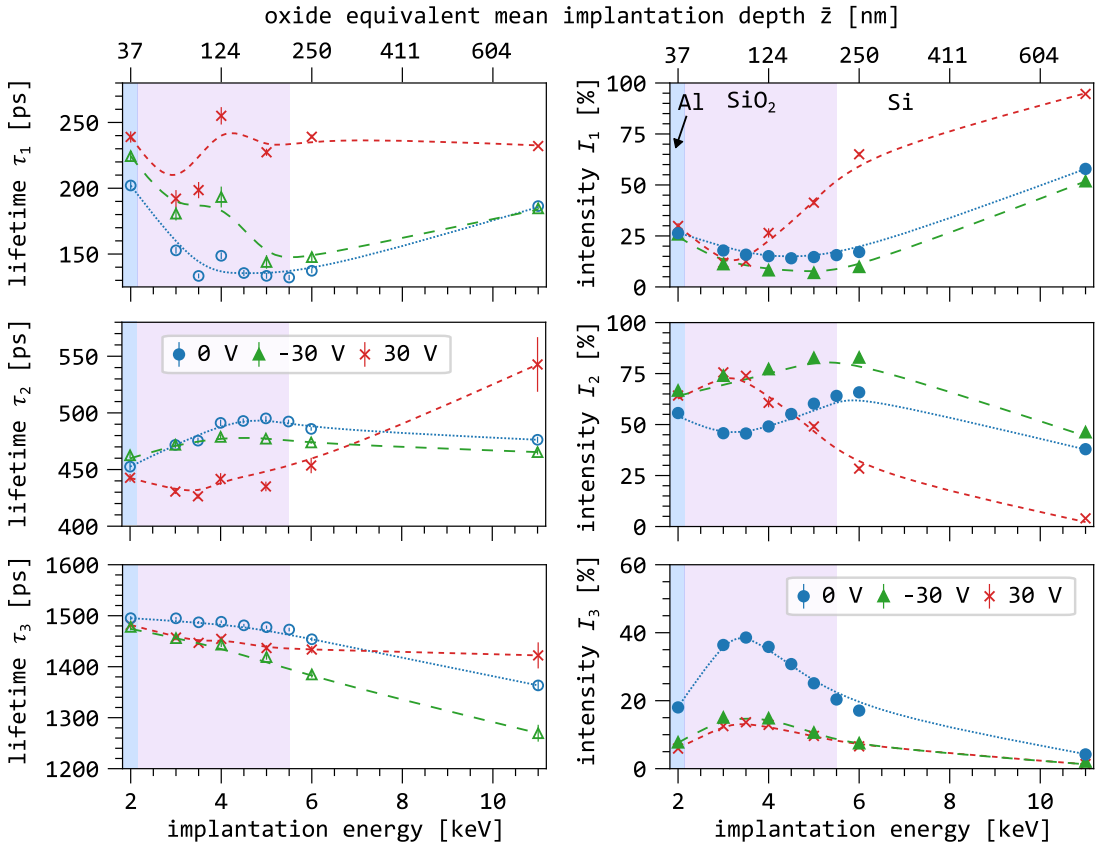

Figure 6.15.: Results of the three-component analysis of the buried oxide lifetime spectra as a function of implantation energy for three different applied gate voltages. As a depth reference, the oxide equivalent mean implantation depth $\bar{z}$ is depicted on the secondary axis. The dashed lines between the data points are guides to the eye. Figure reprinted from [174].

Under **open-circuit conditions** (blue curve), the first lifetime component decreases from 202(2) ps at 2 keV to a minimum of 134(4) ps, then increases for energies above

5.5 keV. Its intensity follows a parabolic trend, with a minimum of 14 % at 4.5 keV. The second component increases from 453(3) ps in the aluminum (2 keV) to 495(2) ps in the oxide, then slightly decreases for higher energies. Its intensity reaches a maximum of 66(1) % at 6 keV, followed by a decrease to 38(1) %. The third component lifetime decreases from 1495(4) ps to 1363(10) ps with increasing energy, while its intensity peaks at 39(1) % in the oxide and drops to 4(1) % at 11 keV.

Under **negative gate bias** (−30 V, green curve), the first component behaves similarly to the open circuit condition but with higher lifetimes between 2 keV and 6 keV. We observe a parabolic intensity minimum at 5 keV and for higher energies, the intensity increases to a maximum of 52(1) % at 11 keV. The second component remains nearly constant between 470 ps and 478 ps, with intensity increasing to 83(1) % at the oxide–semiconductor interface, then decreasing to 46(1) %. The third component lifetime decreases to 1270(17) ps, while its intensity follows a similar trend as under open-circuit conditions, but with a lower peak at 15(1) %.

With a **positive gate bias** (30 V, red curve), the first component reaches a minimum of 192(7) ps at 3.5 keV, then increases up to 240 ps. Its intensity drops to 12(1) %, then rises to 95(1) % at the highest energy. The second component stays around 435 ps below 5.5 keV and increases to 543(24) ps, with intensity peaking at 75(1) % before dropping to 4(1) %. The third component lifetime decreases moderately to 1422(25) ps, and its intensity remains similar to the negative bias case, with a slightly lower maximum of 13(1) %.

Figure 6.15 unambiguously shows the effect of the electric field on the lifetime components as a function of implantation energy. The blue curve (0 V) serves as a reference, showing how the annihilation characteristics change when positrons are influenced only by diffusion and small internal electric fields. In the oxide, the diffusion is very limited with a diffusion length of ≈ 10 nm [178], and thus, oxide-thermalized positrons annihilate close to their location of thermalization when no field is applied. We can summarize the annihilation states based on their energy as follows:

1. free positron annihilation in the Al-gate for $E_{\text{imp}} \leq 2$ keV.
2. positronium and free positron annihilation in the oxide between 2 keV $\leq E_{\text{imp}} \leq 5$ keV.
3. free positron annihilation in the substrate for $E_{\text{imp}} \geq 5.5$ keV.

All lifetimes and intensities from the different gate voltage conditions show a similar starting point at 2 keV. However, the variation in τ and I is the first indicator of a positron drift. This can be concluded from the fact that a fraction of positrons is already implanted into the oxide and subsequently drifts toward one of the interfaces. The lifetimes and intensities for energies between 2.5 keV and 4.5 keV can be attributed to positrons mainly annihilating in the oxide of the MOS capacitor.

For 0 V, the intensity of the o-Ps component is highest, effectively reducing the contribution of the other two annihilation states. When a gate voltage is applied, the intensity of the o-Ps component reduces significantly by $\approx 60\,\%$. This decrease depends only on the electric field strength and not on the direction. We can conclude that the application of the electric field greatly inhibits the formation of o-Ps.

Another observation in Figure 6.15 is the deviation of I_1 and I_2 at around 3.5 keV for the two biased measurement. First, they show the same trend, suggesting that positrons see the same amount of defects, but with different defect sizes. This suggests that vacancy clusters might be the main defect type in the SiO_2 layer. The size of these vacancy clusters varies with the location of positron annihilation within the oxide. They become smaller as the positrons annihilate closer to the SiO_2/Si interface.

In Figure 6.15 above 3.5 keV, the intensities, I_1 and I_2, of the 30 V measurement starts to differ from the −30 V measurement. With increasing implantation energy, a larger fraction of positrons is implanted into the silicon substrate. This fraction then drifts in the near-surface electric field of the silicon layer. For negative gate voltages, the positrons in the oxide still drift to the gate electrode, and positrons in the substrate get drifted back to the SiO_2/Si interface, increasing the intensity I_2 of vacancy clusters present at the interface. For positive gate voltages, positrons in the oxide get drifted to the SiO_2 interface, and substrate-implanted positrons get drifted into the silicon bulk. However, the increase in positron fraction in the substrate alone does not fully explain the intensity change between 3.5 keV and 4 keV:

The positron fraction, F_{ox}, that stops in the oxide remains constant at approximately 80 % for both energies. The positron fraction, F_{Si}, stopping in the silicon substrate increases by 6 % from 3.5 keV to 4 keV. This increase is smaller than the observed change in intensity, $\Delta I_1 \approx 14(1)\,\%$, from 12(1) % to 26(1) %. Therefore, the rise in intensity cannot be attributed solely to annihilation in the silicon substrate. Instead, this change likely includes contributions from annihilation within the oxide. Given its dependence on both implantation depth and electric field strength, this annihilation mode is likely associated with the microstructure near the SiO_2/Si interface.

Above implantation energies of 4.5 keV, the intensity of the first component begins to align with the increasing positron fraction in the silicon substrate, indicating that both lifetimes and intensities are primarily influenced by the electric field in the near-surface region of the silicon layer. At 0 V and −30 V, positrons reach the interface through back-diffusion and drift, respectively. At 30 V, Figure 6.15 clearly shows a trend consistent with defect-free bulk silicon, as positrons are drifted deeper into the substrate.

Doppler Broadening versus Implantation Energy

Doppler broadening measurements are employed in this chapter to obtain information that cannot be derived from lifetime measurements alone or in cases where their interpretation is ambiguous. For instance, previous studies on a similar layer system with approximately half the oxide thickness reported ballistic back-transport of positrons from the silicon layer to the gate [151]. The S–W plot is used to analyze the evolution of the S and W parameter combination as a function of positron energy, thereby providing depth-resolved information. This two-dimensional representation reveals characteristic signatures of the momentum distribution of the annihilating electron–positron pairs. Specific points in the 2D map correspond to distinct regions, such as SiO_2, the interface, or the silicon substrate. For a depth scan across a two-layer system, the measured S and W values represent a linear combination of the respective layer values, weighted by the positron implantation probability (see Section 2.1.2). Consequently, as the positron energy increases, the transition from one material to the other appears as a straight line connecting their characteristic S–W points.

Figure 6.16 shows the S–W plot of the MOS system under three voltage conditions, $-18\,\mathrm{V}$, $-1\,\mathrm{V}$, and $18\,\mathrm{V}$, with the direction of increasing implantation energy indicated. These voltages correspond to the same characteristic bias conditions used in the PALS experiment; however, slightly different values were applied here, as the measurements were performed at VEP using a different power supply. Although the absolute gate voltages differ, the relative influence of the drift on the annihilation states allows the distinction of different drift regimes.

Each point corresponds to a pair of S and W values for a given implantation energy, normalized to the mean silicon bulk value. The point at $3.5\,\mathrm{keV}$ (red circle) is chosen as an energy reference, since this energy has the highest implantation probability in the oxide. This reference enables voltage-induced shifts to be traced along the energy trajectory toward characteristic regions in the plot. The implantation energies are marked at the bottom, which, together with the energy direction, facilitates navigation along the S–W trajectory. The characteristic regions should be understood as approximate areas rather than physical points, defined by known start and end positions and by the observed trajectory of the S–W curves. For the interpretation, it helps to have a close look at the S-W points and their individual energy information, and compare how the S-W points are stretched or compressed along the energy direction in line with the drift directions of the positrons.

Under **open-circuit conditions** (blue curve), the MOS capacitor is effectively field-free, and positron transport is governed solely by diffusion. At very low implantation energies, annihilation occurs mainly at the Al surface and in the aluminum gate, defining the starting point of the trajectory. With increasing energy, the trajectory shifts slightly toward the Al/SiO_2 interface and then proceeds linearly into the SiO_2 region, where the reference point (red circle) is located just in front of the oxide.

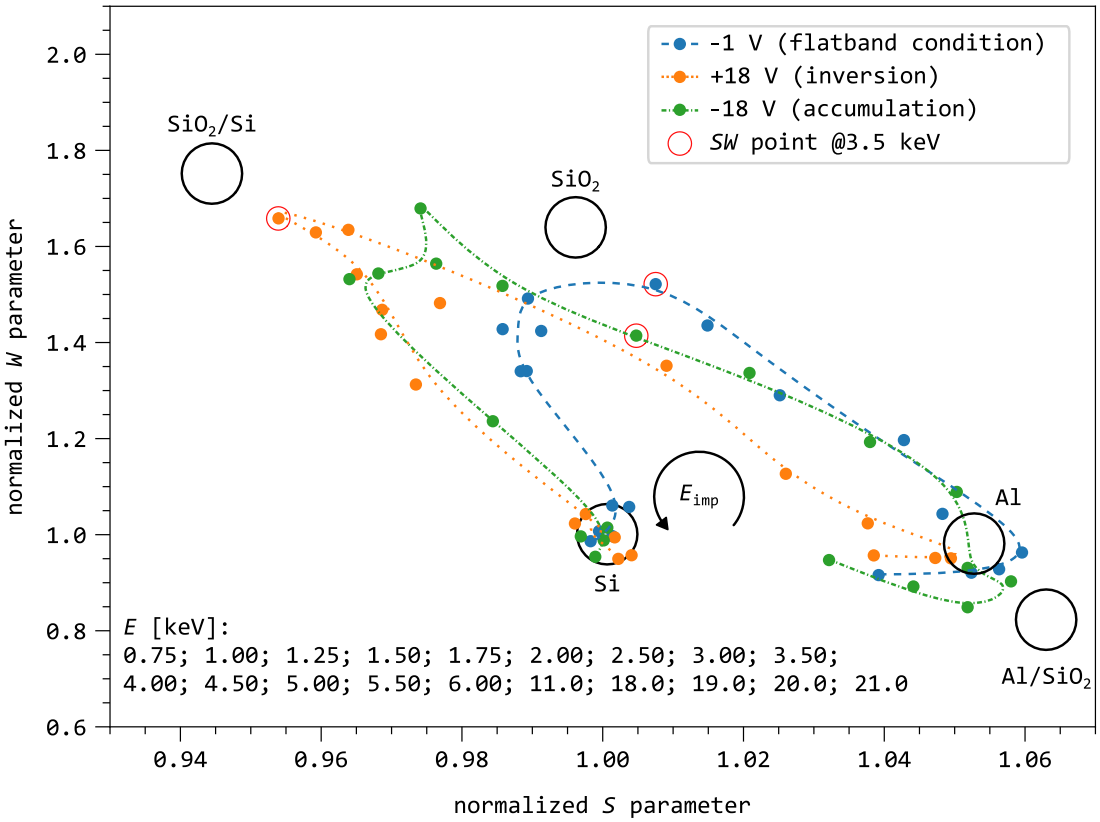

Figure 6.16.: S-W plot of the MOS capacitor under three applied gate voltages ($-18\,\mathrm{V}$, $-1\,\mathrm{V}$, and $18\,\mathrm{V}$). The energy direction, discrete energy steps, and a reference point are indicated for clarity. S and W values are normalized to the mean silicon bulk value.

Between 4 keV and 6 keV, the curve bends toward the SiO_2/Si interface, reflecting the back-diffusion of silicon-implanted positrons, before continuing into the silicon bulk region.

Under **positive voltage conditions** (orange curve), the electric field in the oxide points toward the SiO_2/Si interface, thereby driving oxide-implanted positrons in that direction. This is directly mirrored in the S-W trajectory: as implantation energy increases, positrons are rapidly repelled from the aluminum gate, causing the curve to pass through the oxide and approach the reference point near the SiO_2/Si interface. At higher energies, the increasing probability of positron implantation into the substrate comes into play. Here, the electric field inside the silicon directs positrons into the bulk, and the S-W points at higher energies converge quickly toward the silicon region.

Under **negative voltage conditions** (green curve), the electric field in the oxide points toward the Al/SiO_2 interface, promoting drift-diffusion of oxide-implanted

positrons back to this interface. The trajectory, therefore, resembles that of the flat-band case but shows a weaker approach to the SiO_2 region, as positrons are pulled out of the oxide toward the Al/SiO_2 interface. The reference point thus lies closer to the starting point. With increasing implantation energy, positrons entering the substrate are partially drifted back toward the SiO_2/Si interface, shifting the higher-energy *S*-*W* points in that direction. For instance, the 11 keV *S*-*W* point lies between the SiO_2/Si and Si regions, whereas under the other voltage conditions it is already in the Si region. At even higher energies, the trajectory continues into the silicon bulk. Importantly, if ballistic transport from the substrate back through the oxide into the Al gate is present, the trajectory would bend inside the flat-band curve, moving closer to – or even returning to – the Al region. The clear approach of the SiO_2/Si region observed here demonstrates that substrate-implanted positrons annihilate predominantly at the interface.

In conclusion, the energy-dependent *S*-*W* trajectories align consistently with the expected drift directions imposed by the oxide and substrate electric fields. No evidence of ballistic transport back to the aluminum gate is found.

6.7.3. Bias-dependent Annihilation in the Oxide

The energy-dependent data in Figure 6.15 reveal changes in annihilation characteristics that depend on both implantation depth and applied gate voltage. The voltage dependence is likely linked to positron drift and the resulting shift to different annihilation sites, such as the SiO_2/Si interface. To resolve the field-induced variations in the relative contributions of Ps and free e^+ annihilation, we analyze how the three lifetime components vary with the gate voltage U_g.

The oxide field is ideally uniform across the oxide layer and thus it can be estimated as $E_{ox} = U_g/d_{ox}$, where d_{ox} is the oxide thickness. The calculated oxide fields are listed in Table 6.4.

U_g [V]	−30	−17	−10	−1	0	1	10	19	30
E_{ox} [MVcm^{-1}]	−1.62	−0.89	−0.51	−0.01	0.05	0.11	0.61	1.11	1.72

Table 6.4.: Summary of selected applied gate voltage steps and their corresponding electric field over the 180(10) nm oxide layer.

Figure 6.17 presents the results of the lifetime analysis at an implantation energy of 4 keV. Figure 6.13 may be consulted to recall the implantation profile in the MOS capacitor. At this energy, the mean implantation depth lies approximately in the middle of the SiO_2 layer, with about 80 % of the positrons implanted in the oxide, thereby maximizing the fraction affected by drift. The secondary axis

indicates the corresponding electric field in the SiO_2 layer, derived from the applied gate voltage. The different drift regimes (see Section 3.4) are indicated by colored regions: red – drift toward the Al/SiO_2 interface; white – flat-band region with no distinct drift direction; blue – drift toward the SiO_2/Si interface.

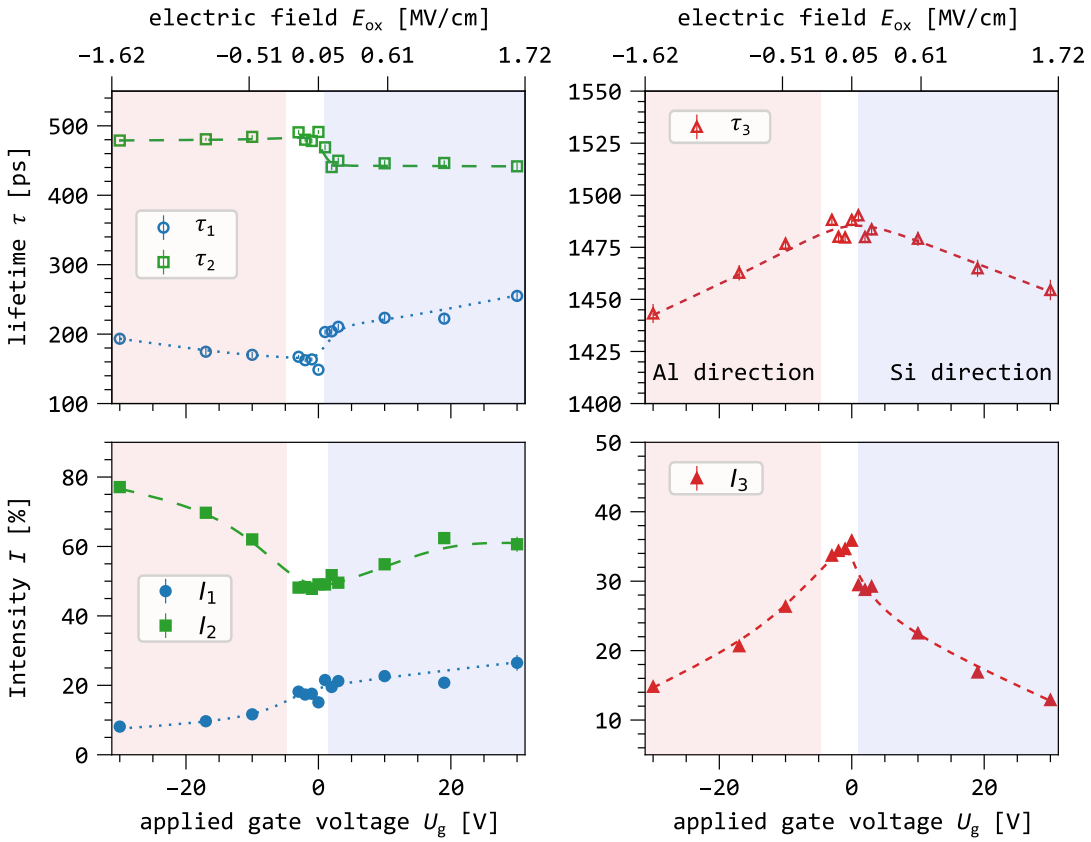

Figure 6.17.: Results of the three-component analysis of the lifetime spectra as a function of the applied gate bias at 4 keV. The drift directions are divided into Al direction (red), flat-band range (white), and Si direction (blue). The theoretical electric field across the oxide is shown on the secondary axis. The experimental data are also presented in Table A.2. Figure reprinted from [174].

The shortest lifetime component (blue dots) shows a distinct minimum of $\tau_1 = 149(5)$ ps at $U_g = 0$ V. With increasing drift toward the Al gate (from $U_g = -30$ V to 0), τ_1 rises to 195(8) ps. In the opposite drift direction, toward the Si substrate, it increases more sharply, reaching 203(4) ps at $U_g = 1$ V and up to 255(7) ps at 30 V. The corresponding intensity I_1 grows steadily from 10(2) % at −30 V to 23(2) % at 30 V.

The intermediate lifetime (green squares) remains comparatively stable. It averages $\tau_2 = 483(9)$ ps for negative voltages and flat-band, decreases in the flat-band range to

445(10) ps, and stays constant for positive voltages. Its intensity I_2, however, varies strongly: it drops from 77 % at −30 V to 48 % at −3 V, stabilizes around 49 % in the flat-band range, and then increases again, saturating at ≈ 60 % for U_g = 20–30 V.

The longest lifetime (red triangles) peaks at τ_3 = 1490(5) ps near the flatband condition and decreases symmetrically by about 3 % in both drift directions. Its intensity I_3 likewise falls with field strength, from 36 % at 0 V to 15 % at −30 V and 13 % at 30 V, respectively.

Drift transport in SiO_2

Two key considerations govern the drift in the oxide layer of the MOS capacitor. First, the electric field can only act on free positrons, not localized in defects or bound in positronium. Second, the difference in positron affinities between the oxide and the adjacent layers creates a potential step that confines positrons within the oxide [153, 181, 182]. Thus, the kinetic energy gained from the electric field used in this experiment is insufficient to overcome this drift barrier with at least $\Delta E \approx 4\,\mathrm{eV}$.

Transport estimates can be made by analogy with charge carriers in semiconductors or metals. The transit time t_d for a free positron to traverse the 180(10) nm oxide layer in an electric field of $1.6\,\mathrm{MVcm^{-1}}$ can be calculated using the mobility from Section 6.7.2, $\mu_+ = 0.12(3)\,\mathrm{cm^2V^{-1}s^{-1}}$. This yields a drift velocity of $v_d = 1.9(5) \times 10^3\,\mathrm{ms^{-1}}$ and a corresponding transit time of t_d = 94(24) ps. Although this value is longer than the estimate reported in [174], which was based on the upper-limit mobility from [152], it remains significantly shorter than the typical positron lifetime in the oxide. Therefore, at this electric field strength, positrons can traverse the oxide layer within their lifetime, provided they are not trapped at defects.

Energy-loss events are essential for positron trapping, as positrons must shed enough energy to fall into a defect's potential well. The electric field contributes only a small fraction of the total positron kinetic energy, about 0.04 % for the mobility used in this work ($\mu_+ = 0.12\,\mathrm{cm^2V^{-1}s^{-1}}$), and roughly 5 % for the higher mobility of $\mu_+ = 1.2\,\mathrm{cm^2V^{-1}s^{-1}}$ reported by Petkov et al. [152]. Consequently, the de Broglie wavelength remains essentially unchanged, and trapping is not expected to be affected by drift.

The experimental results, however, show a significant change in annihilation characteristics even at moderate fields (see Figure 6.17). This effect has been attributed to elastic scattering dominating over inelastic processes, such as the excitation of transversal optical phonons [152]. Since typical acoustic phonon energies are only a few meV, each scattering event causes limited energy loss, requiring multiple interactions before a positron can be trapped at a defect site. Simultaneously, the electric field accelerates positrons between scattering events, reducing the trapping

probability by generating a net current away from defect sites. For weak electric fields, such as in the flat-band range of Figure 6.17, the drift effect is explained by the transport of epithermal positrons, which shifts the implantation profile before thermalization is complete [152].

Discussion of positron drift effects on positronium formation

First, a comparison is made between o-Ps annihilation in the bare oxide and the buried oxide at an applied gate voltage of 0 V. The o-Ps contribution is maximal when the fraction of oxide positrons is largest, and the internal electric field is minimal. The small variation in lifetime ($\approx 5\,\%$) between the buried ($\tau_3 = 1490(5)\,\mathrm{ps}$) and bare oxides ($\tau_3 = 1558(3)\,\mathrm{ps}$) at 0 V indicates that the o-Ps pick-off process is similar for both. In contrast, the large relative difference in intensity ($\approx 16\,\%$) suggests suppression of o-Ps annihilation in the buried oxide, likely due to two factors: the intrinsic electric field at 0 V and the fraction of positrons not thermalized inside the oxide.

Application of a gate voltage strongly reduces o-Ps annihilation, independent of polarity, as seen in the decrease of o-Ps intensity, I_3, in Figure 6.17. The intensity drops by 64 %, from $I_3 = 36(1)\,\%$ to $13(1)\,\%$. This reduction can be explained by charge separation, where the electric field separates free electrons generated during positron thermalization from the positron before positronium formation can occur [83]. The change in o-Ps lifetime is minor ($\approx 2\,\%$). A proportional reduction is expected for para-positronium (p-Ps) intensity. Figure 6.17 confirms this for negative voltages, but for positive voltages, I_1 increases, indicating an alternative annihilation process as positrons drift toward the SiO_2/Si interface. The increase in τ_1 for both polarities to above 125 ps suggests the emergence of a previously hidden annihilation state. The asymmetry in I_1 implies this defect occurs preferentially near the SiO_2/Si interface.

The continuous reduction of o-Ps annihilation is observed as the internal field in the SiO_2 layer exceeds $\approx 0.2\,\mathrm{MV/cm}$ (Table A.2), consistent with earlier studies in α-SiO_2 and polymer materials [83, 183]. Ps suppression aligns with an internal field that hinders Ps formation either during thermalization or trapping. However, lifetime spectra alone cannot unambiguously determine the dominant process.

Discussion of positron drift effects on free positron annihilation

As discussed in the previous section, suppression of positronium formation by the drift effect generates free positrons that can be trapped in defects. This is reflected in the increase of the vacancy cluster component intensity, I_2, for both drift directions (Figure 6.17). An increase in the short component is also observed for positive gate voltages, indicating that an unresolved defect-related lifetime overlaps with p-Ps

annihilation and cannot be distinguished by the conventional lifetime analysis from Equation (2.2). To address this, the simple model from Equation (6.1) is applied to extract the unresolved lifetime (τ_1') and intensity (I_1') from the short component. Figure 6.18 presents the estimated τ_1' and I_1' across the full gate voltage range, with calculated values listed in Table A.3.

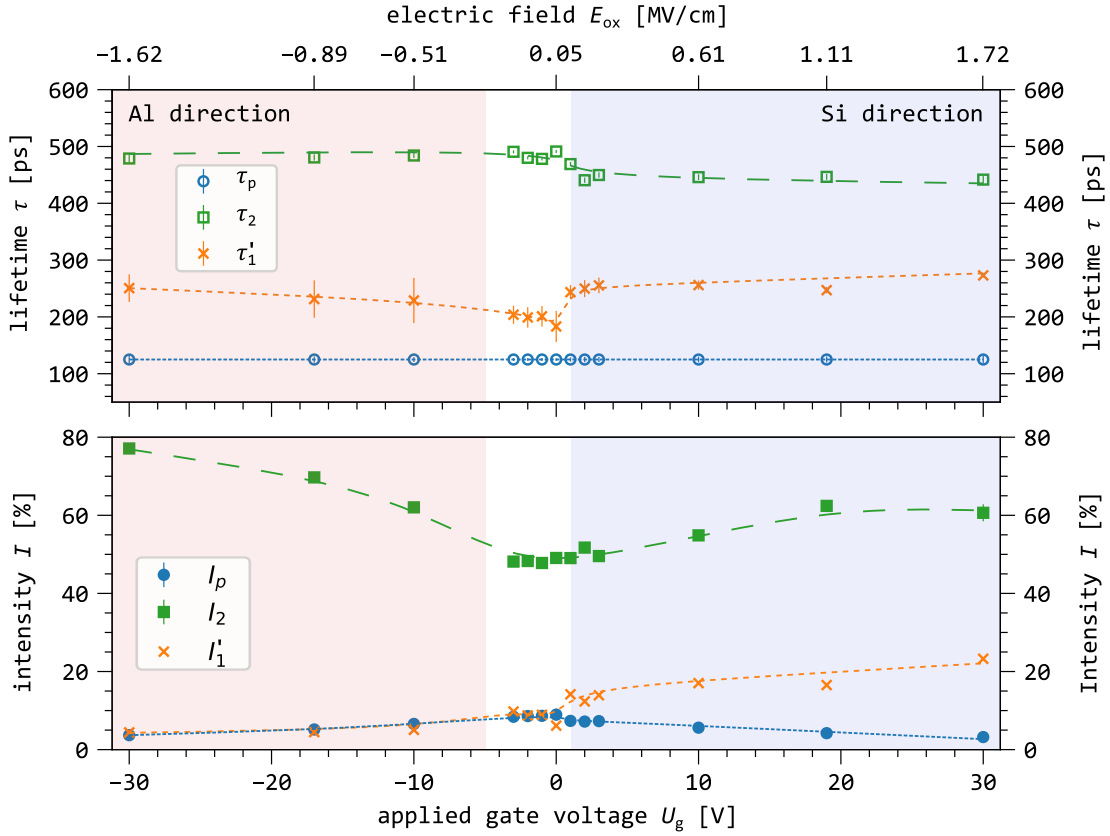

Figure 6.18.: τ_p (blue, p-Ps), τ_2 (green) and intensities I_p, I_2 as a function of the gate voltage U_g at an implantation energy of 4 keV, where positrons are mainly implanted into the SiO_2 layer. The estimated oxide component, τ_1' and I_1' from Equation (6.1), is shown in orange. The drift directions are divided into Al direction (red), flat-band range (white), and Si direction (blue). The dashed lines are eye-guides. Figure reprinted from [174].

The observations in Figure 6.18 can be divided into three regions, corresponding to different positron drift regimes:

Al direction ($-30\,\mathrm{V} \leq U_g \leq -10\,\mathrm{V}$): τ_1' is quasi-constant with an average lifetime of 301(7) ps and intensity $I_1' = 2.8(3)\,\%$. The medium oxide component also remains steady with $\tau_2 = 481(2)$ ps, while I_2 decreases from 77.1(5) % to 62.0(3) %.

Flat-band range ($-3\,\mathrm{V} \leq U_\mathrm{g} \leq 0\,\mathrm{V}$): τ_1' and I_1' remain quasi-constant at 236(2) ps and 5(2) %, respectively. The medium oxide component shows similar stability with $\tau_2 = 485(5)$ ps and $I_2 = 48(4)$ %.

Si direction ($1\,\mathrm{V} \leq U_\mathrm{g} \leq 30\,\mathrm{V}$): τ_1' is quasi-constant at 274(7) ps, while I_1' rises from 10.8 % to 21.7 %. The medium oxide lifetime τ_2 remains near 445(5) ps, and I_2 gradually increases from 49(20) % at 1 V to 61(2) % for $U_\mathrm{g} \geq 20\,\mathrm{V}$.

Both lifetimes remain below the average positronium lifetime of 500 ps at all gate voltages [34]. The variations of these components with the applied electric field indicate that free positrons probe distinct electronic environments within the amorphous SiO_2 network.

6.7.4. Bias-dependent Annihilation in the Substrate

Positron drift is also observed when positrons are implanted into the buried silicon substrate of a metal-oxide/Silicon (MOS) capacitor: positrons diffuse back to the SiO_2/Si interface, where they annihilate. As the implantation depth increases, fewer positrons reach the interface via back-diffusion, reducing their influence on the measured spectra. By applying a gate voltage, the electric field in the near-surface region of the buried silicon can be tuned, modifying drift in addition to diffusion and thereby enhancing or suppressing positron transport to the interface.

To investigate the drift behaviour, we measured the MOS capacitor at a positron implantation energy of 11 keV while varying the gate voltage from −30 V to 30 V. Figure 6.19 presents the results of the three-component lifetime spectra decomposition as a function of gate voltage. At this energy, about 92 % of positrons are implanted into the silicon substrate, with the remaining 8 % stopping in the Al gate or the SiO_2 layer.

The red and blue shaded areas in Figure 6.19 indicate the operating regimes (Figure 3.3) of the MOS capacitor and the corresponding electric field directions. In the red region (**accumulation mode**), positrons are driven toward the SiO_2/Si interface, while in the blue region (**inversion mode**), the drift is toward the silicon bulk. The intermediate white region marks a narrow flat-band region between those regimes, where the drift velocity changes its direction from the interface to the bulk.

The lifetime of the first component, τ_1, has a mean value of 185(2) ps in accumulation mode and rises sharply to 232(2) ps in depletion/inversion mode. The corresponding intensity, I_1, increases from 52 % in accumulation to 95 % in inversion, with a rapid change between 0 V and 1 V. The second component, τ_2, increases from 467(4) ps to 524(49) ps across the same range, while its intensity, I_2, drops from 46 % to 4 %, showing a sharp decrease in the transition region. The third component, τ_3, ranges from a minimum of 1270(16) ps in accumulation to a maximum of 1422(26) ps in inversion, with its intensity, I_3, symmetrically decreasing around 0 V and reaching

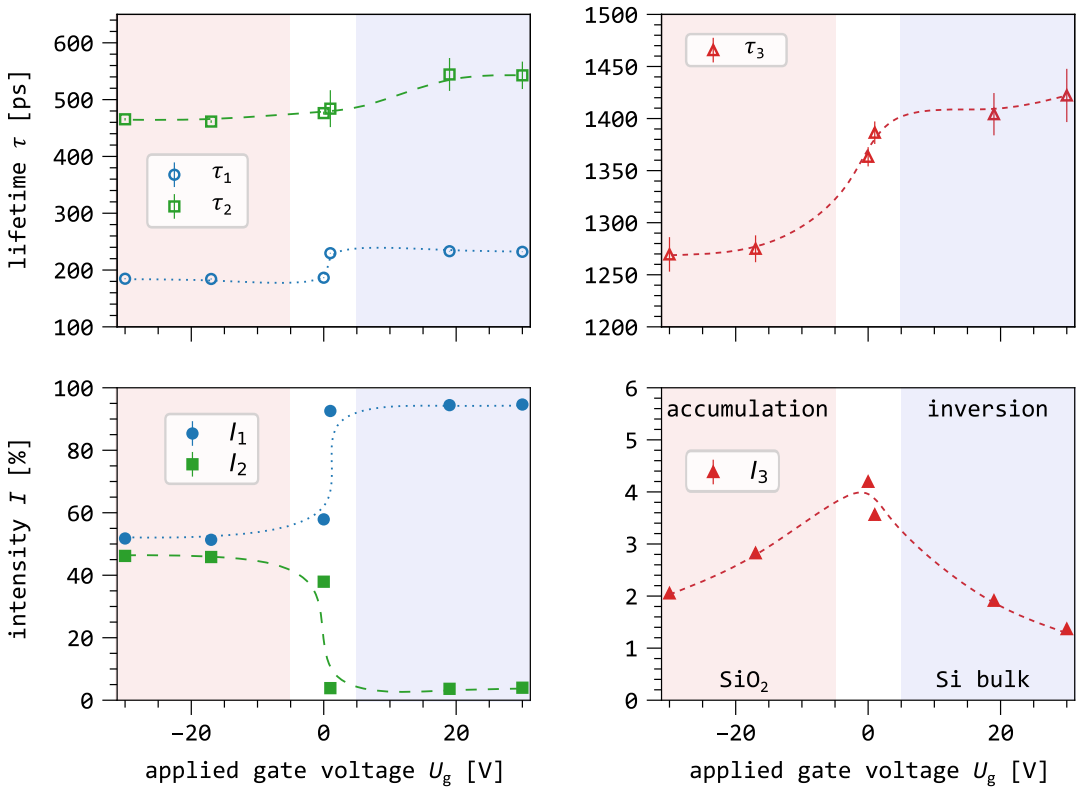

Figure 6.19.: Three-component decomposition of the lifetime spectra at an implantation energy of 11 keV as a function of the gate voltage U_g. The red and blue shaded regions indicate the general direction of the electric field: toward the oxide-substrate interface in the red region and the substrate bulk in the blue region. The lines connecting the data points are only to guide the eye. Figure reprinted from [165].

a maximum of 4 %. Table A.4 in the Appendix summarizes the three-component lifetime analysis results.

e^+ transport in the silicon substrate

The transport of positrons in the silicon substrate near the SiO_2/Si interface can be analyzed in a manner analogous to the oxide case. For illustration, the reader is referred to Figure 6.13, presented at the beginning of this chapter, which shows the positron implantation profile and the electric field distribution in the near-surface region of the silicon. It is evident that positron drift is strongly influenced by the electrical state of the MOS capacitor, as the electric field distribution varies significantly, altering its overlap with the positron implantation profile. For the analysis of positron transport in the silicon substrate, the transport parameters

derived in Section 6.5 are used. These parameters, including the effective diffusion length l^+ and mobility μ_+, provide the basis for quantifying the drift and diffusion behavior of positrons under different gate voltage conditions.

e^+ drift in inversion and depletion mode

In the depletion and inversion modes, the electric field points from the SiO_2/Si interface toward the bulk of the substrate. This field adds a directed drift component to the otherwise random diffusion of positrons, producing a net current away from the interface. As a result, a strong diffusion barrier forms, suppressing back-diffusion to the interface even at relatively low field strengths.

Under depletion conditions, a mean electric field of $\langle E \rangle = 5 \times 10^3\,\mathrm{Vcm}^{-1}$, the mean drift velocity is $\langle v_\mathrm{d} \rangle = 1.8 \times 10^3\,\mathrm{ms}^{-1}$ (Equation (2.21)). Using this velocity, the mean drift length for positrons with a lifetime of $\tau_\mathrm{b} = 221\,\mathrm{ps}$ can be calculated as 390 nm (Equation (2.22)), which is two orders of magnitude greater than the interfacial region thickness. Consequently, even positrons implanted close ($\sim 1\,\mathrm{nm}$) to the interface are efficiently swept into the bulk before losing sufficient kinetic energy to become trapped.

Under inversion conditions, the electric field extends mostly linearly across the depletion region, which reaches a maximum width of w_max. Closer to the interface – within approximately 40 nm (see Figure 6.13), where minority charge carriers are collected – the field strength increases sharply, reaching an average value of $\langle E \rangle = 2.7 \times 10^5\,\mathrm{V/cm}$ (see Table 6.3). This is about two orders of magnitude higher than the mean field in the depletion layer. Such a strong near-interface field effectively shields the interface and prevents most positrons from reaching it. As in the oxide, positron trapping in semiconductors occurs primarily via acoustic phonon scattering, which involves multiple successive collisions near a defect to disperse the binding energy of the defect [35]. Consequently, under the high field conditions, the probability of positron trapping at the interface is strongly reduced.

This behavior is clearly observed in the 11 keV data (Figure 6.19). As the gate voltage increases from the transition region to positive values (blue region), the lifetime component τ_1 rises sharply to values near the bulk lifetime of defect free silicon, 221 ps, accompanied by an increase in its intensity, I_1, to approximately 95 %. Simultaneously, the intensity of the second component, I_2, decreases and nearly vanishes. The persistence of the second and third lifetime components, even at high implantation energies, is attributed to positrons still implanted in the preceding layers, resulting in annihilation within the aluminum gate or the SiO_2 layer. These trends – the convergence of τ_1 toward τ_b, the increase of I_1, and the reduction of I_2 – confirm that positrons are effectively drifted away from the oxide/substrate interface and into the bulk of the substrate.

e^+ drift in accumulation mode

At negative gate voltages applied to the aluminum gate, the electric field is directed toward the SiO_2/Si interface, promoting positron transport back to the interface via drift. The maximum possible drift distance, calculated using Equation (2.25) and the parameters listed in Table 6.3, is approximately 240 nm (see Figure 6.3). This distance represents an approximate range over which the electric field can effectively influence positron motion. When combined with the effective diffusion length in silicon, $l_0^+ = 141(20)$ nm, the estimated total range from which positrons can reach the interface is about 380 nm. However, the limited overlap between the positron implantation profile and this drift–diffusion range (Figure 6.3) suggests that fewer than half of the implanted positrons reach the interface before annihilation.

The C-V measurements show that accumulation is fully established below $U_g \approx -8\,V$ (see Figure 6.2), meaning the field-affected region does not grow with more negative voltages. Therefore, for both $-17\,V$ and $-30\,V$, we assume that the same number of positrons are affected by the drift. This saturation effect is reflected in the results shown in Figure 6.19 at negative voltages.

The effect of positron drift toward the interface ($U_g < 0\,V$) is clearly visible in the data as an increase in the intensity I_2 of the longer-lived lifetime component, τ_2. This increase indicates that more positrons annihilate at the interface or in near-interface defects, rather than in the bulk, consistent with the enhanced back-diffusion under accumulation conditions.

The decrease in τ_1 near the flat-band condition cannot be explained by annihilation in defect-free silicon alone. Based on earlier drift experiments, we consider the following scenarios for positron back-drift:

1. Trapping at the SiO_2 interface [149]: The interface acts as an efficient positron sink, and all positrons that reach the interface annihilate there. This provides the most consistent explanation for the observed lifetime behavior. As the gate voltage becomes more negative, I_1 decreases sharply while I_2 increases, indicating enhanced trapping of positrons at interface defects. Since effective drift to the interface is only possible for a fraction of the positrons implanted into the substrate, this results in a reduced bulk lifetime (see Section 2.3.3).

2. Transport to the gate over the oxide [151]: It was shown that positrons can pass through the interface and annihilate in the gate material. However, we detect no lifetime around 265 ps, which would correspond to the annihilation signature observed in the Al-gate. Such a signal would be expected with an intensity $\approx 25\,\%$. Thus, we can exclude this case.

3. Drift from the silicon into the oxide toward the Al/SiO_2 interface [152]: Here, substrate implanted positrons can surpass the interface and are subsequently affected by the oxide-field, which drives the positrons further toward the

Al/SiO_2 interface. If strong electric fields were driving positrons from the substrate into the oxide and further toward the aluminum gate, the lifetime components at 0 V (weak fields) and −30 V (strong fields) would differ significantly, since the annihilation characteristics at the Al/SiO_2 interface and the SiO_2/Si interface are distinctly different (compare to Figure 6.17). Because no such differences are observed, this scenario can be excluded.

These results suggest, that both components arise, at least in part, from annihilation at or near the SiO_2/Si interface.

6.7.5. Positron Drift–Derived Microstructure

Microstructure of the buried oxide

Analyzing the influence of positron drift on the lifetime spectra enables insights into the microstructure of the oxide that are not accessible under zero-field conditions, where o-Ps annihilation dominates the spectra and obscures other annihilation channels.

In Figure 6.18, the correlation of the lifetime components (τ_1', I_1', τ_2 and I_2) with the gate voltage U_g is consistent with the existence of positron annihilation states in the oxide arising from two categories of subnanometer void populations:

- Population of smaller defects V_s related to τ_1' and I_1'.
- Population of larger defects (voids) V_b related to τ_2 and I_2.

The strength and direction of the electric field influence the type of voids where positrons annihilate. At higher electric fields, between 0.5–1.7 MV/cm, the size of the open spaces in the two types of subnanometer voids tends to be smaller when positrons drift toward silicon (Si) compared to drift toward aluminum (Al). This is shown by shorter lifetimes related to V_s and V_b when the gate voltage changes from negative to positive gate voltages. For the smaller voids (V_s), the lifetime increases by 9%, accompanied by an intensity increase of up to ≈700%. In contrast, for the larger voids (V_b), the lifetime decreases by 7%, while the intensity drops by approximately 24%. This difference in void size and its effect on positron annihilation shows that the electric field gives insight into uneven distributions of the subnanometer voids. As the internal field strength decreases from the Al direction to the flat-band range, the lifetime τ_1' linked to the V_s voids drops clearly, from 301 ps to 239 ps. This decrease of approximately 20% remains unclear.

As previously stated in this segment, free positrons exhibit a higher capture rate in the smaller void population (V_s) when drifted towards the SiO_2/Si interface than when drifted towards the Al/SiO_2 interface. This behavior can have multiple possible explanations.

One is the gradual densification along the oxidation direction, from the surface into the bulk or from the Al/SiO_2 interface to the SiO_2/Si interface [184]. Another possibility is enhanced trapping in near-interface defects, such as silicon dangling bonds (P_b centers) [103, 104]. P_b centers at the interface of thermally oxidized, p-doped Si(100) have already been identified as possible interface defects using two-dimensional angular correlation spectroscopy (2D-ACAR) [185]. Two mechanisms may explain the increase in intensity I_1'. First, positron drift could simply transport more positrons to the interface region, leading to increased trapping at P_b centers. Second, electrons accumulated on the silicon side in inversion may change the charge state of P_b centers through charge carrier trapping. Since positrons are insensitive to positively charged defects, this charge state switching could increase trapping by converting previously positive P_b centers into effective trapping sites. However, based on current data, a definitive explanation for the increase in the intensity of the small void population cannot be given.

In summary, when the electric field is strong enough to suppress positronium formation, the open volume size and the density of voids primarily govern free positron trapping and annihilation. In cases where positronium annihilation dominates, other annihilation channels remain hidden. These channels become accessible only when the positron drift reduces the formation probability of positronium.

Microstructure of the Interface

When positrons are drifted from the silicon side (Figure 6.20, right column), a similar void-like component appears with $\tau_{2,si} = 465(2)$ ps compared to the drift from the oxide side (Figure 6.20, left side). Density Functional Theory calculations revealed that this lifetime corresponds to large vacancy clusters in silicon comprising more than 14 vacancies [186]. The observed 23(5) ps difference between the two directions suggests variation in the local electronic environment at the annihilation sites, depending on whether the positron annihilates on the oxide or silicon side of the interface. On the oxide side, a higher oxygen concentration likely modifies the electronic structure of the voids, possibly through oxygen decoration of the vacancy cluster walls, as proposed by [157]. The higher intensity of this component on the oxide side, approximately 15 %, is further attributed to such clusters being intrinsic defects in the SiO_2, unlike in the defect-free silicon.

The first lifetime component observed during drift within silicon is notably shorter, at 185 ps, than the lowest oxide component (disregarding para-positronium) and the bulk lifetime of silicon. This anomalously low value can only be explained by positron trapping at the interface, reducing the effective bulk lifetime of silicon [46].

The absence of observable interface-related lifetimes (τ_1, 4 keV) during drift from the silicon side may be due to the charge state of the defects. The key distinction between the two drift directions lies in their interfacial electronic state. During

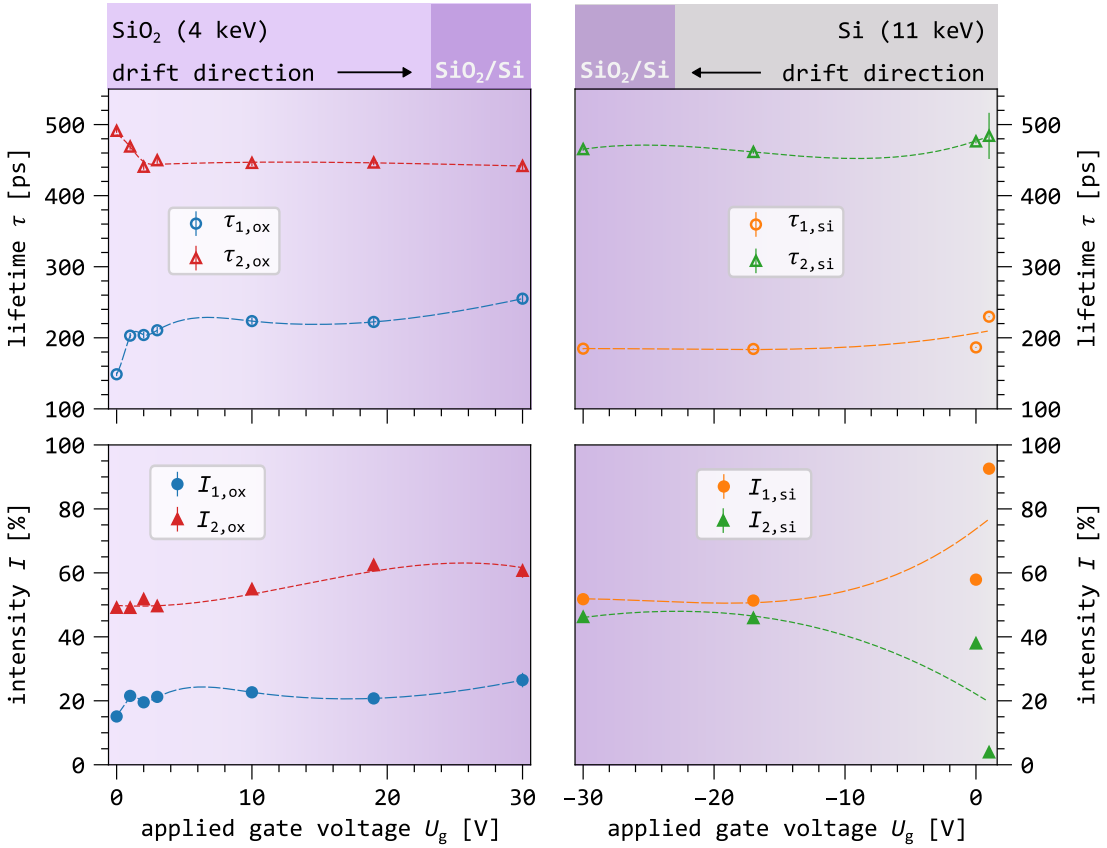

Figure 6.20.: Comparison of lifetime components as a function of the applied gate voltage for oxide-side and silicon-side drift toward the interface. The left column shows the lifetime results for the interface drift from the oxide side toward the SiO_2/Si interface; the right column shows the lifetime results for the drift from the silicon side toward the SiO_2/Si interface. A violet gradient schematically illustrates the influence of the interface on the positron lifetime, with darker shades indicating stronger interface contributions. Figure reprinted from [165].

oxide-side drift (inversion), the MOS capacitor operates in inversion mode, where free electrons at the interface result in negatively charged P_b^- centers, promoting trapping via Coulomb attraction. Conversely, during silicon-side drift (accumulation mode), hole accumulation causes positively charged P_b^+ centers, repelling positrons and reducing their trapping probability.

The results demonstrate that the SiO_2/Si interface exhibits distinct electronic and microstructural characteristics depending on the direction of positron approach. The observed differences in lifetime components highlight the intrinsic asymmetry of the interface, consistent with earlier reports of structural disparities between the oxide and silicon sides [95]. Further insight into the interface structure and positron

drift transport could be gained by extending such experiments to different oxide types (e.g., dry thermally grown, chemically deposited) with varying thicknesses. Equally important is the systematic variation of silicon properties such as doping concentration, doping type, and lattice orientation.

6.8. Conclusion

Drift-assisted Positron Annihilation Lifetime Spectroscopy (PALS) was performed on a Metal-Oxide/Silicon capacitor under gate bias of up to ±30 V. The maximum achieved electric field in the 180(10) nm SiO_2 layer was 1.72 MV/cm. Positron lifetime spectra were recorded as a function of implantation energy and applied gate voltage, and analyzed using a three-component decomposition. The lifetime analysis revealed clear evidence of electric field-induced positron drift within the buried oxide and within the silicon substrate of the MOS capacitor.

The most significant finding was a pronounced suppression of positronium (Ps) formation with increasing field strength, leading to enhanced annihilation of free positrons. This suppression uncovered two distinct populations of subnanometer voids that are otherwise obscured by Ps annihilation. As the electric field increases, the o-Ps contribution diminishes while annihilation in one or both void populations becomes more prominent. Moreover, a clear dependence on the direction of the electric field was observed. Drift towards the Al/SiO_2 interface predominantly enhanced trapping in the larger voids, with a mean lifetime of 481(3) ps. Drift towards the SiO_2/Si interface also increased annihilation in voids, albeit with a shorter mean lifetime of 445(3) ps and thus, slightly smaller compared to the other drift direction. Notably, this drift direction additionally revealed a second, smaller void population, characterized by an average lifetime of 275(7) ps, which did not appear during drift towards the Al interface.

The observed directional dependencies in the lifetimes and intensities indicate spatial inhomogeneities in the distribution of subnanometer voids within the buried oxide layer. This shows the potential of this method for future application on oxide/semiconductor layered systems using novel oxide materials, such as HfO_2 or Gd_2O_5 [32].

Characterizing vacancy-type defects in ultra-thin embedded layers and at buried interfaces is challenging when using conventional low-energy beam-based positron annihilation spectroscopy due to the broad implantation profiles. In this work, we present a proof-of-concept measurement demonstrating how the signal in positron annihilation experiments on such ultra-thin layers or buried interfaces can be enhanced by guiding positrons into the desired regions using externally applied electric fields.

This study shows that the electric field directly influences the annihilation charac-

teristics in the Si-substrate. Under inversion conditions, positrons are transported deeper into the substrate, which is consistent with the lifetime results. During accumulation, a gate voltage-dependent change in the annihilation properties is also observed, deviating from those expected for defect-free silicon. This suggests a back-transport of positrons to the oxide/substrate interface by a drift-diffusion mechanism. The interface annihilation characteristics differ unambiguously from the annihilation characteristics of the bare silicon surface. By comparing the results from the silicon drift to the results in the oxide drift, we can draw a much more detailed picture of the microstructure of the SiO_2/Si interface. The differences in annihilation characteristics for oxide drifted and silicon drifted positrons to the interface, suggest that the defects at the silicon side of the interface are different to those at the SiO_2 side. A possible explanation is charge switching of electronically active defects and chemical differences on both sides of the interface.

In conclusion, drift-assisted positron annihilation lifetime spectroscopy has been shown to be an effective method for characterizing defects at buried interfaces. The methodology is readily applicable to advanced layered material systems under development for thin-film transistor technologies beyond silicon, offering a potential pathway to support the continued scaling envisioned by Moore's law [29].

7. Summary and Outlook

This dissertation has explored the development and application of advanced positron annihilation techniques for the investigation of complex material systems, with particular focus on in-situ environmental control and defect characterization at buried interfaces. Three major lines of work were pursued: the design and commissioning of the TAPIR instrument for temperature–atmosphere controlled positron annihilation studies of polymers (Chapter 4), the upgrade of the PLEPS beamline and target station at FRM-II (Chapter 5), and the demonstration of drift-assisted positron annihilation lifetime spectroscopy (DA-PALS) for probing ultra-thin oxide layers and interfaces in semiconductor devices (Chapter 6). Each represents both a methodological advance and a scientific contribution to the field of positron annihilation spectroscopy (PAS).

The TAPIR instrument was conceived and realized to overcome long-standing limitations in polymer studies, where conventional positron annihilation lifetime spectroscopy (PALS) is generally performed under vacuum and at room temperature. TAPIR enables controlled variation of gas pressure, temperature, and atmosphere, allowing simulation of conditions close to the material's application while maintaining high-quality positron lifetime measurements. Its successful operation was benchmarked through a systematic study of semi-crystalline polystyrene under argon. The experiments revealed that both the size and abundance of free-volume elements (FVEs) are strongly modulated by gas penetration and pressure. In the glassy state, argon-induced plasticization competed with polymer rigidity, producing pressure-dependent changes consistent with the dual-mode sorption model. At higher temperatures, across the glass transition, dynamic FVEs dominated, and the o-Ps lifetime and intensity provided direct evidence of swelling and enhanced molecular mobility. The work demonstrated that gas pressure is not merely an environmental parameter but an active control variable influencing polymer free volume and defect structure. More broadly, the TAPIR platform paves the way for systematic studies of polymers, membranes, and other soft matter materials under technologically relevant conditions such as gas separation, carbon capture, and water desalination.

The Pulsed Low Energy Positron System (PLEPS) has long been one of the most versatile positron beamlines for depth-resolved lifetime measurements. Chapter 5 documented the latest round of upgrades, finalized just before the FRM-II reactor shutdown in 2020. Key improvements included enhanced electrical insulation, re-

fined cable shielding, and modifications to the target station that enabled stable operation at higher implantation energies. As a result, the maximum acceleration voltage was increased from 18 keV to 21 keV, substantially extending the penetration depth accessible to PALS. This is especially significant for studies of high-Z materials such as tungsten and reactor steels, where deeper implantation is necessary to minimize surface contributions and access bulk defect properties. Additionally, the implementation of sample biasing opens new possibilities for experiments involving externally tunable electrostatic conditions. Although the reactor shutdown prevented full exploitation of these upgrades, the documented progress ensures that once operation resumes, the improved PLEPS will be well-positioned to support demanding defect studies in advanced engineering materials.

The final experimental part of this thesis introduced drift-assisted PALS (DA-PALS) as a technique for probing buried interfaces and ultra-thin oxide layers. In semiconductor structures, conventional beam-based PAS is limited by broad implantation profiles, which make it difficult to attribute annihilation signals to nanometer-scale layers. DA-PALS addresses this challenge by using externally applied electric fields to steer positrons toward or away from specific interfaces.

Proof-of-concept measurements on $Al/SiO_2/Si$ capacitors yielded several key insights. First, the suppression of positronium formation under field conditions exposed previously undetectable populations of subnanometer voids in the oxide. Second, strong directional effects were observed: positrons drifting toward the Al/SiO_2 interface predominantly annihilate in large voids with lifetimes of about 480 ps, while drift toward the SiO_2/Si interface reveals two distinct defect populations – large voids with lifetimes of approximately 445 ps and smaller voids with lifetimes of about 275 ps.

Additional experiments examined positron drift within the silicon substrate as the MOS capacitor was biased into accumulation, depletion, and inversion. These results showed that the non-linear electric field in the near-interface region acts as a diffusion barrier during accumulation, but enhances positron transport toward the interface under inversion. A comparison of drift behavior in the oxide and silicon further revealed that the interface annihilation characteristics are asymmetric, likely due to differences in charge states, defect chemistry, and the local electronic environment on either side of the interface.

Together, these findings establish DA-PALS as a sensitive and interface-specific probe of defect structures, with direct relevance to device scaling. As field-effect transistors advance toward thin-film configurations, two-dimensional integrated devices, and gate-all-around architectures, reliable characterization of interface defects will become increasingly critical for ensuring performance and reliability. DA-PALS offers a promising pathway to meet this emerging need.

The advances presented in this dissertation suggest several promising directions for

future research. For soft matter and polymer systems, TAPIR can be extended to investigate a broader range of gas atmospheres, including reactive species such as CO_2, H_2, CH_4, water vapor, or complex gas mixtures, thereby directly connecting positron annihilation spectroscopy with processes of industrial relevance. In addition, further development of TAPIR should focus on enhancing its operational precision. In particular, improvements to the gas circuit and sealing design would enable more accurate control of atmospheres at pressures below 1 atm, as well as stable operation in humid or vapor-rich environments. This would significantly broaden the range of accessible conditions and allow experiments that closely mimic real-world application scenarios. Combining TAPIR experiments with complementary techniques such as permeability measurements would yield a more complete picture of gas–polymer interactions and defect dynamics.

For PLEPS, the design improvements described here should serve as a blueprint for future beamline upgrades worldwide, especially at emerging positron sources. Higher implantation energies and sample bias control will be indispensable for extending PAS studies to materials with high atomic numbers, such as plasma-facing wall materials in nuclear fusion engineering.

For semiconductor interfaces, DA-PALS opens a new experimental window that should be applied systematically to a wider variety of oxide dielectrics, substrate types, and doping configurations. Particularly compelling would be comparative studies of SiO_2, HfO_2, and novel high-k oxides in contact with silicon or two-dimensional semiconductors, such as transition-metal chalcogenides or oxide semiconductors.

In summary, the methodological innovations and experimental demonstrations presented across Chapters 4-6 demonstrate the versatility of positron annihilation spectroscopy when coupled with environmental control and external field manipulation. Together, they broaden the range of material systems accessible to PAS, deepen our understanding of polymer free volumes and semiconductor interfaces, and provide powerful tools for advancing both soft matter applications and next-generation electronic devices.

Bibliography

[1] P. A. M Dirac. "The Quantum Theory of the Electron". In: *Proc. R. Soc. Lond. A* 117 (1928), pp. 610–624. DOI: 10.1098/rspa.1928.0023.

[2] C. A. Anderson. "The Positive Electron". In: *Phy. Rev.* 43 (1933), pp. 491–494. DOI: 10.1103/PhysRev.43.491.

[3] R. A. Ferell. "Theory of Positron Annihilation in Solids". In: *Rev. Mod. Phys.* 28 (1956), pp. 308–337. DOI: 10.1103/RevModPhys.28.308.

[4] R. E. Bell and R. L. Graham. "Time distribution of Positron Annihilation in liquids and Solids". In: *Phys. Rev.* 90 (1953), pp. 644–654. DOI: 10.1103/PhysRev.90.644.

[5] A. Vehanen, P. Hautojärvi, J. Johansson, and J. Yli-Kauppila. "Vacancies and carbon impurities in α-iron: Electron irradiation". In: *Phys. Rev. B* 25 (1982), pp. 762–780. DOI: 10.1103/PhysRevB.25.762.

[6] C. Hugenschmidt, K. Schreckenbach, M. Stadlbauer, and B. Straßer. "First positron experiments at the NEPOMUC". In: *Appl. Surf. Sci.* 252 (2006), pp. 3098–3105. DOI: 10.1016/j.apsusc.2005.08.108.

[7] P. Sperr, W. Egger, G. Kögel, G. Dollinger, C. Hugenschmidt, and C. Piochacz. "Status of the pulsed low energy positron beam system (PLEPS) at the Munich Research Reactor FRM-II". In: *Applied Surface Science* 255 (2008), pp. 35–38. DOI: 10.1016/j.apsusc.2008.05.307.

[8] A. Wagner, M. Butterling, M. O. Liedke, K. Potzger, and R. Krause-Rehberg. "Positron annihilation lifetime and Doppler broadening spectroscopy at the ELBE facility". In: *AIP Conf. Proc.* 1970 (2018), p. 040003. DOI: 10.1063/1.5040215.

[9] B. Wang, Y. Ma, P. Wang, X. Cao, X. Qin, Z. Zhang, R. Yu, and L. Wei. "Developement and application of the intense slow positron beam at IHEP". In: *Chin. Phys. C* 32 (2008), pp. 156–159. DOI: 10.1088/1674-1137/32/2/016.

[10] T. Hyodo, Y. Fukaya, M. Maekawa, I. Mochizuki, K. Wada, T. Shidara, A. Ichimiaya, and A. Kawasuso. "Total reflection high-energy positron diffraction (TRHEPD)". In: *Journ. Phys. Conf. Series* 505 (2008), p. 012001. DOI: 10.1088/1742-6596/505/1/012001.

[11] M. Wenskat, J. Cizek, M. O. Liedke, M. Butterling, C. Bate, P. Hausild, E. Hirschmann, A. Wagner, and H. Weise. "Vacancy-Hydrogen Interaction in Niobium during Low-Temperature Baking". In: *Sci. Rep.* 10 (2020), p. 8300. DOI: 10.1038/s41598-020-65083-0.

[12] Marcel Dickmann, Lucian Mathes, Ricardo Helm, Vassily Vadimovitch Burwitz, Werner Egger, Johannes Mitteneder, Christoph Hugenschmidt, Peter Sperr, Maik Butterling, Maciej Oskar Liedke, Andreas Wagner, Joachim Dorner, Thomas Schwarz-Selinger, and Günther Dollinger. "Identification and Reversible Optical Switching of NV+ Centers in Diamond". In: *Advanced Functional Materials* (2025), p. 2500817. DOI: 10.1002/adfm.202500817.

[13] T. Stassin, R. Verbeke, A. J. Cruz, S. Rodriguez-Hermida, I. Stassen, J. Marreiros, M. Krishtab, M. Dickmann, W. Egger, I. F. J. Vankelecom, S. Furukawa, D. De Vos, D. Grosso, M. Thommes, and R. Ameloot. "Porosimetry for Thin Films of Metal-Organic Frameworks: A Comparison of Positron Annihilation Lifetime Spectroscopy and Adsorption-Based Methods". In: *Adv. Mater.* 33 (2021), p. 2006993. DOI: 10.1002/adma.202006993.

[14] R. Krause-Rehberg and H. S. Leipner. *Positron Annihilation in Semiconductors*. 1th edition. Springer Berlin, 1999. ISBN: 9783540643715.

[15] I. K. MacKenzie, T. L. Khoo, A. B. McDonald, and B. T. A. McKee. "Temperature Dependence of Positron Mean Lives in Metals". In: *Phys. Rev. Lett.* 19 (1967), pp. 964–948. DOI: 10.1103/PhysRevLett.19.946.

[16] B. T. A. McKee, W. Triftshäuser, and A. T. Stewart. "Vacancy-Formation Energies in Metals from Positron Annihilation". In: *Phys. Rev. Lett.* 28 (1972), pp. 358–360. DOI: 10.1103/PhysRevLett.28.358.

[17] S. Mäkinen, H. Rajainmäki, and S. Linderoth. "Low-temperature psoitron-lifetime studies of proton-irradiated silicon". In: *Phys. Rev. B* 42 (1990), pp. 166–173. DOI: 10.1103/PhysRevB.42.11166.

[18] A. Uedono, S. Takashima, M. Edo, K. Ueno, H. Matsuyama, W. Egger, T. Koschine, C. Hugenschmidt, M. Dickmann, K. Kojima, S. F. Chichibu, and S. Ishibashi. "Carrier Trapping by Vacancy-Type Defects in Mg-Implanted GaN Studied Using Monoenergetic Positron Beams". In: *Phys. Status Solidi* (2017), p. 1700521. DOI: 10.1002/pssb.201700521.

[19] X. Hong, Y. C. Jean, H. Yang, S. S. Jordan, and W. J. Koros. "Free-Volume Hole Properties of Gas-Exposed Polycarbonate Studied by Positron Annihilation Lifetime Spectroscopy". In: *Macromolecules* 29 (1996), pp. 7859–7864. DOI: https://doi.org/10.1021/ma9603544.

[20] B. Zgardzinska, T. Goworek, M. Sniegocka, R. Zaleski, and G. Dlubek. "Gas Pressure Induced Porosity of CYTOP Polymer. A Positron Study". In: *Acta Phy. Pol A* 125 (2014), pp. 782–784. DOI: 10.12693/APhysPolA.125.782.

[21] R. W. Baker. "Future directions of membrane gas separation technnology". In: *Ind. Eng. Chem. Res.* 41 (2002), pp. 1393–1411. DOI: 10.1021/ie0108088.

[22] K. Sumida, D. L. Rogow, J. A. Mason, T. M. McDonald, E. D. Bloch, Z. R. Herm, T.-H. Bae, and J. R. Long. "Carbon dioxide capture in metal-organic frameworks". In: *Chem. Rev.* 112 (2012), pp. 724–781. DOI: 10.1021/cr2003272.

[23] M. Elimelech and W. A. Philip. "The future of seawater desalination: energy, technology, and the environment". In: *Science* 333 (2011), pp. 712–717. DOI: 10.1126/science.1200488.

[24] W. Ma, A. Andersson, J. He, and F. H. J. Maurer. "Free Volume Changes, Crystallization, and Crystal Transition Behavior of Syndiotactic Polystyrene in Supercritical CO2 Revealed by Positron Annihilation Lifetime Spectroscopy". In: *Macromolecules* 41 (2008), pp. 5307–5312. DOI: 10.1021/ma8009068.

[25] Y. C. Jean, P. E. Mallon, and D. M. Schrader. *Principles and Applications of Positron & Positronium Chemistry*. 1st. World Scientific Publishing Co. Pte. Ltd., 2003. ISBN: 9812381449.

[26] P. Coleman. *Positrons Beams and Their Applications*. 1th. Addison-Wesley Publishing, 1996. ISBN: 978-981-281-775-4.

[27] C. Wang A. Yan, Z. Wang J. Yan, E. Zhang, Y. Dong, Z. Yan, T. Lu, T. Cui, D. Li, P. Shen, Y. Jin, H. Liu, Y. Yang, and T. Ren. "Thin-Film Transistors for Integrated Circuits: Fundamentals and Recent Process". In: *Adv. Funct. Mater.* 34 (2024), p. 2304409. DOI: 10.1002/adfm.202304409.

[28] S. Wang, X. Liu, M. Xu, L. Liu, D. Yang, and P. Zhou. "Two-dimensional devices and integration towards the silicon lines". In: *Nat. Mat.* 21 (2022), pp. 1225–1239. DOI: 10.1038/s41563-022-01383-2.

[29] K. S. Kim, J. Kwon, H. Ryu, C. Kim, H. Kim, E. Lee, D. Lee, S. Seo, N. M. Han, J. M. Suh, J. Kim, M. Song, S. Lee, M. Seol, and J. Kim. "The future of Two-dimensional semiconductors beyond Moore's law". In: *Nat. Nanotechnol.* 19 (2024), pp. 895–906. DOI: 10.1038/s41565-024-01695-1.

[30] S. Yuvaraja, H. Faber, M. Kumar, N. Xiao, G. I. M. Garcia, X. Tang, T. D. Anthopoulos, and X. Li. "Three-dimensional integrated metal-oxide transistors". In: *Nat. Electron.* 7 (2024), pp. 768–776. DOI: 10.1038/s41928-024-01205-0.

[31] C. S. Lau, S. Das, I. A. Verzhbitskiy, D. Huang, Y. Zhang, T. Talha-Dean, W. Fu, D. Venkatakrishnarao, and K. E. Johnson Goh. "Dielectrics for Two-Dimensional Transition-Metal Dichalcogenide Applications". In: *ASC Nano* 17 (2023), pp. 9870–9905. DOI: 10.1021/acsnano.3c03455.

[32] L. Yin, R. Cheng, X. Wan, J. Ding, J. Jia, Y. Wen, X. Liu, and J. He. "High-k monocrystalline dielectrics for low-power two-dimensional electronics". In: *Nat. Mat.* 24 (2024), pp. 197–207. DOI: 10.1038/s41563-024-02043-3.

[33] E. Fortunato, P. Barquinha, and R. Martins. "Oxide Semiconductor Thin-Film Transistors: A Review of Recent Advances". In: *Adv. Mater.* 24 (2012), pp. 2945–2986. DOI: 10.1002/adma.201103228.

[34] P. Hautojärvi. *Positrons in Solids*. 1th. Springer Berlin, 1979. ISBN: 978-3-642-81318-4.

[35] W. Brandt. "Positron Dynamics in Solids". In: *Appl. Phys.* 5 (1974), pp. 1–23. DOI: 10.1007/BF01193389.

[36] P. J. Schultz and K. G. Lynn. "Interaction of positron beams with surfaces, thin films, and interfaces". In: *Reviews of Modern Physics* 60 (1988), pp. 701–779. DOI: 10.1103/RevModPhys.60.701.

[37] M. J.Puska and R. M. Nieminen. "Theory of positrons in solids and on solid surfaces". In: *Review of Modern Physics* 66 (1994), pp. 841–897. DOI: 10.1103/RevModPhys.66.841.

[38] O. E. Mogensen. *Positron Annihilation on Chemistry*. 1st. Springer Berlin Heidelberg, 1995. ISBN: 9783642851254.

[39] G. F. Knoll. *Radiation Detection and Measurement*. 4th edition. John Wiley & Sons, Inc., 2010. ISBN: 9780470131480.

[40] A. Seeger. "Challenges to Positron and Positronium Physics by Materials Science". In: *Mat. Sci. Forum* 255-257 (1997), pp. 1–34. DOI: 10.4028/www.scientific.net/MSF.255-257.1.

[41] J. Cizek. "Characterization of lattice defects in metallic materials by positron annihilation spectroscopy: A review". In: *J. Mater. Sci. Technol.* 34 (2018), pp. 577–598. DOI: 10.1016/j.jmst.2017.11.050.

[42] P. Kirgegaard, J. V. Olsen, and M. M. Eldrup. *PALSfit3: A software package for analysing positron lifetime spectra*. 2017th ed. Technical University of Danemark, 2017. ISBN: 978-87-92986-61-0.

[43] Luca Ravelli. "Improvement of the Pulsed Low Energy Positron System (PLEPS) for complex problems in materials science". PhD thesis. Munich: University of the Bundeswehr Munich, 2014.

[44] Henk Schut. "A variable energy positron beam facility with applications in materials science". PhD thesis. Delft: Delft University of Technology, 1990.

[45] A. W. Hunt, D. B. Cassidy, P. A. Sterne, T. E: Cowan, R. H. Howell, K. G. Lynn, and J. A. Golovchnko. "Doppler Broadening of In-Flight Positron Annihilation Radiation due to Electron Momentum". In: *Phys. Rev. Lett.* 86 (2001), pp. 5612–5615. DOI: 10.1103/PhysRevLett.86.5612.

[46] R. S. Brusa, C. Macchi, S. Mariazzi, G. P. Karwasz, W. Egger, P. Sperr, and G. Kögel. "Absence of positronium in clean buried nanocavities in p-type silicon". In: *Phys. Rev. B* 71 (2005), p. 245320. DOI: 10.1103/PhysRevB.71.245320.

[47] National Nuclear Data Center. *NuDat 3.0*. URL: https://www.nndc.bnl.gov/nudat3/decaysearchdirect.jsp?nuc=22Na&unc=NDS. (accessed: 17.11.2025).

[48] M. Dickmann, W. Egger, G. Kögel, S. Vohburger, and C. Hugenschmidt. "Upgrade of the NEPOMUC Remoderator". In: *Acta Phys. Pol. A* 137 (2020), pp. 149–151. DOI: 10.12693/APhysPolA.137.149.

[49] W. Heitler. *The quantum theory of radiation*. 3th. Dover Publications, 1953. ISBN: 978-112-416-495-3.

[50] B. Krusche and K. Schreckenbach. "Intense positron sources by pair creation with neutron capture α-rays". In: *NIM-A* 295 (1990), pp. 155–171. DOI: 10.1016/0168-9002(90)90435-9.

[51] C. Hugenschmidt, G. Kögel, R. Repper, K. Schreckenbach, P. Sperr, and W. Thriftshäuser. "First platinum moderated positron beam based on neutron capture". In: *NIM-B* 198 (2002), pp. 220–229. DOI: 10.1016/S0168-583X(02)01527-6.

[52] R. Krause-Rehberg, S. Sachert, G. Bauer, A. Rogov, and K. Noack. "EPOS - An intense positron beam project at the ELBE radiation source in Rossendorf". In: *Appl. Surf. Sci.* 252 (2006), pp. 3106–3110. DOI: 10.1016/j.apsusc.2005.08.109.

[53] J. Dryzek, T. Suzuki, and R. Yu. "Detection of the positron annihilation in flight process in condensed matter". In: *Radiat. Phys. Chem.* 76 (2007), pp. 297–299. DOI: 10.1016/j.radphyschem.2006.03.054.

[54] J. P. Carbotte and H. L. Arora. "Thermalization Time of Positrons in Metals". In: *Can. J. Phys.* 45 (1967), pp. 387–402. DOI: 10.1139/p67-036.

[55] W. Brandt and N. Arista. "Thermalization and diffusion in solids". In: *Phys. Rev. B* 26 (1982), pp. 4229–4238. DOI: 10.1103/PhysRevB.26.4229.

[56] W. Brandt and A. Dupasquier. *Positron Solid State Physics*. Nort-Holland Publishing Company, 1983. ISBN: 0-444-86521-7.

[57] A. F. Makhov. "The penetration of electrons in solids II. The distribution of electrons in depth". In: *Sov. Phys. Solid State* 2 (1960), pp. 1934–1942.

[58] S. Valkealahti and R. M. Nieminen. "Monte Carlo simulations of keV Electrons and Positrons Slowing Down in Solids. II". In: *Appl. Phys. A* 35 (1984), pp. 81–59. DOI: 10.1007/BF00620300.

[59] J. Dryzek and P. Horodek. "GEANT 4 simulation of slow positron beam implantation profile". In: *NIM-B* 266 (2008), pp. 4000–4009. DOI: 10.1016/j.nimb.2008.06.033.

[60] J. Algers, P. Sperr, W. Egger, G. Kögel, and F. H. J. Maurer. "Median implantation depth and implantation profile of 3-18 keV positrons in amorphous polymers". In: *Phys. Rev. B* 67 (2003), p. 125404. DOI: 10.1103/PhysRevB.67.125404.

[61] W. Brandt and R. Paulin. "Positron implantation-profile effects in solids". In: *Phys. Rev. B* 15 (1977), pp. 2511–2518. DOI: 10.1103/PhysRevB.15.2511.

[62] M. Mourino, H. Löbl, and R. Paulin. "Profiles and Absorption Coefficient of Positrons Implanted in Solids from Radioactive Sources". In: *Phys. Lett.* 71A (1979), pp. 106–108. DOI: 10.1016/0375-9601(79)90890-9.

[63] J. Dryzek and K. Siemek. "The Multi-Scattering Model for Calculations of Positron Spatial Distribution in the Multilayer Stack, useful for Conventional Positron Measurements". In: *J. Appl. Phys.* 114 (2013), p. 074904. DOI: 10.1063/1.4818578.

[64] A. Seeger. "Positron diffusion in solids and liquid metals". In: *Appl. Surf. Sci.* 85 (1995), pp. 8–16. DOI: 10.1016/0169-4332(94)00300-9.

[65] W. Egger. "Pulsed low-energy positron beams in materials sciences". In: *Proc. Int. School Phys. 'Enrico Fermi'* Physics with Many Positrons (2010), pp. 419–449. DOI: 10.3254/978-1-60750-647-8-419.

[66] M. Rudan. *Physics of Semiconductor Devices*. 2nd edition. Springer Nature, 2018. ISBN: 978-3-319-63153-0.

[67] X. Gonze, B. Amadon, G. Antonius, F. Arnardi, L. Baguet, J.-M. Beuken, J. Bieder, F. Bottin, J. Bouchet, E. Bousquet, N. Brouwer, F. Bruneval, G. Brunin, T. Cavignac, J-B. Charraud, W. Chen, M. Côté, S. Cottenier, J. Denier, and G. Geneste et al. "The ABINITproject: Impact, environment and recent developments". In: *Compute. Phys. Commun* 248 (2020), p. 107042. DOI: 10.1016/j.cpc.2019.107042.

[68] A. Seeger. "The Study of Defects in Crystals by Positron Annihilation". In: *Appl. Phys.* 4 (1974), pp. 183–199. DOI: 10.1007/BF00884229.

[69] S. DeBenedetti and H. C. Corben. "Positronium". In: *Ann. Rev. Nuc. Part. Sci.* 4 (1954), pp. 191–218. DOI: 10.1146/annurev.ns.04.120154.001203.

[70] S. Berko and H. N. Pendleton. "Positronium". In: *Ann. Rev. Nucl. Part. Sci.* 30 (1980), pp. 543–581. DOI: 10.1146/annurev.ns.30.120180.002551.

[71] R. N. West. "Positron studies of condensed matter". In: *Adv. Phys.* 22 (1973), pp. 263–383. DOI: 10.1080/00018737300101299.

[72] S. DeBenedetti and R. T. Siegel. "The Three-Photon Annihilation of Positrons and Electrons". In: *Phys. Rev.* 94 (1954), pp. 955–959. DOI: 10.1103/PhysRev.94.955.

[73] B. Bergesnen and M. J. Stott. "The Effect of vacancy Formation on the Temperature Dependence of the Positron Lifetime". In: *Solid State Commune.* 7 (1969), pp. 1203–1205. DOI: 10.1016/0038-1098(69)90177-X.

[74] D. C. Connors and R. N. West. "Positron Annihilation and Defects in Metals". In: *Phys. Lett.* 30A (1969), pp. 24–25. DOI: 10.1016/0375-9601(69)90018-8.

[75] A. Dupasquier and A. P. Mills. *Positron Spectroscopy of solids*. IOS Press, 1993. ISBN: 9051992033.

[76] G. Kögel. "Positron diffusion in solids and the reconstruction of the inhomogeneous defect distribution from lifetime measurements". In: *Appl. Phys. A* 63 (1996), pp. 227–235. DOI: 10.1007/BF01567874.

[77] W. Bauer-Kugelmann, J. A. Duffy, J. Störmer, G. Kögel, and W. Triftshäuser. "Diffusivity and surface transition rate of positrons in crystalline silicon as a function of dopant concentration". In: *Appl. Surf. Sci.* 116 (1997), pp. 231–235. DOI: 10.1016/S0169-4332(96)01060-4.

[78] O. E. Mogensen. "Spur reaction model of positronium formation". In: *J. Chem. Phys.* 60 (1974), pp. 998–1004. DOI: https://doi.org/10.1063/1.1681180.

[79] S. V. Stepanov, V. M. Byakov, D. S. Zvezhinsky, G. Duplatre, R. R. Nurmukhametov, and P. S. Stepanov. "Positronium in a Liquid Phase: Formation, Bubble State and Chemical Reactions". In: *Adv. Phys. Chem.* 2012 (2012), p. 431962. DOI: 10.1155/2012/431962.

[80] A. Seeger and F. Banhart. "On the Systematics of Positron Lifetimes in Metals". In: *Phys. Stat. Sol. A* 102 (1987), p. 171. DOI: 10.1002/pssa.2211020117.

[81] T. Hyodo, T. Nakayama, H. Saito, F. Saito, and K. Wada. "The quenching of ortho-positronium". In: *Phys. Status Solidi* 6 (2009), pp. 2497–2502. DOI: 10.1002/pssc.200982118.

[82] M. Eldup, V. P. Shantarovich, and O. E. Morgensen. "Inhibition of Ps formation by strong Ps quenchers". In: *Chem. Phys.* 11 (1975), pp. 129–142. DOI: 10.1016/0301-0104(75)80046-2.

[83] S. V. Stepanov, V. M. Byakov, and Y. Kobayashi. "Positronium formation in molecular media: The effect of the external electric field". In: *Phys. Rev. B* 72 (2005), p. 054205. DOI: 10.1103/PhysRevB.72.054205.

[84] H. J. Ache. "Chemie des Positrons und Positronium". In: *Angew. Chem.* 84 (1972), p. 243. DOI: 10.1002/ange.19720840603.

[85] S. J. Tao. "Positronium Annihilation in Molecular Substances". In: *J. Chem. Phys.* 56 (1972), pp. 5499–5510. DOI: 10.1063/1.1677067.

[86] M. Eldrup, D. Lightbody, and J. N. Sherwood. "The Temperature Dependence of Positron Lifetimes in Solid Pivalic Acid". In: *Chem. Phys.* 63 (1982), pp. 51–58. DOI: 10.1016/0301-0104(81)80307-2.

[87] K. Ito, H. Nakanishi, and Y. Ujihira. "Extension of the Equation for the Annihilation Lifetime of ortho-Positronium at a cavity larger than 1 nm in Radius". In: *J. Phys. Chem. B* 103 (1999), pp. 4555–4558. DOI: 10.1021/jp9831841.

[88] K. Wada and T. Hyodo. "A simple shape-free model for pore-size estimation with positron annihilation lifetime spectroscopy". In: *J. Phys.: Conf. Ser.* 443 (2013), p. 012003. DOI: 10.1088/1742-6596/443/1/012003.

[89] H. Sun, Y. H. Deng, Q. H. Wang, and P. T. Lai. "Choice of Metal as Gate Electrode of Thin-Film Transistor With High-k Gate Dielectric". In: *IEEE Electron Device Lett.* 46 (2024), pp. 286–289. DOI: 10.1109/LED.2024.3514783.

[90] J. K. Park, S. M. Song, J. H. Mun, and B. J. Cho. "Graphene Gate ELectrode for MOS Structure-Based Electronic Devices". In: *Nano Lett.* 11 (2011), pp. 5383–5386. DOI: 10.1021/nl202983x.

[91] G. Barbottin and A. Vapaille. *Instabilities in Silicon Devices*. 1st. Vol. 2. Elsevier Science Publishing, 1986. ISBN: 0-444-87944-7.

[92] S. M. Sze. *Physics of Semiconductor Devices*. 3th edition. John Wiley & Sons, 2007. ISBN: 9780471143239.

[93] H. S. Nalwa. *Silicon-Based Materials and Devices*. 1st. Vol. 2. Academic Press, 2001. ISBN: 0-12-513919-5.

[94] F. M. Li and A. Nathan. *CCD Image Sensors in Deep-Ultraviolet*. 1st. Springer Berlin Heidelberg, 2005. ISBN: 3-540-22680-X.

[95] C. R. Helms and E. H. Poindexter. "The silicon-silicon-dioxide system: Its microstructure and imperfections". In: *Rep. Prog. Phys.* 57 (1994), pp. 791–852. DOI: 10.1088/0034-4885/57/8/002.

[96] C. R. Helms and B. E. Deal. *The Physics and Chemistry of SiO2 and the Si-SiO2 Interface*. 1st. Springer Science+Business, 1988. ISBN: 978-1-4899-0776-9.

[97] W. Beall Fowler and A. H. Edwards. "Theory of defects and defect processes in silicon dioxide". In: *J. Non-Cryst. Solids* 222 (1997), pp. 33–41. DOI: 10.1016/S0022-3093(97)90094-6.

[98] F. J. Grunthaner, P. J. Gunthaner, R. P. Vasquez, B. F. Lewis, and J. Maserjian. "High-Resolution X-Ray Photoelectron Spectroscopy as a Probe of Local Atomic Structure: Application to Amorphous SiO2 and Si-SiO2 Interface". In: *Phys. Rev. Lett.* 43 (1979), pp. 1683–1686. DOI: 10.1103/PhysRevLett.43.1683.

[99] K. Hirose, H. Nohira, K. Azuma, and T. Hattori. "Photoelectron spectroscopy studies of SiO2/Si interfaces". In: *Prog. Surf. Sci.* 82 (2007), pp. 3–54. DOI: 10.1016/j.progsurf.2006.10.001.

[100] E. Hasegawa, A. Ishitani, K. Akimoto, M. Tsukiji, and N. Ohta. "SiO2/Si Interface Structure and Reliablility Characteristics". In: *J. Electrochem. Soc.* 142 (1995), pp. 273–283. DOI: 10.1149/1.2043901.

[101] F. J. Himpsel, F. R. McFeely, A. Taleb-Ibrahimi, J. A. Yarmoff, and G. Hollinger. "Microscopic structure of the SiO2/Si interface". In: *Phys. Rev. B* 38 (1988), pp. 6084–6097. DOI: 10.1103/PhysRevB.38.6084.

[102] N. Awaji, S. Ohkubo, T. Nakanishi, Y. Sugita, K. Takasaki, and S. Komiya. "High-Density Layer at the SiO2/Si Interface Observed by Difference X-Ray Reflectivity". In: *Jpn. J. Appl. Phy.* 35 (1996), pp. 67–73. DOI: 10.1143/JJAP.35.L67.

[103] E. H. Poindexter, P. J. Caplan, B. E. Deal, and R. R. Razouk. "Interface states and electron spin resonance centers in thermally oxidized (111) and (100) silicon wafers". In: *J. Appl. Phys.* 52 (1981), pp. 879–884. DOI: 10.1063/1.328771.

[104] P. J. Caplan, E. H. Poindexter, B. E. Deal, and R. R. Razouk. "ESR centers, interface sates, and oxide fixed charge in thermally oxidized silicon wafers". In: *J. Appl. Phys.* 50 (1979), pp. 5847–5854. DOI: 10.1063/1.326732.

[105] N. Sano, M. Sekiya, M. Hara, A. Kohno, and T. Sameshima. "Improvement of SiO2/Si interface by low-temperature annealing in wet atmosphere". In: *Appl. Phys. Lett.* 66 (1995), pp. 2107–2019. DOI: 10.1063/1.113918.

[106] R. F. Pierret. *Semiconductor Device Fundamentals*. 1th. World Scientific Publishing Co. Re. Ltd., 2000. ISBN: 978-981-281-775-4.

[107] F. Thuselt. *Instabilities in Silicon Devices*. 2nd. Springer Heidelberg, 2011. ISBN: 978-3-642-20031-1.

[108] R. Winter, M. Eizenberg, J. Ahn, and C. McIntyre. "New method for determining flat-band voltage in high mobility semiconductors". In: *Journal of Chemical Physics* 34 (1961), pp. 120–125. DOI: 10.1063/1.1731549.

[109] J. W. Schroder. *Semiconductor material and device characterization*. 3. edition. Wiley, 2006. ISBN: 9780471749097.

[110] E. H. Nicollian and A. Goetzberger. "The si-sio, interface – electrical properties as determined by the metal-insulator-silicon conductance technique". In: *The Bell System Technical Journal* 46 (1967), pp. 1055–1033. DOI: 10.1002/j.1538-7305.1967.tb01727.x.

[111] J. R. Brews. "Rapid interface parameterization using a single MOS conductance curve". In: *Solid-State Electronics* 26 (1983), pp. 711–716. DOI: 10.1016/0038-1101(83)90030-8.

[112] A. Goetzberger, E. Klausmann, and M. J. Schulz. "Interface states on semiconductor/insulator surfaces". In: *CRC Critical Reviews in Solid State Sciences* 6 (1976), pp. 1–43. DOI: 10.1080/10408437608243548.

[113] J. E. Mark. *Physical Properties of Polymer Handbook*. 2nd. Springer Science + Business, 2007. ISBN: 978-0-387-31235-4.

[114] Joahnnes Lehtonen. "Nanoscopic Analysis of Polymers in pressure and Temperature variable Atmospheres by Positron Annihilation Lifetime Spectroscopy". Master's thesis. Neubiberg: University of the Bundeswehr Munich, Aug. 2021.

[115] International Union of Pure and Applied Chemistry. *Keller Manometer LEO5*. URL: https://beta.keller-pressure.com/de/produkte/manometer/digitale-manometer/leo5. (accessed: 01.10.2025).

[116] K. S. Shah, J. Glodo, W. Higgins, E. V. D. van Loef, W. W. Moses, and S. E. Derenzo. "$CeBr_3$ scintillators for gamma-ray spectroscopy". In: *IEEE Symposium Conference Record Nuclear Scinece 2004* (2004), pp. 4278–4281. DOI: 10.1109/NSSMIC.2004.1466835.

[117] Stefan Ritt. *DRS4 Evaluation Board Rev. 5.1 manual*. URL: https://www.psi.ch/en/ltp-muon-physics/documentation. (accessed: 02.01.2025).

[118] M. Petriska, S. Sojak, and V. Slugen. "Positron lifetime setup based on DRS4 evaluation board". In: *Journal of Physics: Conference Series* 505 (2014), p. 012044. DOI: 10.1088/1742-6596/505/1/012044.

[119] D. Petschke, R. Helm, and T. E. M. Staab. "Data on pure tin by Positron Annihilation Lifetime Spectroscopy (PALS) acquired with a semi-analog/digital setup using DDRS4PALS". In: *Data in Brief* 22 (2019), pp. 16–29. DOI: https://doi.org/10.1016/j.dib.2018.11.121.

[120] D. Petriska and T. E. M. Staab. "DDRS4PALS: A software for the acquisition and simulation of lifetime spectra using the DRS4 evaluation board". In: *Software X* 10 (2019), p. 100261. DOI: https://doi.org/10.1016/j.softx.2019.100261.

[121] Danny Petschke. *DDRS4PALS Github Project*. URL: https://github.com/dpscience/DDRS4PALS. (accessed: 02.01.2025).

[122] L. Qiu and Y. Feng. *Thermal Engineering*. de Gryter, 2024. ISBN: 9783111329697.

[123] R. Helm, J. Lehtonen, M. Mayerhofer, J. Mitteneder, W. Egger, R. Verbeke, P. Sperr, G. Dollinger, and M. Dickmann. "Positron-annihilation lifetime spectroscopy with in-situ control of temperature, pressure and atmosphere to determine the free-volume of soft materials". In: *Nuclear Instruments and Methods in Physics Research Section B: Beam Interactions with Materials and Atoms* 549 (2024), p. 165263. DOI: 10.1016/j.nimb.2024.165263.

[124] M. J. Richardson and N. G. Savill. "Derivation of the accurate glass transition temperature by differential scanning calorimetry". In: *Polymer* 16 (1975), pp. 753–757. DOI: https://doi.org/10.1016/0032-3861(75)90194-9.

[125] J. Liu, Q. Deng, and Y. C. Jean. "Free-Volume Distributions of Polystyrene Probed by Positron Annihilation: Comparison with Free-Volume Theories". In: *Macromolecules* 26 (1993), pp. 7149–7155. DOI: https://doi.org/10.1021/ma00078a006.

[126] A. R. Berens and H. B. Hopfenberg. "Diffusion of Organic Vapors at Low Concentration in Glassy PVC, Polystyrene, and PMMA". In: *Journal of Membrane Science* 10 (1982), pp. 283–303. DOI: https://doi.org/10.1016/S0376-7388(00)81415-5.

[127] H. Eslami and F. Müller-Plathe. "Molecular Dynamics Simulation of Sorption of Gases in Polystyrene". In: *Macromolecules* 40 (2007), pp. 6413–6421. DOI: https://doi.org/10.1021/ma070697+.

[128] F. Mozaffari, H. Eslami, and J. Moghadasi. "Molecular dynamics simulation of diffusion and permeation of gases in polystyrene". In: *Journal of Membrane Science* 10 (1982), pp. 283–303. DOI: https://doi.org/10.1016/S0376-7388(00)81415-5.

[129] D. I. Bower. *An Introduction to Polymer Physics*. 1st. Cambridge University Press, 2002. ISBN: 978-0-521-63721-3.

[130] D. J. Plazek and C. A. Bero. "Precise glass temperatures". In: *Journal of Physics: Condensed Matter* 15 (2003), pp. 789–802. DOI: 10.1088/0953-8984/15/11/304.

[131] D. Turnbull and M. H. Cohen. "Free-Volume Model of the Amorphous Phase: Glass Transition". In: *Journal of Vacuum Science & Technology B* 31 (2013), p. 030604. DOI: 10.1116/1.4802478.

[132] M. H. Cohen and G. S. Grest. "Liquid-glass transition, a free-volume approach". In: *Phys. Rev. B* 20 (1979), pp. 1077–1098. DOI: 10.1103/PhysRevB.20.1077.

[133] W.R. Vieth, P.M. Tam, and A.S. Micheals. "Dual Sorption Mechanisms in Glassy Polymers". In: *Journal of Colloid and Interface Science* 22 (1966), pp. 360–370. DOI: https://doi.org/10.1016/0021-9797(66)90016-6.

[134] D. R. Paul. "Gas Sorption and Transport in Glassy Polymers". In: *Berichte der Bunsengesellschaft für physikalische Chemie* 83 (1979), pp. 294–302. DOI: https://doi.org/10.1002/bbpc.19790830403.

[135] R. M. Barrer. "Diffusivities in Glassy Polymers for the Dual Mode Sorption Model". In: *Journal of Membrane Science* 18 (1984), pp. 25–35. DOI: https://doi.org/10.1016/S0376-7388(00)85023-1.

[136] S. Zhou and S.A. Stern. "The Effect of Plasticization on the Transport of Gases in and Through Glassy Polymers". In: *Journal of Polymer Science: Part B: Polymer Physics* 27 (1989), pp. 205–222. DOI: https://doi.org/10.1002/polb.1989.090270201.

[137] K. Ganesh, R. Nagarajan, and J. L. Duda. "Rate of Gas Transport in Glassy Polymers: A Free Volume Based Predictive Model". In: *Industrial & engineering chemistry research* 31 (1992), pp. 746–755. DOI: https://doi.org/10.1021/ie00003a016.

[138] J. Guo and T. A. Barbari. "Unified Dual Mode Description of Small Molecule Sorption and Desorption Kinetics in a Glassy Polymer". In: *Macromolecules* 42 (2009), pp. 5700–5708. DOI: https://doi.org/10.1021/ma9007576.

[139] E. H. Immergut and H. F. Mark. "Principle of plasticization". In: *Advances in Chemistry* 48 (1965), pp. 1–26. DOI: https://doi.org/10.1021/ba-1965-0048.ch001.

[140] Z. Zhang and Y. P. Handa. "An In Situ Study of Plasticization of Polymers by High-Pressure Gases". In: *Journal of Polymer Science: Part B: Polymer Physics* 36 (1998), pp. 977–982. DOI: 10.1002/(SICI)1099-0488(19980430)36:6<977::AID-POLB5>3.0.CO;2-D.

[141] Dieter Schödlbauer. "Aufbau und Inbetriebnahme einer gepulsten Positronenquelle für Lebensdauermessungen". PhD thesis. Munich: University of the Bundeswehr Munich, 1987.

[142] Paul Willutzki. "Verbesserung und Erweiterung des gepulsten Positronenstrahlsystems für temperaturabhängige Lebensdauermessungen von Positronen in Festkörpern". PhD thesis. Munich: University of the Bundeswehr Munich, 2000.

[143] Werner Bauer-Kugelmann. "Technische Weiterentwicklung am gepulsten Positronenstrahlsystem PLEPS". PhD thesis. Munich: University of the Bundeswehr Munich, 2000.

[144] Tönjes Koschine. "Weiterentwicklungen am gepulsten Positronenstrahl und ausgewählte Anwendungen an Membranpolymeren". PhD thesis. Munich: University of the Bundeswehr Munich, 2015.

[145] A. Bergmaier, G. Dollinger, and C. M. Frey. "A compact $\Delta E - E_{\mathrm{res}}$ detector for elastic recoil detection with high sensitivity". In: *NIM B* 136-138 (1998), pp. 638–643. DOI: 10.1016/S0168-583X(97)00877-X.

[146] G. Kögel. "The München scanning positron microscope". In: *Applied Surface Science* 116 (1997), pp. 108–113. DOI: 10.1016/S0169-4332(96)01038-0.

[147] C. Hugenschmidt, C. Piochacz, M. Reiner, and K. Schreckenbach. "The NEPOMUC upgrade and advanced positron beam experiments". In: *New Journal of Physics* 14 (2012), p. 055027. DOI: 10.1088/1367-2630/14/5/055027.

[148] A. Uedono, S. Tanigawa, and Y. Ohji. "Metal/oxide/semiconductor interface investigated by monoenergetic positrons". In: *Phys. Lett. A* 133 (1988), pp. 82–84. DOI: 10.1016/0375-9601(88)90742-6.

[149] P. Asoka-Kumar, T. C. Leung, K. G. Lynn, B. Nielson, M. P. Forcier, Z. A. Weinberg, and G. W. Rubloff. "Positron annihilation studies in the field-induced depletion regions of metal-oxide semiconductor structures". In: *J. Appl. Phys.* 71 (1991), pp. 5606–5609. DOI: 10.1063/1.350540.

[150] Y. Y. Shan, P. Asoka-Kumar, and K. G. Lynn. "Field effect on positron diffusion in semi-insulating GaAs". In: *Phys. Rev. B* 54 (1996), 1982(5). DOI: 10.1103/PhysRevB.54.1982.

[151] M. Clement, J. M. M. de Nijs, P. Balk, H. Schut, and A. van Veen. "Transport of positrons in the electrically biased metal-oxide-silicon system". In: *J. Appl. Phys.* 81 (1997), pp. 1943–1955. DOI: 10.1063/1.364050.

[152] M. P. Petkov, K. G. Lynn, and A. van Veen. "Experimental and theoretical aspects of electric-field-assisted positron kinetics in metal-oxide-silicon systems". In: *Phys. Rev. B* 66 (2002), p. 045322. DOI: 10.1103/PhysRevB.66.045322.

[153] M. J. Puska. "Positron affinities for elemental metals". In: *J. Phys.: Condens. Matter* 1 (1989), p. 6081. DOI: 10.1088/0953-8984/1/35/008.

[154] A. Stesmans and V. V. Afanas'ev. "Electron spin resonance features of interface defects in thermal (100)Si/SiO2". In: *J. Appl. Phys.* 83 (1998), pp. 2449–2457. DOI: 10.1063/1.367005.

[155] M. Sschultz. "Interface States at the SiO2-Si Interface". In: *Surf. Sci.* 132 (1983), pp. 422–455. DOI: 10.1016/0039-6028(83)90551-4.

[156] S. Dannefaer, T. Bretagnon, and D. Kerr. "Vacancy-type defects in crystalline and amorphous SiO2". In: *J. Appl. Phys.* 74 (1993), pp. 884–890. DOI: 10.1063/1.354882.

[157] R. Suzuki, T. Ohdaira, A. Uedono, and Y. Kobayashi. "Positron annihilation in SiO2–Si studied by a pulsed slow positron beam". In: *Appl. Surf. Sci.* 194 (2002), pp. 89–96. DOI: 10.1016/S0169-4332(02)00094-6.

[158] A. Uedono, L. Wei, S. Tanigawa, R. Suzuki, H. Ohgaki, T. Mikado, and Y. Ohji. "Positron annihilation in a metaloxide semiconductor studied by using a pulsed monoenergetic positron beam". In: *J. Appl. Phys.* 74 (1993), p. 7251. DOI: 10.1063/1.355015.

[159] J. W. Arblaster. *Selected Values of the Crystallographic Properties of the Elements*. 1nd edition. ASM International, 2018. ISBN: 9781627081559.

[160] W. M- Haynes, D. R. Lide, and T. J. Bruno. *CRC Handbook of Chemistry and Physics*. 97th. CRC Press, 2017. ISBN: 978-1-4987-5429-3.

[161] H. F. Wolf. *Silicon Semiconductor Data*. 1nd edition. Vol. 9. Pergamon Press, 1967. ISBN: 9780080130194.

[162] A. Novikov. "Experimental measurement of work function in doped silicon surfaces". In: *Solid-State Electronics* 54 (2010), pp. 8–13. DOI: 10.1016/j.sse.2009.09.005.

[163] N. Balaji, C. Park, S. Chung, M. Ju, J. Raja, and J. Yi. "Effects of Low Temperature Anneal on the Interface Properties of Thermal Silicon Oxide for Silicon Surface Passivation". In: *J. Nanosci. Nanotechnol.* 16 (2016), pp. 4783–4787. DOI: 10.1166/jnn.2016.12178.

[164] S. Higashi, D. Abe, Y. Hiroshima, K. Miyashita, T. Kawamura, S. Inoue, and T. Shimoda. "High-Quality SiO2/Si Interface Formation and Its Application to Fabrication of Low-Temperature-Processed Polycrystalline Si Thin-Film Transistors". In: *Jpn. J. Appl. Phys.* 41 (2002), p. 3646. DOI: 10.1143/JJAP.41.3646.

[165] R. Helm, W. Egger, C. Corbel, P. Sperr, M. Butterling, A. Wagner, M. O. Liedke, J. Mitteneder, M. Mayerhofer, K. Lee, G. S. Duesberg, G. Dollinger, and M. Dickmann. "Defect Characterization of the SiO2/Si Interface investigated by Drift-Assisted Positron Annihilation Lifetime Spectroscopy". In: *Nanometerials* 16 (2026), p. 156. DOI: 10.3390/nano16030156.

[166] Akira Matsudaira, Saumitra Raj Mehrotra, Shaikh S. Ahmed, Gerhard Klimeck, and Dragica Vasileska. *MOSCap*. Apr. 2014. DOI: doi:10.4231/D3736M30D. URL: https://nanohub.org/resources/moscap.

[167] Mark R. Pinto, kent smith kent, Muhammad A. Alam, Steven Clark, Xufeng Wang, Gerhard Klimeck, and Dragica Vasileska. *Padre*. Jan. 2006. DOI: doi:10.4231/D30C4SK7Z. URL: https://nanohub.org/resources/padre.

[168] W. Egger, G. Kögel, P. Sperr, and H.-J. Gudladt. "Analysis of defect configuration with positrons lifetime measurements by pulsed low energy beams". In: *Int. J. Mat. Res.* 97 (2006), pp. 1633–1642. DOI: 10.3139/146.101394.

[169] M. Liu, B. Klobes, and J. Banhart. "Positron lifetime study of the formation of vacancy clusters and dislocations in quenched Al, Al-Mg and Al-Si alloys". In: *J. Mater. Sci.* 51 (2016), pp. 7754–7767. DOI: 10.1007/s10853-016-0057-7.

[170] A. Polity, F. Börner, S. Huth, S. Eichler, and R. Krause-Rehberg. "Defects in electron-irradiated Si studied by positron-lifetime spectroscopy". In: *Phys. Rev. B* 58 (1998), pp. 10363–10377. DOI: 10.1103/PhysRevB.58.10363.

[171] J. Kuriplach, A. L. Molares, C. Dauwe, D. Seger, and M. Sob. "Vacancies and vacancy-oxygen complexes in silicon: Positron annihilation with core electrons". In: *Phys. Rev. B* 58 (1998), pp. 10475–10483. DOI: 10.1103/PhysRevB.58.10475.

[172] A. Kawasuso, M. Hasegawa, M. Suezawa, S. Yamaguchi, and K. Sumino. "Studies of divacancy in Si using positron lifetime measurement". In: *Hyperfine Interact.* 84 (1994), pp. 397–406. DOI: 10.1007/BF02060688.

[173] B. Zgardzińska. "The size of smallest subnanometric voids estimated by positron annihilation method. Correction to the Tao-Eldrup model". In: *Chemical Physics Letters* 622 (2015), pp. 20–22. DOI: https://doi.org/10.1016/j.cplett.2015.01.021.

[174] R. Helm, W. Egger, C. Corbel, P. Sperr, M. Butterling, A. Wagner, M. O. Liedke, J. Mitteneder, M. Mayerhofer, K. Lee, G. S. Duesberg, G. Dollinger,

and M. Dickmann. “Defect Studies in Thin-Film SiO2 of a Metal-Oxide-Silicon Capacitor Using Drift-Assisted Positron-Annihilation Lifetime Spectroscopy”. In: *Nanometerials* 15 (2025), p. 1142. DOI: 10.3390/nano15151142.

[175] G. Kögel. “Positron Annihilation at Clean Metallic Surfaces”. In: *Mat. Sci. Forum* 105-110 (1991), pp. 341–348.

[176] M. Hasegawa, M. Saneyasu, M. Tabata, Z. Tang, Y. Nagai, T. Chiba, and Y. Ito. “Positron and positronium studies of irradiation-induced defects and microvoids in vitreous metamict silica”. In: *Nucl. Instrum. Methods Phys. Res., B* 166-167 (2000), pp. 431–439. DOI: 10.1016/S0168-583X(99)01026-5.

[177] A. van Veen, H. Schut, J. de Vries, R. A. Hakvoort, and M. R. Ijpma. “Analysis of positron profiling data by means of VEPFIT”. In: *AIP Conf. Proc.* 218 (1991), p. 171. DOI: 10.1063/1.40182.

[178] S. Van Petegem, C. Dauwe, T. Van Hoecke, J. De Baerdemaeker, and D. Segers. “Diffusion length of positrons and positronium investigated using a positron beam with longitudinal geometry”. In: *Phys. Rev. B* 70 (2004), p. 115410. DOI: 10.1103/PhysRevB.70.115410.

[179] Y. Kong, T. C. Leung, P. Asoka-Kumar, and K. G. Lynn. “Positron mobility in thermally grown SiO2 measured by Doppler broadening technique”. In: *J. Appl. Phys.* 70 (1991), pp. 2874–2876. DOI: 10.1063/1.349353.

[180] Y. Nagai, Y. Nagashima, and T. Hyodo. “Lifetime of delocalized positronium in $\alpha - SiO_2$”. In: *Phys. Rev. B* 60 (1999), pp. 7677–7679. DOI: 10.1103/PhysRevB.60.7677.

[181] O. V. Boev, M. J. Puska, and R. M. Nieminen. “Electron and positron levels in solids”. In: *Phys. Rev. B* 36 (1987), p. 7786. DOI: 10.1002/pssa.2211020117.

[182] J. Kuriplach, W. Anwand, G. Brauer, and W. Skorupa. “Positron characteristics of various SiO2 polymorphs”. In: *Appl. Surf. Sci.* 194 (2002), pp. 84–88. DOI: 10.1016/S0169-4332(02)00093-4.

[183] Y. Kobayashi, C. L. Wang, K. Hirata, and N. Kouchi. “Electric field dependent positronium formation in alpha-SiO2”. In: *Mat. Sci. Forum* 363-365 (2001), p. 138.

[184] G. Brauer, W. Anwand, W. Skorupa, A. G. Revesz, and J. Kuriplach. “Characterization of the SiO2/Si interface by positron annihilation spectroscopy”. In: *Phys. Rev. B* 66 (2002), p. 195331. DOI: 10.1103/PhysRevB.66.195331.

[185] J. P. Peng, K. G. Lynn, P. Asoka-Kumar, D. P. Becker, and D. R. Harshman. “Study of the SiO2-Si Interface Using Variable Energy Positron Two-Dimensional Angular Correlation of Annihilation Radiation”. In: *Phys. Rev. Lett.* 76 (1995), pp. 2157–2160. DOI: 10.1103/PhysRevLett.76.2157.

[186] T. E. M. Staab, A. Sieck, M. Haugk, M. J. Puska, Th. Frauenheim, and H. S. Leipner. “Stability of large vacancy clusters in silicon”. In: *Phys. Rev. B* 65 (2002), p. 115210. DOI: 10.1103/PhysRevB.65.115210.

A. Appendix: Supplementary Data

Python pseudo code for the fit of τ_{av} and I_2 with the DTM (Section 2.3.3)

```
import numpy as np
from scipy.optimize import curve_fit


"""--------------- FUNCTIONS -----------------"""

def intensity_zero(surf_capt_rate, diff_constant):
    return surf_trans_rate/(surf_trans_rate +
            np.sqrt(diff_constant * (lambda_bulk - lambda_surf)))

def model_intensity(energy, surf_trans_rate, diff_constant):
    alpha= np.sqrt(lambda_bulk - lambda_surf)/np.sqrt(diff_constant)
    erf_param_t= (35/density_material) * alpha * energy**(1.7)
    return surf_trans_rate * (1 - np.sqrt(np.pi)/2 * erf_param_t
    * np.exp(erf_param_t**2/4) * special.erfc(erf_param_t/2))
    / (1 + np.sqrt(diff_constant * (lambda_bulk - lambda_surf)))

def model_average_lifetime(energy, surf_trans_rate, diff_constant):
    alpha= np.sqrt(lambda_bulk - lambda_surf)/np.sqrt(diff_constant)
    erf_param_t= (35/density_material) * alpha * energy**(1.7)
    return tau_bulk + (tau_surf - tau_bulk) *
        (1 - (np.sqrt(np.pi)/2) * erf_param_t
        * np.exp(erf_param_t**2/4)
        * special.erfc(erf_param_t/2))
        / (1 + np.sqrt(diff_constant/(surf_trans_rate**2*tau_bulk)))


"""--------------- FITS -----------------"""

#surface transition rate and diffusion constant are in nm/ps and
#nm^2/ps respectively
```

```
#conversion factor nm/ps -> cm/s = 1e5; nm^2/ps -> cm^2/s = 1e-2
#bounds must be adjusted
#(for Si -> Bauer-Kugelmann et. al Appl. Surf. Sci. 1996)

"""------------- Intensity -------------"""

print('\n--------------- Intensity Model ----------------\n')

fit_results_int, conv_int= curve_fit(model_intensity, input_energy,
input_intensity_2, method='dogbox', p0=[ 0.01, 100],
bounds=([0.01,10], [120, 1000]))

#results of diffusion constant D_+ and
#surface transition rate nu stored in popt_int

"""--------- Average Lifetime ---------"""

print('\n------------ average lifetime Model ------------\n')

fit_results_tau, conv_tau= curve_fit(model_average_lifetime,
input_energy, input_average_lifetime, method='dogbox', p0=[ 98, 91],
bounds=([1,10], [1e10, 1000]))

#results of diffusion constant D_+ and
#surface transition rate nu stored in popt_tau
```

LT results from the semi-crystalline Polystyrene (Figure 4.13; Section 4.3)

T [°C]	21(2)	50(1)	75(2)	100(2)	125(3)	150(3)	
p [MPa]							
1×10^{-9}	2021(5)	2064(5)	2122(5)	2283(5)	2475(5)	**2731(5)	τ_3 [ps]
	36.3	38.2	38.4	42.6	43.6	**43.7	I_3 [%]
0.1	2056(3)	2077(5)	2135(5)	2239(5)	2450(5)	2724(6)	τ_3 [ps]
	40.9	41.5	41.7	42.0	42.3	42.8	I_3 [%]
2	2099(5)	2168(6)	2228(5)	2290(5)	2448(5)	2698(6)	τ_3 [ps]
	39.4	41.3	41.7	42.0	43.0	43.1	I_3 [%]
2	2183(6)	2260(6)	2313(6)	2400(6)	2606(6)	*2724(6)	τ_3 [ps]
	38.5	41.0	41.8	41.9	42.8	*43.4	I_3 [%]

Table A.1.: Analysis results of the o-Ps component (τ_3, I_3) as a function of temperature and pressure (data from [123]). The highest temperature was different for some of the measurements. The affected measurement points have been marked with an asterisk (140 °C) and double asterisk (146 °C), respectively. The uncertainty of the intensity was omitted due to the small magnitude of the statistical uncertainty. Reprinted from [123].

LT results in the oxide at 4 keV (Figure 6.17; Section 6.7.3)

U_g [V]	E_{ox} [MV/cm]	τ_1 [ps]	I_1 [%]	τ_2 [ps]	I_2 [%]	τ_3 [ps]	I_3 [%]
−30	−1.62	193(8)	8.1(6)	479(2)	77.1(5)	1443(5)	14.8(1)
−17	−0.89	175(5)	9.7(4)	481(2)	69.7(3)	1463(3)	20.6(1)
−10	−0.51	170(4)	11.6(4)	484(2)	62.0(3)	1477(3)	26.3(1)
−3	−0.12	167(3)	18.2(4)	491(3)	48.1(3)	1488(3)	33.7(2)
−2	−0.06	162(3)	17.3(4)	480(3)	48.3(3)	1480(3)	34.4(2)
−1	0.01	164(3)	17.6(4)	478(3)	47.8(3)	1480(3)	34.6(2)
0	0.05	149(3)	15.1(3)	491(3)	49.1(2)	1488(3)	35.8(2)
1	0.11	203(4)	21.5(8)	469(4)	49.0(7)	1490(3)	29.4(2)
2	0.16	204(5)	19(1)	441(4)	51.7(9)	1480(3)	28.7(1)
3	0.22	211(5)	21(1)	449(5)	50(1)	1484(3)	29.2(2)
10	0.61	224(5)	23(1)	446(4)	55(1)	1479(3)	22.5(1)
19	1.11	222(5)	21(1)	447(4)	62(1)	1465(4)	16.8(1)
30	1.72	255(7)	26(2)	442(5)	61(2)	1456(5)	12.8(1)

Table A.2.: Results of the three-component analysis of the lifetime spectrum of buried SiO_2 at 4 keV implantation energy. Reprinted from [174].

LT results in the oxide at $4\,\mathrm{keV}$ (Figure 6.18; Section 6.7.3)

U_g	E_ox	τ_1'	I_1'	$\bar{\tau}_1'$	$\bar{I}_1'$	$\bar{\tau}_2$	$\bar{I}_2$
[V]	[MV/cm]	[ps]	[%]	[ps]	[%]	[ps]	[%]
−30	−1.62	299	3.2	301	2.9	481	69
−17	−0.89	297	2.8	301	2.9	481	69
−10	−0.51	308	2.8	301	2.9	481	69
−3	−0.12	236	7.0	237	5.5	485	48
−2	−0.06	235	5.8	237	5.5	485	48
−1	0.01	237	6.1	237	5.5	485	48
0	0.05	238	3.2	237	5.5	485	48
1	0.11	268	12.0	275	14.2	445	55
2	0.16	284	10.0	275	14.2	445	55
3	0.22	285	11.5	275	14.2	445	55
10	0.61	271	15.2	275	14.2	445	55
19	1.11	257	15.1	275	14.2	445	55
30	1.72	281	22.1	275	14.2	445	55

Table A.3.: Results of the three- and four-component analysis of the lifetime spectrum of bare SiO_2 at $2\,\mathrm{keV}$ implantation energy. Reprinted from [174].

Lifetime results in the silicon at 11 keV (Figure 6.19; Section 6.7.4)

U_g [V]	τ_1 [ps]	I_1 [%]	τ_2 [ps]	I_2 [%]	τ_3 [ps]	I_3 [%]
−30	185(1)	52(1)	465(2)	46(1)	1270(16)	2.1(1)
−17	184(2)	51(1)	461(2)	46(1)	1274(12)	2.8(1)
0	186(1)	58(1)	476(3)	38(1)	1363(9)	4.1(1)
1	230(1)	93(1)	484(32)	3.8(5)	1386(10)	3.6(1)
19	233(1)	94(1)	544(29)	3.6(3)	1404(20)	1.9(1)
30	232(1)	95(1)	543(24)	4.0(3)	1422(26)	1.3(1)

Table A.4.: Results of the three-component analysis of the 11 keV measurements as a function of the applied gate voltage. The uncertainty of the gate voltage is ±0.5 V. Reprinted from [165].

List of Publications

[1] **R. Helm**, W. Egger, C. Corbel, P. Sperr, M. Butterling, A. Wagner, M. O. Liedke, J. Mitteneder, M. Mayerhofer, K. Lee, G. S. Duesberg, G. Dollinger, and M. Dickmann. "Defect Characterization of the SiO2/Si Interface investigated by Drift-Assisted Positron Annihilation Lifetime Spectroscopy". In: *Nanometerials* 16 (2026), p. 156. DOI: 10.3390/nano16030156.

[2] D. Van Havere, R. Verbeke, Z. Li, L. A. J. Rutgeerts, T. Hooper, P. Dreier, M. Meier-Merzinger, M. Houben, M. Dickmann, **R. Helm**, S. Eyley, H. Frey, K. Nijmeijer, D. Seveno, W. Thielemans, D. Sakellariou, B. D. Freeman, and I. F. J. Vankelecom. "Dual-Crosslinked Poly(epoxyether) Membranes with Exceptional CO2 Affinity for Post-Combustion Carbon Capture". In: *Angew. Chem.* (2025), submitted.

[3] M. Dickmann, M. Kraatz, M. Schneiders, **R. Helm**, Z. Wu, S. W. H. Eijt, W. Egger, M. Mayerhofer, and G. Dollinger. "Two-Component Density Functional Theory Calculations of Positron Lifetimes in Yttrium Oxyhydrides". In: *Phys. Rev. B* (2025), submitted.

[4] M. Dickmann, **R. Helm**, W. Egger, J. Mitteneder, P. Sperr, M. Mayerhofer, M. Butterling, E. Hirschmann, M. O. Liedke, A. Wagner, J. Dorner, T. Schwarz-Selinger, and G. Dollinger. "Defect Evolution in Nitrogen-implanted CVD Diamond During Thermal Annealing: The formation of NV Centers and Vacancy Clusters". In: *Mater. Des.* 262 (2026), p. 115422. DOI: 10.1016/j.matdes.2025.115422.

[5] I. Baert, S. Eyley, **R. Helm**, M. Dickmann, M. Butterling, M. O. Liedke, A. Wagner, W. Thielemans, I. F. J. Vankelecom, and R. Verbeke. "The impact of densification steps on epoxide-based TFC membranes". In: *Sep. Purif. Technol.* 381 (2025), p. 135570. DOI: 10.1016/j.seppur.2025.135570.

[6] J. Mitteneder, M. Mayerhofer, L. Kriese, P. Sperr, **R. Helm**, M. Dickmann, and G. Dollinger. "Controlling a 50 MHz Resonator to Generate a 10 keV Sinusoidal Signal for the SPM Positron Elevator". In: *J. Phys.: Conf. Ser.* 3149 (2025), p. 012008. DOI: 10.1088/1742-6596/3149/1/012008.

[7] J. Mitteneder, G. Kögel, **R. Helm**, M. Dickmann, and G. Dollinger. "Feasibility of a 'Brightness Booster' for the Intense Slow Positron Source NEPOMUC". In: *SSP* 374 (2025), pp. 23–36. DOI: 10.4028/p-LGc6vF.

[8] M. Dickmann, **R. Helm**, W. Egger, J. Mitteneder, J. A. Duffek, P. Jarmatz, and G. Dollinger. "Ab Initio Calculations of Positron Lifetimes in Diamond:

The Bulk, Vacancies and Grain Boundary". In: *SSP* 374 (2025), pp. 145–153. DOI: 10.4028/p-BcfuL0.

[9] **R. Helm**, W. Egger, C. Corbel, P. Sperr, M. Butterling, A. Wagner, M. O. Liedke, J. Mitteneder, M. Mayerhofer, K. Lee, G. S. Duesberg, G. Dollinger, and M. Dickmann. "Defect Studies in Thin-Film SiO2 of a Metal-Oxide-Silicon Capacitor Using Drift-Assisted Positron-Annihilation Lifetime Spectroscopy". In: *Nanometerials* 15 (2025), p. 1142. DOI: 10.3390/nano15151142.

[10] X. Tan, S. Robijns, A. Lamaire, R. Goeminne, N. De Witte, M. Dickmann, R. Verbeke, T. Van der Donck, R. de Oliveira Silva, Q. Ke, Y. Li, I. Aslam, C. Van Goethem, T. Donckels, **R. Helm**, D. Sakellariou, T. Van Assche, V. Van Speybroeck, M. Dusselier, and I. F. J. Vankelecom. "Design of a Tunable, High-performance Mixed Matrix Membrane Platform for Gas Separations". In: *Adv. Mater.* (2025), p. 2502393. DOI: 10.1002/adma.202502393.

[11] Y. Cai, D. Begin, C. Lefevre, C. Sidhoum, E. Elkaim, P. Boulet, P. Desgardin, M. F. Barthe, **R. Helm**, W. Egger, M. Butterling, A. Wagner, V. Papaefthimiou, S. Zafeiratos, D. Cianferani, L. Mager, O. Ersen, C. Corbel, C. Sanchez, and S. Begin-Colin. "Enhanced Electromagnetic Wave Absorption in Mapbi3 Hybrid Perovskite Through a Defect-Tunable Green Synthesis". In: *Small. Struct.* (2025), p. 2500066. DOI: 10.1002/sstr.202500066.

[12] Z. Bozorgmehr, R. Verbeke, C. Van Goethem, D. M. Davenport, S. Eyley, W. Thielemans, M. Dickmann, **R. Helm**, M. Butterling, A. Wagner, M. O. Liedke, M. Hossein Jandaghian A. Volodine, and I. F. J. Vankelecom. "Use of partially miscible solvent as the reagent phase to shorten synthesis time and enhance the performance of poly(epoxyether) TFC-membranes". In: *Sep. Purif. Technol.* 375 (2025), p. 133727. DOI: 10.1016/j.seppur.2025.133727.

[13] M. Dickmann, L. Mathes, **R. Helm**, V. V. Burwitz, W. Egger, J. Mitteneder, C. Hugenschmidt, P. Sperr, M. Butterling, M. O. Liedke, A. Wagner, J. Dorner, T. Schwarz-Selinger, and G. Dollinger. "Identification and Reversible Optical Switching of NV+ Centers in Diamond". In: *Adv. Func. Mater.* (2025), p. 2500817. DOI: 10.1002/adfm.202500817.

[14] N. Lenaerts, R. Verbeke, D. M. Davenport, S. Caspers, K. Kantre S. Eyley, A. Volodine, **R. Helm**, M. Butterling, M. O. Liedke, A. Wagner, W. Thielemans, J. Meersschaut, M. Dickmann, and I. F. J. Vankelecom. "Influence of support pore size and porosity on epoxide-based TFC membranes". In: *J. Memb. Sci.* 722 (2025), p. 123900. DOI: 10.1016/j.memsci.2025.123900.

[15] S. Brenner, M. Dickmann, **R. Helm**, J. Mitteneder, G. Schlick, M. Lehmann, C. Jugert, V. Nedeljkovic, G. Dollinger, and M. Mayerhofer. "A radio-frequency quadrupole prototype additively manufactured as a multi-material component". In: *Prog. Addit. Manuf.* 10 (2025), pp. 3951–3961. DOI: 10.1007/s40964-025-01120-6.

[16] **R. Helm**, J. Lehtonen, M. Mayerhofer, J. Mitteneder, W. Egger, R. Verbeke, P. Sperr, G. Dollinger, and M. Dickmann. "Positron-annihilation life-

time spectroscopy with in-situ control of temperature, pressure and atmosphere to determine the free-volume of soft materials". In: *NIM-B* 549 (2024), p. 165263. DOI: 10.1016/j.nimb.2024.165263.

[17] M. Mayerhofer, S. Brenner, M. Dickmann, M. Doppler, S. Gruber, **R. Helm**, E. Lopez, V. Maier, J. Mitteneder, C. Neukirchen, V. Nedeljkovic-Groha, B. Reinarz, M. Schuch, L. Stepien, and G. Dollinger. "Red and green laser powder bed fusion of pure copper in combination with chemical post-processing for RF cavity fabrication". In: *Instruments* 8 (2024), p. 39. DOI: 10.3390/instruments8030039.

[18] M. Mayerhofer, S. Brenner, **R. Helm**, S. Gruber, E. Lopez, L. Stepien, G. Gold, and G. Dollinger. "Additive Manufacturing of Side-Coupled Cavity Linac Structures from Pure Copper: A first Concept". In: *Instruments* 7 (2023), p. 56. DOI: 10.3390/instruments7040056.

[19] M. Mayerhofer, A. Bergmaier, G. Datzmann, H. Hagn, **R. Helm**, J. Mitteneder, R. Schubert, L. Picardi, P. Nenzi, C. Ronsivalle, H. Wirth, and G. Dollinger. "Concept and performance evaluation of two 3 GHz buncher units optimizing the dose rate of a novel preclinical proton minibeam irradiation facility". In: *PLOS One* 16 (2021). DOI: 10.1371/journal.pone.0258477.

[20] L. Ma, L. Gutierrez, R. Verbeke, A. D'Haesem, M. Waqas, M. Dickmann, **R. Helm**, I. Vankelecom, A. Verliefde, and E. Cornelissen. "Transport of organic solutes in ion-exchange membranes: Mechanisms and influence of solvent ionic composition". In: *Water Research* 190 (2021), p. 116756. DOI: 10.1016/j.watres.2020.116756.

[21] D. Petschke, **R. Helm**, M. Haaks, and T. E. M. Staab. "Limitations on the positron lifetime spectra decomposability applying the iterative least-square re-convolution method using the instrumental responses obtained from 207Bi and 60Co". In: *Acta Physica Polonica A* 137 (2020), pp. 171–176. DOI: 10.12693/APhysPolA.137.171.

[22] D. Petschke, **R. Helm**, and T. E. M. Staab. "Data on pure tin by Positron Annihilation Lifetime Spectroscopy (PALS) acquired with a semi-analog/digital setup using DDRS4PALS". In: *Data in Brief* 22 (2019), pp. 16–19. DOI: 10.1016/j.dib.2018.11.121.

Danksagung

In diesem Kapitel soll es einmal weniger um Physik und mehr um die Menschen gehen, die direkt oder indirekt zum Entstehen dieser Arbeit beigetragen haben. Ohne sie wäre dieses Projekt in der vorliegenden Form nicht möglich gewesen. Sollte jemand im Folgenden nicht namentlich erwähnt sein, bitte ich dies zu entschuldigen – mein Dank gilt selbstverständlich auch ihm oder ihr.

Meinen besonderen Dank schulde ich Prof. Dr. Günther Dollinger, der mir durch seine finanzielle Unterstützung – trotz der unglücklichen Abschaltung des FRM-II – ermöglicht hat, meine Experimente, wenn auch in anderer Form, erfolgreich zum Abschluss zu bringen. Darüber hinaus hat er mir immer wieder vor Augen geführt, meinem eigenen Urteilsvermögen zu vertrauen und alles kritisch zu hinterfragen.

Dr. Werner Egger danke ich für die zahlreichen abendlichen Diskussionen über physikalische Themen – nicht nur über Positronen – sowie für anregende Gespräche über Politik und Geschichte. Besonders hervorheben möchte ich, dass er stets an mich gedacht hat, wenn er in der Bibliothek ausrangierte Bücher sichtete, und mir regelmäßig ein interessantes Werk zukommen ließ. Ich hoffe, dass ich irgendwann die Zeit finde, all diese Bücher zu lesen.

Dr. Marcel Dickmann danke ich für seine wissenschaftliche Neugier und seinen Drang, immer wieder Neues auszuprobieren. Besonders dankbar bin ich ihm für die Einbindung in viele seiner Projekte, die mir nicht nur wertvolle Kontakte verschafft, sondern auch meinen Einblick in die Vielfalt der Materialphysik mit Positronen erweitert haben. Für seinen weiteren Weg in Frankreich wünsche ich ihm alles Gute.

Dr. Johannes Mitteneder danke ich für die damalige Ermutigung, mich am LRT2 zu bewerben – man kann wohl sagen, dass er die "Urschuld" an dieser Arbeit trägt. Außerdem bin ich ihm für seine nie endende Hilfsbereitschaft dankbar, insbesondere im Bereich der Fahrradphysik.

Dr. Michael Mayerhofer danke ich für die anregenden Diskussionen und die sonnigen Nachmittage an der Isar – vor allem jedoch für die Einführung in die Beschleunigerphysik sowie seine Hilfestellungen bei CST Studio.

M.Sc. Johannes Lehtonen danke ich für die hervorragende Zusammenarbeit und sein außerordentliches Engagement beim Bau des TAPIR-Instruments. Ohne seinen

Einsatz wäre dieses TAPIR-Kapitel sicherlich deutlich kürzer ausgefallen.

M.Sc. Jonas Menzel danke ich für seine Arbeit am neuen Chopper-Design und seine fast schon an "schwarze Magie" erinnernden CAD-Fähigkeiten.

Ebenso danke ich Paul, Niklas, Tami, Laura, Vicky, Winfred, Hammiche und Jendrik, die ich während ihrer Bachelor- und Masterarbeiten betreuen durfte. Die Zusammenarbeit mit ihnen war äußerst lehrreich und hat mir wertvolle Erfahrungen für die zukünftige Betreuung von Studierenden vermittelt.

Dr. Peter Sperr danke ich dafür, dass ich trotz seines wohlverdienten Ruhestands weiterhin auf seinen jahrzehntelangen Erfahrungsschatz zurückgreifen durfte. Diese Form des Wissenstransfers ist zweifellos eine der wichtigsten Säulen der Positronen-Community.

Dr. Stefanie Girst danke ich für ihr enormes Organisationstalent, durch das mir sicher einiges an Arbeit erspart blieb und ich mich stärker auf die Anfertigung dieser Schrift konzentrieren konnte.

Lukas Hackel und Ralf Schubert möchte ich besonders danken. Sie haben mit Geduld und Umsicht meine Konstruktionen verbessert und oftmals erst umsetzbar gemacht – auch wenn sie dabei gelegentlich kurz vor dem Nervenzusammenbruch standen.

Dr. Catherine Corbel danke ich für ihre Hilfsbereitschaft und ihre Mitarbeit an unseren Publikationen sowie dafür, dass ich von ihrem enormen Wissensschatz über Positronwechselwirkungen mit Halbleitern und über die Darstellung von Ergebnissen auf Konferenzen profitieren durfte. Darüber hinaus möchte ich hervorheben, dass wir uns als Gruppe glücklich schätzen können, da sie uns an vielen spannenden Forschungsprojekten teilhaben ließ und wertvolle zukünftige Kooperationspartner vermittelt hat.

Dr. Henk Schut danke ich für eine hervorragende und lehrreiche Zeit am Reaktorinstitut in Delft, in der er mich in die Künste der Doppler-Broadening-Spektroskopie eingeführt hat. Ebenso erinnere ich mich gerne an die geselligen Stunden im Reaktorpub, wo wir das ein oder andere Bier miteinander verköstigen konnten.

Vielen Dank an meine Kooperationspartner Prof. Roberto Brusa, Prof. Dr. David Keeble, Dr. Rhea Verbeke und Prof. Dr. Stephan Eijt für die hilfreichen Diskussionen und die Zusammenarbeit über die letzten Jahre.

Ebenso danke ich Dr. Kay Lee, Prof. Dr. Duesberg und Silke Boche für die Kooperation sowie die Herstellung und Vermessung der Metal-Oxide-Halbleiter-Systeme.

Mein besonderer Dank gilt außerdem unseren Kollegen Dr. Andreas Wagner, Dr. Maciej Oskar Liedke, Dr. Maik Butterling (nun an der TU Delft) und Dr. Eric Hirschmann vom Helmholtz-Zentrum Dresden-Rossendorf, die durch ihre hervorragende Arbeit am gepulsten Positronstrahlsystem die erfolgreichen Drift-Experimente

überhaupt erst ermöglicht haben.

Besonders dankbar bin ich meinen Eltern, Rainer und Brigitte, die immer hinter mir standen und durch ihre Unterstützung diese lange wissenschaftliche Ausbildung erst möglich gemacht haben. Ebenso danke ich meiner Frau Christina, die mich während der Anfertigung dieser Arbeit entlastet hat und in dieser Zeit auch meine weniger guten Gemütslagen mit viel Geduld ertragen musste. Schließlich möchte ich auch meiner Schwester Lorraine, ihrem Mann Max und meiner Nichte Luna danken.

Zu guter Letzt danke ich allen Kolleg*innen vom LRT2 und der NEPOMUC-Gruppe für die vielen netten Gespräche und die erinnerungswürdigen Momente während zahlreicher Konferenzen und Dienstreisen.